Experimental study on kinetic instabilities in electron cyclotron resonance heated plasma

Bichu Subhash Bhasi Bhaskar

JYVÄSKYLÄN YLIOPISTO
UNIVERSITY OF JYVÄSKYLÄ

Université Grenoble Alpes

THÈSE

Pour obtenir le grade de

DOCTEUR DE L'UNIVERSITE GRENOBLE ALPES

préparée dans le cadre d'une cotutelle entre l'*Université Grenoble Alpes* et *University of Jyväskylä*

Spécialité : **Physique subatomique et astroparticules**

Arrêté ministériel : le 25 mai 2016

Présentée par

« Bichu / SUBHASH BHASI BHASKAR »

préparée au sein des **Laboratoire de Physique Subatomique & Cosmologie** et **Jyväskylän yliopiston fysiikan laitos**

dans **les Écoles Doctorales Physique,UGA** et **Faculty of Mathematics and Science,JYU**

Etude expérimentale des instabilités cinétiques dans le plasma chauffé à la résonance cyclotronique électronique

Thèse soutenue publiquement le **24 Mai 2022**
devant le jury composé de :

M. Iain David MOORE
Professeur à Jyväskylän Yliopisto, Président
M. Osvaldo Daniel CORTAZAR
Professeur à Universidad Castilla la Mancha, Rapporteur
M. Gilles BAN
Professeur à l'ENSICAEN, Rapporteur
M. Johann COLLOT
Professeur à l'Université Grenoble Alpes, Examinateur
M. Pierre DELAHAYE
Chargé de recherche au Grand Accélérateur National d'Ions Lourds, Examinateur
M. Hannu KOIVISTO
Maître de conférence à Jyväskylän Yliopisto, co-Directeur de thèse
M. Thomas THUILLIER
Ingénieur de recherche au Laboratoire de Physique Subatomique et de Cosmologie, co-Directeur de thèse

ABSTRACT

Subhash Bhasi Bhaskar, Bichu
Experimental study on kinetic instabilities in electron cyclotron resonance heated plasma
Jyväskylä: University of Jyväskylä, 2022, 112 p. (+included articles)

ISSN 2489-9003; 516
ISBN 978-951-39-9137-1 (PDF)
Dissertation.

Electron Cyclotron Resonance Ion Sources (ECRISs) are used to produce Highly Charged Ions (HCI). Ions are created in a magnetised plasma sustained by the resonant interaction of electron gyrofrequency with an externally applied Radio Frequency (RF) electromagnetic wave. It has been established that the ECRIS plasmas exhibit kinetic plasma instabilities, limiting the parameter space available for optimising the extracted beam currents. The thesis is devoted to gaining insights into the mechanisms underlying the formation of these kinetic instabilities on various ECR ion sources. The thesis is divided into six chapters. The first two chapters deal with the relevance of the work in the context of various scientific fields and the background theoretical knowledge required for understanding the processes involved in electron cyclotron resonance plasma production, along with the background on kinetic instabilities. The third chapter is devoted to the technical aspects of ECR ion sources, using one of the ion sources utilised in the experiments as a representative example, as well as an in-depth discussion of the diagnostic methods employed during the course of the dedicated experimental campaigns. One of the goals of this work is to refine the understanding of the physical mechanisms determining the complex relation between the ECRIS magnetic field parameters and the transition from stable to unstable operation regime. As a result, a computational tool was developed to efficiently calculate the three-dimensional magnetic field structure in ECRIS and extract the relevant magnetic field parameters from the closed iso-magnetic field surface where the electron's gyrofrequency equals the frequency of an externally applied electromagnetic wave. Chapter four details the development of this computational tool. Additionally, the same chapter has a comprehensive description of the signal processing code used to conduct statistical analysis on a huge amount of data collected during one of the experimental campaigns devoted to the temporal study of instability-induced electromagnetic emissions. The fifth chapter summarises all experimental campaigns and the major findings obtained. Several of the general characteristics of the ECRIS magnetic field were determined using magnetic field computations

in five different ion sources. A relationship between the energy of hot electrons and the average magnetic field gradient parallel to the magnetic field lines on the resonance surface has been established through experiments conducted with superconducting SECRAL-II ion source at IMP-CAS, China. The effect of magnetic field configuration on managing the hot electron population and consequently controlling the instability was established through studies conducted at GANIL, France, utilising the GTS ion source. The ECRIS at JYFL, Finland was used to conduct an experimental campaign which established a relationship between plasma bremsstrahlung and the energy distribution of electrons lost from confinement, as well as the effect of kinetic instabilities on the shape of energy distribution of lost electrons. Another experimental campaign with JYFL 14 GHz ECR ion source revealed a temporal relation between pulsated emission of electromagnetic wave during instability with the strength of the emitted signal by undertaking a comprehensive statistical analysis of the collected data. The experiment also revealed a grouping (temporally) of electromagnetic emissions due to instability which were previously observed in space and magnetospheric plasma. The final chapter provides a comprehensive discussion of all the experiments performed along with the scope of future research in this field.

Keywords: ECR ion source, plasma physics, plasma instabilities, magnetically confined plasmas, plasma bremsstrahlung, electron energy distribution.

TIIVISTELMÄ (ABSTRACT IN FINNISH)

Elektronisyklotroniresonanssi-ionilähteitä (ECRIS) käytetään korkeasti varattujen ionien (HCI) tuottamiseen. Ionit luodaan magneettisesti vangitussa plasmassa, jota ylläpidetään käyttäen hyväksi elektronien syklotronitaajuuden ja ulkoisesti tuotetun radiotaajuisen (RF) sähkömagneettisen aallon välistä resonanssivuorovaikutusta. Aikaisemmin on havaittu, että ECRIS-plasmoissa esiintyy kineettisiä epästabiilisuuksia, jotka rajoittavat ionilähteen säätömahdollisuuksia korkeasti varattujen ionisuihkujen tuotannon optimoimiseksi. Väitöskirjassa pyritään lisäämään ymmärrystä niistä mekanismeista, jotka ovat eri ECR-ionilähteissä näiden kineettisten epästabiilisuuksien muodostumisen taustalla.

Tutkielma on jaettu kuuteen lukuun. Kahdessa ensimmäisessä luvussa käsitellään työn merkitystä eri tieteenalojen kannalta ja teoreettista taustatietoa, jota tarvitaan elektronisyklotroniresonanssiplasmaan liittyvien tuotantoprosessien sekä kineettisten epästabiilisuuksien ymmärtämiseksi. Kolmas luku on omistettu kokeissa käytettyjen ionilähteiden tärkeimpien teknisten ratkaisujen kuvaamiseksi sekä perusteelliselle keskustelulle diagnostisista menetelmistä, joita käytettiin kokeellisten kampanjoiden aikana.

Yksi tämän työn tavoitteista on löytää tekijöitä, jotka vaikuttavat ECR-ionilähteen plasman siirtymisen stabiilista tilasta epästabiiliin tilaan. Tämän työn tuloksena kehitettiin mm. laskentatyökalu, jolla voidaan nopeasti laskea ECR-ionilähteen kolmiulotteinen magneettikenttärakenne ja määrittää asiaankuuluvat magneettikenttäparametrit suljetusta magneettikenttärakenteesta, jonka sisällä elektroninen lämmittämiseen vaadittava resonanssiehto täyttyy. Neljännessä luvussa käsitellään yksityiskohtaisesti tämän laskentatyökalun kehittämistä. Lisäksi samassa luvussa on kattava kuvaus signaalinkäsittelykoodista, joka kehitettiin myös väitöstyön aikana ja jota käytettiin tilastollisen analyysin tekemiseen suuresta datamäärästä. Tämä data kerättiin epästabiilissa plasmaolosuhteessa ja sen avulla pyrittiin määrittämään epästabiilisuuspurskeisiin liittyviä riippuvuuksia.

Viidennessä luvussa esitetään yhteenveto tähän väitöskirjaan liittyvistä tutkimuskampanjoista ja tärkeimmistä tuloksista. Kampanjoissa käytettyjen viiden ECR-ionilähteen oleellisimmat magneettikentän ominaisuudet laskettiin työssä kehitetyn laskentatyökalun avulla. Kuumien elektronien energian ja keskimääräisen magneettikenttägradientin (resonanssipinnalla, magneettikentän suunnassa) välinen suhde määritettiin edellä mainitun työkalun ja suprajohtavalla SECRAL-II-ionilähteellä kerätyn mittausdatan avulla (IMP-CAS, Kiina). Magneettikentän konfiguraation vaikutus kuumaan elektronipopulaatioon ja siten plasman epästabiliisuuksien hallintaan todettiin tutkimuksissa, jotka tehtiin GANIL:ssa Ranskassa GTS-ionilähdettä käyttäen. Toisessa kampanjassa, jossa käytettiin JYFL:n 14

GHz:n ECR:ää, selvitettiin plasman tuottaman jarrutussäteilyn ja magneettisesta vanginnasta poistuvien elektronien energiajakaumaa sekä kineettisten epästabiilisuuksien vaikutusta karkaavien elektronien energiajakauman muotoon. Toinen kokeellinen kampanja JYFL 14 GHz ECR-ionilähteellä paljasti epästabiilissa plasmassa tapahtuvien epästabiilisuuspurskeiden voimakkuuden ja tapahtumatiheyden välisen ajallisen yhteyden. Kampanjan aikana mitatulle suurelle datamäärälle tehtiin tilastollinen analyysi työssä kehitetyn signaalinkäsittelykoodin avulla. Mittauskampanjan avulla löysimme epästabiilisuuksien ryhmittymisen (ajallisesti), mikä on aiemmin havaittu avaruudessa ja magnetosfäärin plasmassa. Viimeisessä luvussa käsitellään kattavasti kaikkia suoritettuja kokeita sekä tämän tutkimusalan tulevaa tutkimusta.

RÉSUMÉ (ABSTRACT IN FRENCH)

Les sources d'ions à la résonance cyclotronique électronique (ECR) sont utilisées pour produire des ions hautement chargés. Les ions sont produits dans un plasma magnétisé entretenu par l'interaction résonante de la gyrofréquence des électrons avec une onde électromagnétique radiofréquence. Les plasmas ECR présentent des instabilités cinétiques, ce qui limite l'espace des paramètres disponibles pour optimiser les courants d'ions extraits. La thèse est consacrée à l'étude et à la compréhension des mécanismes sous-tendant la formation de ces instabilités cinétiques sur diverses sources d'ions ECR. La thèse est divisée en six chapitres. Les deux premiers traitent de la pertinence du travail dans le contexte de divers domaines scientifiques et des connaissances théoriques de base nécessaires à la compréhension des processus impliqués dans la production du plasma ECR, ainsi que du contexte des instabilités cinétiques. Le troisième chapitre est consacré aux aspects techniques de l'une des sources d'ions utilisées dans les expériences, ainsi qu'à une discussion approfondie des méthodes de diagnostic employées au cours des nombreuses campagnes expérimentales menées. L'un des objectifs de ce travail est d'affiner la compréhension des mécanismes physiques qui déterminent la relation complexe entre les paramètres du champ magnétique de l'ECRIS et la transition du régime de fonctionnement stable au régime instable. Ainsi, un outil numériquea été développé pour calculer rapidement la structure tridimensionnelle du champ magnétique dans une source ECR et extraire les paramètres de champ magnétique pertinents. A savoir, la surface de champ iso-magnétique fermée où la fréquence cyclotronique de l'électron égale la fréquence de l'onde électromagnétique injectée. Le chapitre quatre détaille le développement de cet outil de calcul. En outre, ce chapitre contient une description du code de traitement du signal utilisé pour effectuer une analyse statistique sur une grande quantité de données collectées pendant l'une des campagnes expérimentales ; campagne consacrée à l'étude temporelle des émissions électromagnétiques induites par l'instabilité. Le cinquième chapitre résume l'ensemble des campagnes expérimentales et les principaux résultats obtenus. La plupart des caractéristiques générales du champ magnétique de l'ECRIS ont été déterminées à l'aide de calculs de champ magnétique dans cinq sources d'ions différentes. Une relation entre l'énergie des électrons chauds et le gradient de champ magnétique moyen parallèle aux lignes de champ magnétique sur la surface de résonance a été établie grâce à des expériences menées dans la source d'ions supraconductrice SECRAL-II à l'IMP-CAS, en Chine. L'effet de la configuration du champ magnétique sur la gestion de la population d'électrons chauds et, par conséquent, sur le contrôle de l'instabilité, a été établi par des études menées au GANIL, en France, à l'aide de la source d'ions GTS. Une autre campagne utilisant l'ECR JYFL 14 GHz en Finlande a établi une relation entre le rayonnement bremsstrahlung émis par le

plasma et la distribution d'énergie des électrons s'échappant de la source, ainsi que l'effet des instabilités cinétiques sur la forme de la distribution d'énergie des électrons perdus. Une autre campagne expérimentale sur la source d'ions ECR 14 GHz de JYFL a révélé une relation temporelle entre l'émission pulsée d'ondes électromagnétiques pendant l'instabilité et la force du signal émis en effectuant une analyse statistique complète des données collectées. L'expérience a également révélé un regroupement (dans le temps) des émissions électromagnétiques dues à l'instabilité, phénomène précédemment observées dans les plasmas spatiaux et magnétosphériques. Le dernier chapitre présente une discussion d'ensemble de toutes les expériences réalisées ainsi que la portée des recherches futures dans ce domaine. Les publications associées à cette recherche sont proposées en annexe.

Author Bichu SUBHASH BHASI BHASKAR

Cotutelle dissertation between

Department of Physics
Université Grenoble Alpes
Grenoble, France

and

Department of Physics
University of Jyväskylä
Jyväskylä, Finland

Supervisors Dr. Thomas THUILLIER
Pôle Accélérateurs et Sources d'Ions
Laboratoire de Physique Subatomique et de Cosmologie (LPSC)
CNRS/IN2P3 Grenoble, France

Dr. Hannu KOIVISTO
Department of Physics
University of Jyväskylä
Jyväskylä, Finland

Reviewers Prof. Dr. Gilles BAN
Laboratoire de Physique Corpusculaire de Caen (LPC)
CNRS/IN2P3
Université de Caen Normandie (UCN)
Caen, France

Prof. Dr. Osvaldo DANIEL CORTÁZAR
University of Castilla-La Mancha
Ciudad Real, Spain

Opponent Dr. Pierre DELAHAYE
GANIL, CEA/DRF – CNRS/IN2P3
Caen, France

Jury

Prof. Dr. Iain David MOORE
Department of Physics
University of Jyväskylä
Jyväskylä, Finland

Prof. Dr. Johann COLLOT
Laboratoire de Physique Subatomique et de Cosmologie (LPSC)
LPSC, CNRS/IN2P3
Université Grenoble Alpes
Grenoble, France

PREFACE

This dissertation is the product of research undertaken in the "Laboratory of Subatomic Physics and Cosmology (LPSC)" at Grenoble, France, and in the Department of Physics, University of Jyväskylä (JYFL) at Jyväskylä, Finland. Beginning my doctoral studies in France and subsequently relocating to Finland, I've had the opportunity to work in some of the world's most renowned laboratories and met some incredible people.

Firstly, I would like to thank from the bottom of my heart, my supervisors Dr. Thomas Thuillier and Dr. Hannu Koivisto and whatever I have achieved would not have been possible without the constant guidance and support from these two amazing persons. I would like to express my gratitude to Dr. Thuillier for introducing me to the beautiful world of ECR ion sources and guiding me through the field's fundamentals, which were previously unfamiliar to me. I am deeply indebted to Dr. Koivisto who has not only been a great supervisor but also an excellent mentor who had provided me with a constant source of motivation.

I must acknowledge that I am fortunate to have Dr. Ville Toivanen as a fantastic colleague, guide and friend who made me feel comfortable discussing even the smallest details of the work and helped me in overcoming various obstacles encountered during the Ph.D. life. I am also grateful to have Dr. Olli Tarvainen monitoring my work and helping me in designing the experiments and providing prompt replies to all the scientific queries. I am thankful to Prof. Dr. Osvaldo Daniel Cortázar and Prof. Dr. Gilles Ban for reviewing my dissertation and providing most valuable comments.

I would also like to thank Dr. Maud Baylac and Mr. Julien Angot of LPSC, Grenoble for helping me with the Ph.D. work conducted at LPSC. Additionally, I would like to express my gratitude to Dr. Taneli Kalvas and Mr. Risto Kronholm of JYFL for their computational and technical support during my Ph.D. study. During my doctoral studies I had the fortune to work with different research groups and I would like to take this opportunity to extend my gratitude towards Dr. Ivan Izotov and Dr. Vadim Skalyga of IAP-RAS, Russia for their productive conversations regarding various experimental campaigns at JYFL and Mr. Jibo Li of IMP-CAS, China for the collaborations and the discussions regarding the experimental campaign performed at IMP-CAS.

I would like to extend my gratitude towards my colleagues Mr. Miha Luntinen, Mr. Sami Kosonen, Ms. Niyati Venkatesan, Mr. Sami Demirci and Dr. Kofi Brobbey for their support.

I have no words to adequately express my deepest appreciation for my friends, who have been a continuous pillar of support during the course of my doctoral studies. I whole heartily thank Sajin, Karthik, Niyas, Abhiram, Prabhash, Kiran, Asha, Mithun, Swadish, Anto, Deepak, Thomas, Stephy, Arunkumar, Abhijith, Anjusree, Arya, Brijesh, Deepthy, Induja, Jaismon, Nandan, Sajan, Sibeesh, Susmitha, Roopesh, Jobin, Arsha, Lakshmipriya, Akhil, Krishna, Namanu, Sinara and Sameer for providing the much needed emotional support especially during the hard times of COVID-19.

My greatest debt of gratitude has always been to my parents and sister, who have stood by me through all of my highs and lows and have shown faith in me.

I would like to acknowledge the funding supported by the Academy of Finland Project funding (No: 315855) and University of Grenoble Alpes under the EMERGENCE program.

LIST OF INCLUDED ARTICLES

PI Li, JB and Li, LX and Bhaskar, BS and Toivanen, V and Tarvainen, O and Hitz, D and Li, LB and Lu, W and Koivisto, H and Thuillier, T and Guo, JW and Zhang, XZ and Zhao, HY and Sun, LT and Zhao, HW. Effects of magnetic configuration on hot electrons in a minimum-B ECR plasma. *Plasma Physics and Controlled Fusion* ***62****, 9 095015*, 2020.

PII Toivanen, V and Bhaskar, BS and Koivisto, H and Maunoury, L and Tarvainen, O and Thuillier, T. Influence of axial mirror ratios on the kinetic instability threshold in electron cyclotron resonance ion source plasma. *Physics of Plasmas* ***29****, 1 013501*, 2022.

PIII Bhaskar, BS and Koivisto, H and Tarvainen, O and Thuillier, T and Toivanen, V and Kalvas, T and Izotov, I and Skalyga, V and Kronholm, R and Marttinen, M. Correlation of bremsstrahlung and energy distribution of escaping electrons to study the dynamics of magnetically confined plasma. *Plasma Physics and Controlled Fusion* ***63****, 9 095010*, 2021.

PIV Bhaskar, BS and Koivisto, H and Tarvainen, O and Thuillier, T and Toivanen, V. Quasi-periodical kinetic instabilities in minimum-B confined plasma. *AIP Advances* ***12****, 1 015223*, 2022.

The author has performed the experimental work, the data analysis and the writing of the articles PIII and PIV. The author had an integral role in the computational analysis and took part in the discussion of article PII, and has performed computational analysis for article PI.

CONTENTS

1 INTRODUCTION

The applications of Electron Cyclotron Resonance Ion Sources (ECRIS) have increased dramatically over the last decades. The ECR ion sources are used to produce Highly Charged Ions (HCIs) for various purposes including atomic and nuclear physics experiments, radiation hardness testing of space electronics, radiation therapy for cancer treatment, particle physics experiments and so on. In nuclear and particle physics research, the ECR ion sources are utilised as injectors for linear accelerators, Van-de-Graff generators, synchrotrons and cyclotrons. In atomic and surface physics, the ECR ion sources provide intensive beams of highly charged ions for collision experiments or surface examinations. One significant advantage of this type of ion generator is that ions of all elements can be created. Furthermore, the ion source has almost no wear parts, such as filaments. As a result, steady ion beams can be realised for extended periods of time (days to months), with the sole limitation being the material consumption of the utilised element. Metals that are injected into the source as atoms that are sputtered into the plasma, or that are evaporated from an oven must be replaced after a set time. The ECR ion sources operate at a low gas pressure and have a high plasma ionisation efficiency. As a result, they are particularly adapted for producing ion beams of radioactive, rare, or extremely expensive elements. Since the first commissioning of ECR ion source in 1975, the performance in terms of possible charge states and their intensity has improved rapidly.

In the ECRIS, the highly charged ions are produced in non-equilibrium plasma confined in a magnetic structure. The magnetic confinement is realised by a superposition of solenoid and hexapole magnetic fields, thus creating a minimum-B confinement topology. ECRIS plasmas have been demonstrated to exhibit kinetic plasma instabilities, which strongly limits the intensities of the highly charged ion beams. The kinetic instabilities are driven by the anisotropy and the non-monotonicity of the high-energy tail of the electron velocity/energy distribution

(EVD/EED) of the ECR ion source plasmas. The EED is affected by the magnetic field of the ECRIS. The purpose of this work is to refine the understanding of the physical mechanisms determining the complex relation between the ECRIS magnetic field parameters and the transition from stable to unstable operation regime.

It has long been recognised that controlling kinetic instabilities is one of the most challenging issues in the development of high-temperature fusion plasmas [1] and medical accelerators [2]. Furthermore, such instabilities have also been observed in space plasmas causing coherent radio-emissions from the Solar corona [3, 4, 5] and the Earth's magnetosphere [6, 7, 8, 9]. This thesis also focuses on temporal grouping of cyclotron emissions due to instabilities which has been observed extensively on space plasmas [6, 7, 10, 11] but is reported for the first time here with systematic studies using ECR-heated laboratory plasmas. As a result, the kinetic instability investigations carried out with ECRIS contribute to a better understanding of the instabilities that occur in various laboratory plasmas and space plasmas, which is the primary subject of this thesis.

This thesis is organised as follows: Chapter 2 discusses the theoretical foundation required to understand the operation of ECR plasmas and provides a brief discussion of the theoretical background of kinetic instabilities observed in ECR plasmas. The third chapter describes the ion sources, experimental setups, and diagnostic methods that have been used in the experimental part of this work. Special emphasis has been given to JYFL 14 GHz ECR ion source, which is operated at the Accelerator Laboratory in the Department of Physics at the University of Jyväskylä since most of the experiments were conducted with this ion source. Chapter 4 describes the development of a robust computational tool for obtaining the magnetic field distribution in ECRIS, as well as the development of a signal processing and data analysis tool to study the temporal evolution of instability-induced signals. In Chapter 5 the major findings of the experimental work are summarised. The chapter is organised into four sections: the first section contains the results demonstrating how the magnetic field factors affect the instability of various ion sources, as well as a comparison of five distinct ion sources employed in this thesis work. The second section focuses on the role played by the axial mirror ratios in mitigating hot electrons and their influence on the kinetic instabilities. The third section of Chapter 5 focuses on plasma bremsstrahlung and the energy distribution of lost electrons, with an emphasis on kinetic instability. The fourth section presents the first systematic investigation on the temporal structure and magnitude of the kinetic instabilities in the ECR plasma. Chapter 6 contains a thorough discussion as well as the implications that may be drawn from it.

2 THEORETICAL ASPECTS OF ECR PLASMA

2.1 Fundamentals of plasma physics

Almost all of the matter that can be observed in the universe is in the plasma state. Plasma is a collection of freely moving ions, electrons and neutrals. They are frequently referred to as the "fourth state of matter" due to their unique physical characteristics that distinguish them from solids, liquids, and gases. In the universe, plasmas are formed naturally in the sun, solar wind, earth's magnetosphere, ionosphere, interstellar and intergalactic space, pulsars and even in the region around black holes. Plasma can be created in the laboratory by increasing the temperature of a substance until a high fraction of ionisation is obtained. In the laboratory, there are numerous methods for producing plasma. Depending on the method, the properties of plasma also changes. Since plasma consists of electrically charged particles, it is capable of producing electromagnetic fields as well as interacting with externally imposed electromagnetic fields. This property provides the extra advantage of studying the plasma using both electric and magnetic fields as well. Plasmas are also good electrical and thermal conductor owing to its property of higher electron mobility.

For laboratory plasma, to maintain the plasma state, an external source of energy must be supplied to prevent the charged particles from recombining to neutrals. The range of diverse plasmas found in the universe and in the laboratory is depicted in Fig. 2.1. The plasma studied in this thesis work is denoted by the abbreviation 'ECRIS,' which stands for the Electron Cyclotron Resonance Ion Source.

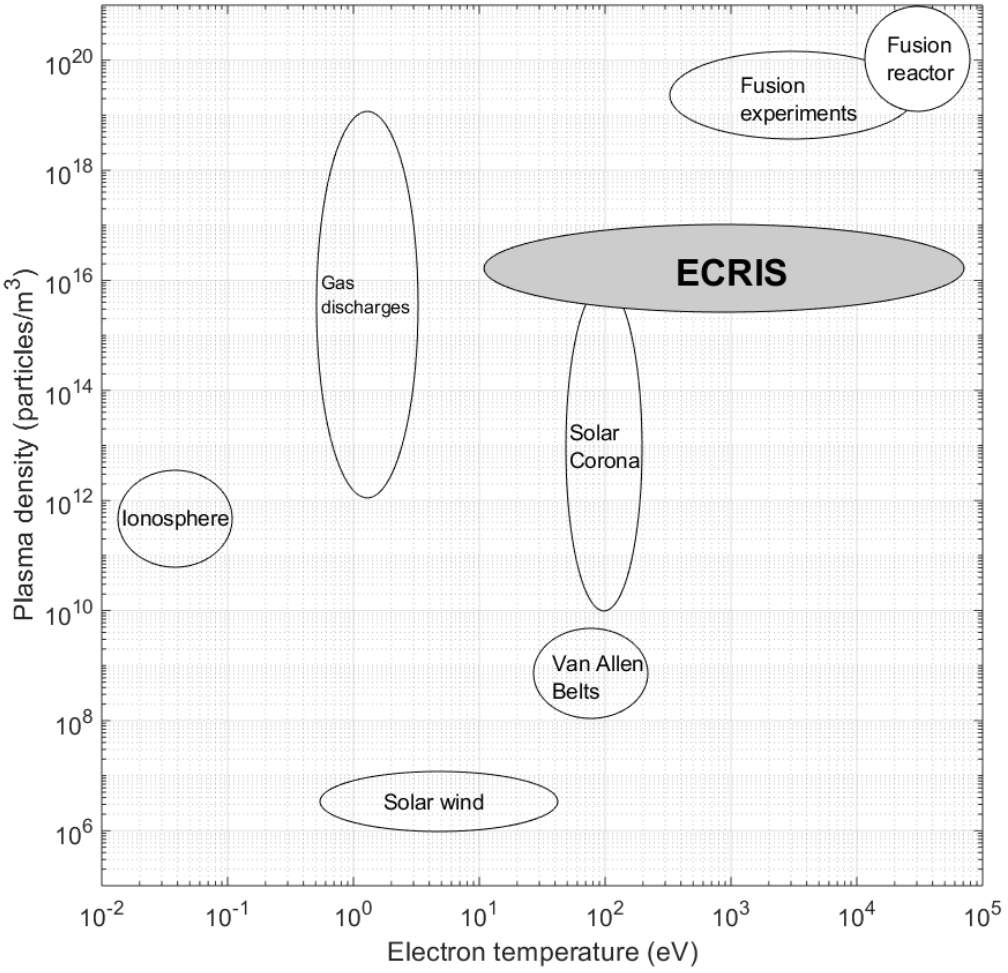

FIGURE 2.1 Plasma found in laboratory and in the nature (*1 eV = 11600 K).

The main macroscopic parameters which define plasma are the electron density (n_e), the ion density (n_i), the neutral particle density (n_o), the ion and electron temperature (T_i and T_e, respectively) and the degree of ionisation (α) which is defined as:

$$\alpha = \frac{n_i}{n_i + n_o} \tag{2.1}$$

Based on its electron and ion temperature, plasmas are also classified into hot and cold plasmas. It is considered cold when $T_i \ll T_e$ and hot when $T_i \cong T_e$; in other words the hot plasma is the one which attains local thermodynamic equilibrium by means of collisions. In Electron Cyclotron Resonance (ECR) plasmas, the ion temperature is low (of the order of eV) compared to that of electron temperature (of the order of keV); hence ECR plasmas can be categorised as non-equilibrium cold plasmas (since $T_i < T_e$).

The ionised charged particles can be categorised as plasma if it satisfies the condi-

tions listed below. The detailed description of each condition is provided in the subsequent sections.

a) The Debye length should be smaller than the size of plasma.

b) The number of particles within a Debye sphere must be large.

c) The plasma frequency should be greater than electron-neutral collision frequency.

Here the plasma is considered as quasi-neutral which means that even though it consists of a collection of positive and negatively charged particles, in equilibrium the overall charge density must cancel each other.

2.1.1 Quasi-neutrality and Debye length

The quasi-neutrality is the phenomenon shown by the plasma to exhibit neutral charge collectively under equilibrium conditions in the absence of external perturbations. In the macroscopic scale, quasi-neutrality can be defined as:

$$\sum_i Z_i n_i = n_e \tag{2.2}$$

where Z_i is the charge state of ion specie i, n_i and n_e are ion and electron number densities, respectively. In the macroscopic scale the quasi-neutrality can be defined as the state where the plasma dynamically adjusts the local charge distribution in response to a perturbation. However in the microscopic scale, the perturbations lead to a local deviation from neutrality and these deviations will be shielded by redistribution of the adjacent charges. This self shielding potential surrounding a point test charge is known as Debye–Hückel potential which is given by the equation:

$$\phi(r) = \frac{q}{4\pi\epsilon_0 r} exp\left(-\frac{\sqrt{2}r}{\lambda_D}\right) \tag{2.3}$$

where ϵ_0 is permittivity of free space, r is the distance from the charge and λ_D is the Debye length, where λ_D can be defined as the characteristic dimension below which the plasma quasi-neutrality is broken locally and hence plasma becomes sensitive to electric field at distances less than λ_D. The Debye length is given by the equation:

$$\lambda_D = \sqrt{\frac{\epsilon_0 k_B / e^2}{n_e / T_e + \sum_j Z_j^2 n_j / T_i}} \tag{2.4}$$

where k_B is the Boltzmann constant, n_e is the electron density, T_e is the electron

temperature, e is the charge of electron and n_j is the density of atomic species j with positive ionic charge $Z_j e$. Often the ion term is excluded in the definition of the Debye length, and as a result, the formula (2.4) reduces to:

$$\lambda_D = \sqrt{\frac{\epsilon_0 k_B T_e}{n_e e^2}} \tag{2.5}$$

The Debye sphere is a sphere with a radius λ_D, and by definition the plasma only interacts with the charge that is contained inside the sphere. The average number of the electrons contained within the Debye sphere is given by:

$$\Lambda = \frac{4}{3}\pi \lambda_D^3 n_e \tag{2.6}$$

Since the shielding effect arises from the collective behaviour of particles, the Debye sphere must include a large number of electrons, i.e.

$$n_e \lambda_D^3 \gg 1 \tag{2.7}$$

2.1.2 Plasma Frequency

Plasma frequency is defined as the frequency at which plasma oscillates in an attempt to regain charge neutrality after an external perturbation. Those oscillations are driven by the electrons which are more mobile than ions. When the plasma strives to restore charge neutrality, an electric field is created, and due to the enormous mass difference between electrons and ions, the electrons react more rapidly to the perturbation. As a result, plasma oscillates (w.r.t quasi-static ions) at a frequency (angular) given by:

$$\omega_p = \sqrt{\frac{n_e e^2}{\epsilon_0 m_e}} \tag{2.8}$$

where ω_p is the plasma frequency, e and m_e are the charge and the mass of electrons, n_e is the number density of electrons and ϵ_0 is the permittivity of free space. When electrons collide with neutral particles, the electron plasma frequency is dampened. Consequently, the collision frequency must be less than the plasma frequency to exhibit collective behaviour. Another consequence of plasma frequency is that the plasma can reflect electromagnetic waves with frequency $\omega < \omega_p$. When plasma is sustained by an EM wave of frequency ω_{RF}, another consequence arising from expression (2.8) is that there exists a maximum critical density $n_{e,crit}$ above which the EM wave cannot anymore penetrate into the plasma:

$$n_{e,crit} = \frac{\epsilon_0 m_e \omega_{RF}^2}{e^2} \tag{2.9}$$

2.1.3 Plasma sheath and plasma potential

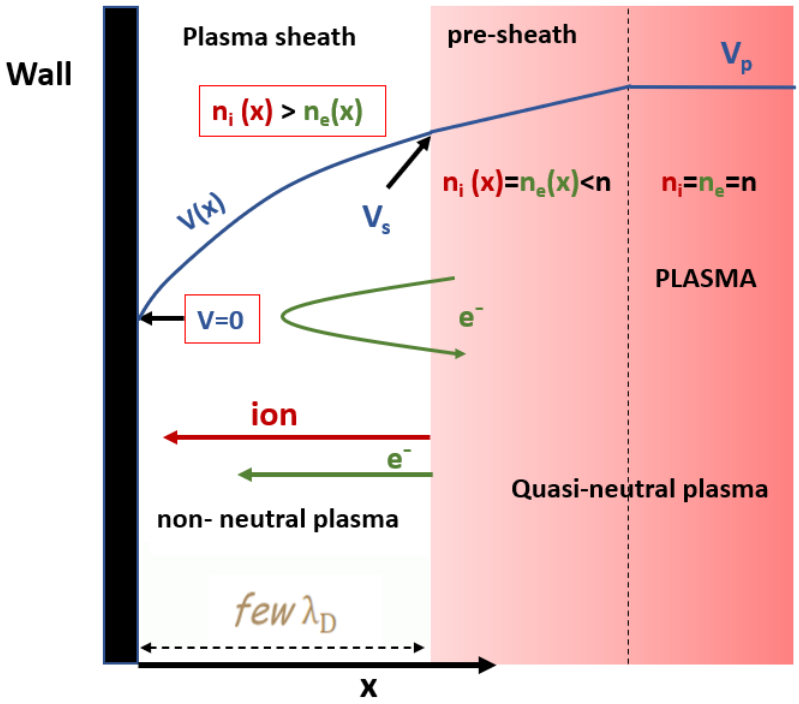

FIGURE 2.2 Plasma sheath formation near the wall of the plasma containing structure.

In a laboratory plasma, the plasma is usually surrounded by solid walls and since the electrons are significantly lighter than ions, they can escape from plasma much quicker than ions, assuming no restraining potential barrier exists. As a result, a positive charge builds up in the plasma core leading to a potential difference between the plasma and surrounding structures. At the edge of the plasma, close to the solid wall, an electric field develops locally within a scale of few Debye lengths from the wall. This local electric field retards the electron's motion while accelerating the ion toward the wall as shown in Fig. 2.2. The energetic electrons reach the wall whereas low energetic electrons returns back to the plasma. The boundary between plasma core and the wall can be divided into two regions: (1) the pre-sheath region where the plasma remains quasi-neutral i.e. the electron density (n_e) and ion density (n_i) remains equal and (2) the plasma sheath region where non-neutral plasma is present with higher ion density compared to the electron density within a thickness of the order of a few Debye lengths. In the plasma sheath region, the process of ion acceleration and electron retardation continues until an equilibrium is reached between flux of electrons and ions lost to the wall and the corresponding potential difference between plasma core and the wall is defined as plasma potential which is denoted by V_p in the figure.

2.2 Operation principles of ECR plasma

2.2.1 Motion of charged particle in magnetic field

Motion of a charged particle in a homogeneous static magnetic field is considered here. The equation of motion of a charged particle is given by:

$$m_q \frac{\mathrm{d}\vec{v}}{\mathrm{d}t} = q(\vec{E} + \vec{v} \times \vec{B}) \tag{2.10}$$

where $\vec{B}$ is the external magnetic field, $\vec{E}$ is the electric field, m_q and q are the mass and the charge of the charged particle which is moving with a velocity $\vec{v}$. Here $\vec{E} = 0$ since the static magnetic field alone is under consideration. Traditionally, the velocity is decomposed into $\vec{v} = \vec{v}_{\parallel} + \vec{v}_{\perp}$ where $\vec{v}_{\parallel}$ and $\vec{v}_{\perp}$ are the velocity components parallel and perpendicular to the magnetic field, respectively. By applying Lorentz's force law and Newtons second law of motion, it is found that the charged particle follows a helical orbit in the plane perpendicular to $\vec{B}$ with a radius defined as Larmor radius (or gyroradius) given by the expression:

$$r_L = \frac{m_q v_{\perp}}{qB} \tag{2.11}$$

The rotation frequency of the particle in the magnetic field is called cyclotron frequency and it is defined as

$$\omega_c = \frac{qB}{m_q} \tag{2.12}$$

For the electron the generalised cyclotron frequency is given by

$$\omega_{ce} = \frac{eB}{\gamma m_e} \tag{2.13}$$

where γm_e is the relativistic mass of electron, γ is $1 + \frac{E_k}{511\ keV}$ and E_k is the kinetic energy in unit of keV.

2.2.2 Magnetic mirror effect and loss cone

The physical quantities which vary slowly or adiabatically with respect to the periodicity of particle motion can be called as adiabatic invariants. In a magnetic mirror confined plasma, magnetic moment is adiabatically invariant since the magnetic field variation with respect to one particle revolution is negligible. The radial confinement is achievable because of the conservation of the magnetic

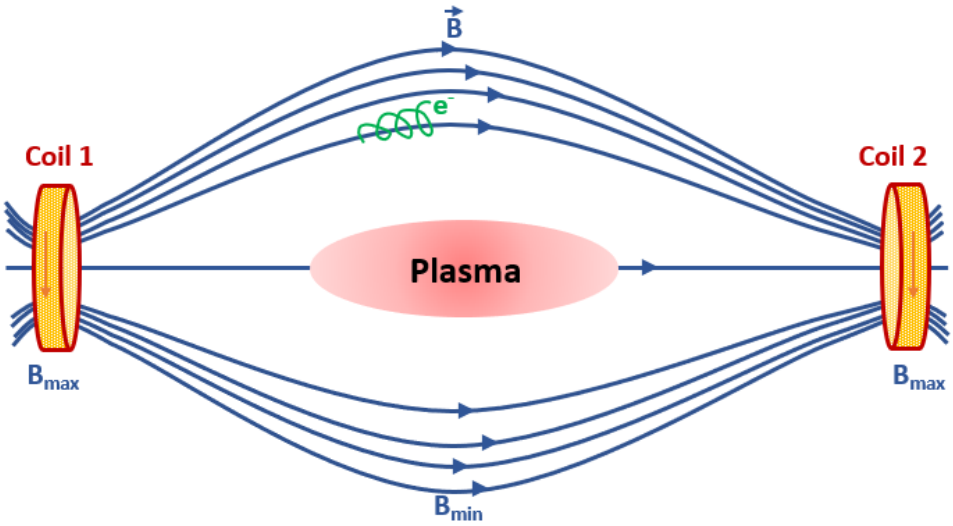

FIGURE 2.3 Magnetic bottle generated using two coils.

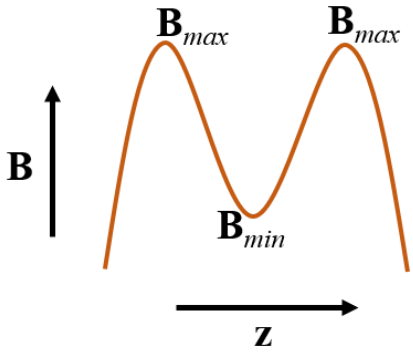

FIGURE 2.4 Axial mirror field produced by two coils as shown in Fig. 2.3 where the particle is trapped axially in between the magnetic field maxima (B_{max}).

moment. The presentation for the particle's magnetic moment (μ) can be obtained using following steps:
The magnetic moment of a charged particle q is given by $\mu = IA$, where I is the circulating current produced due to gyromotion of charged particle which embraces an area $A = \pi r_L^2$ whose Larmour radius is r_L. The circulating current $I = \frac{q\omega}{2\pi}$ where the angular frequency $\omega = \frac{v_\perp}{r_L} = \frac{qB}{m}$. Therefore the particle's magnetic moment (μ) and its total energy (E) is

$$\mu = \frac{\frac{1}{2}mv_\perp^2}{|B|} \approx const \tag{2.14}$$

$$E = \frac{1}{2}m\left(v_\parallel^2 + v_\perp^2\right) = const \tag{2.15}$$

where m is the charged particle's mass, $v_\parallel$ and $v_\perp$ are the parallel and perpendicular components of particle's velocity, respectively. When the particle propagates

through a region of increasing magnetic field, the value of $v_\perp$ increases and because the total energy is conserved, the value of $v_\parallel$ must decrease. As a result, the value of $v_\parallel$ reduces to zero when $E = \mu B$ and the particle is reflected back. This location is called reflection/mirror point. If the charged particle maintains a non-zero parallel velocity at the maximum magnetic field (B_{max} in Fig. 2.3), it will escape from the confinement specified by the so-called loss cone defined by the equation:

$$E > \mu B_{max} \tag{2.16}$$

which implies that,

$$v_\parallel^2 \geq v_\perp^2 (R - 1) \tag{2.17}$$

where $R = \frac{B_{max}}{B_{min}}$, which is called the mirror ratio.

It can be further asserted that the ratio of particle's perpendicular and parallel velocities determines whether it remains confined in the mirror field or not (as shown in Fig. 2.5). This ratio can be represented in terms of the pitch angle (θ), which is defined in velocity space ($v_\perp, v_\parallel$) as $\tan(\theta) = \frac{v_\perp(s)}{v_\parallel(s)}$ at location s. Consequently, at the reflection point $v_\parallel$ tend to zero, hence the pitch angle (θ) becomes 90^o. Thus, in terms of the pitch angle, the condition for the charged particle to remain confined in the magnetic mirror is given by:

$$sin(\theta) \geq \sqrt{\frac{B_{min}}{B_{max}}} \tag{2.18}$$

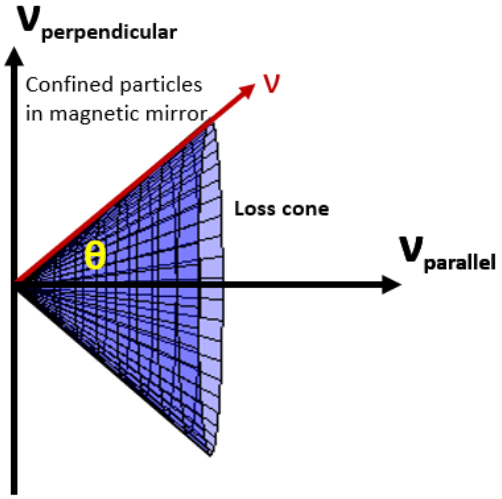

FIGURE 2.5 The loss cone of the magnetic mirror field in the velocity space.

2.2.3 Electron cyclotron resonance mechanism

In order to understand the ECR mechanism, let's consider an electron at rest in a constant magnetic field B and a time varying radio frequency electric field having an angular frequency ω_{RF}. The wave propagates perpendicularly to the direction of the external magnetic field. The electron gains energy from this externally applied electric field when it satisfies the ECR condition given by:

$$\omega_{RF} = \omega_{ce} \tag{2.19}$$

where ω_{ce} is the electron cyclotron frequency defined by equation (2.13). The electron gains energy with the evolution of time and its position and velocity can be determined by solving the Lorentz equation. The solution describes the spiral-like electron motion as is shown in Fig. 2.6.

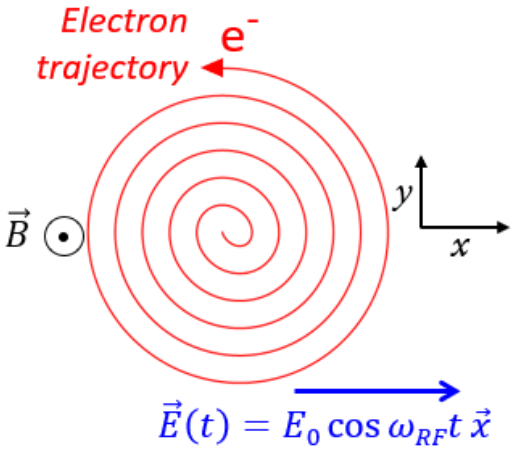

FIGURE 2.6 The electron motion in the XY plane when the external electric field of angular frequency ω_{RF} is applied in a direction perpendicular to the constant magnetic field $\vec{B}$.

In reality, the electron will have an initial velocity when it interacts with electric field and therefore it introduces a phase shift between the electric field $\vec{E}$ and electron velocity $\vec{v}$. Now depending on the phase difference (ϕ) between $\vec{E}(t)$ and $\vec{v}(t)$, the electron gains/loses energy.

Now in order to understand the global effect on an electron population on ECR mechanism one has to consider a random distribution of electron velocity and phase difference and then compute the average kinetic energy of the whole system with the evolution of time. It has been found that there would be a net gain in the average electron kinetic energy with the evolution of time and this process is called stochastic heating. When the electrons becomes relativistic (T>=10 keV), the ECR mechanism in a constant magnetic field breaks as $\omega_{RF} \neq \frac{qB}{\gamma m}$ and the

electron heating stops. The ECR heating can expand up to relativistic energy if electrons propagate along the increasing magnetic field. There, the electrons can pass through the surface where the resonance condition is met: i.e. $\omega_{RF} = \frac{qB}{\gamma m}$

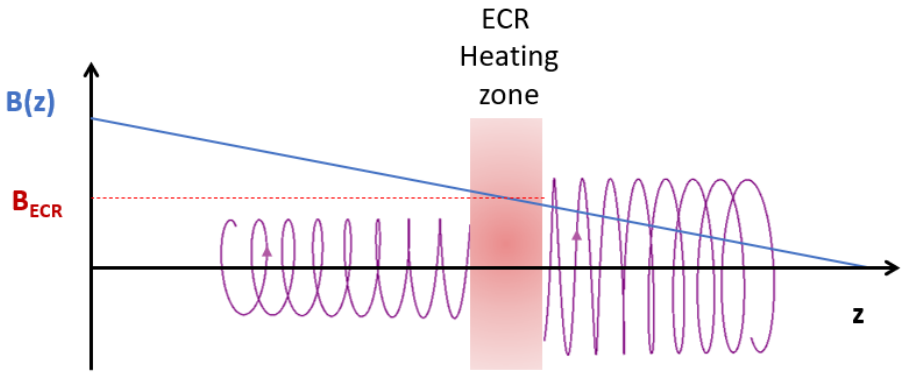

FIGURE 2.7 Effect of local magnetic field gradient on increase in electron energy. Figure reproduced from T. Thuillier lecture on ECR ion sources at KOPAS, Sejong, South Korea, December 10-14, 2012.

When the electron passes through the local resonance surface, its transverse velocity can increase slightly, resulting in a modest rise in its kinetic energy. The average increase in the energy can be determined using the following relation [12]:

$$< E_{ECR} >= \frac{\pi e^2 E_r^2}{m_e \omega_{ce} \mid \alpha \mid v_{\parallel}} \tag{2.20}$$

where $< E_{ECR} >$ is the average energy gained by an electron when it pass through the resonance zone, E_r is the magnitude of electric field component and α is given by:

$$\alpha = \frac{e}{\gamma m_e \omega_{ce}} \left(\frac{\partial B}{\partial z}\right)_{res} \tag{2.21}$$

where $\left(\frac{\partial B}{\partial z}\right)_{res}$ is the local magnetic field gradient at resonance and therefore the average energy gained by an electron is inversely proportional to the magnetic field gradient at the resonance zone.

2.2.4 Dynamics of production of Highly Charged Ions (HCIs)

In ECR plasmas, the primary ionisation process is by means of inelastic electron collisions with neutral atoms, molecules or ions and this process is known as electron impact ionisation (shown by the relation (2.22)). For realisation of the electron impact ionisation the energy of the colliding electrons must be greater

than the ionisation potential of the atoms or molecules which is attained by above mentioned processes

$$A^{n^+} + e^- \rightarrow A^{n+1} + 2e^- \tag{2.22}$$

Successive electron impact collisions can produce highly charged ions. The charge exchange also occurs through ion-neutral collisions (the charge exchange between elements A and B is shown in (2.23)) and it is the main process through which high charge state of an ion can be destroyed.

$$A^{n^+} + B \rightarrow A^{(n-m)^+} + B^{m^+} \tag{2.23}$$

Apart from these, one can also cite the radiative recombination process where an electron is captured by an ion, however this process is secondary in the ion sources producing multi-charged ions. The radiative recombination mechanism is given by the following expression:

$$A^{n^+} + e^- \rightarrow A^{(n-1)+} + h\nu \tag{2.24}$$

where $h\nu$ is the photon energy emitted as a result of the process.

The ion density time evolution in the plasma can be described by three main processes: 1) step-by-step ionisation by energetic electrons, 2) charge exchange reactions between highly charged ions and neutrals and 3) diffusion loss processes. The time evolution of the ion density of a particular charge state q of species i can be modelled by the zero dimensional balance equation [13]:

$$\begin{aligned}\frac{dn_i^{\mathrm{q}}}{dt} = {} & n_e \langle \sigma_1 v \rangle^{ion}_{q-1\rightarrow q} n_i^{q-1} - n_e \langle \sigma_1 v \rangle^{ion}_{q\rightarrow q+1} n_i^{q} + \\ & n_{0_i} \langle \sigma_2 v \rangle^{cx}_{q+1\rightarrow q} n_i^{q+1} - n_{0_i} \langle \sigma_2 v \rangle^{cx}_{q\rightarrow q-1} n_i^{q} - \frac{n_i^q}{\tau_i^q}\end{aligned} \tag{2.25}$$

where n_i^q is the ion density of charge state q, n_e is the electron density, σ_1 is the ionisation cross section and σ_2 is the charge exchange cross section, v is the speed of the particle, n_{0_i} is the neutral density of atoms and τ_i^q is the ion confinement time of charge state q, $< \sigma v >$ is the average of charge exchange/ionisation cross section while considering a normal velocity distribution of particles with velocity v. In this equation the electron impact ionisation is represented by the first two terms where the superscript 'ion' is the abbreviation for ionisation in which the first term gives the production rate of charge state q from $q-1$ and the second term gives the losses due to further ionisation from charge state q to $q+1$. The

third and fourth term similarly shows the charge exchange reactions between the ions and the neutrals which is superscripted by 'cx' in which each terms gives the charge exchange reaction from the $q+1$ to q and q to $q-1$, respectively. Finally, the last term describes the diffusion and transport losses of ions which determines the rate at which ions are extracted or lost from the confinement. For the production of high charge states, it is crucial to minimise all destructive processes, like charge exchange, and hence the neutral pressure must be kept as low as possible.

2.2.5 Particle velocity distribution in plasma

When the plasma is at thermal equilibrium, the velocity distribution of particles in plasma can be defined by Maxwell-Boltzmann (MB) distribution given by equation (2.26). In plasma, the term temperature can be defined as the mean kinetic energy of the particles averaged over the Maxwell-Boltzmann distribution.

$$F(v) = \frac{1}{\pi^{(3/2)} v_{th}^3} \exp\left(-\frac{v^2}{v_{th}^2}\right) \tag{2.26}$$

where v_{th} is the thermal velocity of particles which is given by $v_{th} = \sqrt{2k_B T/m}$, k_B is the Boltzmann constant, T is the absolute temperature and m is the mass of particles constituting the system. In the case of ECR plasmas, the ion and electron has different temperature and it also exhibit different distribution. It has been established that in ECR plasmas the electron velocity distribution is considered to be anisotropic [14, 15, 16, 17] in nature due to its heating mechanism as explained in above sections however, the exact electron velocity/energy distribution remains elusive. If, for instance Bi-Maxwellian distribution function is considered, then it can be written as :

$$F(v_\parallel, v_\perp) = \frac{1}{\pi^{(3/2)} v_{th_\parallel} v_{th_\perp}^2} \exp\left(-\frac{v_\perp^2}{v_{th_\perp}^2} - \frac{v_\parallel^2}{v_{th_\parallel}^2}\right) \tag{2.27}$$

where $v_{th_\parallel}$ and $v_{th_\perp}$ are the electron thermal velocities with respect to the magnetic field direction. For the Bi-Maxwellian distribution the electrons distributed within the magnetic field decouple and hence there would be two different temperatures with respect to the magnetic field direction.

2.2.6 Working principle of ECR ion source

In ECR ion sources, the plasma is confined inside the minimum-B structure, so termed because the magnetic field is weakest in the chamber's centre and increases in all directions from there. It is typically implemented using a set of solenoids for axial confinement and a multipole (often hexapole) for radial confinement. A

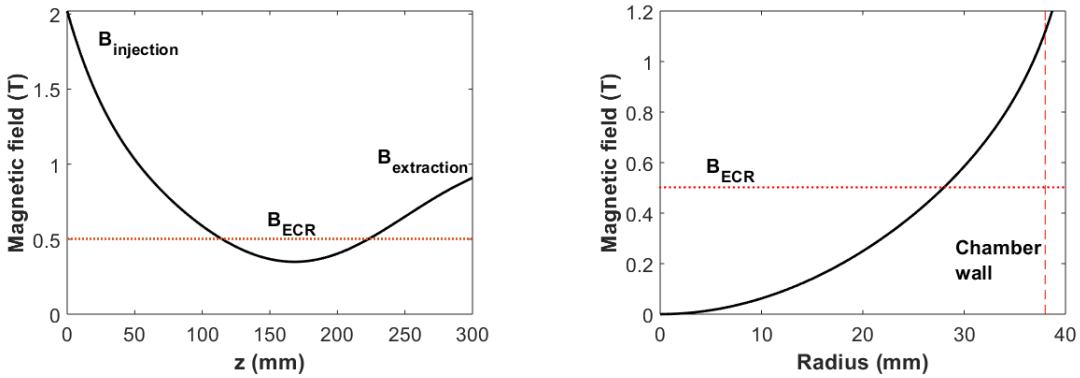

(a) Axial confinement (b) Radial confinement

FIGURE 2.8 a) axial magnetic field produced by the solenoids and b) radial magnetic field produced by the permanent magnet hexapole. The red dotted line corresponds to the resonant magnetic field for 14 GHz ECR heating.

typical plot of axial and radial magnetic field is shown in Fig. 2.8, where B_{ECR} is the magnetic field corresponding to resonance zone (the B_{ECR} corresponding to 14 GHz heating frequency is 0.502 T). The formation of closed resonance surface and superposed magnetic field is depicted in Fig. 2.9. The magnetic field modelling is described in detail in Section 4.1.

Plasma is generated in an ECR ion source by injecting microwaves with a frequency that corresponds to the cyclotron resonance frequency of electrons in a constant magnetic field. The magnetic field serves three critical functions in the ECR ion source. Firstly, it confines the plasma. For room temperature ion sources, the solenoidal magnetic field is realised by water cooled copper coils and the hexapole magnetic field is realised by permanent magnets. In the case of superconducting ECR ion sources the both fields, solenoidal and hexapolar, are realised by using superconducting wires. Secondly, the magnetic field is required to form a closed surface within the plasma chamber so that it satisfies the ECR condition i.e. ω_{ce}= ω_{RF}. The magnetic field associated with this resonance zone is denoted by the symbol B_{ECR}, and the surface on which the resonance occurs is referred to as the resonant/ECR surface. Thirdly, the magnetic field suppresses the magnetohydrodynamic instabilities (MHD) by satisfying the following conditions:

$$\frac{\partial B}{\partial r} \geq 0 \tag{2.28}$$

and

$$n_e k_B T_e \ll \frac{B^2}{2\mu_0} \tag{2.29}$$

where equation (2.28) provides the condition that the magnetic field strength must increase radially and equation (2.29) gives the condition that the particle pressure due to the plasma electrons must be significantly lower than the magnetic pressure provided by the external magnetic field.

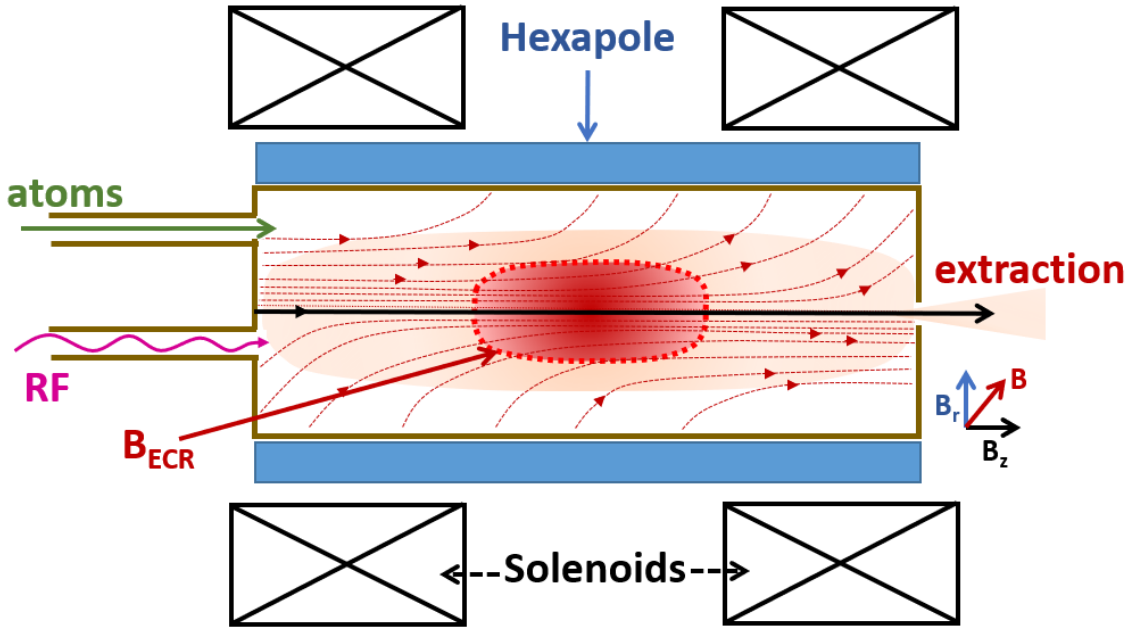

FIGURE 2.9 A schematic front view of ECR ion source showing ECR cross section, superposed magnetic field lines, RF injection, neutral particle injection and the magnet system.

In ECRIS, electron cyclotron resonance heating is primarily accomplished using microwaves generated by a radio frequency oscillator and imparted to a microwave amplifier at an angular frequency (ω_{RF}). Once the microwave in the radio frequency range (ω_{RF}) is launched into the plasma chamber, it provides electrons with energy in a path perpendicular to the magnetic field's direction, igniting plasma when they collide with neutral particles. For as long as the electron is in the resonance volume, the average energy of the electrons bouncing between the magnetic mirror increases when they interact with the electromagnetic field at frequency (ω_{RF}). The electrons repeatedly pass the resonance surface. This causes the electrons to stochastically heat up. By applying the Fokker-Planck equation, which Lieberman and Lichtenberg use extensively [18, 19], one may compute the energy obtained by an electron during each passage through the ECR zone and the evolution of the electron energy distribution function. An electron can acquire or lose kinetic energy in the resonance zone depending on the phase between its velocity vector and the electric field component of microwave orthogonal to the external magnetic field (as discussed in Section 2.2.3). The net energy gain over multiple subsequent passes is positive.

Magnetic field gradient and ECR heating:
The magnetic field gradient parallel to the field $\left(\frac{\vec{B}\cdot\nabla\vec{B}}{|\vec{B}|}\right)$ on the resonance surface has a significant effect on the energy received by the electron passing through the resonant surface in one pass (as mentioned in Section 2.2.3). The effect of magnetic field gradient in single electron acceleration and resulting stochastic heating of ECR

plasmas is explained by Canobbio [20]. The transverse velocity of the electrons ($v_\perp$) increases considerably in resonance while the parallel component remains unchanged. Therefore the time electron spends in the resonance zone determines the extend to which electron is heated and it can be increased as the magnetic field gradient at the resonance surface is decreased. In other words the electron experience an energy kick each time it passes through the resonance zone and the time spent (δT) in the resonance zone is given by the equation:

$$\delta T \approx \left(\frac{\nabla B v_\parallel \omega}{B_{ECR}} \right)^{-1/2} \tag{2.30}$$

where ∇B is the local magnetic field gradient, $v_\parallel$ velocity parallel to local magnetic field ω is the ECR heating frequency and B_{ECR} is the magnetic field at resonance. Thus, it can be concluded that the smaller the magnetic field gradient, the more efficiently electrons are heated.

These highly energetic electrons subsequently ionise neutral atoms, molecules or ions through the electron impact ionisation processes. In this process, the ions remain cold, which benefits the ion beam extraction in two ways: (a) it improves the extracted beam quality by reducing the energy spread and (b) it increases the time spent by ions in the plasma, which is helpful for producing highly charged ions via step-wise ionisation. Throughout the process, the neutral pressure must be kept low enough (of the order of 10^{-7} $mbar$) to minimise the charge exchange reaction between the neutrals and highly charged ions while at the same time the confinement time of the ions has to be long enough (tens of milliseconds) to form highly charged ions. The long confinement time increases the possibility of the ion to collide with neutral atom and as a result the charge state of the ion would decrease from the charge state q to the charge state $q-1$. These highly charged ions are believed to be electrostatically contained within a local potential dip created by magnetically confined electrons [21] as shown in Fig. 2.10.

Similar to simple magnetic mirror confinement, in ECRIS the increase in longitudinal velocity of electron also results in escape of electron from the confinement as discussed in Section 2.2.2 which is defined by mirror ratio $R = \frac{B_{max}}{B_{min}}$. However in the case of ECR ion sources the mirror ratio is defined as $R = \frac{B_{max}}{B_{ECR}}$, where B_{ECR} is the magnetic field strength at resonance zone because electrons traversing the resonance surface have a significant influence on their transverse velocity and hence there will be violation of adiabatic nature of magnetic moment at resonance zone as shown in Fig. 2.11.

As a result of stochastic heating, there will be a build up of very energetic electrons due to the increase in the transverse velocity of electron which results in anisotropy of EVDF as mentioned in Section 2.2.5.

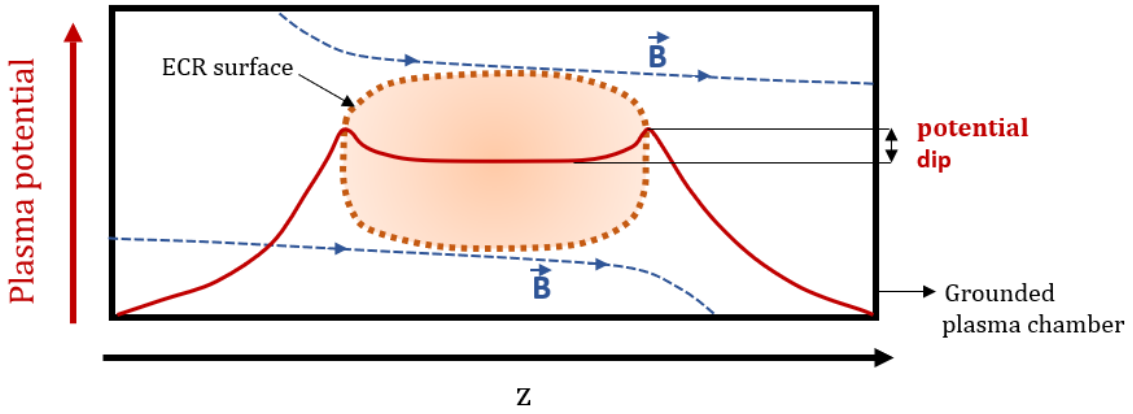

FIGURE 2.10 The cross sectional view of plasma chamber showing ECR surface cross section and a representation of plasma potential dip, which is responsible for the electrostatic confinement of ions.

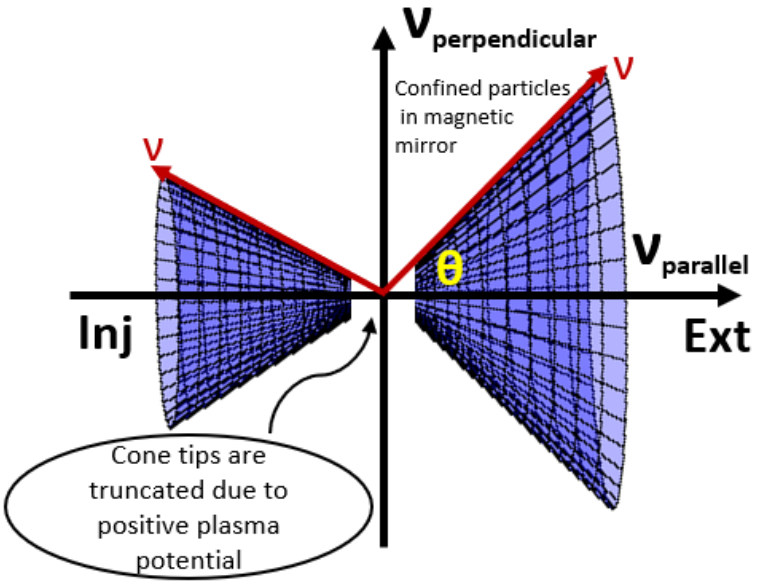

FIGURE 2.11 Loss cones of magnetic mirror field in the velocity space. The injection (Inj) end of the chamber has higher magnetic field compared to the extraction (Ext), therefore the pitch angle of the loss cone (θ) is larger at the extraction.

Considering all the above mentioned factors, the semiempirical magnetic scaling laws have been formulated to maximise the performance of the ECR ion sources. These scaling laws are summarised in the section below.

ECRIS scaling laws:
ECRIS can be developed using a set of scaling laws first presented by Geller *et al.*, which gave a simplified method for estimating the source's performance [22]. These can be summarised as follows:

$$
\begin{aligned}
I_{peak} &\propto f_{RF}^2 \\
B_{inj}/B_{ECR} &\geq 4 \\
B_{ext}/B_{ECR} &\geq 2 \\
B_{rad}/B_{ECR} &\geq 2 \\
B_{min}/B_{ECR} &\approx 0.8 \\
B_{ext}/B_{rad} &\approx 0.9
\end{aligned}
\tag{2.31}
$$

Where I_{peak} is the extracted current at the peak of ion charge state distribution scales with the square of input RF frequency. B_{inj} and B_{ext} are the maximum axial magnetic field strengths at the injection and the extraction ends of the plasma chamber, respectively, and B_{rad} is the maximum radial magnetic field strength at the wall of the plasma chamber (see Fig. 2.8). B_{ECR} is the magnetic field strength corresponding to the resonance zone which is derived from the equation 2.12 and B_{min} is the minimum axial magnetic field. It has also been proposed recently that there is also a scaling factor between the RF power and the RF frequency [23] given by:

$$P_{RF} \propto f_{RF}^2 \tag{2.32}$$

which means that the power required for operation of ion sources in their full capacity should also scale up to the square of heating frequency.

2.3 Kinetic instabilities in ECR plasma

Kinetic instabilities are common in open plasma traps with magnetic mirrors due to the resonant interaction between energetic electrons and electromagnetic waves. Additionally, these instabilities have been observed to induce coherent radio-emission from the solar corona [3, 4, 5], the Earth's magnetosphere [6, 7, 8, 9] and laboratory plasmas [24, 25, 26, 27, 28, 29, 30, 31]. One of the key objectives of an ion source is to produce highly charged ions (HCIs), and kinetic instabilities have been reported to obstruct the generation of HCIs. As a result, investigations of kinetic instabilities on many ECR ion sources have been conducted in order to optimise source performance. Melin *et al*. [32] reported the first observation of kinetic instabilities in ECRIS in 1989. The dedicated experimental campaigns to study kinetic instabilities and their effect on ECR plasma and extracted ion beam properties were conducted much later by mainly the JYFL (Finland) and IAP-RAS (Russia) research teams using diagnostics for microwave and bremsstrahlung emissions from the plasma to determine the onset of kinetic instabilities (see e.g. [33, 28, 34, 35]). A series of experimental campaigns were conducted to understand the effect of various source parameters on kinetic instabilities and to comprehend better its effect on different charge states. For example, it was observed that the intensity of low charge state ions increases whereas the intensity of highly charge ions decreases as a result of the kinetic instabilities [31]. The investigations indicated that the ratio of minimum magnetic field to the magnetic field strength at the resonance field (i.e. B_{min}/B_{ECR}) had the strongest correlation with the instability threshold.

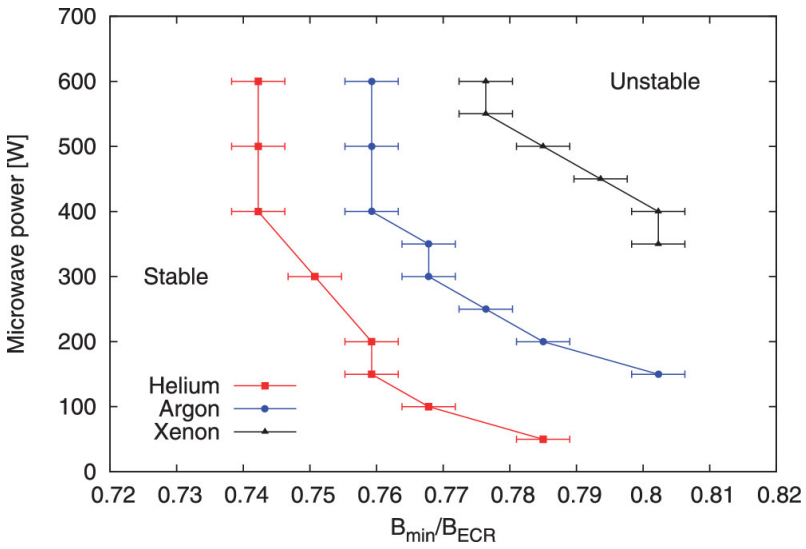

FIGURE 2.12 The threshold of transition from stable to unstable region for different gas and different microwave power is plotted as a function of B_{min}/B_{ECR} to find the effect of magnetic field on instability. Reprinted with permission from [35]. Copyright 2016, AIP Publishing LLC

.

The plasma instability studies were later extended by utilising spectrum analyzers [36, 37, 38] and high-bandwidth oscilloscopes [28, 29] to extract further details of the microwave emissions. It was identified with spectrum analyzers that the instability induced microwave emissions occur at discrete frequencies below the input heating frequency [37]. The high-bandwidth oscilloscope was used to extract the temporal structure of the instability emission frequency evolution. With extensive post-processing it was found that the frequency of the emitted wave falls monotonically as a function of time following the initial microwave burst [28, 29]. It has also been found that the unstable plasma can be stabilised by the introduction of secondary heating frequency [39].

Kinetic instabilities were also observed in the afterglow mode by Izotov *et al*. [40], which is a mode employed in ECRIS by delivering pulsed RF wave to obtain higher ion currents compared to the typical continuous wave operating regime [41, 42]. The afterglow occurs when the RF is switched off and the plasma starts to decay in which the energy stored by the well confined relativistic hot electron is swiftly released in the form of EM radiation and particle losses.

In ECR plasmas the electron energy distribution (EED) is non-Maxwellian and it has been qualitatively approximated as a sum of three Maxwell-Boltzmann distributions with cold ($E_{e,cold} = 10 - 100$ eV), warm ($E_{e,warm} = 1 - 10$keV) and hot electron ($E_{e,hot} > 10$ keV and can reach up to 1 MeV) energies [14, 43]. However, the exact EED remains unknown to this day. The cold electron population is thought to be in charge of maintaining plasma neutrality and determining the dielectric properties of plasma, while the warm electron population is responsible for ionisation process and the hot electron population is in charge of electron confinement and storing "free energy" (also known as stored energy)[14]. When the hot electron population grows due to the increase in $v_{\perp}$ relative to $v_{\parallel}$ (as a result of heating mechanism explained in above sections), region of positive gradient in the electron energy distribution is formed (as shown in Fig. 2.13). The electrons are lost from the confinement by means of four processes namely Coulomb collisions, RF scattering, inelastic (ionising) losses and finally by means of kinetic instabilities.

Here we focus on kinetic instabilities and it occurs as a result of an increase in the positive gradient of the Electron Velocity Distribution Function (EVDF) beyond a threshold [44]. The energy accumulated in the non-collisional hot electron population is released all at once as in the form of microwave energy [34, 45] which is followed by the escape of hot electrons from confinement, which eventually breaks the ion confinement inside the ECR zone, and therefore bursts of hot electrons are followed by ion bursts. The threshold satisfies the inequality condition provided in equation (2.33) as given in Ref. [39, 34, 45]

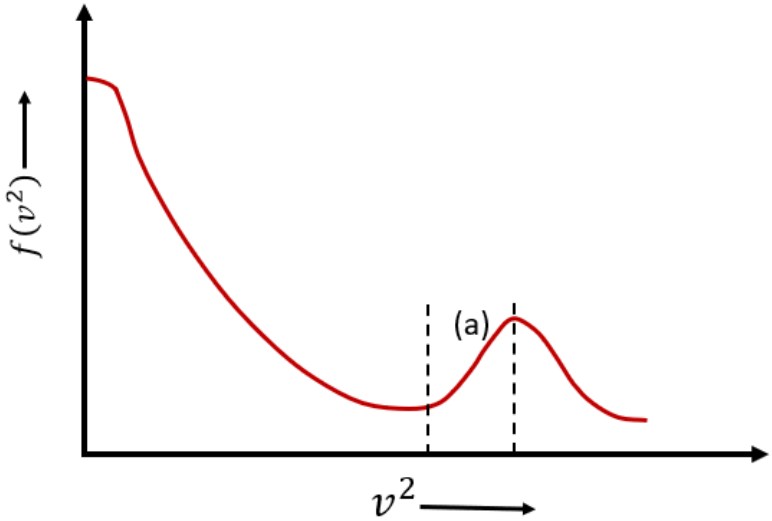

FIGURE 2.13 An illustration of an electron energy distribution with a positive gradient represented by region (a) in the figure.

$$\frac{dE_\mu}{dt} \approx \langle \gamma - \delta \rangle E_\mu > 0 \tag{2.33}$$

where E_μ is the volumetric energy of microwave emitted, γ is the growth rate of the amplified EM-wave and δ is its damping rate. The growth rate (γ) depends on the positive gradient of the electron velocity distribution function (in other words the ratio of number density of hot electrons to cold electrons i.e. $\frac{N_{e,hot}}{N_{e,cold}}$) whereas the damping rate (δ) depends on the volumetric absorption of the wave energy by the background plasma and plasma chamber structures. The time evolution of number density of hot electrons ($N_{e,hot}$) is given by the balance equation [46, 47]:

$$\frac{dN_{e,hot}}{dt} \approx -\kappa N_{e,hot} E_\mu + S(t) - L(t) \tag{2.34}$$

The build-up rate of the EED energy content is connected to the source term $S(t)$ and the loss term $L(t)$. The source term depends on the plasma heating factors like input RF power and the magnetic field gradient as discussed in Section 2.2.3. The loss term is influenced by different hot electron loss processes, such as collisional losses, rf-scattering and energy damping by inelastic processes. An additional loss channel for the hot electrons is from the interaction between electromagnetic waves and hot electrons which is denoted by the term $\kappa N_{e,hot} E_\mu$, where κ is a coefficient that describes the amplification of the electromagnetic wave as a result of the interaction between the wave and the hot electrons. In particular, this factor becomes prominent during the onset of the kinetic plasma instabilities when the condition given by equation (2.33) are satisfied. Consequently, the energy exchange happens between the hot electrons and the wave which leads to the decrease in transverse velocity ($v_\perp$) of the electrons and subsequently falls into

the loss cone. A more comprehensive theoretical description of kinetic instabilities is exceedingly complicated and beyond the scope of this work. However, there have been some brave efforts by Shalashov *et al.* [45, 48] to provide a more theoretical explanation regarding this phenomenon. This thesis focuses on a wide experimental approach to provide insight to support the theoretical explanation illustrated by equation (2.34).

3 EXPERIMENTAL SETUP AND METHODS

The main motivation of this thesis work was to study ECR-heated plasma to define the most influential parameter triggering the kinetic plasma instabilities. In order to produce comprehensive results and to answer the original research question, the research was performed using a variety of ECR ion sources. These included: JYFL 14 GHz ECRIS (JYFL, Finland) [49], PHOENIX Booster [50] and PHOENIX V3 (LPSC, France) [51], GTS (GANIL, France) [52], and the third generation superconducting ECR ion source SECRAL-II (IMP-CAS, China) [53]. The plasma properties were studied using a wide variety of non-invasive diagnostics both in stable and unstable plasma configurations. The research included diagnostics for microwave emission, electron flux, bremsstrahlung and ion currents. The ion sources used in this thesis work are described in Section 3.1. The diagnostic techniques and methods are discussed in detail in Section 3.2.

3.1 ECR ion sources

ECR ion sources are widely used for the production of highly charged heavy ion beams for various applications. The production of highly charged ions and ion beams requires high-level vacuum conditions, sufficient plasma confinement, adequate plasma heating, controlled particle injection and proper beam formation and beam optics to ensure the transport of the high-intensity and high-quality ion beams for their further use. Figure 3.1 presents a typical ECR ion source setup used for the production of highly charged ion beams. The setup includes three main entities: A) ion production, B) ion beam formation and C) q/m (ratio of charge over mass) selection and current measurement. The majority of the experiments for this thesis were realised using the JYFL 14 GHz ECR ion source at the Accelerator Laboratory in the Department of Physics, University of Jyväskylä.

Hence this ion source is explained in detail in Section 3.1.1, as a representative example of a second generation ECRIS, to describe the main features of an ECR ion source. The other ECR ion sources that have been used to strengthen and broaden the experimental work are described in Section 3.1.2. The main principles of operation of all these ion source setups is the same, thought there are variations in the exact constituents and assemblies of each of them.

3.1.1 JYFL 14 GHz ECRIS

The JYFL 14 GHz ECRIS is a room temperature ECR ion source which is currently operated for the production of medium to high charge state heavy ion beams for the K-130 cyclotron [54]. The functions of the above mentioned entities (highlighted in Fig. 3.1) of the ion source are discussed in detail below.

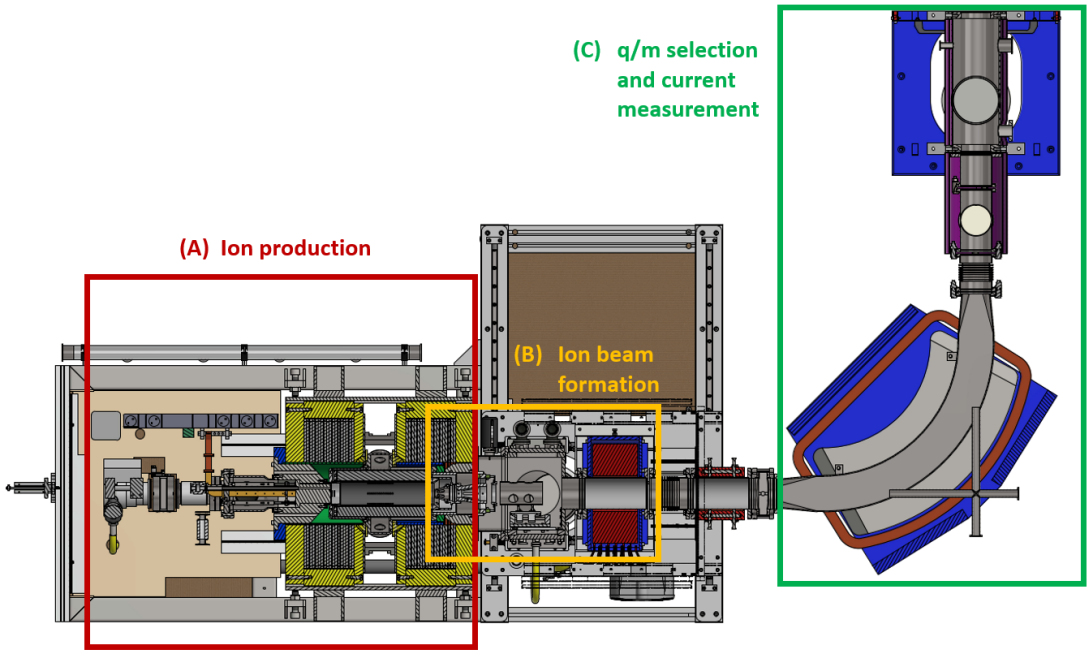

FIGURE 3.1 Top cross section view of JYFL 14 GHz ECR ion source setup including sections for ion production (A), ion beam formation (B) and q/m selection and ion current measurement (C).

(A) Ion production

The ion production section of the JYFL 14 GHz ECRIS is presented in Fig. 3.2. This section includes the necessary equipment to produce vacuum, optimised B-minimum structure for magnetic confinement and to allow plasma heating through the electron cyclotron resonance mechanism.

Vacuum conditions:
The highly charged ions are produced in the plasma chamber. The cylindrical

chamber of JYFL 14 GHz ECRIS is made of aluminium and it is 28 cm in length and 7.6 cm in diameter. The injection end of the chamber consists of a biased disc [55], a gas injection inlet, waveguide feedthroughs for microwave injection and a port for miniature oven [56] or MIVOC (Metal Ions from VOlatile Compounds) [57]. The injection part of the source, including the components for gas feeding and microwaves, is pumped with a 100 l/s turbomolecular pump. The vacuum in the plasma chamber is realised using a 500 l/s turbomolecular pump connected to a pumping chamber that surrounds the axial center of the plasma chamber and provides pumping through six radial openings located between the poles of the permanent magnet hexapole that surrounds the plasma chamber (see Fig. 3.2 and 3.3). Using this setup it is possible to reach chamber pressures below 10^{-7} mbar (baseline vacuum without particle injection). The pressure is monitored at one of the six radial pumping ports present at the axial centre of the chamber. The pressure has to be kept low enough in order to minimise charge exchange between neutrals and highly charged ions. This increases the life-time of highly charged ions and therefore their production efficiency (see Eq. (2.25)). The material used for construction of plasma chamber has a significant effect on the source performance because it acts also as a source of secondary electrons which helps in increasing the plasma electron density [58, 59].

A negatively biased electrode (which is commonly referred to as biased disc) is placed axially to the injection end of the plasma chamber, facing directly at the plasma. One of the primary roles of the biased disc is to provide electrostatic mirroring effect for the axially escaping cold electrons so that the electrons gets reflected back to plasma. It has also been observed that the biased disc helps to lower the plasma potential which in turn favours plasma confinement [60]. Biased disc is also a source of secondary electrons. In one of the experimental campaigns presented in this thesis the biased disc was also used as an instability diagnostic, as is explained in detail in Section 3.2.2.

Plasma confinement:
In JYFL 14 GHz ECRIS, the plasma chamber is enclosed by a Nd-Fe-B hexapole permanent magnet array (Fig. 3.3) which in turn is surrounded by two solenoidal coils (Fig. 3.2). The superposition of the solenoidal and the hexapolar magnetic fields forms a minimum-B structure with closed magnetic field isosurfaces inside the plasma chamber, as discussed in Section 2.2.6. Soft iron is added in the injection end of the chamber in order to increase the magnetic field strength at the injection and to ensure that the weakest axial mirror is at the extraction. This directs the ion losses towards the extraction region through the plasma electrode aperture and into the ion beam formation section of the ion source. The magnets and soft iron configuration is designed in such a way that the magnetic scaling laws for the production of highly charged ions are satisfied (see Section 2.2.6).

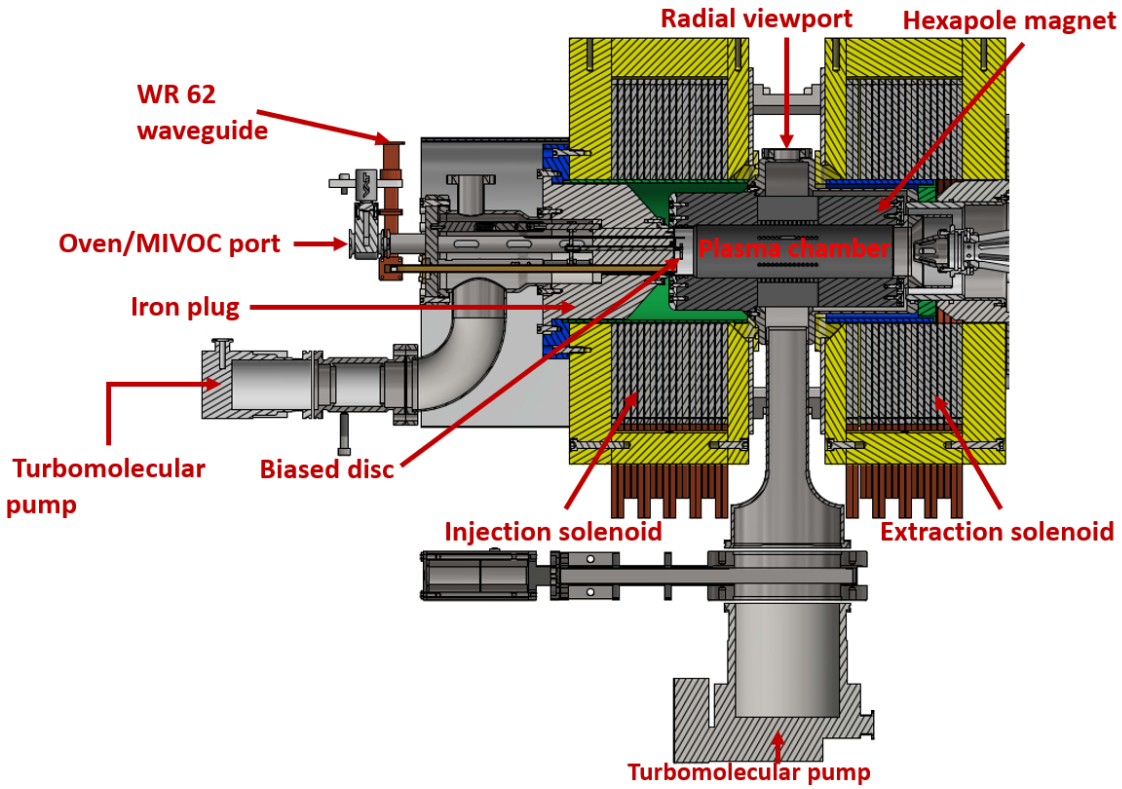

FIGURE 3.2 A cross section view of the ion production section of JYFL 14 GHz ECRIS illustrating the main components: plasma chamber, magnet system for plasma confinement, microwave injection, oven and MIVOC access port and the location of the turbomolecular pumps for satisfying the vacuum conditions. There is also a gas injection tube which goes through the injection plug but it is not visible in the presented cross section view.

Plasma heating:
The JYFL 14 GHz ECRIS can operate in one or two frequency heating modes with the primary frequency of 14.055 GHz coming from a klystron with a maximum power of 1 kW and the secondary microwave frequency generated by a TWTA which is capable of operating in the range of 8 GHz to 18 GHz [61] with a maximum power of 250 W. The WR62 waveguide is used to transport the primary frequency to the plasma chamber whereas the other WR75 waveguide is used for the secondary frequency. The WR62 waveguide is suitable for the frequency range of 12.4-18 GHz and the WR75 for 10-15 GHz with cut-off frequencies of 9.49 GHz and 7.87 GHz, respectively. The WR75 waveguide can also be used as a diagnostic port for plasma instability studies which will be discussed in detail in Section 3.2.

Particle injection:
The methods for injecting particles are essentially determined by the state of the selected element at room temperature (i.e. gaseous or solid). Additionally, the primary plasma where the element of interest is injected is usually generated and

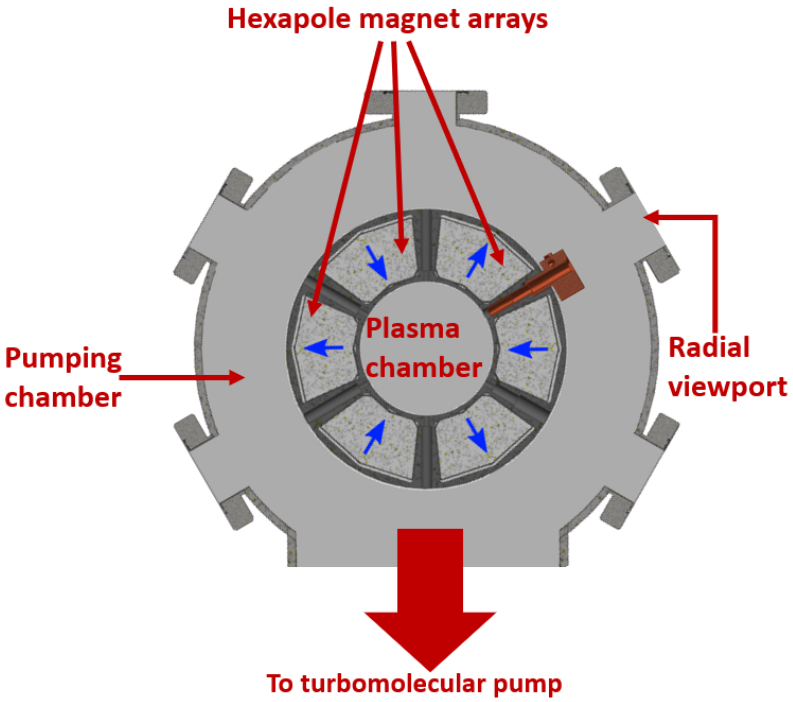

FIGURE 3.3 Cross section of JYFL 14 GHz ECRIS in between the solenoids showing the permanent magnet arrays that form the hexapolar magnetic field inside the plasma chamber for radial plasma confinement. The figure also shows the six radial ports that connect the plasma chamber to the surrounding pumping chamber. The radial view port specified in the figure (top right) was used for diagnostics in one of the experimental campaigns discussed in Chapter 5.

maintained utilising oxygen, nitrogen, or helium, which is commonly referred to as buffer gas. Gaseous materials are fed into the plasma chamber through the gas feeding line and the feed rate is precisely controlled by a dozing valve. The buffer gas is typically fed at a rate of $0.1 - 1$ cm^3/hour. The material of interest is then introduced into the buffer plasma via the other gas feeding line in the case of gases or using the most appropriate approach established for the element of interest in the case of solids. The lower particle feed rates favour production of highly charged ions whereas higher feed rates favour increase of extracted beam current for low charge states. The buffer gas element is lighter than the target element in order to maximise the ion beam intensity and efficiency of production. This is referred to as the "gas mixing technique" [62, 13]. The mixing ratio of the heavier element typically varies between 1-40% and the mixing ratio is optimised to maximise the beam intensity of the requested ion charge state. Solid elements are injected into the chamber using various techniques like inductively or resistively heated ovens [63, 56, 64], introducing the sample directly into the chamber by means of sputtering [65] or by using MIVOC (Metal Ions from VOlatile Compounds) method [57] when the element to be ionised is a part of a volatile organic compound.

(B) Ion beam formation

The ion beam formation section (commonly referred to as the beam extraction system) of the JYFL 14 GHz ECRIS is presented in Fig. 3.4. Plasma losses from the confinement are concentrated at locations where the magnetic field is lowest. Therefore the magnetic confinement is designed in such a way that it directs the losses towards the plasma electrode aperture located in the extraction end of the plasma chamber. The plasma electrode of JYFL 14 GHz ECRIS has an aperture of 8 mm in diameter.

The extraction system consists of a puller electrode, einzel electrode and a grounded electrode in a single stack. A proper geometrical and accelerating electric field structure between the plasma and the puller electrodes and for the einzel lens have to be designed carefully in order to optimise the ion beam properties for the further beam line components downstream the ion beam formation section. This design is based on ion optical simulations, which in the case of the JYFL 14 GHz ECRIS have been performed using the IBSimu simulation code [66]. The simulation procedure for JYFL 14 GHz ECIS extraction system has been explained in detail in Ref. [67].

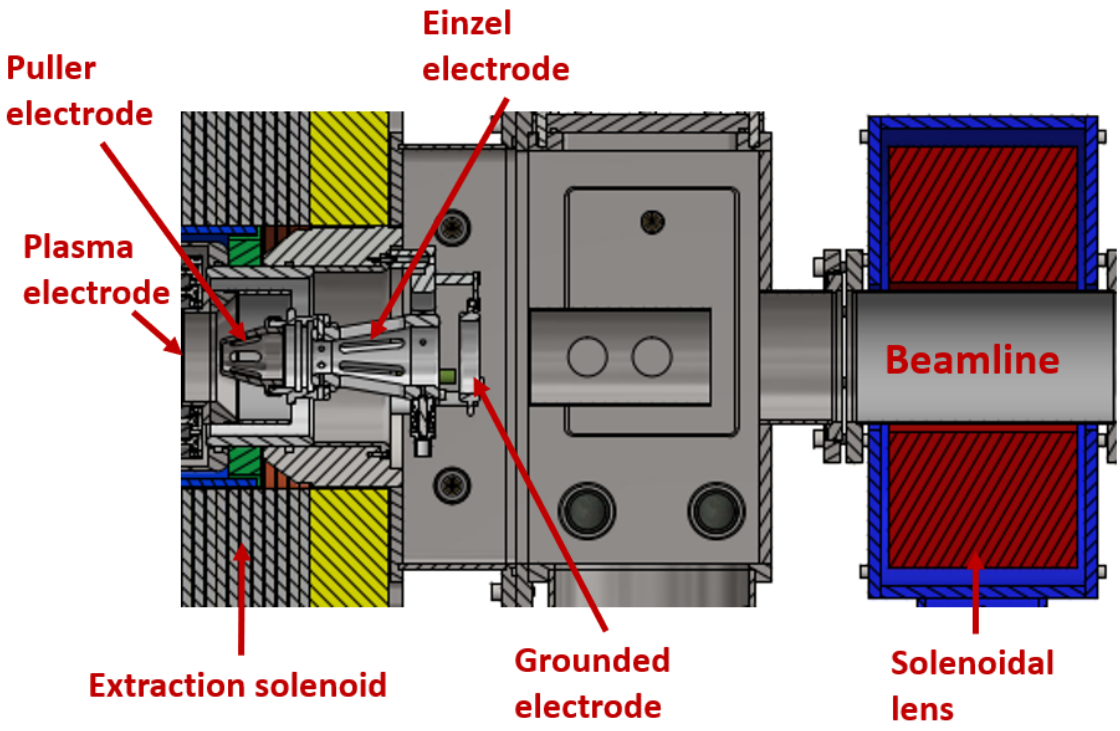

FIGURE 3.4 Cross section view of the ion beam formation section of the JYFL 14 GHz ECR ion source. The system comprises of a plasma electrode and an asymmetric einzel lens structure that combines the functionality of the einzel lens and the puller electrode. The extraction electrodes are followed by a focusing solenoid.

The plasma chamber along with the plasma electrode is kept at high potential (which is typically called the extraction voltage). This value determines the extracted beam energy, and the exact value is determined by the accelerator injection system settings to produce the requested final accelerated ion beam energy. In the case of the JYFL 14 GHz ECRIS which delivers the beam to the K-130 cyclotron the extraction voltages are typically around 10 kV. The puller electrode has a negative potential to optimise the beam formation and its typical value is close to -1 kV in the case of the JYFL 14 GHz ECRIS. The einzel electrode is typically operated around -10 kV. A detailed description of the extraction system of JYFL 14 GHz ECRIS is given by Toivanen *et al.* in Ref. [68].

(C) q/m selection and beam current measurement

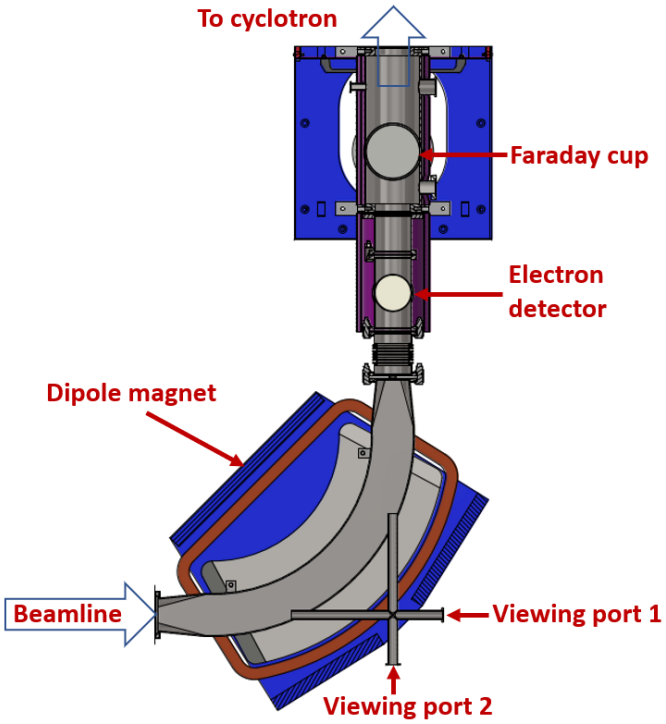

FIGURE 3.5 Top view of beamline consisting of the dipole magnet which provides q/m separation of ions and are detected using Faraday cup. The figure also shows the location of an electron detector which was inserted for an experimental campaign discussed in detail on chapter 5.

The charge to mass ratio (q/m) selection and beam current measurement section of the JYFL 14 GHz ECRIS setup is presented in Fig. 3.5. The extracted beam is transported through the focusing elements (the extraction electrodes and a solenoid) and XY-steering magnet to the dipole magnet (also known as the analysing magnet or the spectrometer magnet). The dipole magnet provides an area of homogeneous transverse magnetic field with respect to the beam direction, which bends the incoming ions based on their q/m ratio, resulting in the separation of the different

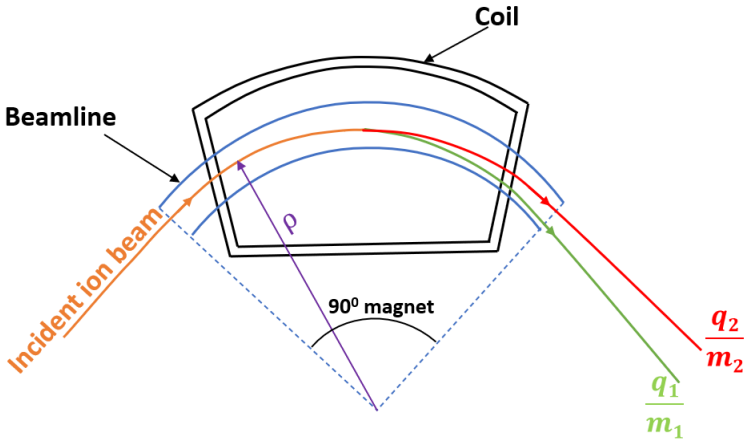

FIGURE 3.6 A schematic of the q/m separation using a dipole magnet. The incident ions are bent through the dipole magnet with a bending radius ρ which depends on the ion q/m ratio (assuming a fixed acceleration voltage for all the ions, see Eq. (3.1)). Based on this the different ion species in the incident beam are separated as they pass through the magnet.

ion species as illustrated in Fig. 3.6. The separation is based on the difference in the magnetic rigidity of the ions, given by the expression:

$$B\rho = \sqrt{\frac{2mV_{ext}}{q}} \tag{3.1}$$

where V_{ext} is the ion source extraction voltage, m and q are the mass and charge of the ion and ρ is the radius of curvature of the ion path due to the magnetic field B of the dipole magnet (see Fig. 3.6). The dipole magnet of JYFL 14 GHz ECRIS has a bending angle of 90 degrees and a bending radius of 487 mm. Therefore the ions with bending radius of 487 mm will be transported through the dipole magnet and along the following beam line. The instantaneous current of the q/m separated beam downstream from the dipole magnet can be measured using a Faraday cup (FC). It is a metal cup on which a colliding beam of charged particles generates an electric current when connected to a grounded circuit. An ammeter is typically used in the circuit to measure this current. The Faraday cup is equipped with a negatively biased ring electrode at its entrance to repel secondary electrons (emitted as a result of the ion stopping) back into the cup cavity and thus prevent the overestimation of the ion current due to the otherwise escaping electrons. In the campaigns performed with the JYFL 14 GHz ECRIS the FC was connected to a transimpedance amplifier, which is a simple current-to-voltage converter that also has the capability to amplify the output voltage. The amplifier's output can be connected to an oscilloscope, a picoscope, or some other type of data gathering system. The charge state distribution of the extracted ion beam is obtained by measuring the beam current from the FC while sweeping the magnetic field of the

dipole magnet. An example of a charge state distribution from an argon plasma is shown in Fig. 3.7. The beam can be further transported to the cyclotron by displacing the Faraday cup from the path of the charged particle beam.

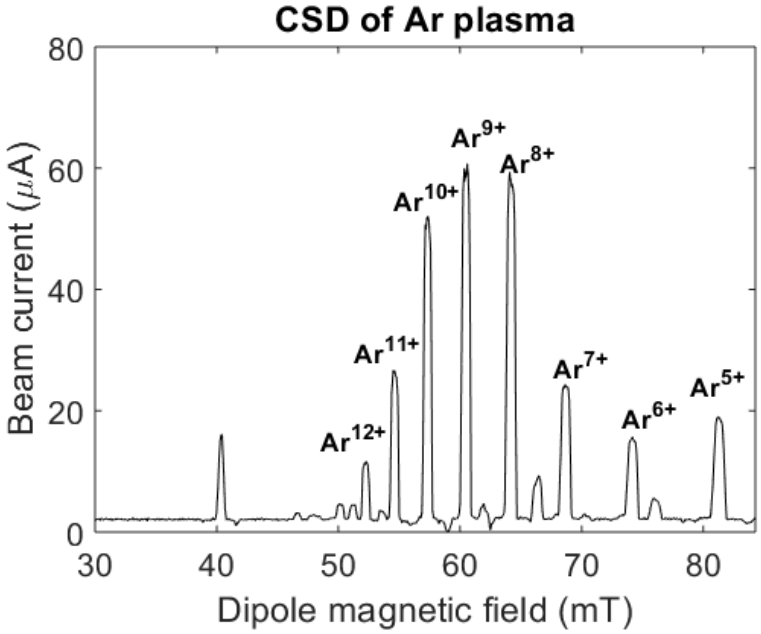

FIGURE 3.7 An example of a charge state distribution of argon ions measured with the Faraday cup as a function of the dipole magnetic field. The measurement was performed in stable plasma regime with the JYFL 14 GHz ECR ion source at 10 kV extraction voltage and 220 W of 12 GHz microwaves from a TWTA.

3.1.2 General description of the different ion sources used in the experiments

The experimental work described in this thesis was performed with five different ion sources, namely JYFL 14 GHz ECRIS (Finland) which is described in detail in Section 3.1.1, PHOENIX Booster and PHOENIX V3 at LPSC (France), GTS at GANIL (France), and the third generation superconducting ECR ion source SECRAL-II (China). The magnetic field modelling was carried out for all of these ion sources, and dedicated instability experiments were conducted with all of the second generation ion sources. The code for the modelling was developed during the course of this thesis work and the code is described in Section 4.1.

The magnetic field structure of each ion source varies due to their distinct structures. Compared to the other sources, the GTS ion source offers the extra capability of varying the position of the central coil. For instance, the central coil is kept towards the injection section in Fig. 3.8 as it is the nominal operational coil setting for GTS. A general comparison between all the sources used for studies are listed in Table 3.1. The table also presents the maximum obtained beam currents of

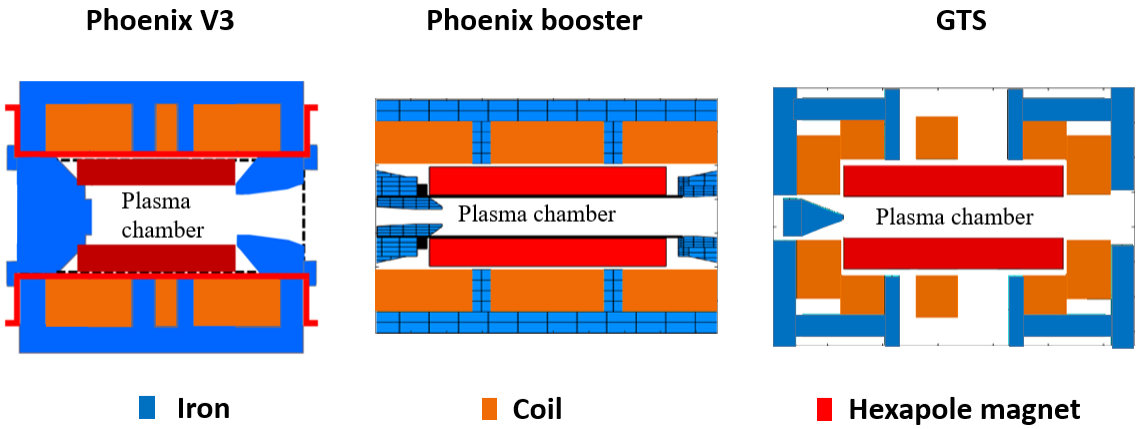

FIGURE 3.8 Cross section views of PHOENIX V3, PHOENIX Booster and GTS magnetic structures comprising of 3 solenoidal coils, a permanent magnet hexapole and soft iron.

Ar^{14+} to provide a point of comparison for the performance of the sources. It is worth noting that this performance is achieved at different RF powers and also by introducing multiple heating frequencies. For example, the peak current for the JYFL 14 GHz ECRIS has been acquired using a two-frequency heating method, while the peak current for the SECRAL-II has been obtained using a three-frequency heating method. This highlights how different sources can have different additional capabilities which enhance the production of the HCIs.

TABLE 3.1 General characteristics of the different ion sources that were used in the experimental campaigns. The main parameters compared here are the length and radius of the plasma chamber and the heating frequencies typically used with the sources. In order to have a comparison of source performance, the intensity of Ar^{14+} beam current is also included. *JYFL 14 GHz ECRIS.

Parameters	**JYFL***	**PHOENIX (B)**	**PHOENIX-V3**	**GTS**	**SECRAL II**
$Length(mm)$	300	280	234	302	401
$Radius(mm)$	38	36	44.5	39.5	62.5
$Freq.(GHz)$	14, 10.75-12.75	14.5, 18	18	14.5	18, 24
Ar^{14+} (μA)	49	-	130	37	1040

SECRAL-II is the only third generation ECR ion source used in the studies of this thesis. It is composed of a superconducting hexapole and solenoid coils, which provides the added benefit that the hexapolar magnetic field strength can also be varied. Additionally, it is unique in design, as the plasma chamber is encased inside the solenoidal coils which themselves are subsequently enclosed inside the hexapolar coils, as is shown in Fig. 3.9.

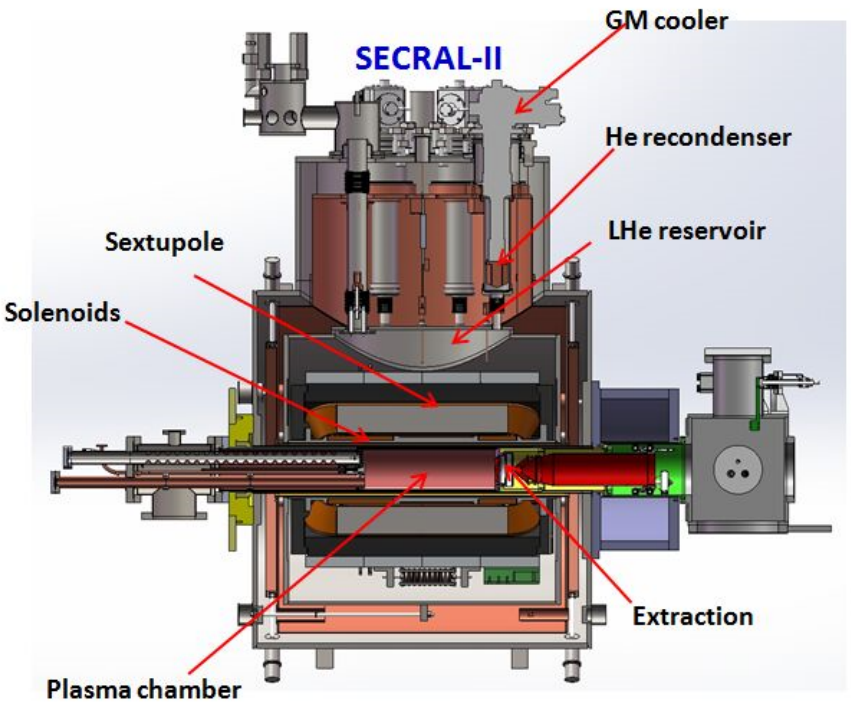

FIGURE 3.9 Cross section view of SECRAL-II superconducting ECR ion source. Reproduced from [69] with the permission from IOP Publishing.

3.2 Instability diagnostics

The anisotropy in the electron energy distribution is the primary cause of kinetic instabilities in ECR plasmas, as addressed in detail in Section 2.3. These instabilities can be identified by detecting either the microwave emission, the subsequent hot electron burst (which on collision with walls cause thick target bremsstrahlung), or by detecting the transients in the extracted ion beam current. The diagnostic techniques used in this work to detect and measure the afore-mentioned plasma transients are presented in depth in this section.

3.2.1 Microwave emission detection techniques

Plasma instabilities can be detected by measuring the plasma emitted microwaves, which are considered to be the primary diagnostic signal indicating the onset of the instability event. The microwave emission can be detected using three main diagnostic methods: (1) Schottky diode, (2) spectrum analyzer, and (3) direct measurement of the microwave emission using a high bandwidth oscilloscope. In this work, the experiments were carried out using a Schottky diode and spectrum analyzers and therefore they are described in detail below.

The Schottky diode detection setup is easy to implement, cheap and also fast with

temporal resolution in the order of 10 *ns*. In this work a low-barrier Schottky diode was connected to the secondary WR75 waveguide port of JYFL 14 GHz ECRIS to detect microwave bursts related to the kinetic instabilities. In order to protect the diode, the signal is first passed through power limiters and attenuators, as is shown in Fig. 3.10. The diode is capable of detecting signals within a frequency range of $0.01 - 50$ GHz, but the waveguide restricts the detection of frequencies below its cutoff frequency (WR75 has a cutoff frequency of 7.8 GHz). Moreover, the amplitude of each frequency measured by the diode may also be distorted because of the frequency dependent coupling efficiency of the emitted microwaves into the diagnostic waveguide and transport efficiency through the waveguide system. The output of the diode was directly connected to an oscilloscope/picoscope which together offered a temporal resolution of < 1 µs. An example of the microwave burst detected using a Schottky diode is shown in Fig. 3.11.

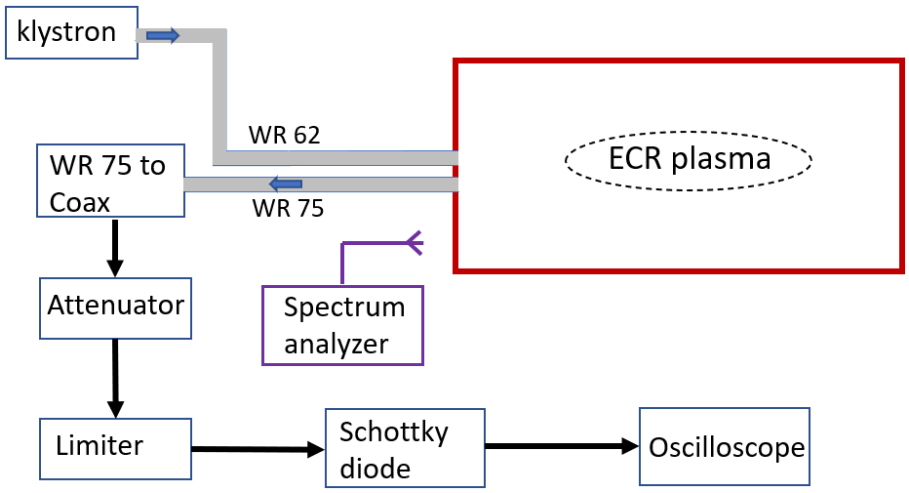

FIGURE 3.10 Microwave detection network diagram. The network diagram shows the microwave emission detection using a microwave antenna and spectrum analyzer setup placed outside the plasma chamber and also by using a Schottky diode which is connected to the WR75 waveguide diagnostic port. The Schottky diode is protected using an attenuator and a power limiter. The output from the diode is read using an oscilloscope.

The frequency information of the microwave emission cannot be retrieved using the Shottky diode. For this purpose a quarter wave monopole antenna positioned outside the ion source was connected to a spectrum analyzer. The spectrum analyzer detects the transmitted frequency by scanning across a range of frequencies separated into discrete channels, and each frequency is identified over a user-specified dwell time. The network diagram for the detection of microwave emissions is presented in Fig. 3.10. Figure 3.12 shows an example of a frequency spectrum measured with a spectrum analyzer in unstable plasma conditions. In the stable plasma operation regime only the heating frequency is present in the measured frequency spectrum.

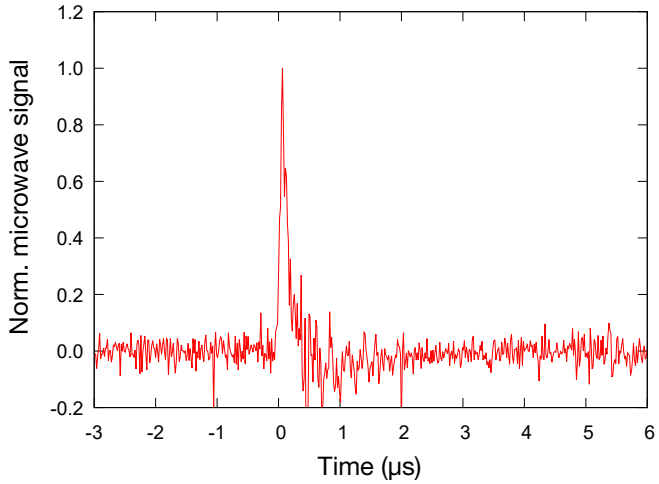

FIGURE 3.11 An example of a microwave burst detected with the Schottky diode setup described in Fig. 3.10.

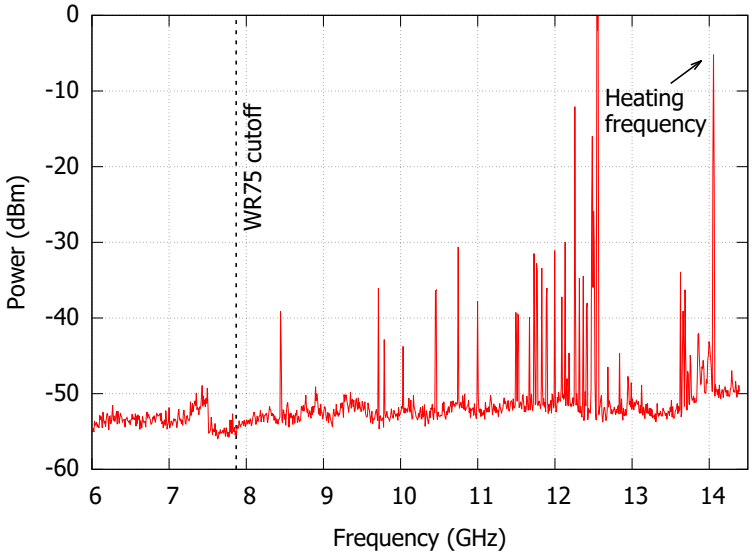

FIGURE 3.12 Microwave emission spectrum measured with a spectrum analyser in unstable plasma regime. The measurement was performed with 7.8 s sweep time. Reproduced from [37], with the permission of AIP Publishing.

One of the characteristics shown by the unstable plasma is its transition from quasi-periodical (or pulse-periodical) emissions of microwaves to continuous emission, a so-called Continuous Wave (CW) instability regime. In this CW instability regime only the continuous fixed-frequency emissions are observed with the spectrum analyser, as is shown in Fig.3.13.

3.2.2 Hot electron emission detection

At the beginning of the instability event the electrons transfer their kinetic energy to plasma wave and therefore the electron confinement strongly decreases. As

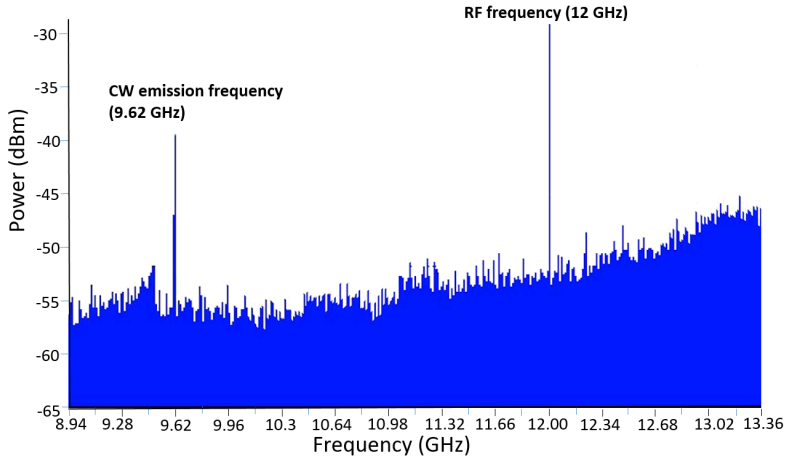

FIGURE 3.13 Spectrum analyser spectrum showing the continuous wave emission peak in unstable plasma regime. Reproduced from supplementary material of [70], with the permission of IOP Publishing.

a result, the microwave emission is followed by a sudden flux of electrons. The electrons expelled from the confinement can be detected using the biased disk at the injection end of the plasma chamber. Some part of the escaping electrons enters the extraction region and traverse further into the beam line through the plasma electrode aperture. In this case the lost electron energy distribution (LEED) of these escaping electrons can be determined by using the dipole magnet downstream from the ion source as an energy dispersive spectrometer, followed by an electron detector, as is shown in Fig. 3.14.

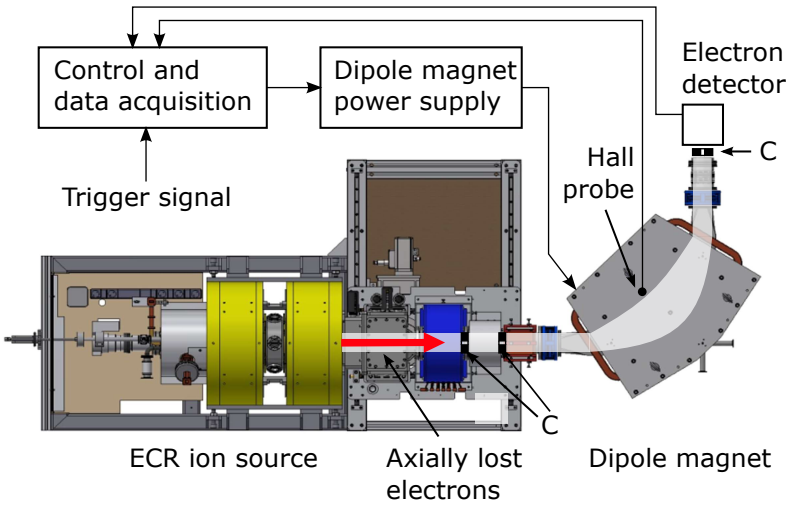

FIGURE 3.14 The LEED diagnostic setup at JYFL. The electrons lost from the confinement of the JYFL 14 GHz ECRIS are transported through the collimators (C), the dipole magnet (energy separator) and detected using the electron detector.

The electron detector consists of a biased cathode followed by a sequence of grids to amplify the electron current generated by the secondary electrons emitted from the cathode. The amplified current is detected using a grounded anode which is

connected to a transimpedance amplifier and then to an oscilloscope/picoscope. The lower limit of electron energy that is detectable is defined by the voltage of the biased cathode. For example, in Ref. [70] the voltage of -3.5 kV was used which sets a lower limit of 3.5 keV for the detected electron energy.

The polarity of the ion source dipole magnet was inverted from its normal positive ion operation method for the electron energy distribution measurements. This entailed replacing the original power supply with one that is more precise and has a small enough current step to adequately sample the electron energy. The maximum current that the power supply can deliver also determines the maximum measurable energy of electrons. A calibrated Hall-probe was used to accurately measure the magnetic field inside the dipole magnet, allowing for high-precision estimation of the electron energy. The dipole magnetic field was ramped from $0-8$ mT to obtain electron energies corresponding to $0-1.4$ MeV. After ramping the magnetic field of the dipole magnet and monitoring the electron current downstream of the magnet, the energy distribution of the electrons released from the source is computed. Finally, to obtain the correct shape of the LEED the energy dependent transmission efficiency of the lost electrons and the energy dependent yield of released secondary electrons from the cathode of the electron amplifier were included in the data analysis. These details have been explained in detail by Izotov *et al.* in Ref. [17]. An example of processed LEED signal obtained using this set up is shown in Fig. 3.15.

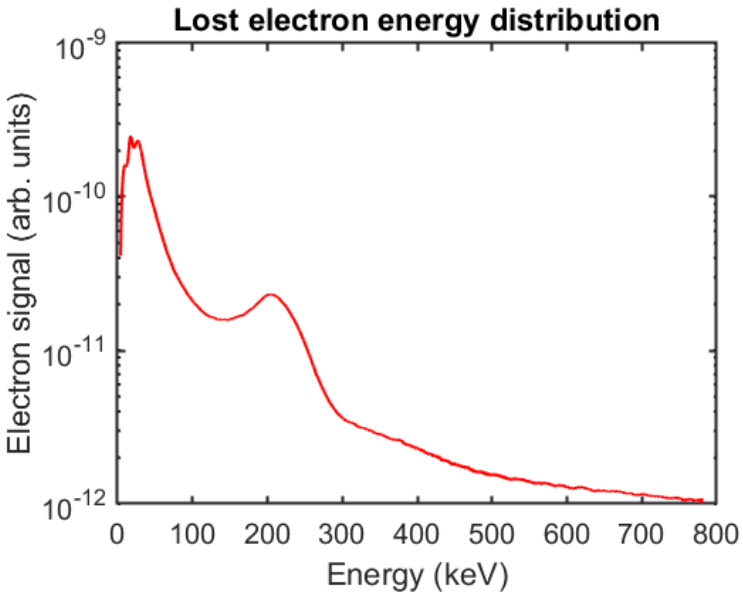

FIGURE 3.15 An example of an analysed LEED signal measured with the JYFL 14 GHz ECRIS setup.

The measured LEED was analysed by determining the total and average energy of the electrons by performing the calculations described in the following. The total

electron energy can be calculated using the expression:

$$F = \int_{\epsilon_{min}}^{\epsilon_{max}} f(\epsilon) \cdot d\epsilon \tag{3.2}$$

and the average electron energy can be obtained as:

$$\epsilon_{avg} = \frac{1}{F} \int_{\epsilon_{min}}^{\epsilon_{max}} f(\epsilon) \cdot \epsilon \cdot d\epsilon \tag{3.3}$$

where ϵ denotes the electron energy, $f(\epsilon)$ denotes the measured LEED, and ϵ_{min} and ϵ_{max} denote the minimum and maximum energies, respectively.

A distinct local maximum is typically observed in the LEED measurements (as can be observed clearly in Fig. 3.15). This "hump" can be further analysed by fitting the measured LEED with a combination of an exponential decay (λ) and a Gaussian function (G) as shown in Fig. 3.16. These functions are defined as follows:

$$\lambda(\epsilon) = a * exp(b * \epsilon) \tag{3.4}$$

and

$$G(\epsilon) = a_1 \, exp(-((\epsilon - b_1)/c_1)^2) \tag{3.5}$$

where a, b, a_1, b_1 and c_1 are constants obtained from the fitting and ϵ is the electron energy in keV.

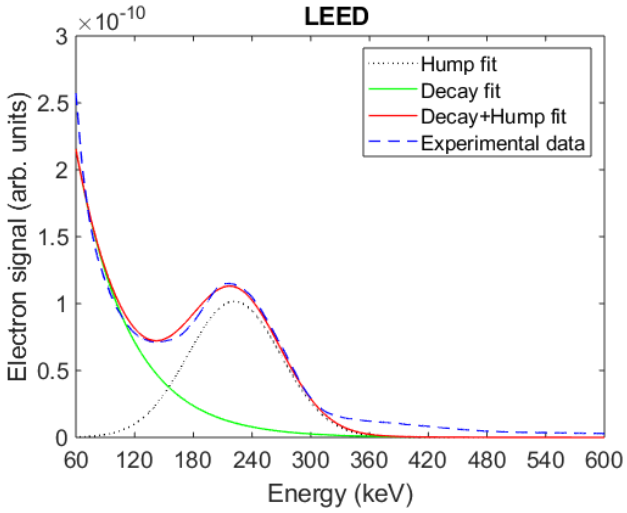

FIGURE 3.16 Determination of the high energy hump from the experimentally measured data using fitting functions. The fit is made by a combination of exponential decay function $\lambda(\epsilon)$ and a Gaussian function $G(\epsilon)$. Reproduced from supplementary material of [70], with the permission of IOP Publishing.

From the Gaussian section of the fitted function, the total and average electron energies associated with the hump were then computed. The total energy was calculated with equation

$$\epsilon_{tot,hump} = \int_{\epsilon_{min}}^{\epsilon_{max}} G(\epsilon) \cdot d\epsilon \tag{3.6}$$

and the average energy with the equation

$$\epsilon_{avg,hump} = \frac{1}{\epsilon_{tot,hump}} \int_{\epsilon_{min}}^{\epsilon_{max}} G(\epsilon) \cdot \epsilon \cdot d\epsilon \tag{3.7}$$

The next diagnostic method implemented for measuring the instability-induced electron emissions is using the biased disc. It is located at the injection end of the plasma chamber and can be used as a probe to detect the rapid transients of the electron and ion fluxes emitted during the plasma instability. These transients are on the order of μs with electron currents reaching momentarily hundreds of mA, which cannot be handled by the biased disc's power supply. As a result, the circuit between the biased disc and the power supply was adjusted by the addition of a capacitor (C) in parallel with the power supply for charge storage. The current through the circuit is monitored by measuring the potential difference across a resistor placed in series with the biased disc (R_1). In Fig. 3.17, V_{source} is the source potential and V_{BD} is the voltage provided by the biased disc power supply and resistor R_2 is the capacitor discharge resistor.

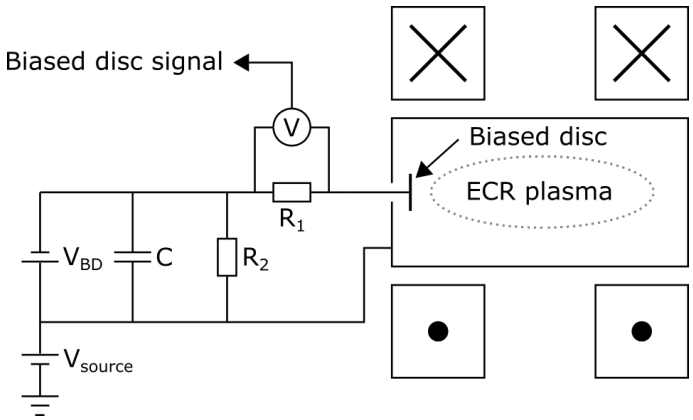

FIGURE 3.17 Biased disc used as a diagnostic for instability detection. The electron/ion transient in the biased disc current is detected by measuring the potential difference across the resistor R_1. Figure reproduced from [37], with the permission of AIP Publishing.

Figure 3.18 shows an example of a signal recorded from the biased disc during an instability. The negative current is due to an electron burst caused by the instability, followed by a longer (temporally) positive current due to the ion burst. It is noted that the total charge expelled by the ions and the electrons is approximately equal, indicating that the quasi-neutrality of the confined plasma is regained following the instability event, as demonstrated by Tarvainen *et al.* [71].

3.2.3 Bremsstrahlung diagnostics

As was presented in the previous section, the instability process results in an abrupt loss of high-energy electrons. These lost electrons follow the magnetic

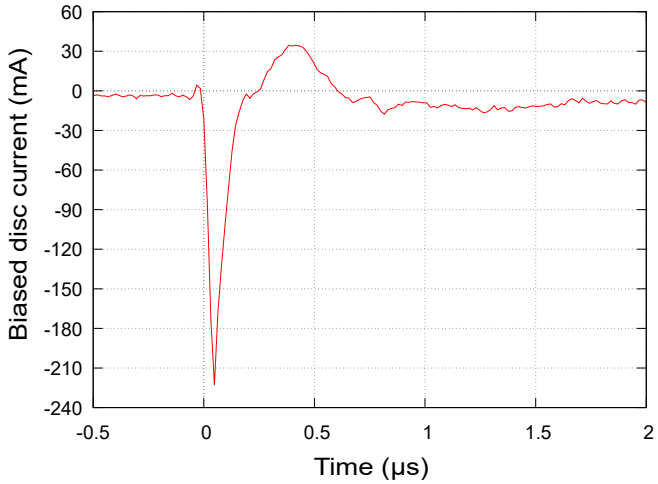

FIGURE 3.18 An example of an instability-induced signal obtained using the biased disc diagnostic setup. The negative peak corresponds to the current due to the electron burst and the positive peak corresponds to the current due to the following ion burst.

field lines and interact with the plasma chamber structures at the magnetic poles resulting in thick target bremsstrahlung emission at the interaction point. Thus the bremsstrahlung bursts can be detected to study and identify plasma instability events.

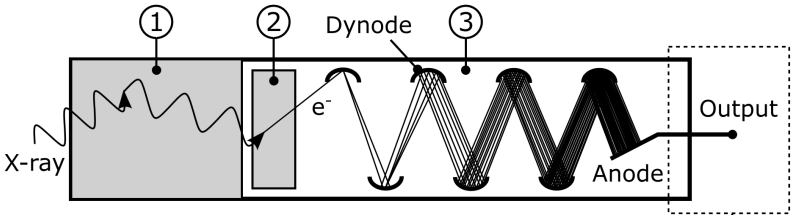

FIGURE 3.19 X-ray scintillator with photomultiplier tube for detection of x-ray signal during the instability event. The detection system consists of an x-ray scintillator (1), photocathode (2) and photomultiplier tube (3).

Standard x-ray diagnostics such as x-ray scintillators coupled with photomultiplier tubes (PMT) presented in Fig. 3.19 can be used to investigate the instability-induced radiation transient and its properties. When the instability-induced bremsstrahlung photon interacts with the scintillator material, it causes electron excitations. The volume of the scintillator material is critical because it is strongly related to the detection efficiency, particularly in the high-energy tail of the bremsstrahlung spectrum. The material emits a pulse of photons in the visible light spectrum as a result of the x-ray photon absorption and subsequent de-excitations. These photons are converted to electrons using a photocathode ((2) in Fig. 3.19) and the electron signal is amplified using a series of dynodes (labelled as (3) in Fig. 3.19) by the process of secondary electron emissions from each dynode. Hence, there is an exponential increase in the electron current which

is detected in the collector anode at the end of the dynode chain. The PMT can be operated in the current mode or in the voltage mode. In the current mode the signal output from the anode is connected to a transimpedance amplifier which amplifies the electron current and then converts it to a voltage signal. This signal can then be directly connected to an oscilloscope or picoscope. In the voltage mode the output signal of PMT is detected across a capacitor between the anode and the output of the tube. In the current mode the signal amplitude is proportional to the power flux of x-rays while in the case of voltage mode it is proportional to the change of the power flux. In this work the PMT was operated in the current mode.

The studies employed a Bismuth Germanate (BGO) scintillator together with a sodium doped caesium iodide PMT. The scintillator reacts rapidly to the external photon flux with its fluorescence decay time in the order of 300 *ns* and secondary electron amplification time characteristic in the order of 100 *ns* [72], therefore it does not hinder the temporal resolution of the instability detection setup. It should be noted that the RC constant of the transimpedance amplifier (or any other data collection device) determines the temporal resolution of the detected bremsstrahlung transient signal. Fig. 3.20 shows an example of an instability-induced x-ray signal measured with an x-ray scintillator.

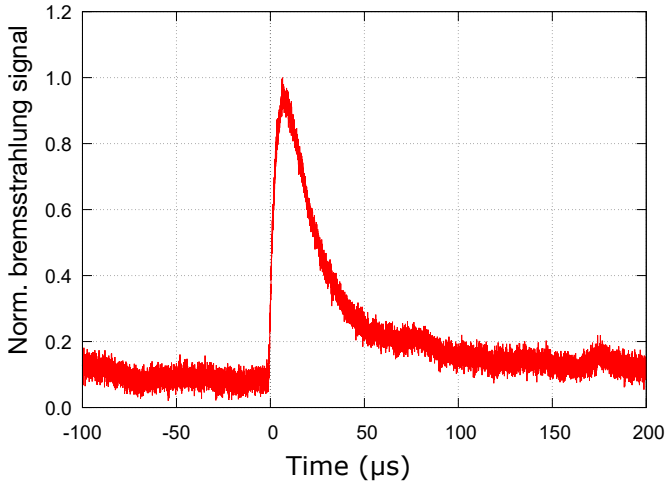

FIGURE 3.20 A sample of the x-ray signal that is generated during an instability event and detected by the x-ray scintillator.

The photon emission due to bremsstrahlung can also be investigated using an energy sensitive semiconductor detector. Amptek XR-100 CdTe detector [73] was used as part of this thesis work. It has a 12.5 μm beryllium window and an active volume of Cadmium Telluride (CdTe). When the bremsstrahlung photon traverses through the beryllium window and falls on the active volume, it generates electron-hole pairs. The number of electron-hole pairs produced are directly proportional to the incident photon energy. The measurements must be correlated by the efficiency of the detector, as the lowest photon energy that is detectable depends on the

thickness of the beryllium window and the highest detectable energy depends on the thickness of the active volume. For instance, in the case of the Amptek XR-100 the detection efficiency is maximum for the range of $20 - 50\ keV$ and therefore a proper efficiency calibration over the range of the spectrum has to be performed. Under the influence of a high voltage, the generated electron-hole pairs drift towards opposite electrodes, resulting in a current pulse that is amplified and converted to a voltage signal by a preamplifier and fed to the processing electronics. Finally a histogram is created from the measured events from which the correct energy distribution data can be retrieved after the detector has been properly calibrated with photon emissions of known energies.

There is also a possibility that the detector could record pile up of events if the incident bremsstrahlung photon count rate is very high. Pile up of signals occurs when the detector records different single events as one event of combined energy. Another factor concerning the measurement is the dead-time of the detector; it is the signal processing time after an event where the system is not able to detect new incoming signals. It is essential that the dead time is minimised by controlling the flux of incoming photons with a proper collimator setup. The Amptek XR-100 incorporates a feature for automatically detecting and rejecting pile ups. In the experiments conducted as part of this thesis work, the photon count rates were always less than 250 counts/second, which results in insignificant dead time. For instance, the detected dead time for the photon count rate of 5000 counts/second was 1.67 % when the same detector was used in another campaign.

It must be noted that these detectors provide time averaged energy distribution of bremsstrahlung which is a limitation considering the detection of the onset of the instability which is characterized by the sudden bursts of bremsstrahlung photons. An example of time averaged bremsstrahlung spectrum obtained using this setup is shown in Fig. 3.21.

The bremsstrahlung spectrum can be analysed by calculating the total and average photon energies. The analysis is done in a similar way as described for the LEED measurements with Eqs. (3.6) and (3.7), however in this case the calculation is done for photons instead of electrons. One more quantity can be calculated from this spectrum, which is generally referred to as spectral temperature (T_s). The spectral temperature is calculated under the assumption that the electron energy distribution in the plasma is Maxwellian, however, it has been established that ECR plasmas contain multiple electron populations, and thus the electron energy distribution is not strictly Maxwellian in shape [14, 15, 16, 17]. Consequently the spectral temperature cannot be used to estimate the actual electron temperatures. However, it is still an important quantity which can be used to draw inferences from parametric sweeps about the changes in the electron population and also to compare the produced results with those from other sources. The spectral temperature is obtained from a linear fit of the bremsstrahlung spectrum in the

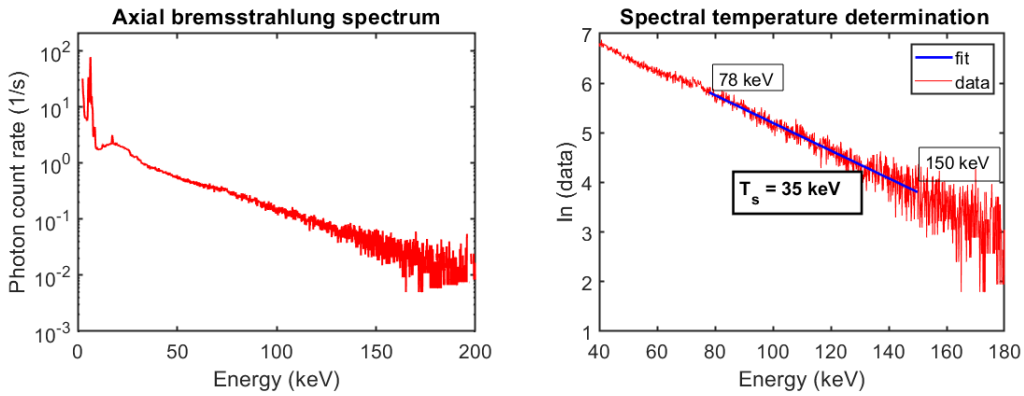

(a) (b)

FIGURE 3.21 (a) Bremsstrahlung spectrum measured from JYFL 14 GHz ECR with Amptek XR-100 CdTe detector in the axial direction. The detector was kept in vacuum with a direct line of sight to the confined plasma. (b) The method of determining the spectral temperature from the measured bremsstrahlung spectrum.

logarithmic scale. The method of determining the spectral temperature is described in detail in the supplementary material of the article Bhaskar *et al.* which is attached in the Appendix PIII.

3.2.4 Ion emission detection

The instability induced electron burst will strongly affect the quasineutrality of plasma and consequently ions are emitted in the time scale of the order of μs to regain the quasineutrality (as demonstrated in Fig. 3.18). These sudden bursts of electrons and ions affect the sequential ionisation processes in the plasma, as described in Section 2.2.4, which has direct influence on the production of ions. The impact of this process on the ion beam intensities can be studied using the dipole magnet - Faraday cup combination described earlier in this chapter.

The Faraday cup is positioned in the beamline downstream from the dipole magnet, as illustrated in Fig. 3.5. The plasma instabilities induce quasi-periodic oscillations of the extracted ion beam current and therefore the Faraday cup can be utilised to measure the ion beam current transient during the instability event while the magnetic field of the dipole is kept constant. The setup allows for the measurement of the change in beam current for a certain charge state of interest by selecting the corresponding dipole current. The biased disc can also be used to detect transient ion flux, as detailed in previous section.

A transimpedance amplifier converts the Faraday cup current to voltage, which the oscilloscope/picoscope records. It is worth noting that different charge states are affected by the instability in different ways. High charge state ions show an

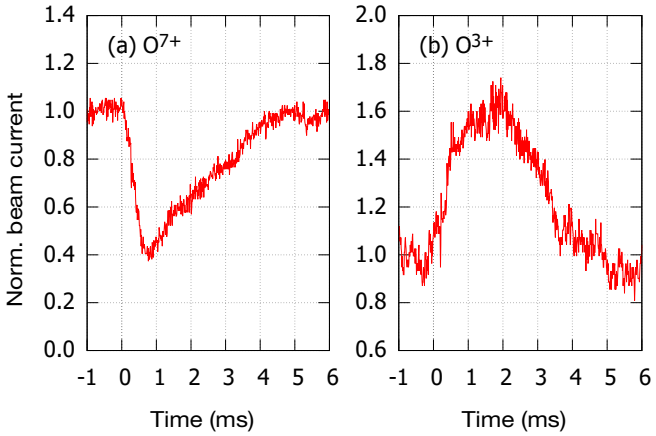

FIGURE 3.22 The effect of instability event on a high charge state (O^{7+}) and a low charge state (O^{3+}) oxygen beam current. The signals were recorded using the Faraday cup of the JYFL 14 GHz ECRIS setup.

abrupt decrease at the onset of the instability, followed by recovery in the *ms* time scale, while low charge state ions show the opposite behaviour, with a temporary increase, as shown in Fig. 3.22.

4 DEVELOPMENT OF COMPUTATIONAL TOOLS

This chapter is dedicated to the computational tools that were developed to analyse and comprehend the experimental findings with regard to various experiments connected to the kinetic instabilities. The first section of this chapter focuses on the development of the computational code which can rapidly compute the three dimensional magnetic field distribution of ECR ion sources, generate the iso-magnetic surfaces corresponding to the resonance zone and extract relevant magnetic field parameters from it. The goal is to use it to investigate the role played by these magnetic field parameters when the source exhibits kinetic instabilities.

The second section presents the code developed for the analysis of the multi-diagnostic signal data collected during the experimental campaign to study the quasi-periodic instabilities in ECR plasma. The code was used to process the signals that resulted from the detection of the instability-induced bursts of electromagnetic waves and particles escaping from the plasma volume. The code was also used to perform a statistical analysis of the preprocessed data to study the temporal features of the instabilities, especially the link between the magnitude and the repetition rate of the instability events.

4.1 Three dimensional modelling of ECRIS magnetic field

Magnetic field modelling is necessary when designing ECR ion sources. The three dimensional modelling of the ECR ion source magnetic field is often performed using commercially available OPERA-3d along with its analysis program TOSCA [74] and freely available software package RADIA [75] which is interfaced using MATHEMATICA. This requires 3D model of the ion source magnetic components and then, using this model, the 3D magnetic field distribution in the ion source is

generated by using boundary integral method. In the case of multiple magnetic field simulation calculations, it become a time consuming process that limits the number of studied field configurations. Consequently, it was decided to develop a new computational tool capable of swiftly producing three-dimensional magnetic field distributions based on approximations.

To execute a quick computation, the magnetic field must be calculated analytically. This was accomplished by the superposition of two-dimensional axial and hexapolar magnetic fields and following the procedures which is explained in detail in the subsequent section. When a comparison was made with the RADIA model, the analytical magnetic field was found to show an error of ≤ 10 % , which is within the acceptable range for this investigation. The analytical computation of magnetic field and the procedures for obtaining various ECR parameters are detailed in depth in the subsequent sections.

The development process of the computational tool can be divided into three sub-sections :

(a) Rapid computation of magnetic field vector in the ion source.

(b) From the computed magnetic field: extract the three dimensional iso-magnetic field surface which satisfies the condition for ECR resonance i.e. $B_{ECR} = \frac{\omega_{RF}\gamma m_e}{e}$ (see Equations. (2.13) and (2.19)).

(c) Extract the magnetic field properties like magnetic field gradient distribution over the resonant surface, volume of the resonant surface, surface area of the resonant surface and other numerous parameters of interest.

The iron structure and the solenoidal coils of the ion source were modelled using a two dimensional planar/axisymmetric magnetic field modelling software called FEMM (Finite Element Method Magnetics) [76]. The axial magnetic field was obtained by using this two dimensional finite element solver and an example of the FEMM output modelled for the JYFL 14GHz ECRIS (which is presented in Section 3.1.1) is displayed in Fig. 4.1. The off-axis magnetic field components can be expressed analytically as a Taylor expansion of a function defined on-axis (i.e. $B_z(0,z)$) as follows [77]:

$$B_z(r,z) = B_z(0,z) - \frac{r^2}{4}\frac{d^2}{dz^2}B_z(0,z) + \frac{r^4}{64}\frac{d^4}{dz^4}B_z(0,z) - \ldots + (-1)^n \frac{r^{2n}}{2^{2n}(n!)^2}\frac{d^{2n}}{dz^{2n}}B_z(0,z) \tag{4.1}$$

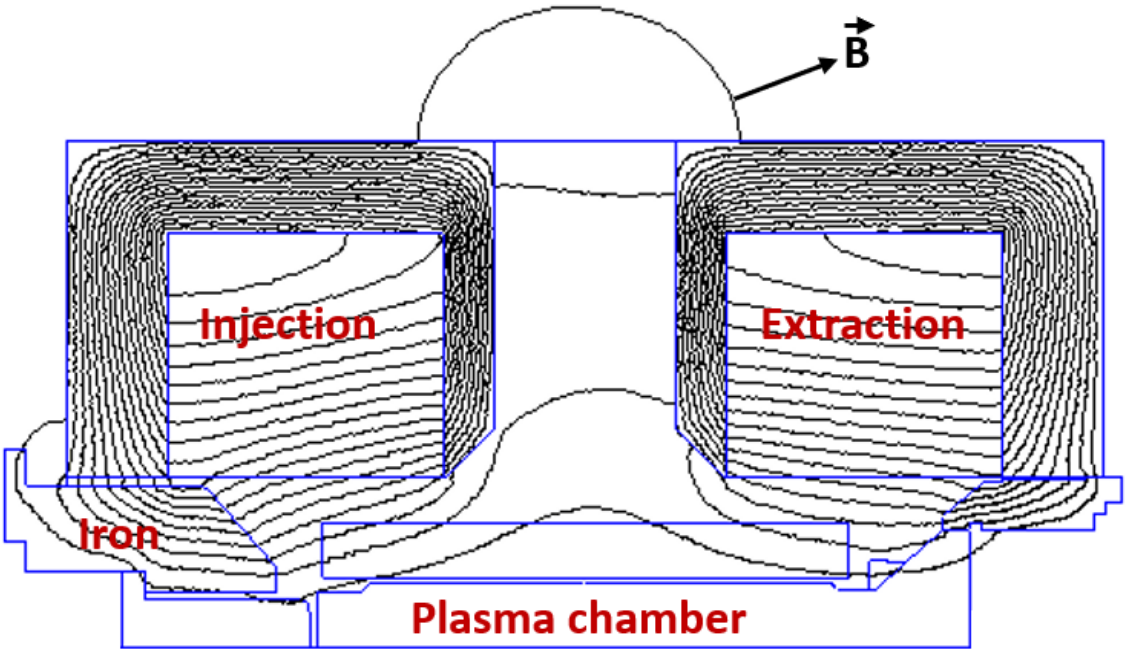

FIGURE 4.1 The cross-sectional view of the solenoidal magnetic field of the JYFL 14GHz ECRIS. The magnetic field was calculated using FEMM.

$$B_{\mathrm{r}}(r,z) = -\frac{r}{2}\frac{d}{dz}B_{\mathrm{z}}(0,z) + \frac{r^3}{16}\frac{d^3}{dz^3}B_{\mathrm{z}}(0,z) - \ldots + (-1)^n \frac{r^{2\mathrm{n}\text{-}1}}{2^{2n-1}(n!)(n-1)!}\frac{d^{2\mathrm{n}\text{-}1}}{dz^{2n-1}}B_{\mathrm{z}}(0,z) \tag{4.2}$$

where $B_z(r,z)$ represents the axial component of the magnetic field at a distance r from the axis and $B_{\mathrm{r}}(r,z)$ represents the radial component.

The axial field was represented by a 6^{th} order polynomial fit to the values calculated using FEMM which is given by the Equation (4.3) [78]:

$$B_{\mathrm{z}}(0,z) = A_0 + A_1 z + A_2 z^2 + \cdots + A_6 z^6 \tag{4.3}$$

Substituting Equation 4.3 in Equations 4.1 and 4.2 gives

$$\begin{aligned} B_{\mathrm{z}}(r,z) = {} & A_0 + A_1 z + A_2\left(z^2 - \frac{1}{2}r^2\right) + A_3\left(z^3 - \frac{3}{2}r^2 z\right) \\ & + A_4\left(z^4 - 3r^2z^2 + \frac{3}{8}r^4\right) + A_5\left(z^5 - 5r^2z^3 + \frac{15}{8}r^4 z\right) \\ & + A_6\left(z^6 - \frac{15}{2}r^2z^4 + \frac{45}{8}r^4z^2 - \frac{5}{16}r^6\right) \end{aligned} \tag{4.4}$$

$$B_{\mathrm{r}}(r,z) = -\frac{1}{2}A_1 r - A_2 rz - A_3\left(\frac{3}{2}rz^2 - \frac{3}{8}r^3\right) - A_4\left(2rz^3 - \frac{3}{2}r^3 z\right) - A_5\left(\frac{5}{2}rz^4 - \frac{15}{4}r^3z^2 + \frac{15}{16}r^5\right) - A_6\left(3rz^5 - \frac{15}{2}r^3z^3 + \frac{15}{8}r^5 z\right) \tag{4.5}$$

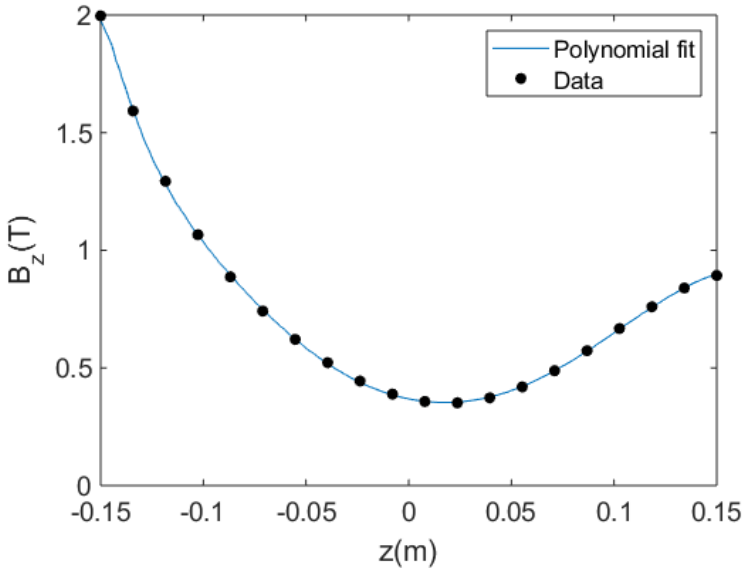

FIGURE 4.2 The axial magnetic field calculated with FEMM is presented by black dots and the magnetic field calculated using the polynomial fit function is presented by a blue line.

As the solenoidal current changes, the axial magnetic field also varies, thus for each current setting a unique set of coefficients $A_0, A_1, ..., A_6$ would be obtained. Therefore in order to obtain the analytical expression for the magnetic field as a function of the solenoid current, a large set of files containing all combinations of the magnetic field for every 20 ampere current steps were generated using FEMM. For each current value, the polynomial fit was performed to obtain the coefficients $A_0, A_1, ..., A_6$. The coefficients were then expressed as a function of each solenoid current by fitting it with a quadratic equation in terms of injection, central (for 3 solenoid systems) and extraction currents represented by (4.6)

$$A_j = \sum_{m=1}^{3}\sum_{n=1}^{3} a_{mnj}(I_m)^{n-1} \tag{4.6}$$

where a_{mnj} were obtained by solving a set of over determined equations and I_m represents coil current. For instance if we consider three solenoid system, then I_1 would represent the injection solenoid current, I_2 would be the central solenoid current and I_3 would represent the extraction solenoid current.

In the ECR ion source, the radial confinement is realised using a hexapole magnet as explained in Section 2.2.6. The hexapole is approximated by a hard edge model where the radial field is only transverse, i.e. does not have the axial magnetic field component, and the two dimensional model generated using FEMM would be sufficient for this purpose. The analytical values for the radial and the azimuthal magnetic fields were calculated using a multi-pole expansion :

$$\begin{aligned} B_{\mathrm{r}}(r,\theta) &= \sum_{i}^{\infty} B_{\mathrm{r,i}}(r,\theta) \\ B_{\theta}(r,\theta) &= \sum_{i}^{\infty} B_{\theta,\mathrm{i}}(r,\theta) \end{aligned} \tag{4.7}$$

where

$$\begin{aligned} B_{\mathrm{r,i}}(r,\theta) &= J_i \left(\frac{r}{r_{ref}}\right)^{i-1} \cos(i\theta) \\ B_{\theta,\mathrm{i}}(r,\theta) &= -J_i \left(\frac{r}{r_{ref}}\right)^{i-1} \sin(i\theta) \end{aligned} \tag{4.8}$$

In Equation 4.8 the radius r is the radial coordinate, θ is the azimuthal angle and r_{ref} denotes the reference radius (i.e the chamber radius). By solving the equations 4.8 simultaneously with the radial and azimuthal magnetic field values obtained from the modelled hexapolar field, the values for coefficients J_i are obtained with real values given by coefficients $J_3, J_9, J_{15} \cdots, J_{33}$ and the other values remain zero due to the field symmetry. The first six real value coefficients were used in the Equation (4.8) to obtain the analytical expression for the hexapolar magnetic field.

After obtaining the analytical expression for both solenoidal and hexapolar magnetic fields, the three dimensional magnetic field values were obtained by superposition of these magnetic fields. Subsequently the total magnetic field at any location inside the ion source chamber can be calculated using a function whose variables are spatial locations of the point of interest (in cartesian co-ordinate system) and the solenoid current corresponding to all three solenoids (two solenoids in case of the JYFL 14 GHz ECRIS).

Figure 4.4 shows the cross section of the magnetic field lines inside the JYFL 14 GHz ECRIS. The magnetic fields were calculated using the analytic solutions described above. The red circle shown in the figure corresponds to the inner surface of the plasma chamber.

The resonance zone corresponding to iso-magnetic field value B_{ECR} was extracted using the inbuilt matlab function isosurf.m [79] which divides the entire chamber

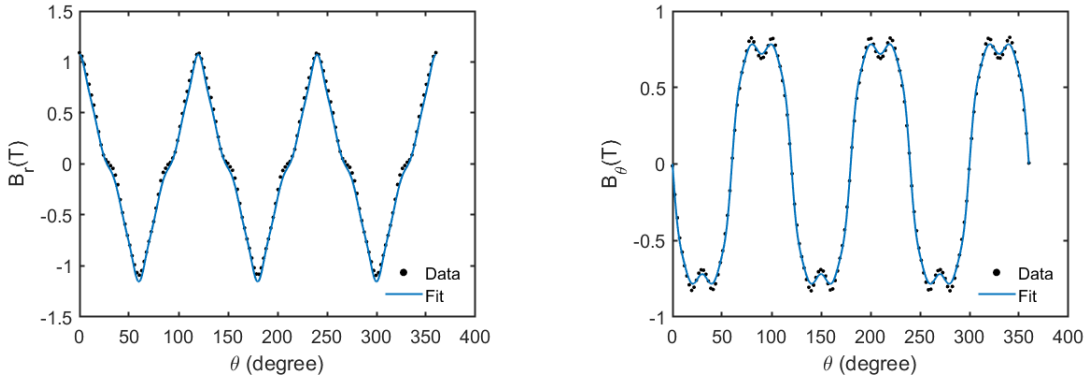

(a) (b)

FIGURE 4.3 The radial and the azimuthal magnetic fields for the hexapole magnet of the JYFL 14GHz ECR calculated at the surface of the chamber by using FEMM and the fitted function. The values of θ = 0, 60, 120, 180, 270 and 360 represent the magnetic poles of the hexapole.

volume into cubes of equal size, identifies the cubes corresponding to magnetic field value B_{ECR} and generate the three dimensional surface by means of triangular mesh. The surface generated by this method is shown in Fig. 4.5.

From the triangular meshed ECR surface, the ECR surface area and volume are calculated. The magnetic field gradient parallel to the field line $\left(\frac{\vec{B}\cdot\nabla\vec{B}}{|\vec{B}|}\right)$ was also calculated on the centroid of each triangle forming the ECR surface (see Fig. 4.5). However since every triangle in the mesh on ECR surface does not have the same area, a proper weighing factor (G_i) is given based on the area of the triangle. The weighted gradient G_i for i^{th} triangle defined as

$$G_i = \frac{g_i \times S_i}{\sum_1^N S_i} \tag{4.9}$$

where $g_i = \left(\frac{\vec{B}\cdot\nabla\vec{B}}{|\vec{B}|}\right)_{C_i}$ is the gradient at centroid of i^{th} triangle and S_i represents the surface area of i^{th} triangle. The mean gradient of the magnetic field is given by

$$< \nabla B_{ECR} >= \frac{\sum_{i=1}^N g_i}{N} \tag{4.10}$$

A typical histogram distribution of weighted magnetic field gradient is shown in Fig. 4.6 and the spatial distribution of magnetic field gradient over the ECR surface is shown in Fig. 4.7. The sharp peaks corresponds to the ECR zone ends where the field gradients is quite homogeneous on a large surface perpendicular to the ECRIS axis z .

As discussed in Section 2.2.3 one of the factors that contribute to plasma heating

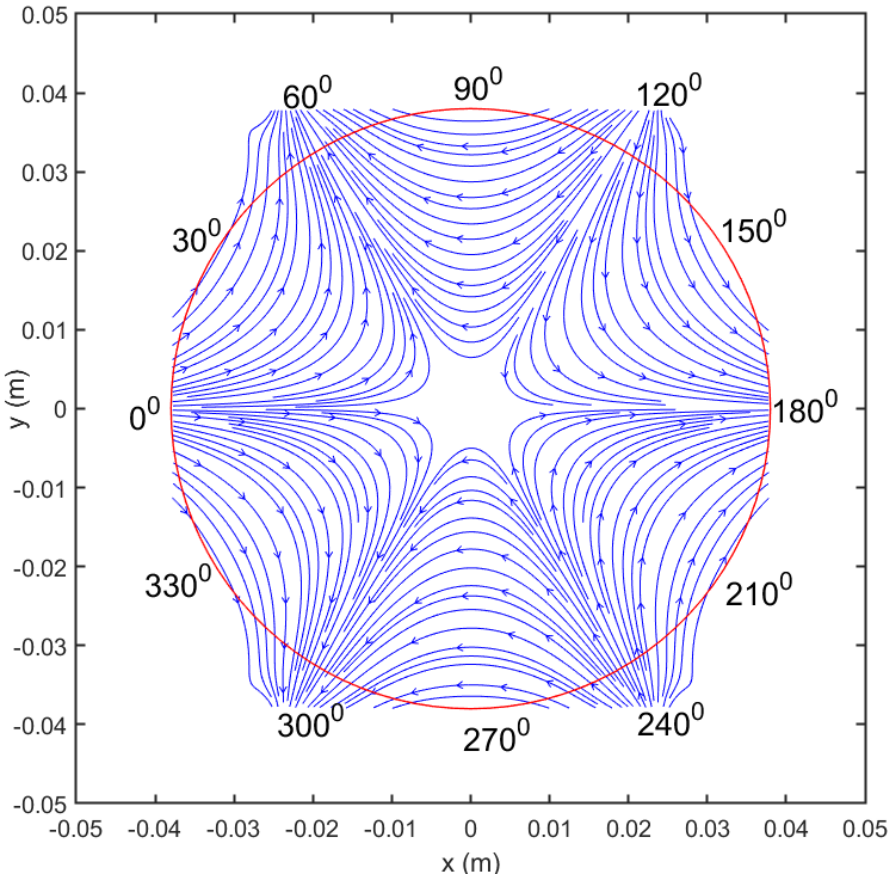

(a) X-Y cross section of total magnetic field lines inside the chamber, the co-ordinates (0,0) represents the geometrical centre of the chamber.

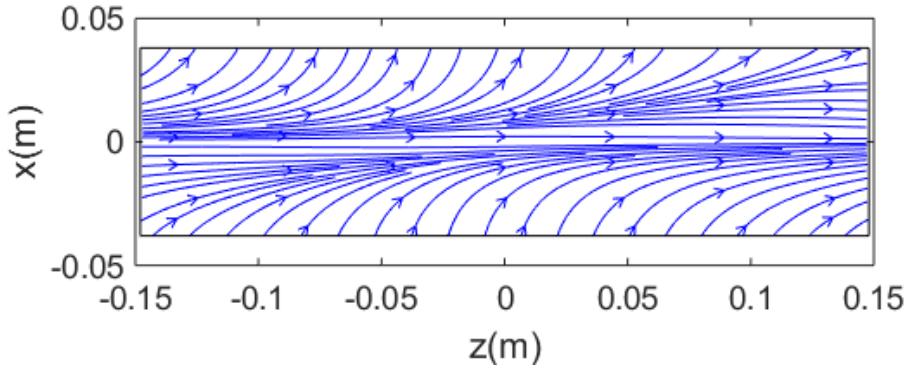

(b) Z-X cross section of total magnetic field lines inside the chamber

FIGURE 4.4 The analytically modelled magnetic field lines inside the plasma chamber of the JYFL 14GHz ECR ion source.

is the gradient of the magnetic field, hence the average magnetic field gradient parallel to the magnetic field lines are extracted using the tool presented here. Another relevant magnetic field parameter which has been used by the ECRIS community to study the magnetic field properties is the magnetic field strength at the last closed surface $|B_{max,closed}|$, which is defined as the maximum magnetic field strength required for having a closed magnetic field within the plasma chamber [80]. It is obtained by finding the minimum of total magnetic field at the poles

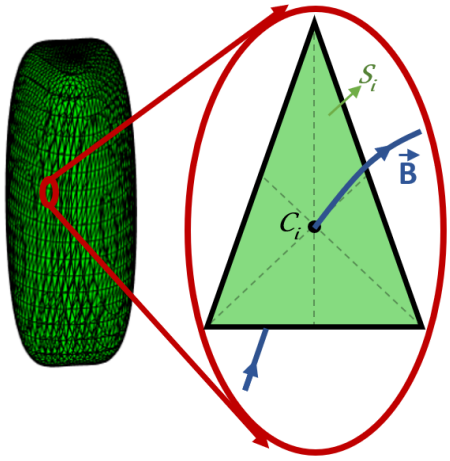

FIGURE 4.5 Three dimensional iso-magnetic field surface generation by dividing the surface into triangles and zoomed in view calculation of magnetic field gradient parallel to the magnetic field line $\vec{B}$ through the centroid of the triangle C_i whose surface area is S_i.

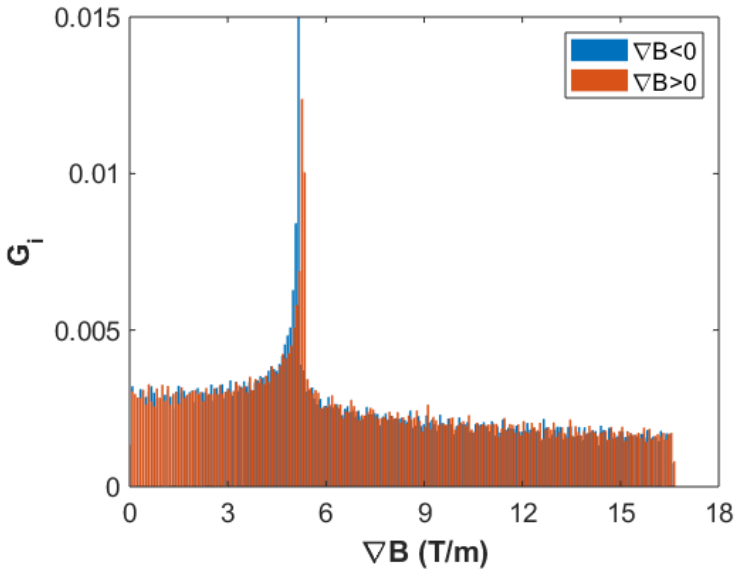

FIGURE 4.6 Histogram plot of magnetic field gradient distribution on the ECR surface.

($\theta = 0^o$ *and* 60^o), between the poles ($\theta = 30^o$) (along the pole lines) and extraction magnetic field (B_{ext}) (along the axis), as shown in Fig. 4.8.

In general, a rapid and reliable magnetic field computation has been developed in connection with the ECR zone, which can be used to any ECR ion sources as long as its axial magnetic field data along with radial, and azimuthal magnetic field at chamber wall of the hexapole magnet are known.

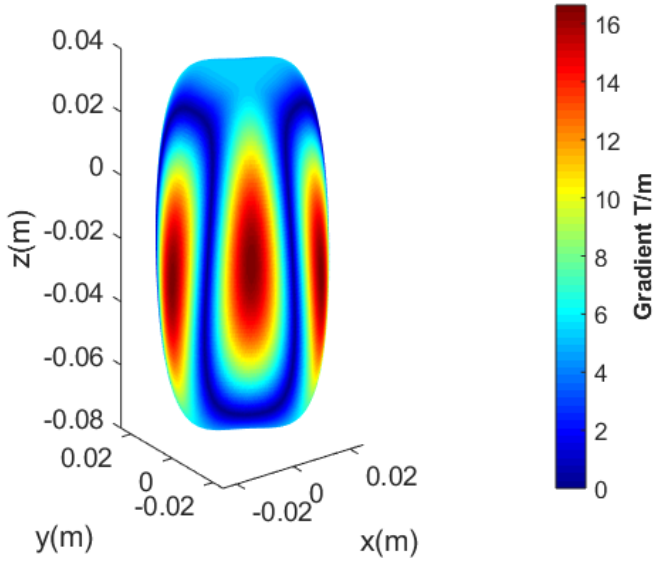

FIGURE 4.7 An example of spatial distribution of magnetic field gradient in the ECR surface for the JYFL 14GHz ECR for resonance surface corresponding to 14 GHz RF heating.

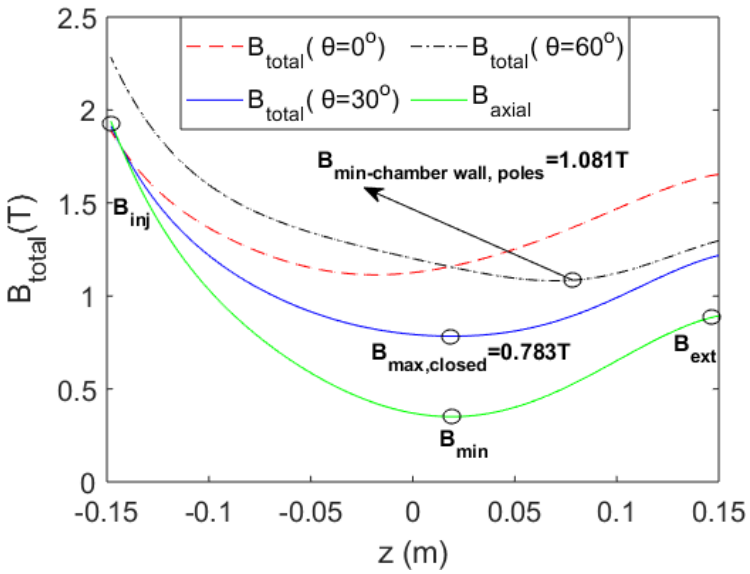

FIGURE 4.8 The total magnetic field was calculated along the poles at the plasma chamber wall for two different angles; $\theta = 0$ *and* 60 degree represents two adjacent poles. $|B_{min-chamberwall,poles}|$ is the minimum magnetic field at the chamber walls near poles of the hexapole. Reprinted with permission from the supplementary material of [70]. Copyright 2021, AIP Publishing LLC.

4.2 Development of data analysis tools for investigating experimentally obtained kinetic instability signals

The objective of one of the thesis experimental campaign was to study the relation between the amplitude of the instability bursts and the time between them. The

experimental campaign was performed by detecting several transient signals like microwave, x-ray and charged particle emission related to the instability. Numerous diagnostic techniques were used, including a BGO scintillator for the detection of x-ray bursts (see Section 3.2.3), a Schottky diode for the detection of microwave bursts (see Section.3.2.1), and the biased disc for the detection of electron and ion bursts (see Section. 3.2.2). All the signals were measured simultaneously to improve the reliability of the data and to avoid misinterpretations. The signals were recorded using a picoscope which was connected to a computer. The sampling rate of all channels (signals) was defined by the fastest transient signal, i.e. by the microwave signal with a temporal resolution of 16 *ns*. This sampling rate was required to have enough data points during the microwave transient as per Nyquist–Shannon sampling criterion [81]. In order to have enough statistics the total measurement time for each source settings was 10 seconds. These all together resulted in an enormous amount of data: for instance one 10 seconds data set resulted in approximately 10 GB of binary data. Therefore, the analysis tool had to be developed which is able to identify each instability peak and which can be used for a statistical analysis.

Figure. 4.9 shows the bursts of microwave and x-ray signals measured simultaneously during the unstable plasma conditions. Due to the high temporal resolution required for accurate determination of the microwave signal (16 *ns* used in the measurements) the data collection time with picoscope was limited to one second since there was a restriction in file size imposed by the picoscope. In order to have a sufficient statistics, the measurement was repeated ten times in total to obtain a data set of 10 seconds for each source setting. Figure. 4.10 shows examples of the temporal behaviour of a single x-ray and microwave signal measured using the scintillator setup and the Schottky diode, respectively, as described in Section 3.2. The same temporal resolution was used for all signals (microwave, x-ray, biased disc and Faraday cup) for the synchronisation of the signals. Most of the analysis was done for the x-ray signals as is justified and explained in Section 5.4.

The isolated x-ray peak was detected using inbuilt Matlab peak detection function (findpeaks.m [82]) which was used to extract the timestamp and FWHM of each peak by using a peak amplitude threshold with respect to the background signal. For each data set the amplitude threshold was cautiously chosen so that the peak identifier detects the bursts which was simultaneously observed also by other diagnostics. The timestamp of the peak (burst) was used to isolate the peak and calculate the actual amplitude (h) of the peak from the baseline (see Fig. 4.11). The baseline was calculated by averaging a moving time window of 800 *ns*, the time window was very small compared to the time separation between two peaks. The area enclosed by the instability burst (peak) was calculated by integrating over the peak with a threshold set to of 5 % above the baseline and until the point when the signal at the trailing edge of the peak had reached the baseline value. In Fig.

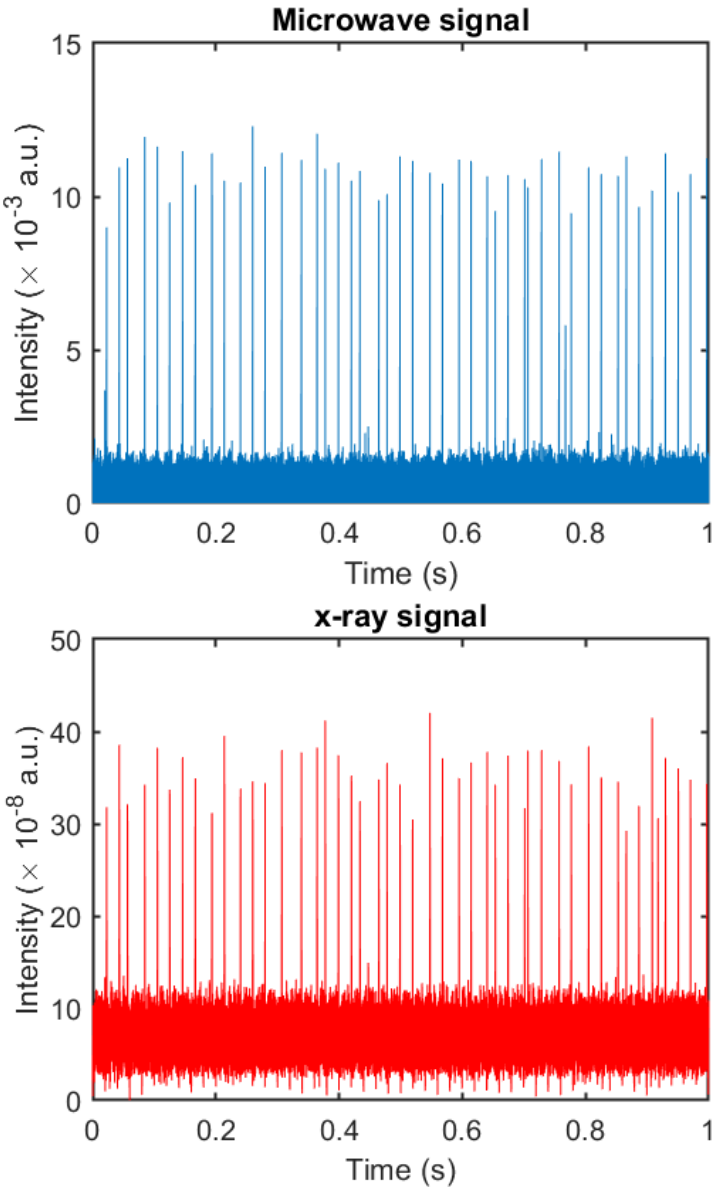

FIGURE 4.9 Raw data of microwave signal measured using Schottky diode and the x-ray signal measured using BGO scintillator for 1 *s* in unstable plasma regime.

4.11 this integrated section is highlighted by red colour. On the further analysis it was found that the instability bursts were found to be grouped (See Fig. 4.12) which complicated the area calculation owing to the longer trailing end of the x-ray peak (due to the RC constant of transimpedance amplifier). This issue was addressed by selecting a data set of well separated single bursts and finding a relation connecting the amplitude and the area of each peak. Fig. 4.13 shows a linear fit for the measured data points. This fit was used to calculate the area of each x-ray peak for all the further analysis.

The grouped instability bursts were analysed further by classifying each group of burst (hereafter termed as instability event) by choosing a suitable threshold time for classifying the events. The threshold time must be selected such that

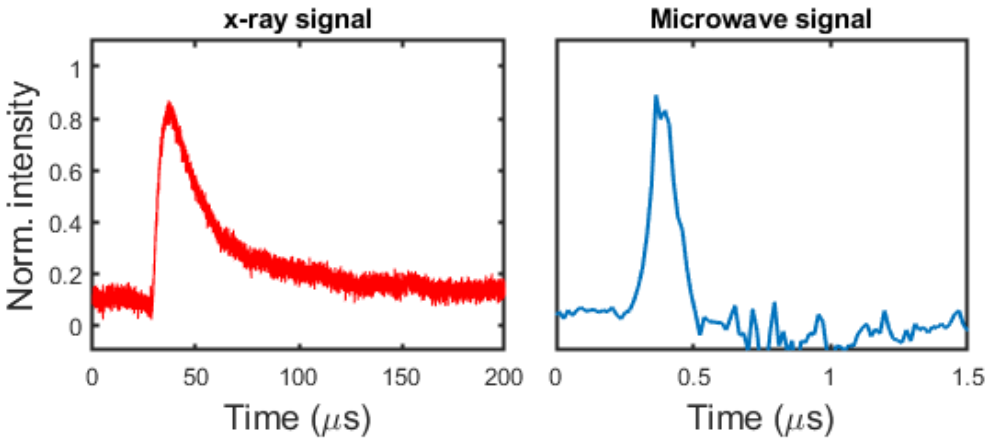

FIGURE 4.10 The single bursts of the x-ray and microwave signals during the instability burst. The signals are measured with a time resolution of 16 *ns* so that both the microwave and x-ray bursts are well resolved.

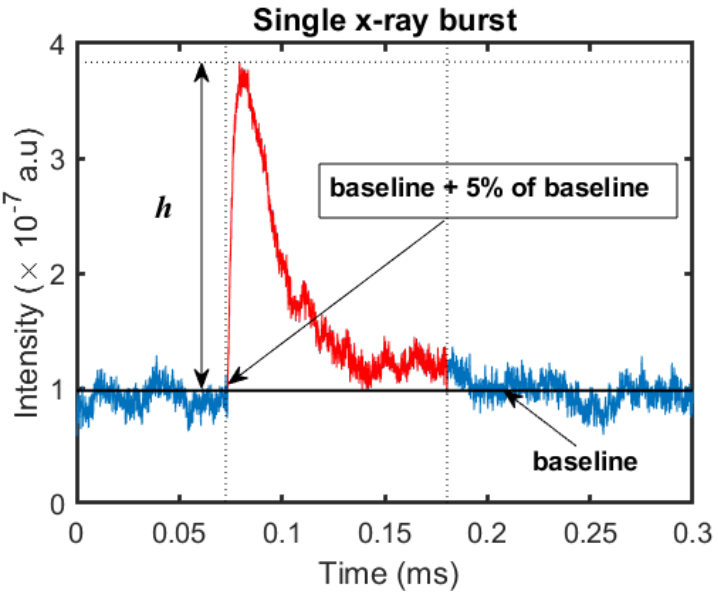

FIGURE 4.11 The amplitude of the single instability burst and its corresponding area is calculated for each burst of x-ray signal. The baseline is determined by obtaining a moving average time window of 800 *ns* from the background signal.

bursts and events may be distinguished unambiguously. As a result, a histogram distribution of time difference between each burst was created for each 10 second data set, revealing the time threshold to be determined. The histogram plot for one such data set is shown in Fig. 4.14 where the dashed line represents the chosen threshold value, and the distribution on the left depicts the time difference between individual bursts, while the distribution on the right depicts the time difference between events.

The analysis was advanced by segregating each and every event based on the number of bursts in each event. The number of bursts in each event is henceforth

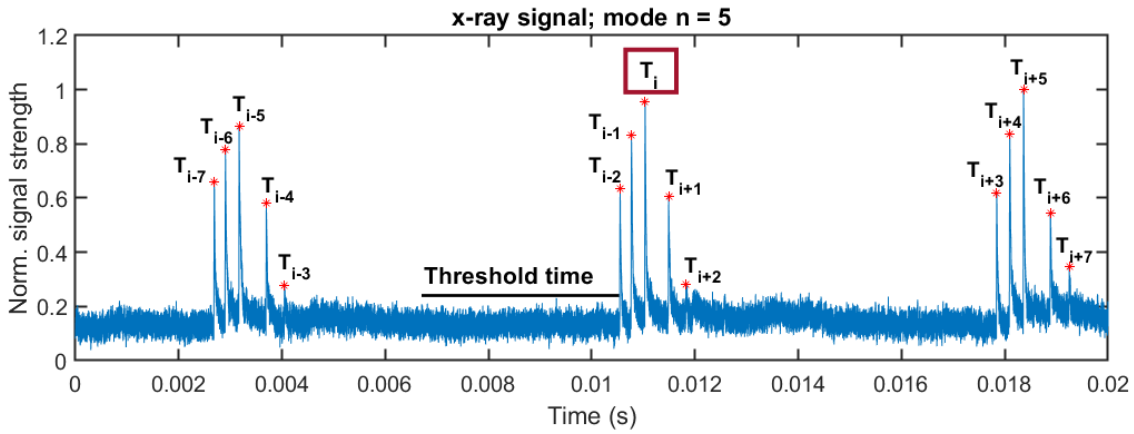

FIGURE 4.12 Illustration of the instability event with mode $n = 5$ along with the indexing of each burst to classify occurrence of an event .

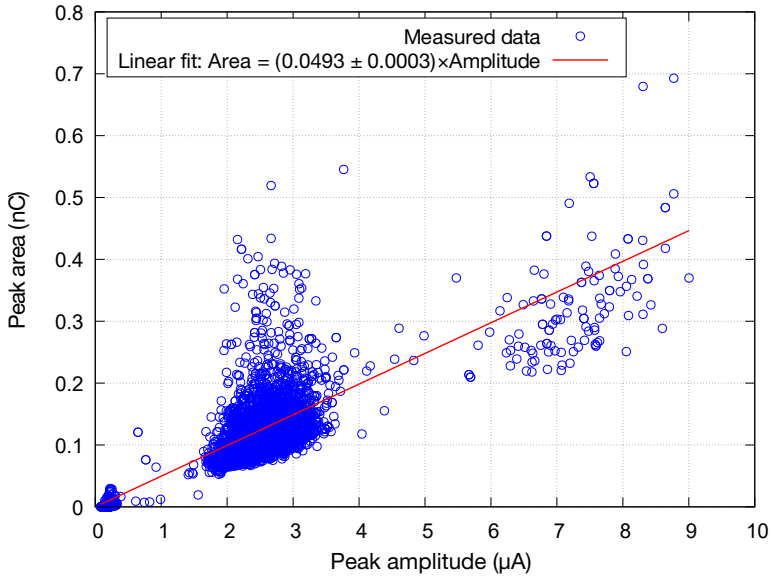

FIGURE 4.13 The experimental data for the single burst x-ray events measured with the scintillator setup. The linear fit gives the correlation between the measured burst amplitude and the corresponding peak area. Reprinted with permission from supplementary material of [38]. Copyright 2022, AIP Publishing LLC

represented by "mode n" where the value of n represents the total number of bursts in an event. For example Fig. 4.12 represents mode $n = 5$ where each event has 5 instability bursts. Each individual burst in an event is indexed as mode m. The n value of a particular event was determined from the assigned timestamps of each bursts. In Fig. 4.12 for burst T_i the mode n is calculated by obtaining the time difference between the reference burst and the adjacent burst (i.e. T_i-T_{i-1},T_{i+1}-T_i etc) and each time difference is examined until the time difference becomes $\geq$ to the threshold time. For every burst T_i this condition is performed for 10 bursts in the forward direction and 10 in the backward direction since the maximum number of bursts observed were found to be 10. The flowchart of the

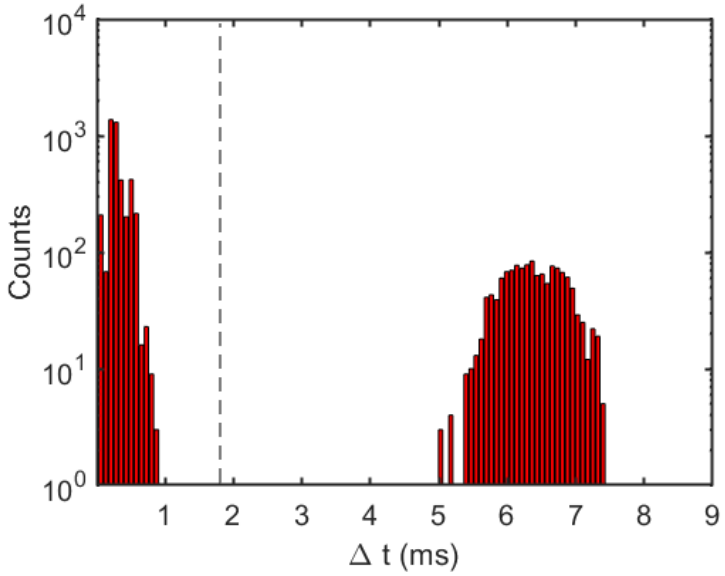

FIGURE 4.14 The determination of threshold time for identifying the events from the bursts, the dotted line represents the threshold value and Δt represents time difference between the adjacent bursts.

peak classification and database building is shown in Fig. 4.15.

Thus for each and every individual bursts in the whole data set is indexed as (n, m) where n represents total number of bursts in an event and m represents burst number in an event. For example in Fig. 4.12 the sample signal for mode n=5 is shown where the instability burst T_{i-2} is indexed as $(5, 1)$ (i.e. n=5 and m=1); similarly T_{i-1} as $(5, 2)$; T_i as $(5, 3)$ and so on.

Hence, with the newly-developed analytical tool, it is easy to identify instability bursts, determine their magnitude and integrated area, as well as categorise the "grouped" instability events according to the number of bursts in each event. Section 5.4 presents the main findings of this experimental campaign.

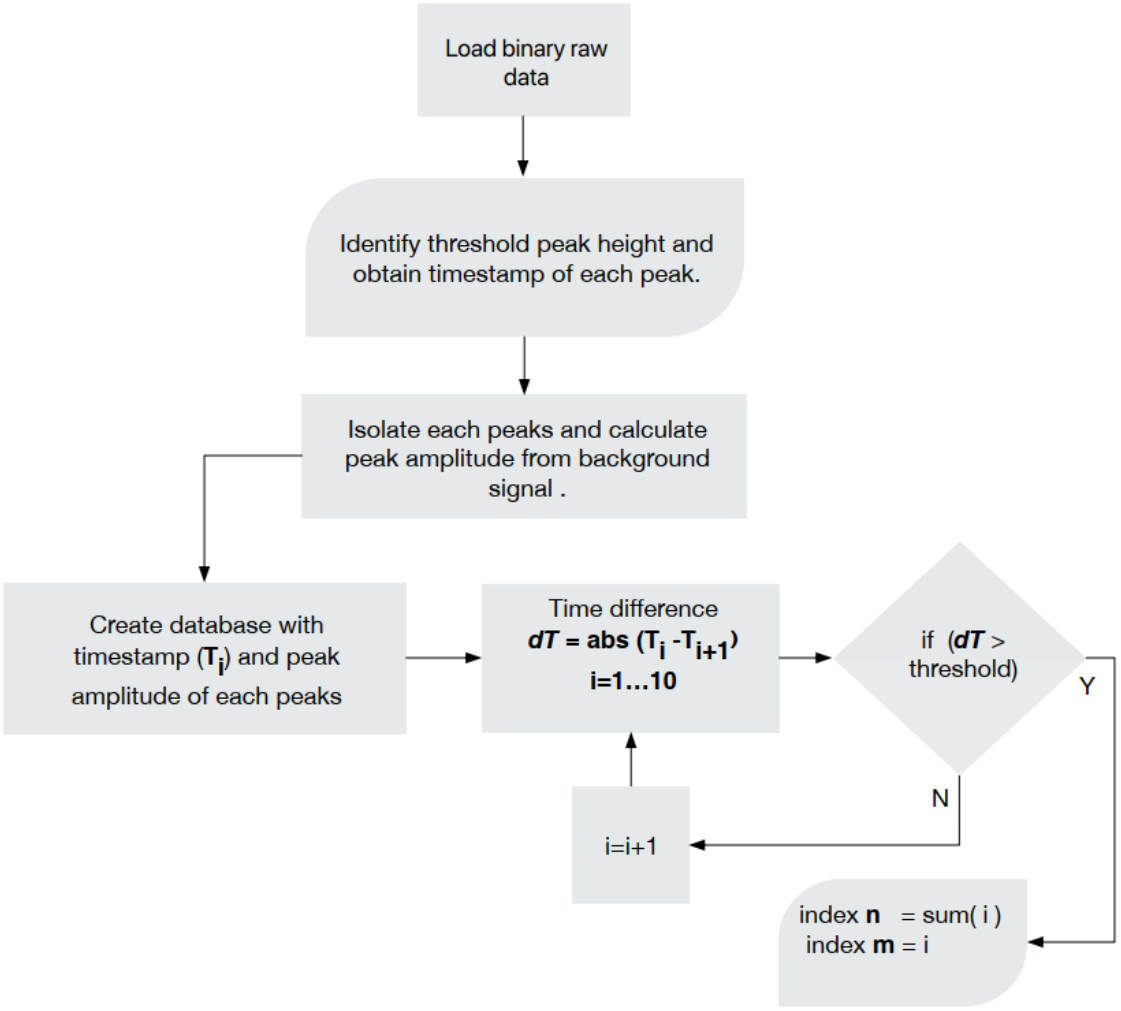

FIGURE 4.15 Flowchart of data processing algorithm to classify peaks and give proper indexing (mode (n, m)) for each peaks.

5 EXPERIMENTAL WORK AND MAIN RESULTS

This chapter summarises the experimental campaigns performed as part of this thesis work and presents the most prominent findings of each campaign. It is split into four sections. The first section discusses the major conclusions drawn as a result of the computational modelling of the ECRIS magnetic field structures. The second section examines the effect of ECRIS magnetic field mirror ratios on the kinetic instability threshold on the GTS ion source. In the subsequent section, the experimental campaign employing the JYFL 14 GHz ECR ion source which was used to determine the correlation between plasma bremsstrahlung and the energy distribution of the electrons lost from the magnetic confinement is discussed. The final section discusses the temporal structure and characteristic features of the kinetic instabilities.

5.1 Implementation of the magnetic field modelling code

Modelling of ECRIS magnetic field can reveal new important information and insight which can play a crucial role in supporting experimental studies conducted with ECR ion sources. The computational tool developed as part of this work (see Section 4.1) has been used for this purpose in the experimental campaigns that focused on investigating kinetic instabilities in different ion sources. The first part of this section focuses on highlighting the capabilities of this tool to model the ECRIS magnetic field structures of various ion sources and study the different aspects of their properties. The last part details a concrete example where the tool was used to complement the experimental study performed with the fully superconducting SECRAL-II ion source.

Modelling of the room temperature ECR ion sources used in the thesis work:

The computational tool has been used to model the magnetic field of JYFL 14 GHz ECRIS, LPSC PHOENIX Booster, LPSC PHOENIX V3 and GANIL GTS. The magnetic field configuration of each ion source was varied by altering the current of the solenoids. The magnetic field parameters ($< \nabla B_{ECR} >$, ∇B_{inj}, ∇B_{ext}, $|B_{max,closed}|$) and the volume (V_{ECR}) enclosed by the ECR resonance zone were calculated for all the ion sources. The behaviour of B_{min}/B_{ECR} was studied as a function of the afore-mentioned magnetic field parameters. This study was realised since B_{min}/B_{ECR} ratio has been found to exhibit a prominent effect in determining the instability threshold as reported in Refs. [33, 31, 69]. As an example, Fig. 5.1 shows the dependence between B_{min}/B_{ECR} and the average magnetic field gradient ($< \nabla B_{ECR} >$) for the ion sources used in this work. The result shows the capability of the code and also provides more insight to how the plasma heating is affected by the variation of the B_{min}/B_{ECR} ratio, namely that as the ratio increases, the average gradient decreases enhancing the electron heating. This could explain why the B_{min}/B_{ECR} ratio has become such a convenient way to quantify the magnetic field variation, and the eventual onset of instabilities, in many previous instability studies. Figure 5.1 shows that the typical instability threshold of $B_{min}/B_{ECR} \approx 0.8$, which has been reported for many ion sources, corresponds to a well defined value of the average magnetic field gradient for the all the sources included in this study. As the electron heating efficiency is directly linked to the magnetic field gradient, this forms a direct connection from the experimental B_{min}/B_{ECR} threshold value to the enhanced build up of hot electron population through efficient electron heating and the consequent onset of the instabilities.

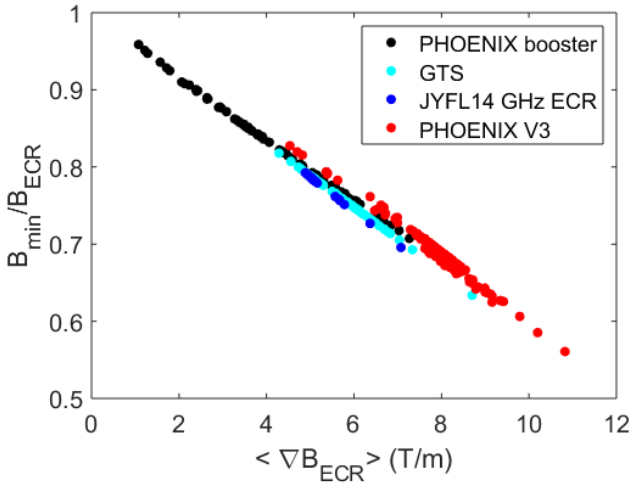

FIGURE 5.1 Relation between B_{min}/B_{ECR} and the average magnetic field gradient parallel to the magnetic field line on the ECR surface for different ion sources calculated using the developed computational tool.

It is also worth noting that the volume enclosed by the cold electron ECR zone exhibited a similar relation and hence it was studied by plotting V_{ECR} with respect

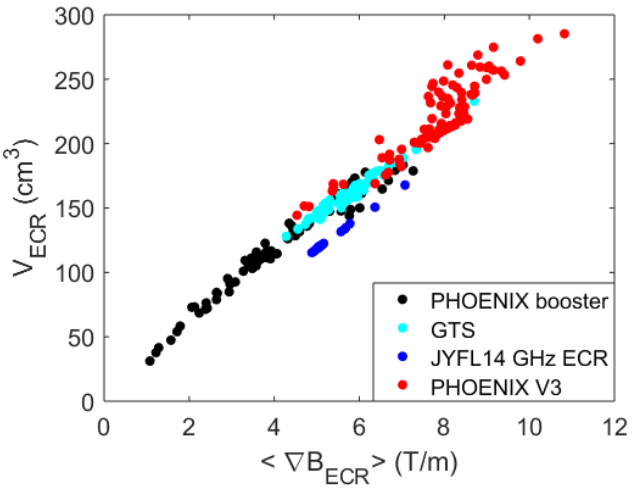

FIGURE 5.2 Relation between $< \nabla B_{ECR} >$ and volume enclosed by the resonance zone for different ion sources calculated using the developed computational tool.

to $< \nabla B_{ECR} >$. The result is presented in Fig. 5.2. The other magnetic field parameters like ∇B_{inj} and ∇B_{ext} exhibited a general decreasing trend with the increase in B_{min}/B_{ECR} ratio. Additionally, the $|B_{max,closed}|$ exhibited no general trend with the change in B_{min}/B_{ECR} ratio. Hence, it can be deduced that except for $|B_{max,closed}|$, all other calculated parameters exhibit a general trend with the B_{min}/B_{ECR} ratio and that all parameters under consideration are interconnected.

Distribution of the magnetic field gradients:
The distribution of the magnetic field gradient parallel to the field lines on the surface of the ECR zone $\left(\frac{\vec{B}\cdot\nabla\vec{B}}{|\vec{B}|}\right)$ was studied for all the above-mentioned ion sources. The gradient distribution can be visualised by plotting it in the form of histograms as described in Section 4.1 and illustrated in Fig. 4.6. When the distribution was plotted for all the ion sources, a common feature of the resulting distributions was observed. It was found that for all the sources two clear local maxima existed in the histograms, corresponding to the most probable gradients (See Fig. 5.3). The two maxima correspond to the most probable gradient for the histogram for $\nabla B < 0$ and $\nabla B > 0$. The distributions were analysed further in order the deduce the spatial locations of these most probable gradients in the ECR surface. In Fig. 5.3 the most probable gradients are shown in black. As the figure shows, these locations mainly correspond to the injection and extraction ends of the ECR surface. This means that the most probable gradient values are equal with the axial gradient values (i.e. $\nabla B_{inj/ext}$), which have traditionally been used to estimate the effect of varying magnetic field conditions on the gradient and consequently on the electron heating efficiency.

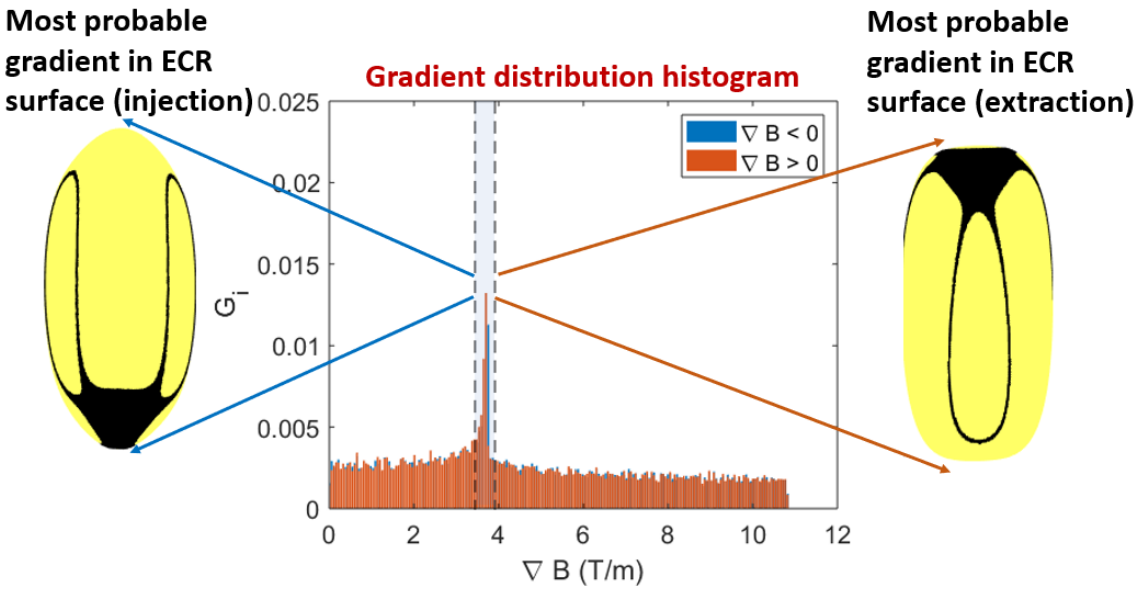

FIGURE 5.3 The most probable gradients for the ion sources under investigation were found to be at the injection and the extraction ends of the ECR surface (i.e. ∇B_{inj} and ∇B_{ext} respectively). The ECR surface is colour coded in yellow and the location of most probable gradient is colour coded in black in the ECR surface. The most probable gradient of the $\nabla B < 0$ part of the gradient distribution corresponds to the injection gradient and $\nabla B > 0$ to the extraction gradient. The figure represents magnetic field gradient distribution calculated for GTS ion source.

The instability threshold studies:
The experimental studies to identify the instability threshold were performed with the JYFL 14 GHz ECRIS, LPSC PHOENIX Booster, LPSC PHOENIX V3 and GANIL GTS using the diagnostic methods described in Section 3.2. The fundamental objective of these investigations was to study whether a single magnetic field parameter can be identified that determines the onset of plasma instabilities. As mentioned previously (see Section 3.1.2), each of the ion sources is unique in terms of plasma chamber dimensions, coil arrangements and other structural details, and hence these differences impact on their magnetic field distributions as well. This study was carried out by adjusting the currents of the injection, central, or extraction solenoids (which modifies the magnetic field structure) while maintaining all the other source parameters constant, such as RF power, neutral gas pressure, and plasma heating frequency (the experimental conditions are provided in Table 5.1). In each of these cases, the magnetic field was modified by ramping the currents in each solenoid (within the practical limits) of the ion sources until the instability threshold was achieved. For example, in the case of the JYFL 14 GHz ECRIS the instability threshold was obtained by varying the injection and the extraction solenoid in the range of $400 - 600$ A ($B_{inj} = 1.75 - 2.13$ T, $B_{min} = 0.26 - 0.42$ T and $B_{ext} = 0.75 - 1.06$ T). For instance, in this case the injection solenoid current was kept at a particular value (say 400 A) and then the

extraction solenoid current was varied until the instability threshold was reached. Then the injection solenoid current was increased by 5 A and the above step was repeated to obtain a new threshold value. These steps were repeated for the whole ranges of all the solenoid currents. Similarly for PHOENIX V3 and PHOENIX Booster, the same method was repeated, but as these sources have a three solenoid magnetic system, each three solenoid currents were varied separately to obtain the instability threshold. For PHOENIX V3 the injection solenoid current was varied between 800 and 1200 A, the central solenoid current between -1100 and -100 A and the extraction solenoid current between 800 and 1200 A ($B_{inj} = 1.43 - 2.06$ T, $B_{min} = 0.25 - 0.62$ T and $B_{ext} = 0.87 - 1.27$ T). The PHOENIX V3 has a central solenoid with reverse polarity compared to the injection and extraction solenoids, hence the current is denoted with a negative sign here. For PHOENIX Booster the injection solenoid current was varied between 700 and 1200 A, the central solenoid current between 0 and 345 A and the extraction solenoid current between 600 and 800 A ($B_{inj} = 1.02 - 1.43$ T, $B_{min} = 0.20 - 0.51$ T and $B_{ext} = 0.69 - 0.92$ T). With the PHOENIX ion sources the threshold determination was performed by keeping the current in two solenoids constant at a time and varying the third one; then the experiment was repeated by step wise increments of solenoid current by 10 amperes. Hence, the instability threshold was obtained for a whole range of possible combinations of the solenoid currents within the ranges mentioned above. In the case of GTS , the injection solenoidal current was varied between 950 and 1200 A and extraction coil currents were varied between 950 and 1100 A ($B_{inj} = 1.97 - 2.17$ T and $B_{ext} = 0.97 - 1.09$ T) and the instability threshold was obtained by varying the central coil current alone. In GTS the instability study was performed slightly differently and is explained in detail on next section (i.e. Sec. 5.2).

TABLE 5.1 Experimental conditions for determining the instability threshold for the different ion sources under consideration. *JYFL represents JYFL 14 GHz ECRIS.

Experimental conditions	**JYFL***	**PHOENIX (B)**	**PHOENIX-V3**	**GTS**
RF power (W)	400	450	400	400
RF frequency (GHz)	14.055	14.529	17.9	14.5
Injected gas	O_2	*He and* O_2	N_2	*Ne*
Source potential (kV)	0	0	30	10
Biased disc potential (V)	-60	nil	floating	-100

The calculated magnetic field properties at the boundary between the stable and the unstable regimes, i.e. at the instability threshold, are presented in Table 5.2 for the different ion sources. The three solenoid system featured in PHOENIX V3, PHOENIX Booster and GTS ion sources offers more flexible magnetic field adjustment compared to the two solenoid system of the JYFL 14 GHz ECR ion source, which explains why the instability threshold regions presented for this ion

source are significantly smaller compared to the other sources. Table 5.1 provides details of the RF heating frequencies used for the sources along with the calculated magnetic field parameters of interest: (a) B_{min}/B_{ECR} ratio which is the ratio of minimum of magnetic field value to that of magnetic field corresponding to ECR value; (b) $< \nabla B_{ECR} >$ corresponds to the average magnetic field gradient on the ECR surface calculated by the method described by Eq. 4.10; (c) ∇B_{inj} and ∇B_{ext} are the local axial magnetic field gradients at the injection and extraction ends of the ECR zone; (d) V_{ECR} is the volume enclosed by the ECR zone and (e) $|B_{max,closed}|$ is the maximum value of the magnetic field strength to obtain a closed magnetic isosurface inside the plasma chamber. All these parameters were calculated for the instability threshold values, denoted by the subscript $'th'$ in the table. The parameters presented in Table 5.2 show a wide range of threshold values (the range for JYFL 14 GHz ECRIS is narrower due to the more limiting two solenoid structure, as mentioned above).

TABLE 5.2 Comparison of the magnetic field parameters calculated for the different ion sources under investigation at the instability threshold. These parameters were calculated using the magnetic field modelling tool discussed in Section 4.1 for the experimentally obtained instability threshold conditions. The RF frequency of each ion source, used in the calculations involving the ECR condition, is also presented. *JYFL is short for JYFL 14 GHz ECRIS. **In the case of JYFL 14 GHz ECRIS, the variation in $|B_{max,closed}|_{,th}$ is less than 0.002 T, and consequently the range of variation has been rounded to a single value.

Parameters	**JYFL***	**PHOENIX(B)**	**PHOENIX-V3**	**GTS**
$RF\ Freq.\ (GHz)$	14	14.5	18	14.5
$B_{min}/B_{ECR,th}$	0.78 - 0.79	0.76 - 0.96	0.61 - 0.83	0.63 - 0.82
$< \nabla B_{ECR} >_{,th}\ (T/m)$	4.8 - 5.1	1.1 - 5.9	4.5 - 9.8	4.3 - 8.7
$\nabla B_{inj,th}\ (T/m)$	4.4 - 4.6	1.6 - 4.3	5.2 - 8.6	3.4 - 5.3
$\nabla B_{ext,th}\ (T/m)$	4.6 - 4.8	1.6 - 3.8	5.7 - 8.6	3.5 - 5
$V_{ECR}, th\ (cm^3)$	115 - 122	31 - 173	144 - 264	128 - 233
$\|B_{max,closed}\|_{,th}\ (T)$	0.80**	0.68 - 0.91	0.86 - 0.98	0.97 - 1.07

As a next step the distribution of the gradient over the resonance zone for the different ion sources was studied. The specificity of each magnetic field structure for the different ion sources can be visualised more clearly by modelling the magnetic field distribution for one fixed $< \nabla B_{ECR} >$ value (i.e same B_{min}/B_{ECR} value). In this particular case 4.8 T/m was chosen and the resulting distributions are illustrated in Fig. 5.4. This choice was made because for all the ion sources this particular value of average gradient is one of the threshold values that were determined experimentally (see Table 5.2). Additionally, this choice correlates with the B_{min}/B_{ECR} value of ≈ 0.8, which has been identified and reported as an instability threshold value in several publications. Moreover, it also corresponds

to one of the semi-empirical magnetic field scaling law values defined for ECR ion sources (see Section. 2.2.6). All the plots in Fig. 5.4 are scaled identically, and the colours in the plots depict the gradient of the local magnetic field with blue being the lowest and yellow the highest absolute gradient value. The method to obtain these plots is explained in Section 4.1. The corresponding histograms of the gradient distributions are shown in Fig. 5.5. It is observed that despite of several similar features in the gradient distributions, the details in the resonant surface geometry are different between the different ion sources.

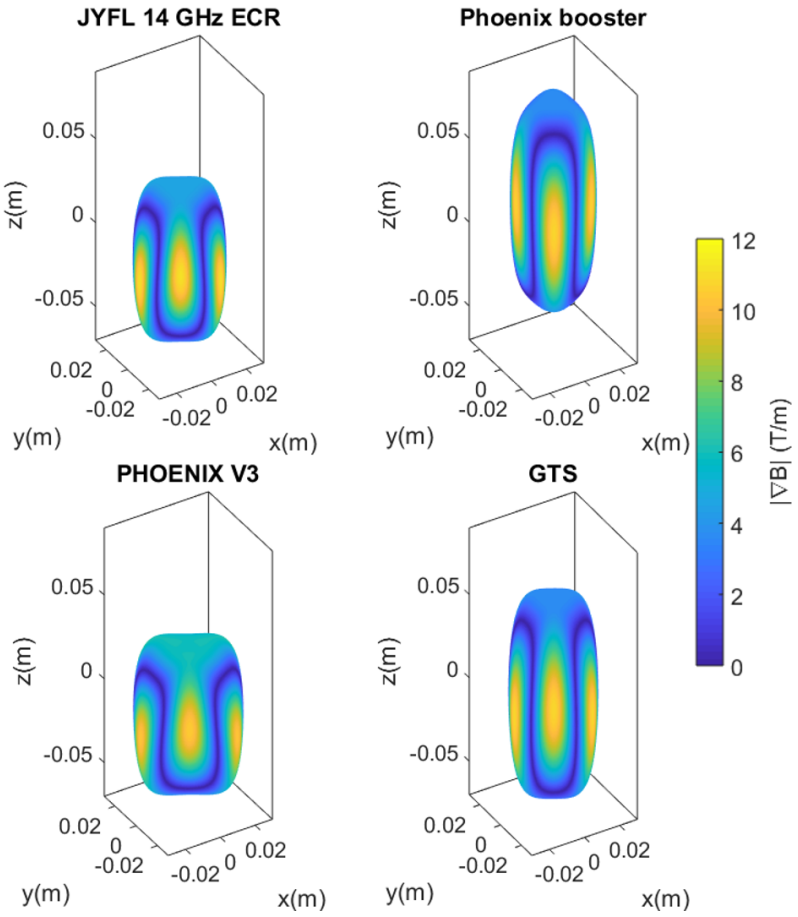

FIGURE 5.4 Spatial gradient distributions over the ECR surfaces of the different ion sources with $< \nabla B_{ECR} >$ of 4.8 T/m and $B_{min}/B_{ECR} \approx 0.8$.

Considering all the points presented above, it can be generally concluded that the role of the magnetic field in determining the instability threshold cannot be easily defined in the context of a single parameter, like magnetic field geometry or its gradient distribution over the ECR surface. It is evident from Table 5.2 that the flexibility in modification of magnetic field is source dependent and each source provides a wide range of threshold values for all the studied magnetic field parameters. No single magnetic field parameter emerged as a defining criterion for triggering the instability condition, implying a more complicated interaction between the magnetic field and other plasma-related parameters that ultimately

results in the transition from a stable to an unstable plasma regime.

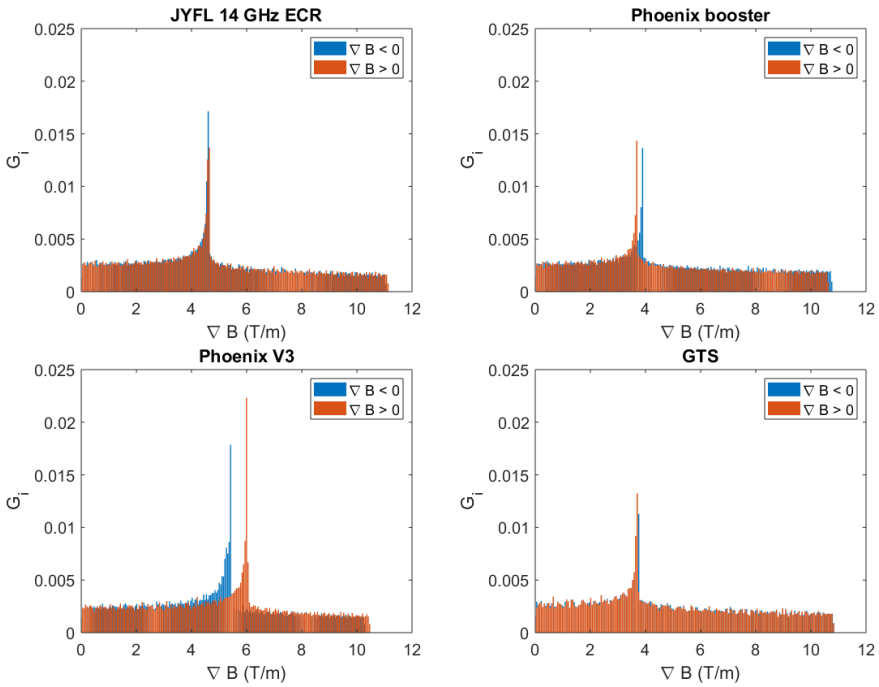

FIGURE 5.5 Gradient distribution histograms for the different ion sources with $< \nabla B_{ECR} >$ of 4.8 T/m and $B_{min}/B_{ECR} \approx 0.8$.

An example of the use of the modelling tool to support experiment:
In the experimental campaign with the third generation superconducting ECR ion source SECRAL-II, the effect of the various magnetic field parameters on the hot electron population was studied by examining the bremsstrahlung spectra measured with an energy sensitive semiconductor detector (See Section 3.2.3). The changes in the hot electron population were quantified by calculating the spectral temperature from the measured bremsstrahlung spectra (as described in Section 3.2.3). The magnetic field modelling tool was used to model the magnetic field of the SECRAL-II ion source and it was crucial in the interpretation of the experimental results aimed at determining the effect of magnetic field on the hot electron population in the experimental campaign performed by Li *et al.* [69] (paper attached as Appendix PI).

In the campaign, the magnetic field parameters of the ion source, B_{inj}, B_{ext}, B_{min}/B_{ECR}, the axial magnetic field gradient at injection, ∇B_{inj}, and extraction, ∇B_{ext}, were varied independently and the effect of the magnetic field variations on the hot electron populations were studied by quantifying the impact on the measured bremsstrahlung spectral temperature. Moreover, since the SECRAL-II ion source is a fully superconducting ion source, it offered the possibility to vary the radial magnetic field B_r (which is not possible in the case of room temperature ECRIS). It must be noted that in the experiment while varying each of the above mentioned magnetic field parameters separately, all other source parameters were

kept constant. Though the experiments were conducted by varying the magnetic mirror ratios, a direct correlation with ECR heating process has been theoretically explained using the magnetic field gradient and its influence on electron heating (as detailed in Section 2.2.3). Thus, a further physical insight, and a direct link to electron heating, could be provided by calculating the average magnetic field gradient parallel to field lines across the ECR surface, $< \nabla B_{ECR} >$, for each magnetic field configuration under consideration. This has been achieved by using the developed magnetic field modelling tool. It has thus lead to one of the critical conclusions from the experimental results, namely showing that the increase in spectral temperature is correlated with the decrease in $< \nabla B_{ECR} >$, as is illustrated in Fig. 5.6. This behaviour corroborates well with the theoretical explanation of the ECR heating and the role that the magnetic field gradient plays in this process, as explained by Canobbio *et al.* [20] (see Section 2.2.3). Consequently, by demonstrating this relation, we can directly interlink the increase in hot electron temperature, quantified by the measured increase in the spectral temperature, to the decreasing magnetic field gradient and thus the enhanced electron heating.

The stability of the SECRAL-II plasma was monitored throughout the campaign with a Schottky diode. As a result, two observations were made: (1) the plasma had a tendency to have a transition from the stable to the unstable plasma regime when the B_{min}/B_{ECR} ratio exceeded the value of about 0.8. (2) The spectral temperature increases with increasing B_{min}/B_{ECR} (and decreasing average gradient), but saturates when the instability threshold is exceeded. The first observation supports the finding reported in numerous studies where different ECR ion sources have been used to define the plasma instability threshold in terms of B_{min}/B_{ECR} (see e.g. Refs. [33, 31, 69]). The fundamental reason why the transition occurs at this exact B_{min}/B_{ECR} value remains elusive, but the result that the increase of this ratio goes hand in hand with the decreasing average gradient indicates clearly that this process is connected to the improved heating rate of electrons and the consequent build up of the hot electron population. The second observation suggests that the enhanced hot electron losses due to the onset of instabilities acts to limit the accumulation of the hot electron population in the plasma, which is reflected as the saturation of the spectral temperature in the unstable plasma regime. A detailed description of the experimental setup and a comprehensive discussion of the observed results has been published in the article [69] which is also included as Appendix PI.

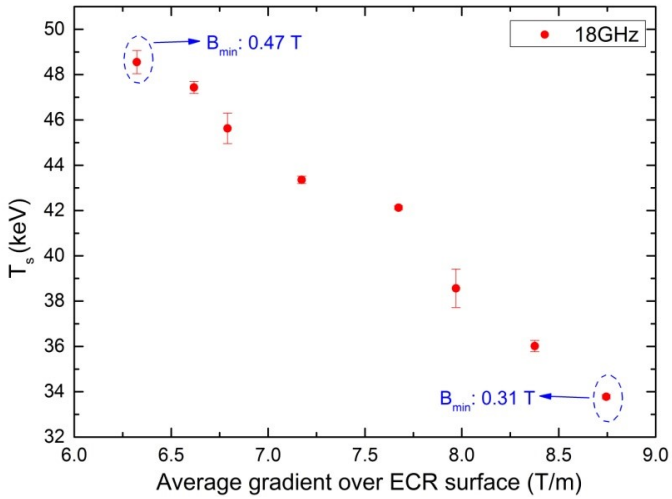

FIGURE 5.6 The correlation between the calculated average magnetic field gradient over the ECR surface ($< \nabla B_{ECR} >$) and the measured spectral temperature (T_s) for SECRAL-II ion source operated at 18 GHz heating frequency. The minimum of the magnetic field (B_{min}) was increased from 0.31 T to 0.47 T.

5.2 The influence of axial mirror ratios on the instability threshold

The fundamental cause of kinetic plasma instabilities is the accumulation of hot electron population in the ECR plasma and the consequent anisotropy in the EEDF, as stated in Section 2.3. Moreover, based on the observation by Li *et al.* [69] (Appendix PI) regarding the influence of mirror ratios on the instability threshold, it can be hypothesised that managing the hot electron population by RF scattering or by modifying the magnetic field structure and consequently the electron confinement conditions could influence the transition from stable to unstable plasma regime. It has also been discovered that lowering the extraction magnetic field increases the flux of electrons that escape via the plasma electrode [83], which experimentally demonstrates the link between axial magnetic confinement and electron losses. This effect was studied further using the GTS ion source to investigate the influence of the axial magnetic mirrors on the instability threshold. GTS was chosen for this study since it has a unique feature of a movable central coil that provides additional flexibility in modifying the magnetic field structure. The instability threshold was obtained by varying the current in the central coil for a series of different magnetic field configurations achieved by using a set of different fixed injection and extraction coil current values. This method was used, because the central coil has the most prominent effect on the minimum magnetic field B_{min} [84, 69] and previous studies [83, 85] have demonstrated that B_{min} has the greatest impact on the electron energy distribution (EED) and consequently on the onset of the plasma instabilities.

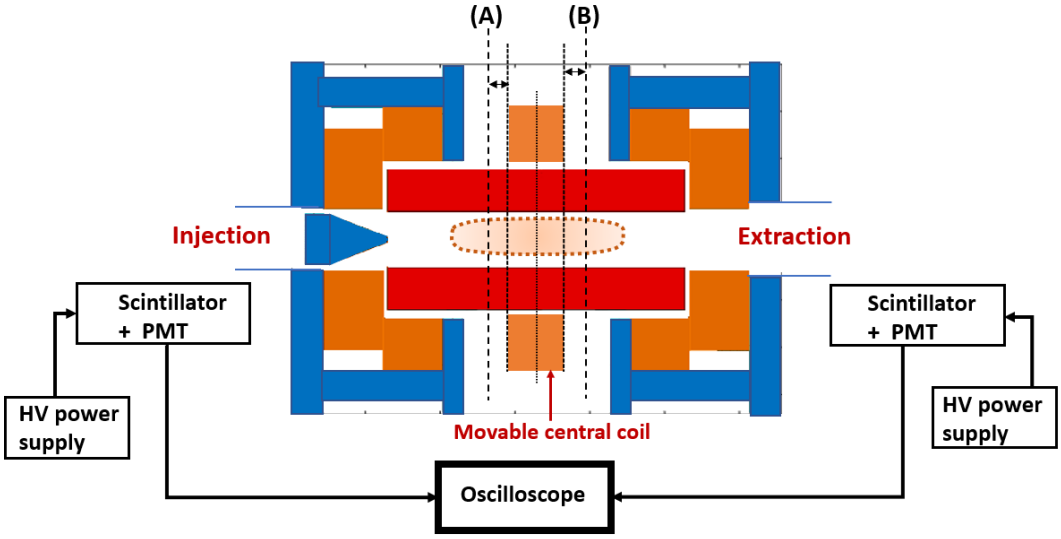

FIGURE 5.7 A schematic of the experimental setup with the GTS ion source. The central coil can be moved towards the injection (A) or the extraction (B) end of the chamber from the centre position between the injection and extraction coils. The appearance of bremsstrahlung bursts, measured with x-ray scintillators coupled with photomultiplier tubes (PMT), was used to determine the onset of plasma instabilities. The output of the PMTs were monitored with an oscilloscope.

The experiment was conducted with the central coil at three different axial positions: at the injection end ((A) in Fig. 5.7), at the axial centre of the plasma chamber (and hexapole), and at the extraction end ((B) in Fig. 5.7). For each position of the central coil, the following sets of measurements were performed: (i) With a fixed extraction coil current, the current of the injection coil was varied (thus varying B_{inj}) in discrete steps and for each injection coil current the current in the central coil was ramped up (thus increasing B_{min}) to obtain the instability threshold. (ii) With a fixed injection coil current, the current of the extraction coil was varied (thus varying B_{ext}) in discrete steps and for each extraction coil current the current in the central coil was ramped up to obtain the instability threshold. (iii) The injection and extraction coil currents were both varied simultaneously in discrete steps and for each injection/extraction coil currents, the central coil current was ramped up to obtain the instability threshold.

The transition from stable to unstable plasma regime, i.e. the instability threshold, was detected using two BGO x-ray scintillators (as discussed in Section 3.2) which were placed close to the injection and extraction ends of the ion source, as shown in Fig. 5.7. The experiments were conducted using neon plasma and the input microwave power (400 W), biased disc potential (-100 V) and extraction voltage (10 kV) were kept constant during all the measurements.

The weakest mirror of the confining magnetic field structure determines where

the majority of plasma losses occur, and thus it is expected that the modification of this mirror field has the strongest impact on the electron losses and consequently on the instability threshold. As a result, the magnetic field structure of the GTS ion source was carefully calculated for all the coil current combinations used in the experiments, taking into account the influence of the solenoid field on the radial mirror ratio. The radial mirror ratio was determined at the poles, as these locations are relevant for the plasma losses. Based on these calculations it was determined that the extraction field always defined the weakest mirror; the minimum magnetic field at the chamber walls at the locations of the poles of the hexapole magnet were found to be in all cases $10 - 22\%$ higher than the extraction field at the location of the extraction aperture, which defines the axial mirror ratio at the extraction. Consequently, the extraction magnetic field B_{ext} defines the global loss cone in all the measured cases.

Figure 5.8 presents a representative example of how the instability threshold, quantified by the B_{min}, depends on the varied axial mirrors. In this case the central coil was set at the extraction position (denoted by (B) in Fig. 5.7). The blue points in the plot represent the experimental results obtained from the experimental process described above as (i), red points represent results from (ii) and green points represent results obtained from (iii). It was discovered that when the B_{ext} is increased by means of increasing the extraction coil current, the threshold B_{min} decreases. This behaviour was observed in all the cases irrespective of the location of the central coil, however the effect was more evident when the central coil was kept in the extraction or central positions.

These findings imply that the shift from the stable to the unstable plasma regime can be controlled by altering the electron confinement (and thus electron losses) by varying the weakest mirror of the magnetic trap, in this case B_{ext}. The relation between the magnetic mirror ratio (R) and the escape probability of electrons (p) is given by $p = a(1 - \sqrt{1 - \frac{1}{R}})$; where a is the isotropy factor of the electron velocity distribution; for instance $a = 1$ for perfectly isotropic distribution and $a < 1$ if $v_{\perp} > v_{\parallel}$. Consequently, lowering the mirror ratio leads to a higher escape probability of electrons. It has also been deduced by several earlier experimental and numerical studies of ECR plasmas that most of the plasma energy content is carried by the dense hot electron population which is confined within the ECR surface [86, 87, 88]. Consequently it can be argued that changing the magnetic field alters the volume and thus the RF power density within the ECR surface, which impacts the hot electron population. Therefore the volume enclosed by the ECR surface was also calculated for all the measured cases. It is enough to study the change in volume, as the RF power was kept constant in the experiments. This calculation was performed using the computational tool described in Section 4.1, and it was found that with increasing extraction magnetic field, the volume enclosed by the ECR zone increased (i.e the power density decreased). This effect

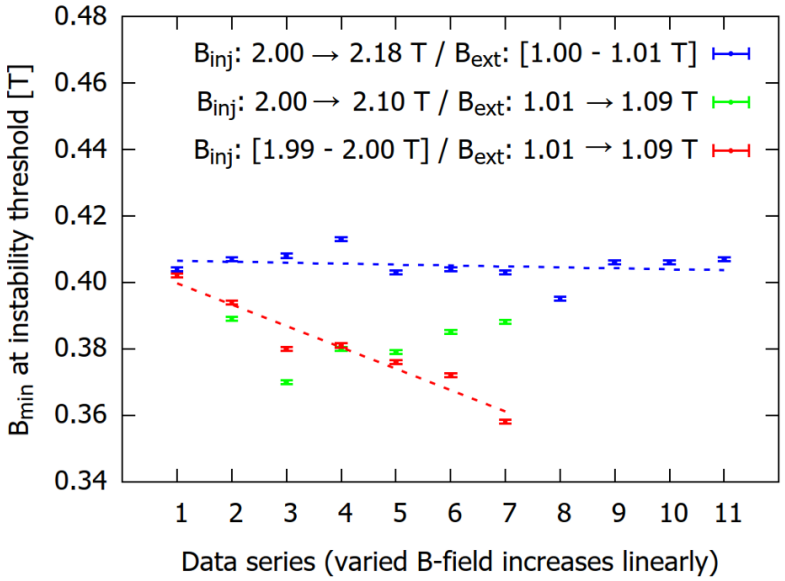

FIGURE 5.8 B_{min} at the instability threshold when the axial mirror fields are varied. In this case the central coil was kept at the extraction position (i.e. position (B) in Fig. 5.7). The blue points shows the variation of injection magnetic field from 2 to 2.18 T while keeping the extraction field almost constant. Similarly the green points shows the variation of both the injection and the extraction fields and finally the red point shows the variation of the extraction magnetic field while keeping the injection magnetic field approximately constant.

should lead to the mitigation of the hot electron population build up and thus have a stabilizing effect on the plasma and result to an increase in the instability threshold (in terms of B_{min}). However, the opposite behaviour was observed experimentally. Another factor which could affect the hot electron population is the change in $< \nabla B_{ECR} >$ and the consequent change in the effectiveness of electron heating (as mentioned in Section 5.1). Hence $< \nabla B_{ECR} >$ was also calculated for all the measured cases, and it was found that the $< \nabla B_{ECR} >$ increased with increasing B_{ext}. This implies that lowering the B_{ext} results in more efficient heating, which should enhance the hot electron build up and lead the instability threshold to shift towards lower B_{min} values. However, the opposite behaviour was again observed experimentally. These two observations imply that, at least in this case, the effect of changing the electron confinement by adjusting the weakest mirror field dominates over the effects that the changing power density and average gradient have on the electron heating. As a result, this experiment contributes more credence to the initial hypothesis that managing the hot electron population is critical for controlling the occurrence of plasma instabilities, and controlling the electron confinement/losses is one way to achieve this. The detailed experimental setup and a comprehensive discussion of the results has been provided in Ref. [89] which is also attached as Appendix PII.

5.3 The relation between the lost electron energy distribution and the plasma bremsstrahlung

Bremsstrahlung measurements have been widely used as an indirect method to study the parametric dependence of hot electron population in ECRIS plasma without perturbing it [90, 91, 92, 93, 94, 95, 96, 97, 86, 98, 99]. In this campaign a combination of bremsstrahlung diagnostics and measurement of the energy distribution of electrons lost from the confinement was used to address two primary questions:
(a) Can time averaged bremsstrahlung measurements with energy dispersive semiconductor detectors be used as a diagnostic to determine the onset of plasma instabilities?
(b) Is there a correlation between the plasma bremsstrahlung spectra and the energy distribution of the electrons lost from the magnetic confinement?

The widely used bremsstrahlung measurement technique provides a non-invasive method for studying the properties of ECR plasmas. However, the de-convolution of the plasma bremsstrahlung or the wall bremsstrahlung to obtain the Electron Energy Distribution (EED) of confined or lost plasma electrons has been found to be extremely difficult despite some notable efforts [97, 100, 101]. In this context simultaneous measurement of bremsstrahlung and energy distribution of lost electrons could provide insight into the relation between the actual energy distribution of electrons and the plasma bremsstrahlung. Though lost electron energy distribution (LEED) measurement is not deemed to represent the energy distribution of the confined plasma [102], it can be argued that the effect of the ion source parameters are reflected on both the confined EED and the LEED. Also, it should be emphasised that LEED measurements require a modification to the source's normal operating regime, whereas bremsstrahlung measurements can be performed under normal operating conditions, and thus establishing a link between the properties of the bremsstrahlung and the LEED could provide a way to use bremsstrahlung measurement as a proxy to extract more useful information about the EED. Additionally, the experimental campaign was also designed to study if one can recognise the transition from the stable to unstable plasma regime by measuring the time averaged bremsstrahlung emissions.

The experimental campaign was realised with the JYFL 14 GHz ECRIS. In order to measure the bremsstrahlung spectrum, a semiconductor detector (Amptek XR-100 CdTe) was connected to a vacuum feedthrough to place the detector input inside the ion source (radial measurement) or beamline (axial measurement) vacuum enclosure in order to minimise the attenuation of low-energy photons due to interaction with air or other structures (see Section 3.2.3). The axial bremsstrahlung measurement was realised through the view port 1 of the dipole magnet (see Fig. 3.5) so that the detector had a direct line of sight to the confined plasma through

the ion source plasma electrode aperture. The radial bremsstrahlung spectra was measured through one of the radial view ports of the ion source (shown in Figs. 3.2 and 3.3). Along with the axial bremsstrahlung measurement, the electrons lost from the confinement were measured simultaneously by utilising the dipole magnet and the electron detector combination as discussed in Section 3.2.2. An x-ray scintillator (see Section 3.2.3) and a spectrum analyzer with external microwave antenna (see Section 3.2.1) were used to monitor the occurrence of plasma instabilities during the measurements. The schematic of the complete experimental setup is presented in Fig. 5.9.

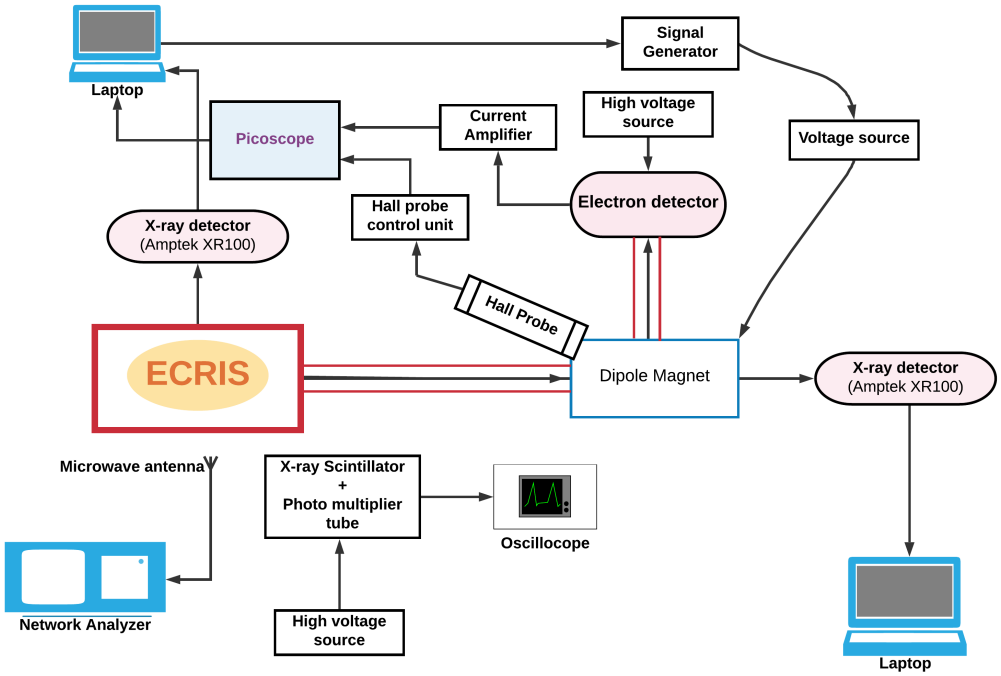

FIGURE 5.9 A schematic of the experimental setup that was used to measure the axial and radial bremsstrahlung spectra and the LEED while simultaneously monitoring the occurrence of plasma instabilities. Reprinted with permission from [70]. Copyright 2021, IOP Publishing.

The experiment was performed by varying the ion source's main operational parameters, such as magnetic field strength, microwave power and neutral gas pressure, and observing the influence on the axial and radial bremsstrahlung spectra and the lost electron energy distribution (LEED). The magnetic field sweep was performed by ramping the current of both the injection and the extraction solenoids at the same time from 470 A to 570 A ($B_{inj} = 1.87 - 2.06$ T, $B_{min} = 0.32 - 0.41$ T and $B_{ext} = 0.86 - 1.00$ T) with current increments of 10 A. The B_{min}/B_{ECR} ratio, which varied from 0.64 to 0.82, was chosen as a convenient way to quantify the magnetic field variation when presenting the results (as this has been done often in previous publications). The microwave power sweep was conducted by varying the input microwave power from the klystron in equal steps (100 - 700 W in steps of 100 W) and the neutral gas pressure was varied

by increasing the plasma off neutral particle pressure from 2×10^{-7} mbar to 10×10^{-7} mbar. The pressure was measured using a penning gauge located at one of the radial ports of the ion source. It's worth noting that when one of the source parameters was varied, the other parameters were kept at constant baseline values, which were defined as: solenoid coil currents at 500 A ($B_{inj} = 1.93$ T, $B_{min} = 0.35$ T and $B_{ext} = 0.90$ T), microwave power at 300 W, neutral gas pressure (plasma off) at 3.5×10^{-7} mbar and biased disc potential at -70 V. All measurements were performed with oxygen plasma. It must be noted that for all these cases the source was grounded to allow the electrons to escape freely from the plasma chamber through the extraction aperture. The axial bremsstrahlung was measured in conjunction with the LEED, after which the x-ray detector was relocated to the radial measurement position and the parameter sweeps were repeated to measure the radial bremsstrahlung spectra.

In order to address the first research question, the same experimental setup was used to study the bremsstrahlung spectra and LEED obtained around the transition from stable to unstable plasma regime. In this case, the TWTA was used as a primary source of microwave heating which provided a larger frequency bandwidth compared to the klystron and thus more statistics of instability threshold data can be obtained (i.e. by crossing of the threshold with several heating frequencies). The instability threshold was determined by increasing the ion source magnetic field (by increasing the coil currents) until a transition from stable to unstable plasma was observed from the appearance of bremsstrahlung bursts in the x-ray scintillator signal. Then the bremsstrahlung spectrum and LEED were measured in the stable and unstable sides of this threshold. The measurement was repeated with three different plasma heating frequencies; 11.56, 12 and 13 GHz. Thus the spectra on both sides of the instability threshold were obtained for four different heating frequencies including the input heating frequency from klystron. Examples of bremsstrahlung spectra and LEED measured in stable and unstable plasma regimes are presented in Fig. 5.10.

As is seen in Fig. 5.10, the measured bremsstrahlung spectra do not show a clear distinction between the stable and the unstable regimes. Thus it can be concluded that the temporally averaged bremsstrahlung measurements using semiconductor detectors is not sufficient for determining the transition from stable to unstable regime of ECR-heated plasma. This is most likely due to the short duration of the instability-induced bremsstrahlung signals (in the order of tens of microseconds [33, 38]) when compared to the quiescent plasma period between the emissions (in the order of milliseconds), as also discussed in Ref. [37]. However, in the case of LEED, a clear difference is observed between the two stability regimes. The high energy hump (at around 220 keV) which is clearly observed with stable plasma conditions disappears when the plasma becomes unstable (as illustrated in Fig. 5.10). It is worth noting that during instability the electron emission happens

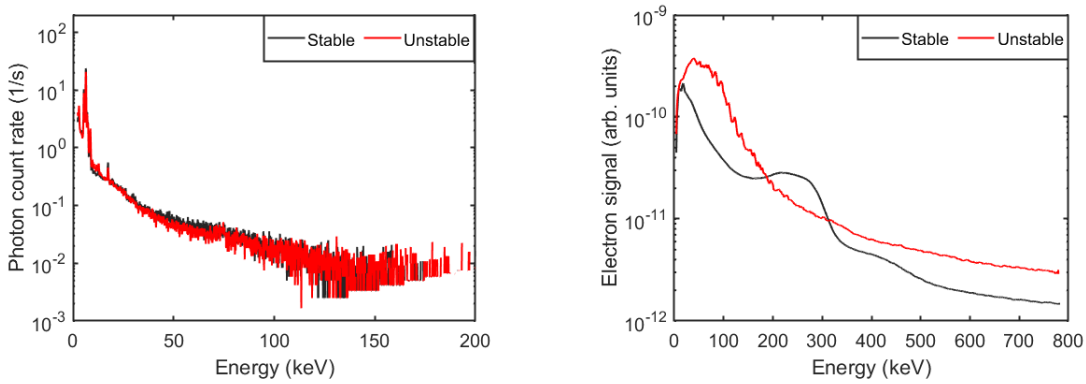

(a) Bremsstrahlung spectra.

(b) Lost electron energy distribution.

FIGURE 5.10 The variation in the bremsstrahlung spectrum and the LEED in the stable and unstable region. In the stable case the ratio $B_{min}/B_{ECR} = 0.73$ and in unstable case $B_{min}/B_{ECR} = 0.82$. In both the cases the input RF power was 300 W and the neutral gas pressure was at 3.5×10^{-7} mbar .

in short bursts (around 0.5 μs [85, 71, 38]) and hence, for the same reasons as for the above discussed bremsstrahlung, the time averaged LEED measurements would be insufficient to detect it. The high energy hump measured in the time averaged LEED during stable plasma is a consequence of RF scattered electrons, as discussed by Izotov *et al.* [83]. However, plasma instabilities introduce a new loss channel for these hot electrons, which mitigates the hot electron population build up and consequently the amount of RF scattered electrons. As a consequence, in the time averaged measurement, this leads to the apparent disappearance of the hump.

In order to address the second research question, the bremsstrahlung spectra were analysed further by calculating the total photon energy, average photon energy and the spectral temperature (as explained in Section 3.2.3). Similarly, the measured LEEDs were analysed by calculating the total and average energy of the lost electrons, as well as the total and average energies of the electrons in the high energy hump, using the methods explained in Section 3.2.2. This analysis was performed for all the parameter sweeps. It was observed that the RF power only influenced the total energy of bremsstrahlung and LEED (i.e. the the level of the measured distributions, not the shape) and the neutral gas pressure had a very weak effect on both distributions. The magnetic field was found to have the most prominent effect on the distributions. It was observed that increase in B_{min}/B_{ECR} ratio resulted in a decrease in total photon energy and total electron energy obtained from the axial bremsstrahlung spectrum and LEED measurements, however the average photon energy decreased whereas the average electron energy increased. The radial bremsstrahlung measurement exhibited the opposite behaviour, i.e. an increase in both the average and total photon energies. This is most likely be due to the directionality of volumetric plasma bremsstrahlung emission and the effect of anisotropy in electron energy

distribution as a result of the changing magnetic confinement conditions, as has been discussed in detail in Ref. [70] (included as Appendix PIII). With further analysis of the spectra, it was found that there is a correlation between the spectral temperature calculated from the bremsstrahlung spectra and the average energy of the LEED high energy hump. This result is illustrated in Fig. 5.11. The figure shows that the spectral temperature (both axial and radial) increases when the magnetic field strength is increased, quantified here by the increasing B_{min}/B_{ECR} ratio; similar increasing effect is also observed in the average energy of the LEED high energy hump. Thus the general behaviour of these two parameters exhibit a clear correlation as a function of the increasing B_{min}/B_{ECR} ratio. Further details and results of the campaign are discussed in detail in Ref. [70] which is attached as Appendix PIII.

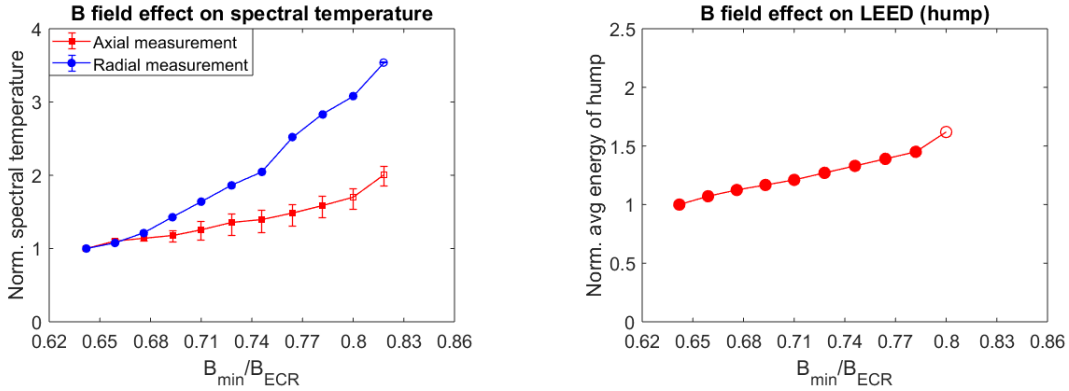

FIGURE 5.11 The relation between spectral temperature from bremsstrahlung spectra and the average energy of the high energy hump in the LEED data is illustrated as a function of the magnetic field. The open circles and squares represent unstable plasma region. At the first unstable point closest to the threshold (i.e. $B_{min}/B_{ECR} = 0.8$), a small remnant of the high energy hump was still observed in the measured LEED, and hence it is also included in the figure. At the higher B_{min}/B_{ECR} values the hump disappeared completely.

5.4 Temporal study of quasi-periodical instabilities

The purpose of this experimental campaign was to gain a comprehensive understanding of the temporal features of the electromagnetic and particle emissions from ECR-heated plasma that occur in the unstable plasma regime. Especially, the experimental campaign was designed to study the relation between the magnitude of these instability-induced emissions during the instability events and the quiescent time between successive events. This section summarises the main motivation, the employed experimental methods and the most prominent results obtained by analysing the acquired experimental data with the dedicated data analysis tool that is described in Section 4.2. A detailed description of the campaign and all the obtained results has been published in Ref. [38] which is attached as Appendix PIV.

The main motivation for this study comes from the theory of kinetic instabilities, which is described in Section 2.3. As per this theory, the ratio of the number densities of hot electrons to the cold electrons $\left(\frac{N_{e,hot}}{N_{e,cold}}\right)$ determines the onset of the instabilities in ECR-heated plasma when it exceeds a certain threshold. At this point the interaction between the hot electrons and the inherent low amplitude electromagnetic waves increases exponentially, resulting in a burst of electromagnetic waves. This is followed by emission of hot electrons, which decreases the hot electron population and results in temporary stabilisation of the plasma. Consequently, following the burst of EM waves the energy content of the plasma electron energy distribution (EED) drops from a maximum value present just prior to the onset of the instability to a minimum value defined by the total hot electron losses (described by Eq. (2.33)). Between these two extremes there is a build up of energy which depends on the electron heating rate (source term $S(t)$) and electron loss rate (loss term $L(t)$) described in Eq. (2.34). Therefore it can be hypothesised that the repetition rate of the instability emissions can be correlated with the source and loss terms during the quiescent period in between the instability emissions and that these terms are influenced by the source parameters (as reported in [33, 103]) and the energy loss resulting from the instability. Subsequently, this leads to two scenarios: (i) If high amount of energy is released in an instability event (i.e. a large magnitude instability emission), then this would lead to a long time to recover until the next instability event occurs. (ii) Alternatively, if the plasma parameters are perturbed in such a manner that the energy threshold required for triggering the instability changes between consecutive instability events, then this leads to a situation where a long accumulation time leads to a large magnitude instability emission. In the following text the quiescent time corresponding to scenario (i) is called *recovery time* and that corresponding to scenario (ii) is called *accumulation time* for the sake of convenience. An experimental campaign was performed to study the instability burst magnitude versus recovery/accumulation time by using

various diagnostic methods, as described below.

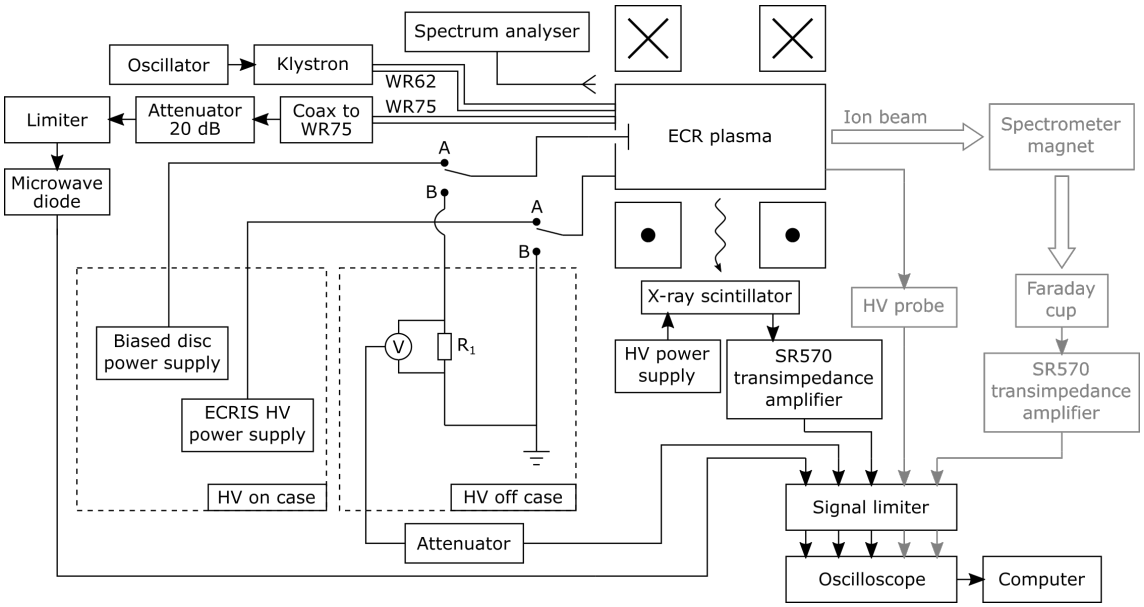

FIGURE 5.12 A schematic of the diagnostic setup used for the experiment. Ion beam current and HV platform voltage were monitored to ensure the proper operation of the ion source during the experiments and are shown in the schematic (in grey) for the sake of completeness, but were not part of the main analysis. Reprinted with permission from [38]. Copyright 2022, AIP Publishing LLC.

The experiment was performed with the JYFL 14 GHz ECRIS and the schematic of the experimental setup is shown in Fig. 5.12. The plasma was generated using 14 GHz heating frequency from the klystron through the WR62 waveguide (see Section 3.1.1). The instability events were detected simultaneously using three different diagnostics:

a) Schottky diode connected to the WR75 waveguide of the ion source for detecting the microwave emissions as described in Section 3.2.1.
b) Biased disc diagnostic for measuring the charge contained in the electron and ion bursts from the plasma during the instabilities. The measurement setup is described in Section 3.2.2.
c) BGO x-ray scintillator for the detection of bremsstrahlung emissions as described in Section 3.2.3.

In addition to these, the microwave emission frequency spectrum was also monitored using a spectrum analyzer to ensure that it satisfies the condition for maser type kinetic instability regime (as defined by Izotov *et al.* in Ref. [28]). All the signals were measured simultaneously with a picoscope [104] and stored to a computer. The time resolution required for the data collection was determined based on the fastest signal, in this case the microwave burst, and the same resolution was used for all the diagnostic signals to ensure the temporal synchronicity

of all the recorded diagnostic data. Hence, the resolution of 16 ns was chosen to obtain well resolved microwave bursts, duration of which is in the order of ~ 0.5 μs. This provides a very good temporal resolution for the other signals that exhibit a longer duration (for example, the x-ray signals typically have a duration in the order of tens of μs). In order to obtain sufficient statistics for the data analysis, a substantial number of instability events had to be detected. Consequently, for each experimental condition a total of 10 s of data was collected. The multi-channel recording with the high temporal resolution lead to a large amount of total collected data. Performing a statistical analysis for this amount of data also necessitated the development of the dedicated analysis tool (see Section 4.2).

For all the measurements, the ion source was kept at unstable mode and the effect of different source parameters on the temporal properties of the observed instabilities was studied. For instance, the effect of the magnetic field on the instability was studied by first establishing the threshold B_{min}/B_{ECR} value and then increasing the B_{min}/B_{ECR} in steps (by increasing both of the injection and extraction solenoid coil currents equally) and recording the instability signals. Like all the previously mentioned experimental campaigns, in this case also when one source parameter was varied, the others were kept constant. The influence of magnetic field was studied by varying both solenoid coil currents between 535 A and 575 A ($B_{\mathrm{min}}/B_{\mathrm{ECR}}$ between 0.765 and 0.837), while keeping the RF power and the plasma-off neutral gas pressure at 400 W and 3.5×10^{-7} mbar, respectively. Similarly, the input RF power was varied between 400 W and 600 W while keeping the coil currents at 540 A ($B_{\mathrm{min}}/B_{\mathrm{ECR}} = 0.774$) and plasma-off neutral gas pressure at 3.5×10^{-7} mbar. The plasma-off neutral particle pressure was varied between 3.0×10^{-7} mbar and 4.5×10^{-7} mbar with constant RF power of 300 W and coil currents at 575 A ($B_{\mathrm{min}}/B_{\mathrm{ECR}} = 0.837$). The study was conducted with the source high voltage at 10 kV and biased disk at -70 V. The experiment was repeated by switching off the source high voltage and also by grounding the biased disc; in this case the biased disc was also used as an instability diagnostics as described in Section 3.2.2.

It was observed during the campaign that the detected instability-induced events did not occur only as single bursts of electromagnetic radiation and charged particles with quiescent periods between them, but the bursts were often grouped into rapid sequences of multiple bursts followed by a long quiescent period between the groups. Hence a new analysis process had to be developed to include the information regarding the grouping of instability bursts into the data analysis. Consequently, the dedicated data analysis tool which is described in Section 4.2 was developed. In addition, an indexing scheme had to be developed to describe the different temporal properties of the grouping. Fig. 5.13 presents an example of the observed grouping and illustrates the definitions of the indexing and the

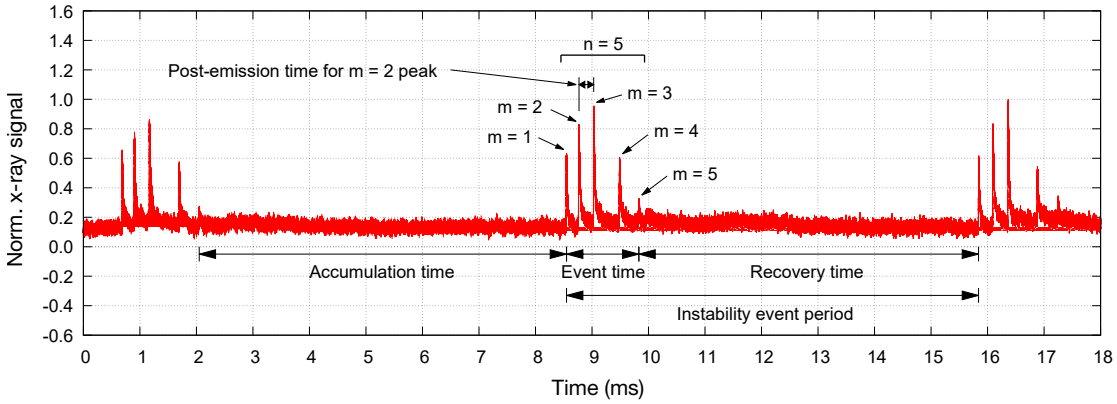

FIGURE 5.13 An example of measured x-ray signal presenting the indexing and the time definitions used in the data analysis. *Accumulation time* is the time between the last burst of the previous event and the first burst of the event under consideration; *recovery time* is the time between the last burst of the event under consideration and the first burst of the the succeeding event; *event time* is the duration of a particular event (time from the first to the last burst) and *post-emission time* is the time difference between one particular burst ('m') in an event and the successive burst in the same event.

different time definitions that were adopted to classify the different observed group patterns. Henceforth each group of instability bursts occurring in quick succession is called an *instability event* of mode n, where n is the total number of the individual bursts in the event. Each of these bursts is indexed with m starting from the first one, i.e. the index m goes from 1 to n for each event. As an example, Fig. 5.13 demonstrates three consecutive events of mode $n = 5$ and within the event the index m goes from 1 to 5. Thus by knowing the time stamp of each burst and the mode values (n, m) one can single out a particular instability burst and obtain its details. For instance, a burst with time stamp of 9 ms and mode values $(5, 3)$ describes an instability burst which occurs at $t = 9$ ms and belongs to an event which contains a total of 5 bursts out of which the burst under consideration is the third one. It was observed that these grouped instability events were detected with all the used diagnostics. The x-ray signal was chosen for the data analysis since it was found to be the most reliable. This choice was made because of two main reason:

(1) The detection of the microwave signals with the Schottky diode is bandwidth limited. It has been observed that the frequency corresponding to the instability-induced microwave emission can exhibit a decreasing trend in subsequent emissions, as has been reported by [29, 37, 105]. Consequently, if the frequency goes below the cutoff frequency set by the WR75 waveguide (7.87 GHz) it will not reach the diode. Furthermore, even before the cutoff the signal becomes strongly attenuated and might fail to be detected. The data collected during this campaign supports this view, as it was observed that in some cases the last burst(s) of an

event that were seen in the x-ray signal were absent in the microwave data. One such case has been provided as an example in the supplementary material of article [38] which is attached as Appendix PIV.

(2) The charged particles emitted during instability bursts can be measured directly using the biased disc, unlike x-ray which is a measure of wall bremsstrahlung resulting from high energy electrons colliding with chamber walls. Hence biased disc is a direct diagnostic to measure the plasma emissions. However, the biased disc signal could be measured only in the source high voltage 'OFF' case. But in order to perform the experiments also in the normal operational conditions of the ECRIS, the source high voltage had to be switched 'ON'. In this scenario, the biased disc signal could be used to analyse the high voltage 'OFF' cases and the x-ray signal to analyse the high voltage 'ON' cases, but this would add the extra complications of analysing two different signals and taking into account the issues related to both of them. This issue was addressed by comparing the biased disc signal and the x-ray signal in the source high voltage 'OFF' case and a direct relation between the measured electron charge and the x-ray signal intensity was established (presented in Fig. 4 of the published article [38], attached as Appendix PIV). Thus it was validated that the x-ray signal recreates the key features of the biased disc signal, and consequently the x-ray signal was chosen for the analysis of all the measured cases.

The analysis of the experimental data yielded two major results:

(a) The instability emissions were found to be grouped into fast sequences of quasi-periodic bursts with a temporal separation of around ~ 100 μs between the individual bursts. These grouped bursts were separated by a longer quiescent period that lasted in the order of $1 - 10$ ms depending on the source settings. It was observed that in the unstable regime the plasma typically exhibited a distribution of n modes, even with fixed source parameters. The observed n modes ranged from 1 to 10 and the distribution of the modes was influenced by the source settings. The occurrence of the grouping seems to imply that there is an underlying restriction of the amount of energy that can be expelled from the plasma through a single instability burst. The distribution of mode n is also found to be influenced by various source parameters. An example of variation in mode n as a function of B_{min}/B_{ECR} is illustrated in Fig. 5.14.

(b) It was found that the recovery time exhibits a clearer correlation with the energy expelled in an instability event than the accumulation time, i.e. higher amount of energy expelled during an instability event leads to a longer recovery time. This is shown in Fig. 5.15, where the average energy expelled during an instability event is presented as a function of the accumulation and recovery times for different n modes (see Section 4.2 for further analysis details). Thus it can be concluded that the experimental results support the scenario (i), described at

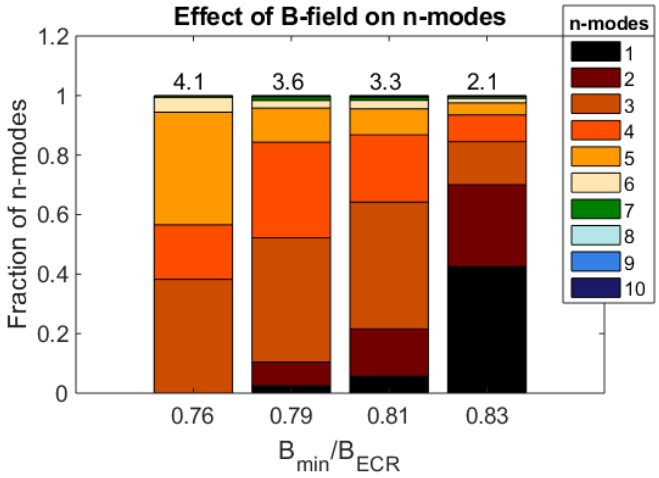

FIGURE 5.14 An example of the variation in mode n distribution as a function of the source parameters, shown here for varied B_{min}/B_{ECR} ratio. The average value of mode n is denoted above each bar.

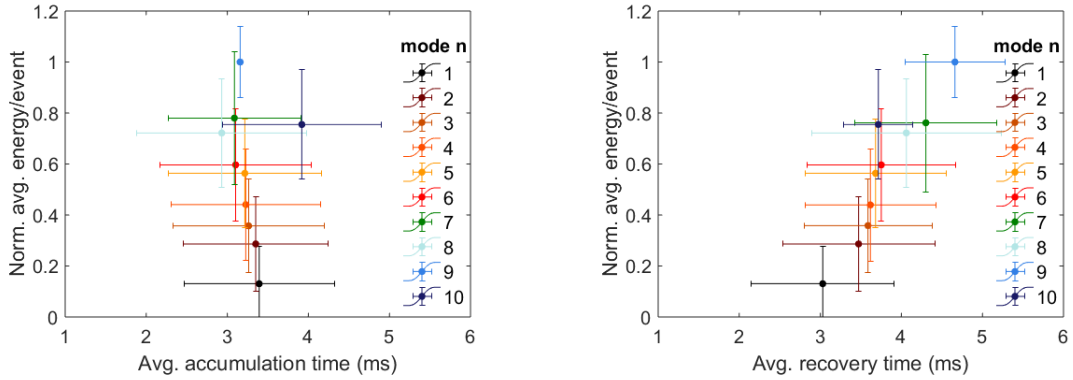

FIGURE 5.15 The relation between the average energy expelled by an instability event and the associated accumulation and recovery times. The data is presented separately for each of the observed n modes. The error is calculated from the statistical standard deviation of the total number of data collected for each mode n.

the beginning of this section, to be the correct one in the case of ECRIS plasmas. Further details and results obtained from the campaign are discussed in detail in Ref. [38] by Bhaskar *et al.* which is also attached as Appendix PIV.

6 DISCUSSIONS AND CONCLUSIONS

This thesis examined the fundamental physics underlying the formation of kinetic instabilities in ECR plasmas. Increase in the anisotropy of the electron energy distribution function is deemed to be the reason for the development of kinetic instabilities both in laboratory and space plasmas [106, 44], and this anisotropy is due to the build up in the energy carried by the hot electron component of the EED. As per the theoretical model developed by Shalashov *et al.* [48], the build up of hot electrons which ultimately leads to the onset of kinetic instabilities in ECRIS is defined using the balance equation $\frac{dN_{e,hot}}{dt} \approx -\kappa N_{e,hot} E_{\mu} + S(t) - L(t)$, which is explained in Section 2.3. In this thesis, various experiments have been performed and analysed in the context of the existing theory to study the different processes that affect the balance equation, eventually leading to the development of kinetic instability.

Prior to the beginning of this thesis work, various works on ECRIS have been performed by JYFL and IAP-RAS groups to study the kinetic instabilities in ECR-heated plasmas. These studies have deduced that the ECRIS magnetic field (especially the B_{min}/B_{ECR} ratio) has the most influence in determining the instability threshold for the plasma. These studies led to a conclusion that $B_{min}/B_{ECR} \approx 0.8$ is deemed as a typical instability threshold and similar conclusion has been obtained using different ion sources, highlighting the relevance of the magnetic field in kinetic instabilities found in ECRIS. A new magnetic field modelling tool was developed as a part of this thesis to study the link between the experimental observations and different properties of the magnetic field structure. As an example, it was observed that lowering the average magnetic field gradient ($< \nabla B_{ECR} >$) leads to higher spectral temperatures, determined from the plasma emitted bremsstrahlung, suggesting an increase in the hot electron population which is consistent with the established theory of the magnetic field gradient's role in electron heating (as described in Section 2.2.3). This subsequently influences

the build up of the electron energy in the EED, which can be directly attributed to the source term ($S(t)$) in the balance equation.

The study progressed by analysing the effect of B_{min}/B_{ECR} on the $< \nabla B_{ECR} >$, calculated using the developed computational tool. It was found that the $< \nabla B_{ECR} >$ decreases linearly with increasing B_{min}/B_{ECR} for all the ion sources studied as a part of this thesis. This indicates that increasing B_{min}/B_{ECR} enhances the electron heating, which has a direct influence on the source term of the balance equation. Consequently, the onset of kinetic instabilities at $B_{min}/B_{ECR} \approx 0.8$ can also be justified with this same argument; decrease in $< \nabla B_{ECR} >$ resulting to more efficient electron heating and the consequent build up of hot electrons that eventually, at some point, lead to the conditions that trigger the instabilities. Further analysis into the magnetic field gradient distribution also resulted in identifying one more peculiar observation, that seems to be general for all ECR ion sources (or at least for the sources that were studied as part of this work): the link between the most probable magnetic field gradient value on the ECR surface and the on-axis gradients ($\nabla B_{inj/ext}$). Hence the variation in on-axis magnetic field gradient has a dominant effect in the $< \nabla B_{ECR} >$ which explains why the experimentally determined spectral temperature varied with the $\nabla B_{inj/ext}$ as measured by Li *et al.* [69].

In order to further refine the understanding of the relation between the ECRIS magnetic field structure and the instability threshold, an extensive set of instability measurements were performed with four different ECR ion sources. For all the ion sources the magnetic field properties at the instability thresholds were calculated and studied in an attempt to identify the most crucial property of the magnetic field that defines the transition from the stable to the unstable plasma regime. However, no such single parameter or property emerged from this study; this is most likely due to the influence and the complex interplay of all the other plasma parameters which affect the conditions required for the onset of the kinetic instabilities, as is also reflected by the different terms in the balance equation. However, it was observed that with suitable source settings, all the studied ion sources exhibited a transition from the stable to the unstable plasma regime at the same $< \nabla B_{ECR} >$ value of 4.8 T/m (or $B_{min}/B_{ECR} \approx 0.8$); thus it can be speculated that for all these ion sources the source term ($S(t)$) is dominant at this average gradient value, consequently causing the onset of instability. This study emphasises on the complexity of plasma behaviour and the inherent difficulty in decoupling the magnetic field's influence from the other factors affecting the balance equation.

The loss term ($L(t)$) in the balance equation and the role of electron confinement in determining the instability threshold was studied by means of two different approaches. First, the GTS ion source was used to study the effect of controlling the axial magnetic mirrors in order to influence the hot electron population by

adjusting the electron losses through the global loss cone. This was possible with the GTS ion source because the extraction magnetic field defines the global loss cone for the electron confinement, and thus the extraction magnetic field strength can be used to control the electron losses and thus influence the build up of energy in the EED and the consequent onset of kinetic instabilities. Secondly, the instability studies were also performed using the JYFL 14 GHz ECRIS by measuring the electron energy distribution of the electrons lost from the confinement (LEED). When the ion source was at stable operation regime, the measured LEED exhibited a local maximum at around 220 keV, previously referred to as the 'high energy hump'. It has been observed that this high energy hump is not observed when the plasma becomes unstable. The origin of this hump has been studies numerically and experimentally by Izotov *et al.* [85, 83] and it has been attributed to electrons lost via RF scattering. In the balance equation RF scattering also plays a role in the determination of the loss term ($L(t)$). It was observed that the number density of electrons lost by means of the RF scattering decreased with the increase in B_{min}/B_{ECR} ratio. This implies that while the increase in B_{min}/B_{ECR} ratio affects the electron heating (by means of lowering $< \nabla B_{ECR} >$), at the same time it also affects the electron confinement, which contributes to the triggering of the instability by mitigating the hot electron losses. This study has also resulted in obtaining a correlation between the average electron energy of the high energy hump and the measured spectral temperature from the bremsstrahlung measurement.

Further study into the energy released during the instability was correlated to the recovery time that is required for the build up of the energy content in the EED. The statistical study on the energy released per instability event versus the recovery time required for the subsequent event suggests that the higher the energy released, the longer the time required for the build up of energy in the EED for the following event. The energy released during an instability event can be correlated to the first term of the balance equation, i.e. $\kappa N_{e,hot} E_{\mu}$, which determines the interaction between the amplified electromagnetic wave and the hot electron population. This study has also revealed that the electromagnetic emissions due to the kinetic instabilities are found to be typically grouped into individual bursts occurring in quick succession (separated by ~ 100 μs), followed by a longer quiescent period of $1 - 10$ *ms* before the succeeding event. This phenomenon implies that the amount of energy emitted during a single emission burst is fundamentally limited. This is an intriguing observation, and a more comprehensive theoretical examination is necessary in the future to explain this experimentally observed behaviour. This grouping of instabilities has been observed earlier in space and magnetosphere plasma, but it was studied systematically for the first time with ECRIS plasmas as a part of this thesis work. Hence this experiment has also demonstrated that ECR ion source plasmas are a suitable candidate for studies of space plasma phenomena in laboratory conditions.

This thesis work has provided important new information about the main processes that determine the occurrence of kinetic instabilities in ECR-heated plasmas. However, many questions still remain. A better understanding of the amount of energy expelled during the instabilities is needed. This thesis has provided a good starting point to study the fundamental limitation of the energy that is expelled during a single instability burst of an instability event that consists of multiple consecutive bursts, as suggested by the experimental results. More information could be obtained of this phenomenon by studying the time resolved bremsstrahlung spectra and LEED during the instability bursts. The experimental study could also be further extended by exploring the effect of two-frequency heating – which has been reported [39] to mitigate plasma instabilities – on the grouping of the instabilities. However, a detailed theoretical study is necessary to ultimately understand this phenomenon and to answer the remaining fundamental questions concerning the complex properties and processes associated with the kinetic plasma instabilities.

REFERENCES

[1] D. Dickinson, C. M. Roach, S. Saarelma, R. Scannell, A. Kirk and H. Wilson. *Physical Review Letters*, **108**, 135002 (2012).

[2] N. Gambino, S. Myalsky, L. Adler, A. De Franco, F. Ecker, G. Guidoboni, C. Kurfürst, L. Penescu, M. Pivi, C. Schmitzer *et al. Journal of Instrumentation*, **14**, C05017 (2019).

[3] D. Melrose and G. A. Dulk. *The Astrophysical Journal*, **259**, 844 (1982).

[4] L. Vlahos. *Solar Physics*, **111**, 155 (1987).

[5] P. Robinson. *Solar physics*, **134**, 299 (1991).

[6] E. Benediktov, G. Getmantsev, N. Mityakov, V. Rapoport and A. Tarasov. *Cosmic Research*, **6**, 791 (1968).

[7] D. A. Grunett. *Journal of geomagnetism and geoelectricity*, **30**, 257 (1978).

[8] R. A. Treumann. *The Astronomy and Astrophysics Review*, **13**, 229 (2006).

[9] C. Wu. *Space Science Reviews*, **41**, 215 (1985).

[10] V. Trakhtengerts and M. Rycroft. *Whistler and Alfven mode cyclotron masers in space*. Cambridge University Press (2008). doi:10.1017/CBO9780511536519.

[11] C. Trigilio, P. Leto, G. Umana, C. Buemi and F. Leone. *The Astrophysical Journal Letters*, **739**, L10 (2011).

[12] M. Lieberman and A. Lichtenberg. *Principles of Plasma Discharges and Materials Processing* (2005). URL https://onlinelibrary.wiley.com/doi/abs/10.1002/0471724254.fmatter.

[13] G. Melin, A. G. Drentje, A. Girard and D. Hitz. *Journal of applied physics*, **86**, 4772 (1999).

[14] C. Barué, M. Lamoureux, P. Briand, A. Girard and G. Melin. *Journal of applied physics*, **76**, 2662 (1994).

[15] A. Girard, C. Lécot and K. Serebrennikov. *Journal of Computational Physics*, **191**, 228 (2003).

[16] S. Singh, N. Chand and D. Patil. *Vacuum*, **83**, 372 (2008).

[17] I. Izotov, O. Tarvainen, V. Skalyga, D. A. Mansfeld, T. Kalvas, H. Koivisto and R. Kronholm. *Plasma Sources Science and Technology*, **27**, 025012 (2018).

[18] F. Jaeger, A. Lichtenberg and M. Lieberman. *Plasma Physics*, **14**, 1073 (1972).

[19] M. Lieberman and A. Lichtenberg. *Plasma Physics*, **15**, 125 (1973).

[20] E. Canobbio. *Nuclear Fusion*, **9**, 27 (1969).

[21] G. Shirkov. *Review of Scientific Instruments*, **71**, 850 (2000).

[22] R. Geller. *Electron Cyclotron Resonance Ion Sources and ECR Plasmas* (1996).

[23] C. Lyneis. In *Proc. of International Workshop on ECR Ion Sources (ECRIS'16), Busan, Korea, August 28 - September 1, 2016*, number 22 in International Workshop on ECR Ion Sources, pages 1–4 (2016).

[24] W. Ard, R. Dandl and R. Stetson. *The Physics of Fluids*, **9**, 1498 (1966).

[25] A. Vodopyanov, S. Golubev, A. Demekhov, V. Zorin, D. Mansfeld, S. Razin and V. Trakhtengerts. *Plasma Physics Reports*, **31**, 927 (2005).

[26] A. G. Shalashov, E. D. Gospodchikov, I. V. Izotov, D. A. Mansfeld, V. A. Skalyga and O. Tarvainen. *Europhysics Letters*, **124**, 35001 (2018).

[27] B. Eliasson, M. Viktorov, D. C. Speirs, K. Ronald, D. Mansfeld and A. D. R. Phelps. *Phys. Rev. Research*, **2**, 043272 (2020).

[28] I. Izotov, O. Tarvainen, D. Mansfeld, V. Skalyga, H. Koivisto, T. Kalvas, J. Komppula, R. Kronholm and J. Laulainen. *Plasma Sources Science and Technology*, **24**, 045017 (2015).

[29] I. Izotov, T. Kalvas, H. Koivisto, R. Kronholm, D. Mansfeld, V. Skalyga and O. Tarvainen. *Physics of Plasmas*, **24**, 043515 (2017).

[30] S. Golubev and A. Shalashov. *Physical review letters*, **99**, 205002 (2007).

[31] O. Tarvainen, J. Laulainen, J. Komppula, R. Kronholm, T. Kalvas, H. Koivisto, I. Izotov, D. A. Mansfeld and V. Skalyga. *Review of Scientific Instruments*, **86**, 023301 (2015).

[32] G. Melin, F. Bourg, P. Briand and R. Geller. *Le Journal de Physique Colloques*, **50**, C1 (1989).

[33] O. Tarvainen, I. Izotov, D. Mansfeld, V. Skalyga, S. Golubev, T. Kalvas, H. Koivisto, J. Komppula, R. Kronholm, J. Laulainen *et al. Plasma Sources Science and Technology*, **23**, 025020 (2014).

[34] D. Mansfeld, I. Izotov, V. Skalyga, O. Tarvainen, T. Kalvas, H. Koivisto, J. Komppula, R. Kronholm and J. Laulainen. *Plasma Physics and Controlled Fusion*, **58**, 045019 (2016).

[35] O. Tarvainen, T. Kalvas, H. Koivisto, J. Komppula, R. Kronholm, J. Laulainen, I. Izotov, D. Mansfeld, V. Skalyga, V. Toivanen and G. Machicoane. *Review of Scientific Instruments*, **87**, 02A703 (2016).

[36] E. Naselli, D. Mascali, M. Mazzaglia, S. Biri, R. Rácz, J. Pálinkás, Z. Perduk, A. Galatá, G. Castro, L. Celona, S. Gammino and G. Torrisi. *Plasma Sources Science and Technology*, **28**, 085021 (2019).

[37] V. Toivanen, B. Bhaskar, I. Izotov, H. Koivisto and O. Tarvainen. *Review of Scientific Instruments*, **93**, 013302 (2022).

[38] B. Bhaskar, H. Koivisto, O. Tarvainen, T. Thuillier and V. Toivanen. *AIP Advances*, **12**, 015223 (2022).

[39] V. Skalyga, I. Izotov, T. Kalvas, H. Koivisto, J. Komppula, R. Kronholm, J. Laulainen, D. Mansfeld and O. Tarvainen. *Physics of Plasmas*, **22**, 083509 (2015).

[40] I. Izotov, T. Kalvas, H. Koivisto, J. Komppula, R. Kronholm, J. Laulainen, D. Mansfeld, V. Skalyga and O. Tarvainen. *Review of Scientific Instruments*, **87**, 02A729 (2016).

[41] A. Kulchar, O. Eldridge, A. England, C. Bush, P. Edmonds, G. Kelley, C. Loring, Y.-K. Peng, J. Wilgen and S. Borowski. *The Physics of fluids*, **27**, 1869 (1984).

[42] C. Pierret, L. Maunoury, S. Biri, J. Pacquet, O. Tuske and O. Delferriere. *Review of Scientific Instruments*, **79**, 02B703 (2008).

[43] G. Douysset, H. Khodja, A. Girard and J. Briand. *Physical Review E*, **61**, 3015 (2000).

[44] M. Viktorov, A. Shalashov, D. Mansfeld and S. Golubev. *EPL (Europhysics Letters)*, **116**, 55001 (2017).

[45] A. Shalashov, M. Viktorov, D. Mansfeld and S. Golubev. *Physics of Plasmas*, **24**, 032111 (2017).

[46] A. Demekhov. *Radiophysics and Quantum Electronics*, **30**, 547 (1987).

[47] A. Shalashov, S. Golubev, E. Gospodchikov, D. Mansfeld and M. Viktorov. *Plasma Physics and Controlled Fusion*, **54**, 085023 (2012).

[48] A. G. Shalashov, E. D. Gospodchikov and I. Izotov. *Plasma Physics and Controlled Fusion*, **62**, 065005 (2020).

[49] H. Koivisto, P. Heikkinen, V. Hänninen, A. Lassila, H. Leinonen, V. Nieminen, J. Pakarinen, K. Ranttila, J. Ärje and E. Liukkonen. *Nuclear Instruments and Methods in Physics Research Section B: Beam Interactions with Materials and Atoms*, **174**, 379 (2001).

[50] T. Lamy, J. Bouly, J. Curdy, R. Geller, A. Lacoste, P. Sole, P. Sortais, T. Thuillier, J. Vieux-Rochaz, K. Jayamanna *et al. Review of scientific instruments*, **73**, 717 (2002).

[51] T. Thuillier *et al.* In *Proc. of International Workshop on ECR Ion Sources (ECRIS'16), Busan, Korea, August 28 - September 1, 2016*, International Workshop on ECR Ion Sources, pages 48–49 (2016).

[52] D. Hitz, D. Cormier, J. Mathonnet, A. Girard, G. Melin, F. Lansaque, K. Serebrenikov and L. Sun. In *Proceedings of the 15th International Workshop on Electron Cyclotron Resonance Ion Sources*. Jyväskylä, Finland (2002).

[53] L. Sun, H. Zhao, H. Zhao, W. Lu, J. Guo, Y. Cao, Q. Wu, C. Qian, Y. Yang, X. Fang *et al. Review of Scientific Instruments*, **91**, 023310 (2020).

[54] E. Liukkonen. In *Cyclotrons And Their Applications-Proceedings Of The13th International Conference, Vancouver, 1992*, page 22. World Scientific (1993).

[55] G. Melin, C. Barue, F. Bourg, P. Briand, J. Debernardi, M. Delaunay, R. Geller, A. Girard, K. Golovanivsky, D. Hitz *et al. Recent Developments and Future Projects on ECR ion sources at Grenoble*. Technical report (1991).

[56] R. Harkewicz. *Review of scientific instruments*, **67**, 2176 (1996).

[57] H. Koivisto, J. Ärje and M. Nurmia. *Nuclear Instruments and Methods in Physics Research Section B: Beam Interactions with Materials and Atoms*, **94**, 291 (1994).

[58] Z. Xie, C. Lyneis, R. Lam and S. Lundgren. *Review of scientific instruments*, **62**, 775 (1991).

[59] T. N. T. Nakagawa. *Japanese journal of applied physics*, **30**, L930 (1991).

[60] V. Mironov, K. Stiebing, O. Hohn, L. Schmidt, H. Schmidt-Böcking, S. Runkel, A. Schempp, G. Shirkov, S. Biri and L. Kenez. *Review of scientific instruments*, **73**, 623 (2002).

[61] *CPI TWTA*. https://www.cpii.com/docs/datasheets/18/mkt227.pdf.

[62] *Drentje,A.G., Proc. of the 6th Workshop on ECR ion sources, Berkeley (1985), pg 73.*

[63] D. Clark and C. Lyneis. *Le Journal de Physique Colloques*, **50**, C1 (1989).

[64] H. Koivisto, P. Frondelius, T. Koponen, P. Lappalainen, T. Ropponen, M. Savonen, P. Suominen, O. Tarvainen, K. Tinschert and G. Ciavola. *Chinese Physics C*, **31**, 41 (2007).

[65] R. Harkewicz, P. Billquist, J. Greene, J. Nolen Jr and R. Pardo. *Review of scientific instruments*, **66**, 2883 (1995).

[66] T. Kalvas, O. Tarvainen, T. Ropponen, O. Steczkiewicz, J. Ärje and H. Clark. *Review of Scientific Instruments*, **81**, 02B703 (2010).

[67] V. Toivanen, T. Kalvas, H. Koivisto, J. Komppula and O. Tarvainen. *Journal of Instrumentation*, **8**, P05003 (2013).

[68] V. Toivanen, T. Kalvas, H. Koivisto, J. Komppula and O. Tarvainen. In *the proceedings of the 20th International Workshop on Electron Cyclotron Resonance Ion Sources (ECRIS2012), Sydney Australia*, pages 25–28 (2012).

[69] J. Li, L. Li, B. Bhaskar, V. Toivanen, O. Tarvainen, D. Hitz, L. Li, W. Lu, H. Koivisto, T. Thuillier *et al. Plasma Physics and Controlled Fusion*, **62**, 095015 (2020).

[70] B. Bhaskar, H. Koivisto, O. Tarvainen, T. Thuillier, V. Toivanen, T. Kalvas, I. Izotov, V. Skalyga, R. Kronholm and M. Marttinen. *Plasma Physics and Controlled Fusion*, **63**, 095010 (2021).

[71] O. Tarvainen, R. Kronholm, T. Kalvas, H. Koivisto, I. Izotov, V. Skalyga, V. Toivanen and L. Maunoury. *Review of Scientific Instruments*, **90**, 123303 (2019).

[72] G. F. Knoll. *Radiation detection and measurement*. Wiley, New York (1983).

[73] *Amptek CdTe detector*. https://www.amptek.com/products/x-ray-detectors/cdte-x-ray-and-gamma-ray-detectors/xr-100cdte-x-ray-and-gamma-ray-detector.

[74] *TOSCA software*. http://www.rcnp.osaka-u.ac.jp/~sakemi/OPERA/user-3d.pdf.

[75] *RADIA software*. https://www.esrf.fr/Accelerators/Groups/InsertionDevices/Software/Radia.

[76] *FEMM software*. https://www.femm.info/wiki/HomePage.

[77] M. Szilagyi. *Electron and ion optics*. Springer Science & Business Media (2012).

[78] J. Vaughan. *IEEE Transactions on Electron Devices*, **19**, 144 (1972).

[79] *Matlab function isosurf*. https://se.mathworks.com/help/matlab/ref/isosurface.html.

[80] D. Leitner. In *10th International Particle Accelerator Conference*, pages 2224–2229 (2019).

[81] C. Shannon. *Proceedings of the IRE*, **37**, 10 (1949).

[82] *Matlab function findpeak*. https://se.mathworks.com/help/signal/ref/findpeaks.html.

[83] I. Izotov, A. Shalashov, V. Skalyga, E. Gospodchikov, O. Tarvainen, V. Mironov, H. Koivisto, R. Kronholm, V. Toivanen and B. Bhaskar. *Plasma Physics and Controlled Fusion*, **63**, 045007 (2021).

[84] O. Tarvainen, J. Angot, I. Izotov, V. Skalyga, H. Koivisto, T. Thuillier, T. Kalvas and T. Lamy. *Plasma Sources Science and Technology*, **26**, 105002 (2017).

[85] I. Izotov, O. Tarvainen, V. Skalyga, D. Mansfeld, H. Koivisto, R. Kronholm, V. Toivanen and V. Mironov. *Review of Scientific Instruments*, **91**, 013502 (2020).

[86] D. Mascali, L. Celona, F. Maimone, J. Maeder, G. Castro, F. P. Romano, A. Musumarra, C. Altana, C. Caliri, G. Torrisi, L. Neri, S. Gammino, K. Tinschert, K. P. Spaedtke, R. Rossbach, J Lang and G. Ciavola. *Review of Scientific Instruments*, **85**, 02A956 (2014).

[87] V. Mironov, S. Bogomolov, A. Bondarchenko, A. Efremov, V. Loginov and D. Pugachev. *Plasma Sources Science and Technology*, **29**, 065010 (2020).

[88] R. Rácz, S. Biri, J. Pálinkás, D. Mascali, G. Castro, C. Caliri, L. Neri, F. Romano and S. Gammino. In *Proceedings of the 22nd International Workshop on Electron Cyclotron Resonance Ion Sources*. Busan, Korea (2016).

[89] V. Toivanen, B. Bhaskar, H. Koivisto, L. Maunoury, O. Tarvainen and T. Thuillier. *Physics of Plasmas*, **29**, 013501 (2022).

[90] K. Bernhardi and K. Wiesemann. *Plasma Physics*, **24**, 867 (1982).

[91] C. Barue, P. Briand, A. Girard, G. Melin and G. Briffod. *Review of scientific instruments*, **63**, 2844 (1992).

[92] R. Friedlein, D. Küchler, C. Zippe, G. Zschornack and H. Tyrroff. *Hyperfine interactions*, **99**, 225 (1996).

[93] K. Wiesemann. *Review of Scientific Instruments*, **79**, 02B506 (2008).

[94] R. Baskaran, T. Selvakumaran, G. Rodrigues, D. Kanjilal and A. Roy. *Review of Scientific Instruments*, **79**, 02A324 (2008).

[95] H. Zhao, H. Zhao, L. Sun, H. Wang, D. Xie, B. Ma, X. Z. Zhang, X. Li, X. Ma, Y. Zhu *et al. Plasma Sources Science and Technology*, **18**, 025021 (2009).

[96] A. Gumberidze, M. Trassinelli, N. Adrouche, C. I. Szabo, P. Indelicato, F. Haranger, J.-M. Isac, E. Lamour, E.-O. Le Bigot, J. Mérot, C. Prigent, J.-P. Rozet and D. Vernhet. *Review of Scientific Instruments*, **81**, 033303 (2010).

[97] S. Kasthurirangan, A. Agnihotri, C. Desai and L. Tribedi. *Review of Scientific Instruments*, **83**, 073111 (2012).

[98] R. Rácz, S. Biri, Z. Perduk, J. Pálinkás, D. Mascali, M. Mazzaglia, E. Naselli, G. Torrisi, G. Castro, L. Celona, S. Gammino and A. Galatà. *Journal of Instrumentation*, **13**, C12012 (2018).

[99] G. Castro, D. Mascali, M. Mazzaglia, S. Briefi, U. Fantz and R. Miracoli. *Physical Review Accelerators and Beams*, **22**, 053404 (2019).

[100] K. Bernhardi. *Computer Physics Communications*, **19**, 17 (1980).

[101] R. Friedlein and G. Zschornack. *Nuclear Inst. and Methods in Physics Research, A*, **349**, 554 (1994). ISSN 01689002. doi:10.1016/0168-9002(94)91226-2.

[102] M. Sakildien, O. Tarvainen, R. Kronholm, I. Izotov, V. Skalyga, T. Kalvas, P. Jones and H. Koivisto. *Physics of Plasmas*, **25**, 062502 (2018).

[103] B. Isherwood, E. Pozdeyev, G. Machicoane, J. Stetson and D. Neben. In *Proceedings of the 23rd International Workshop on ECR Ion Sources (ECRIS'18), International Workshop on ECR Ion Sources*, pages 157–161 (2018).

[104] *Picoscope 5000 series*. https://www.picotech.com/oscilloscope/5000/flexible-resolution-oscilloscope.

[105] D. Mascali, E. Naselli and G. Torrisi. *Review of Scientific Instruments*, **93**, 033302 (2022).

[106] M. Viktorov, D. Mansfeld and S. Golubev. *EPL (Europhysics Letters)*, **109**, 65002 (2015).

ORIGINAL PAPERS

PI

EFFECTS OF MAGNETIC CONFIGURATION ON HOT ELECTRONS IN A MINIMUM-B ECR PLASMA

by

Li, JB and Li, LX and Bhaskar, BS and Toivanen, V and Tarvainen, O and Hitz, D and Li, LB and Lu, W and Koivisto, H and Thuillier, T and Guo, JW and Zhang, XZ and Zhao, HY and Sun, LT and Zhao, HW 2020

Plasma Physics and Controlled Fusion **62**, 9 095015

Effects of magnetic configuration on hot electrons in a minimum-B ECR plasma

Effects of magnetic configuration on hot electrons in a minimum-B ECR plasma

J. B. Li[1], L. X. Li[1,2], B. S. Bhaskar[3,4], V. Toivanen[3], O. Tarvainen[3,5], D. Hitz[1], L. B. Li[1], W. Lu[1], H. Koivisto[3], T. Thuillier[4], J. W. Guo[1], X. Z. Zhang[1,2], H. Y. Zhao[1,2], L. T. Sun[1,2;a)] and H. W. Zhao[1,2]

[1]*Institute of Modern Physics (IMP), Chinese Academy of Sciences, Lanzhou 730000, China*

[2]*School of Nuclear Science and Technology, University of Chinese Academy of Sciences, Beijing 100049, China*

[3]*University of Jyväskylä, Department of Physics, PO Box 35 (YFL), 40500 Jyväskylä, Finland*

[4]*Laboratoire de Physique Subatomique et de Cosmologie, 53 avenue des Martyrs, 38026 Grenoble Cedex, France*

[5]*STFC ISIS Pulsed Spallation Neutron and Muon Facility, Rutherford Appleton Laboratory, Harwell, OX110QX, UK*

a) E-mail: sunlt@impcas.ac.cn

Abstract

To investigate the hot electron population and the appearance of kinetic instabilities in highly charged electron cyclotron resonance ion source (ECRIS), the axially emitted bremsstrahlung spectra and microwave bursts emitted from ECRIS plasma were synchronously measured on SECRAL-II (Superconducting ECR ion source with Advanced design in Lanzhou No. II) ion source with various magnetic field configurations. The experimental results show that when the ratio of the minimum field to the resonance field (i.e. B_{min}/B_{ecr}) is less than ~0.8, the bremsstrahlung spectral temperature T_s increases linearly with the B_{min}/B_{ecr}–ratio when the injection, extraction and radial mirror fields are kept constant. Above this threshold T_s saturates and the electron cyclotron instability appears simultaneously. This study has also demonstrated that T_s decreases linearly with the increase of the average gradient over the ECR surface when the on-axis gradient and hexapole field strengths are constant. In addition, it is found that T_s decreases with the increase of the gradient at the resonance zone (∇B_{ecr} on axis and $<\nabla B_{ecr}>$) at relatively low mirror ratio and is insensitive to the gradient at high mirror ratio when B_{min} is constant. Compared to a recent study taken on a fully superconducting ECRIS (Benitez et al. 2017 *IEEE Trans. Plasma Sci.* **45** 1746-54), in which it was concluded that T_s is only sensitive with B_{min}, this article shows different results discussing the mechanisms behind the correlation of magnetic field parameters to T_s.

1. Introduction

Electron cyclotron resonance (ECR) ion sources are used to produce a wide range of ions, from singly charged to multiply charged ions (MCIs) and have been widely applied to both basic and applied scientific research due to their efficiency and reliability [1, 2]. In the past decades, a series of well performing ECR ion sources

were developed at the Institute of Modern Physics (IMP) [3-10] and continuous efforts were spent to deepen the understanding of the plasma mechanisms involved in these ion sources and thereby to further improve their performances [11-16].

The plasmas in modern ECRISs are commonly confined in a so-called minimum-B field which is a superposition of solenoid and sextupole fields. Electrons in the plasma are heated by the process of electron cyclotron resonance that takes place where the electron cyclotron frequency is approximately equal to the injected microwave frequency. MCIs are created through stepwise electron impact ionization by the electrons heated in the ECR. However, hot electrons, with energies of several hundreds of keV or more should be avoided as they do not contribute significantly on the ionization process but can add a significant heat load to the cryostat of modern superconducting ECRISs through absorption of wall bremsstrahlung photons [17, 18]. Meanwhile, it has been shown that [19-21] ECR plasmas are prone to electron cyclotron instabilities driven by hot electrons with strongly anisotropic electron velocity distribution (EVD), which will lead to ms-scale oscillation of the extracted beam current.

This article deals with experimental studies of the hot electron population of a highly charged ECR ion source. As collisions between electrons and ions within the plasma volume lead to bremsstrahlung radiation, the analysis of bremsstrahlung spectra is a powerful diagnostic tool for studying the hot electron population [22, 23] and can also be used to probe the electron heating mechanism in ECR produced plasmas, from compact all-permanent magnet [24] to large fully superconducting devices [13, 25]. To compare our results with previous articles published on the same subject, bremsstrahlung measurement was chosen to diagnose the plasma of SECRAL-II ion source. Meanwhile, since the electron cyclotron instabilities are driven by hot electrons interacting resonantly with electromagnetic plasma waves, the measurement of characteristic microwave emission emitted from the ECRIS plasma can be used as a direct plasma instability diagnostics method [19] and was also employed in this study to investigate the appearance of electron cyclotron instabilities.

A number of previous studies taken on ECRISs [13, 25-27] show that the magnetic field configuration is extremely important for the production of hot electrons in minimum-B topology. Although these earlier studies showed important results, the mechanism behind the correlation of magnetic field parameters to the bremsstrahlung spectral temperature T_s is not yet clear. Furthermore, it has been demonstrated that the most critical ion source tuning parameter affecting the appearance of electron cyclotron instabilities and beam current oscillations is the magnetic field [19], but the possible correlation between bremsstrahlung spectra and the appearance of electron cyclotron instabilities are still unknown. Therefore, to further investigate the effects of magnetic configuration on hot electrons in a minimum-B ECR plasma, in this paper we present a detailed experimental study of the hot electron population through synchronous measurements of plasma bremsstrahlung and instability-induced microwave signal in a much wider range of magnetic configurations than those presented in previous articles (including the

so-called turbulent region where instabilities occur). The experimental setup and equipment are described in section 2; in section 3, the experimental results are reported; a discussion about the data is then shown in section 4, followed by the conclusions in section 5.

2. Experimental setup

2.1 SECRAL-II ion source

SECRAL-II ion source has been successfully designed and developed at IMP [28]. This ion source is a third generation ECR machine optimized for the operation at 18, 24 and 28 GHz. The superconducting magnet assembly of SECRAL-II (shown in Figure 1) consists of three axial solenoid coils and a sextupole to generate the minimum-B magnetic field configuration. The magnetic field profile is typically 3.7 T at the injection, 2.2 T at the extraction with a radial field of 2.0 T at the Ø125 mm chamber wall. As the source magnet is fully superconducting, SECRAL-II has the flexibility of easily varying the magnetic structure by independently changing the injection field, B_{inj}, the extraction field, B_{ext}, the minimum-B value, B_{min} and the radial field, B_r, so that one can investigate the effect of magnetic field configuration in detail.

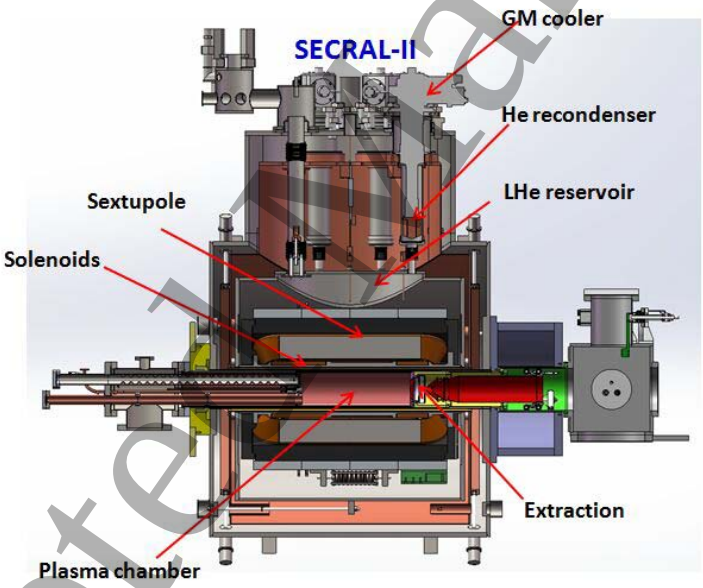

Figure 1: Layout of the SECRAL-II ion source.

2.2 Bremsstrahlung detection system and spectral temperature T_s determination

As SECRAL-II is fully superconducting, the only possibility to install a diagnostic is on a line-of-sight through the source axis. The axially emitted bremsstrahlung spectra from SECRAL-II are measured with an Amptek XR-100T-CdTe detector and PX5 digital pulse processor [29] through an Al window located at the end of the straight-through port of the beam analyzing magnet (shown in Figure 2). The detector is a semiconductor type with a detection efficiency of 10% or greater in the

energy range of 10 to 300 keV and is placed behind the straight-through port. In order to focus on the center of the plasma and prevent wall bremsstrahlung interfering with the detection system, a lead collimation system is designed with MCNP (Monte Carlo N-Particle Transport Code) [30, 31] and is set up between the straight-through port and the detector. In addition, an X-ray blocking made of tantalum (diameter: 30 mm, thickness: 20 mm) is installed on the optical axis, it blocks the X-rays from entering the collimation system and reaching the detector when inserted. The measurement solid angle is restricted to 6.7E-8 sr and the energy calibration of the spectrum is done using standard radioactive sources with known gamma lines. It is acknowledged that thick target bremsstrahlung emitted into backward angles from the biased disc located at the injection end of the ion source may contribute to the recorded spectra. Since the energy distribution of the electrons causing this contribution is unknown, it is impossible to estimate the ratio of the plasma bremsstrahlung and (biased disc) wall bremsstrahlung. However, as most of the radiation power from the biased disc is emitted into forward angles, and the area defined by the acceptance of the collimation system (Ø14 mm at the extraction aperture) includes only a small part of the extraction system, the main contribution to the bremsstrahlung spectra is therefore considered to be the plasma bremsstrahlung produced in the volume visible to the detector.

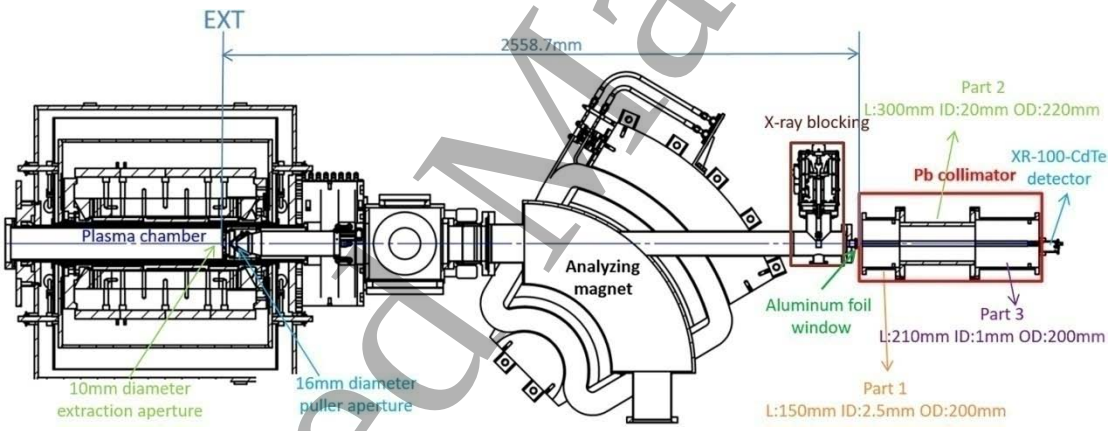

Figure 2: Bremsstrahlung detection system on SECRAL-II.

A parameter called the spectral temperature T_s is often used to characterize the bremsstrahlung spectra. T_s is inferred from the linear part of the semi-logarithmic representation of the recorded spectrum for which the spectral power $j(E) \propto \exp(-E/T_s)$, where E is the photon energy. We should note that this spectral temperature is not a direct measure of the temperature of the hot electrons, since the electron energy distribution in an ECRIS plasma is believed to be strongly non-Maxwellian [32]. This statement is supported by recent experiments measuring the energy distribution of electrons escaping from a minimum-B ECRIS [33]. For these reasons T_s must be regarded as qualitative measure of the hot electron (average) energy at best. Bearing these limitations in mind one can use T_s to study

the influence of the external source parameters such as magnetic field strength, injected microwave power etc. on the hot electron population in relative terms. In our study, the bremsstrahlung spectra presented below are corrected by the detector efficiency and the spectral temperature T_s is obtained by the linear fit at the energy range 80–200 keV (shown in Figure 3).

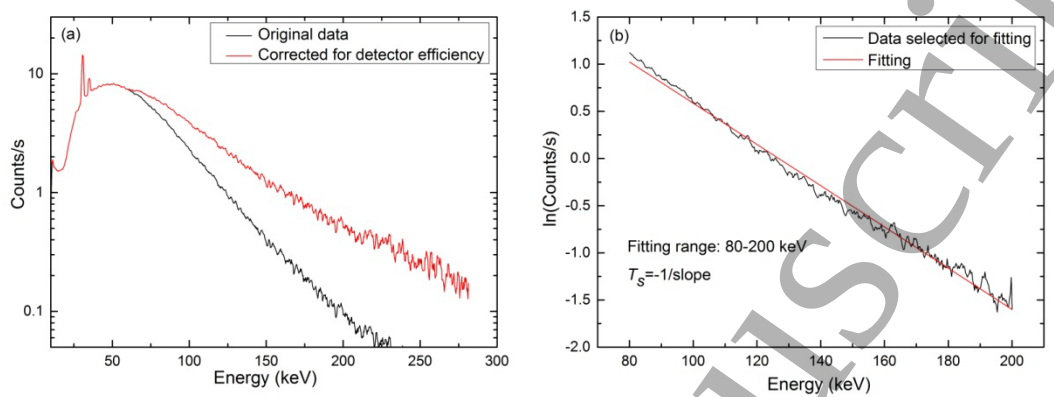

Figure 3: (a) Spectra corrected for detector efficiency. (b) A linear fitting of the semi-log plot of the data.

2.3 Microwave signal measurement and electron cyclotron instability

Figure 4 shows the experimental setup of the microwave signal measurement. A Low-Barrier Schottky Diode detector (0.01-26.5 GHz, 10 ns resolution) is connected to a WR-62 waveguide port at the injection of the ion source. The microwave signal emitted by the plasma is guided into oscilloscope through WR-62 waveguide port, high voltage break, waveguide-to-coaxial transition and adjustable attenuator (usually set to 20 dB).

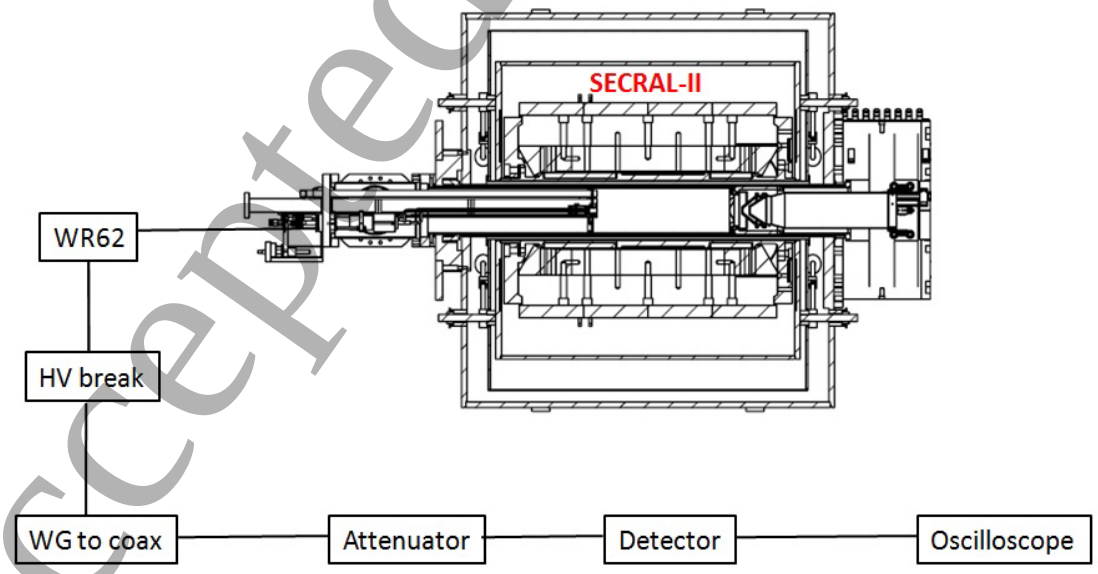

Figure 4: Schematic figure of experimental setup of microwave signal measurement.

The theoretical research shows that electron cyclotron instability is driven by hot electrons interacting resonantly with electromagnetic plasma waves, therefore the emission of microwaves from ECR plasma is a characteristic feature of the electron cyclotron plasma instability as discussed in a recent paper by Shalashov et al. [34] addressing the dynamics of periodic microwave emission and corresponding temporal modulation of the electron energy distribution. Following Refs. [35-38] the energy of the microwave emission E_μ can be described by $\frac{dE_\mu}{dt} \approx (\gamma - \delta)E_\mu$, where γ and δ are mode-dependent growth and damping rates, respectively. Since the growth rate is proportional to the ratio of hot to cold electron densities ($\gamma \propto \frac{N_{e,hot}}{N_{e,cold}}$), and the damping rate is determined by volumetric absorption of the wave energy by the collisional background plasma and external losses ($\delta \propto \nu_e + R$, where R represents the reflection/wall loss term), once the condition $\gamma > \delta$ is reached, the intensity of the microwave emission will increase exponentially with time (usually lasts for about 10-100 ns) as reported e.g. by Izotov et al. [39]. The measurement setup does not allow detecting the emission frequencies associated with the instability. However, it has been shown previously with 14 GHz ECR ion sources that [39, 40] the instability-induced emission frequencies are predominantly lower than the plasma heating frequency. The intensity of the instability-induced microwave burst exceeds the continuous (background) signals of the plasma electron cyclotron emission (ECE) and the primary heating frequency coupled into the diagnostics port by several orders of magnitude. Figure 5 shows a typical microwave signal on SECRAL-II when the electron cyclotron instability is triggered.

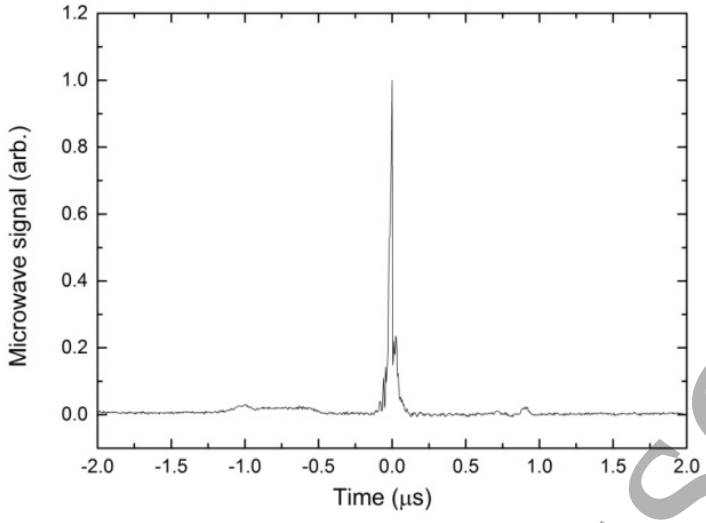

Figure 5: Example of microwave signal associated with the electron cyclotron instability.

3. Experimental results

In all measurements the ion source is operated with xenon plasma and first tuned for Xe^{20+} production. Typical extraction voltage is 20 kV and bias disc voltage is -40-50 V at a power level of 1500 W, data are measured with similar gas pressure of 1-2*10^{-7} mbar. Previous theoretical and experimental studies [25, 41-43] indicate that the minimum magnetic field B_{min} and the gradient parallel to the magnetic field at the resonance zone, $\left|\left(\vec{B}/\left|\vec{B}\right|\right)\cdot\nabla\vec{B}\right|_{ecr}$, referred hereafter simply as ∇B_{ecr} are the key parameters of the magnetic field configuration and play an important role in magnetically confined ECR plasma, so in the first part of this study, B_{min} is changed while the other fields (B_{inj}, B_{ext} and B_r) are held constant. Figure 6 shows the magnetic field configuration for the 18 and 24 GHz settings. For the 18 GHz case, B_{min} is changed from 0.32 T to 0.52 T with B_{inj}, B_{ext} and B_r at 1.75 T, 1.32 T and 1.20 T, respectively. For the 24 GHz case, similarly, B_{min} is varied from 0.45 T to 0.66 T with fixed B_{inj}, B_{ext} and B_r separately (2.60 T, 1.81 T and 1.66 T). Here, the B_r value is taken in the plane where the radial component of the solenoid field is zero, i.e. B_r represents the hexapole field component. The experimental results in Figure 7 show that the spectral temperature T_s increases almost linearly with the increase of B_{min} for both 18 and 24 GHz heating up to certain values, i.e. 0.51 T and 0.66 T for 18 and 24 GHz, respectively. When B_{min} exceeds the above values, electron cyclotron instabilities are detected and T_s deviates from the increasing trend observed below the instability threshold (this conclusion is supported by additional data presented in Section 4).

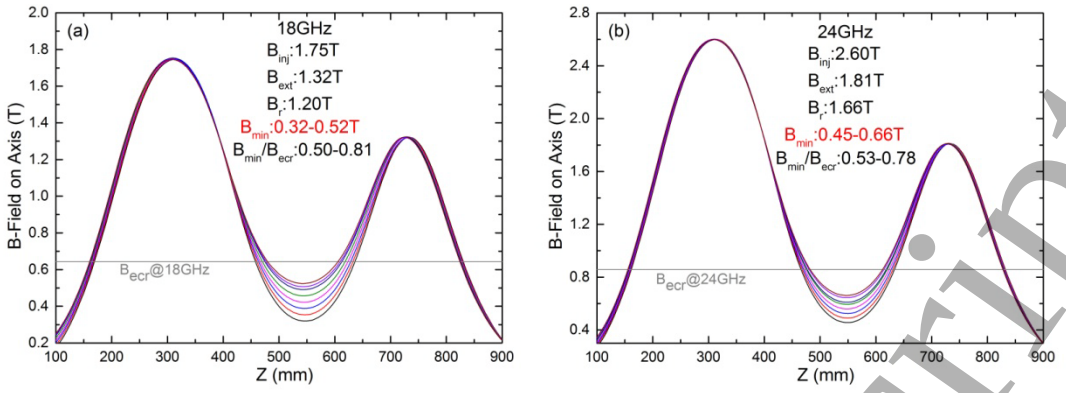

Figure 6: Axial magnetic fields for 18 GHz (a) and 24 GHz (b) heating with constant injection, extraction and radial fields.

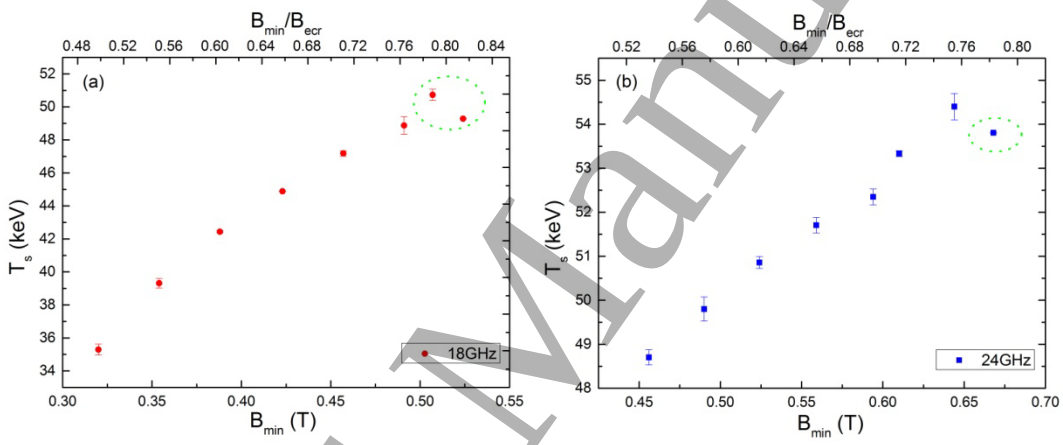

Figure 7: Spectral temperature T_s as a function of B_{min} with constant injection, extraction and radial fields for 18 GHz (a) and 24 GHz (b) heating. The circled data points are the cases where the instabilities are detected.

However, one should note that in these cases when B_{min} is changed, on-axis ∇B_{ecr} is also simultaneously changed. So in the part two of the study, on-axis ∇B_{ecr} is held approximately constant (18 GHz: ~6.3 T/m, 24 GHz: ~9.2 T/m) but B_{min} is changed for the two heating frequencies 18 and 24 GHz (shown in Figure 8). For 18 GHz heating, B_{min} is varied from 0.31 T to 0.47 T with a constant B_r at 1.02 T, the corresponding variations of the injection and extraction fields are 1.13 T to 2.65 T and 1.03 T to 1.68 T, respectively. For 24 GHz, B_{min} is varied from 0.39 T to 0.57 T with a fixed B_r (1.44 T), accordingly, the injection and extraction fields are changed from 1.76 T to 3.43 T and 1.45 T to 2.05 T. It is seen from Figure 9 that when on-axis ∇B_{ecr} is held approximately constant, T_s depends almost linearly on B_{min} for both two heating frequencies. Meanwhile, electron cyclotron instabilities do not appear.

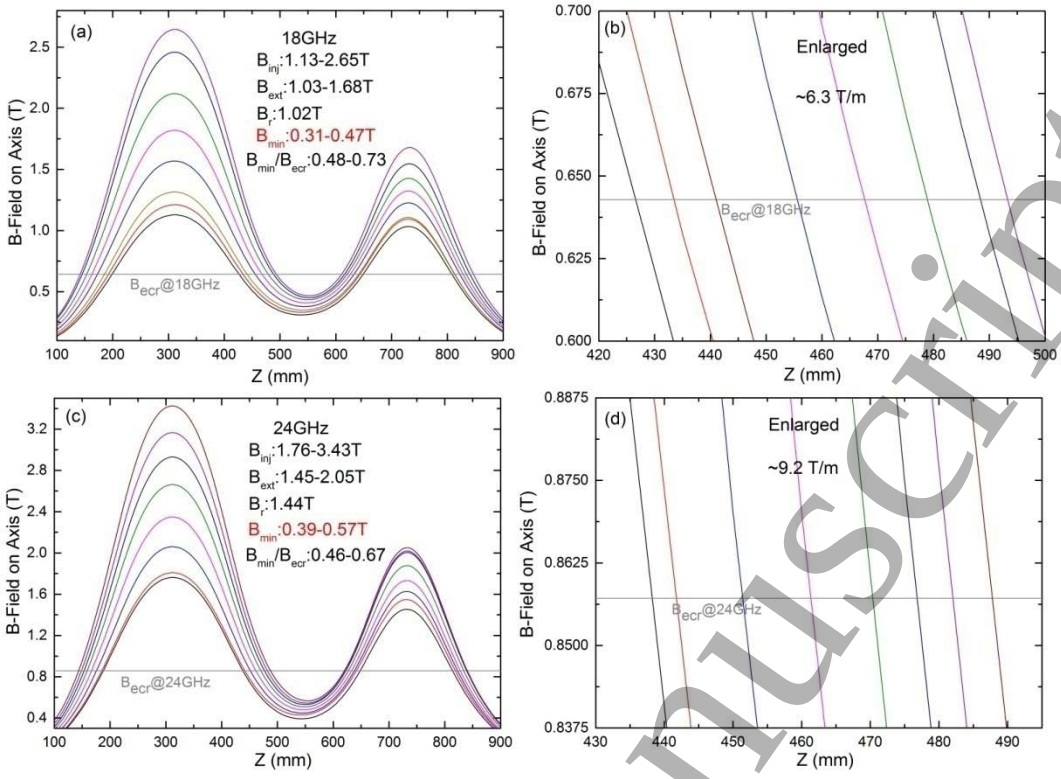

Figure 8: Axial magnetic fields for quasi-constant on-axis ∇B_{ecr} at 18 GHz (a & b) and 24 GHz (c & d) heating.

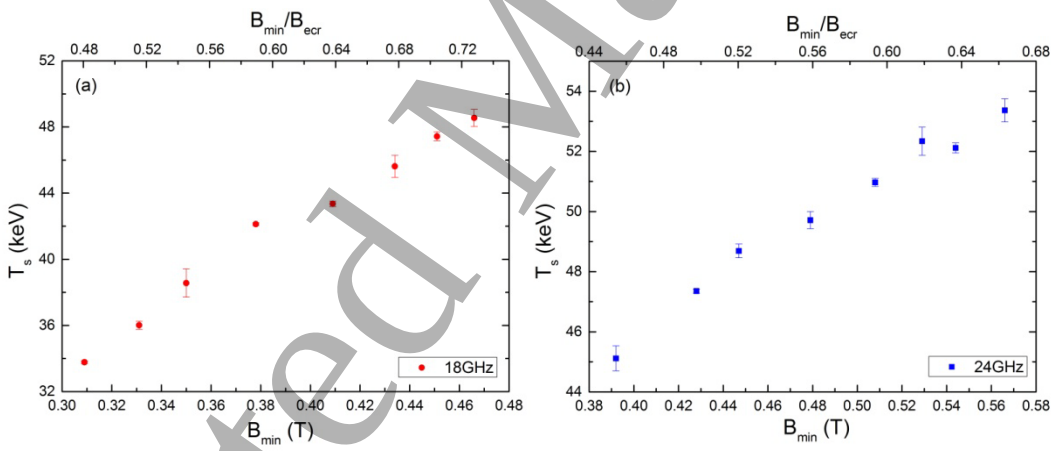

Figure 9: Spectral temperature T_s for 18 (a) and 24 (b) GHz heating at quasi-constant on-axis ∇B_{ecr}.

For comparison, in the third experimental part, B_{min} is kept constant and we vary on-axis ∇B_{ecr} for 18 and 24 GHz (see Figure 10). At 18 GHz, with B_{min} and B_r held constant at 0.40 T and 1.05 T, the injection and extraction fields are varied from 1.06 T to 2.41 T and 1.10 T to 1.50 T. While, at 24 GHz, the injection and extraction fields are varied from 2.12 T to 3.58 T and 1.61 T to 2.14 T corresponding to B_{min} = 0.59 T and B_r = 1.53 T. Figure 11 shows that the resulting T_s decreases with the increase of ∇B_{ecr} at low mirror ratio and is insensitive to the gradient at high mirror ratio for both 18 and 24 GHz heating. Electron cyclotron instabilities are not found at any point in this sweep.

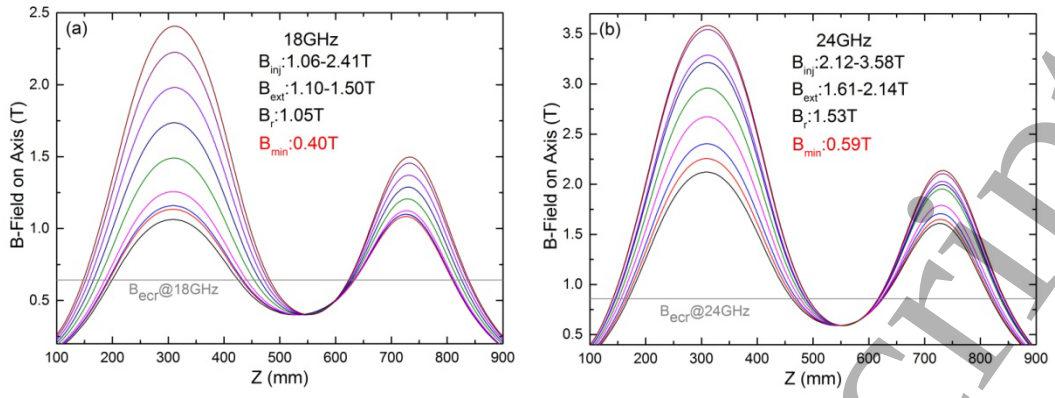

Figure 10: Axial magnetic fields when B_{min} is kept constant (a) at 18 GHz, (b) at 24 GHz.

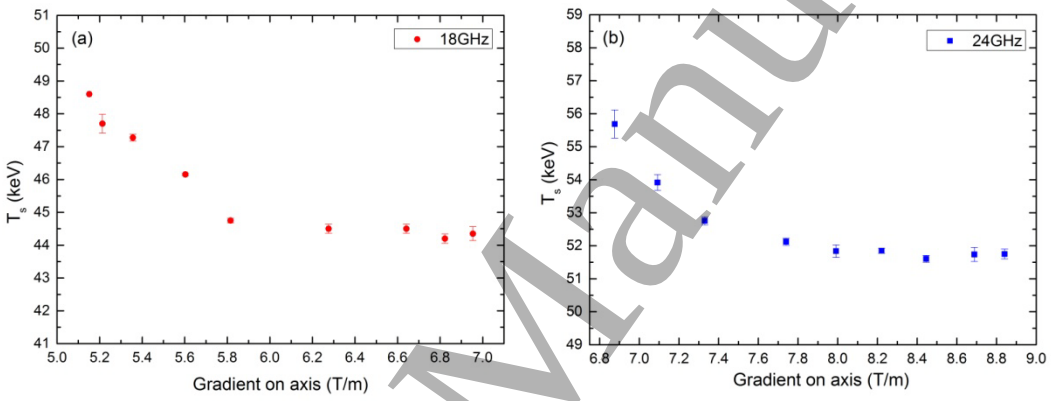

Figure 11: Spectral temperature T_s as a function of on-axis ∇B_{ecr} for 18 (a) and 24 (b) GHz heating with constant B_{min}.

Since the increase of the axial mirror fields (and on-axis gradient at constant B_{min}) changes the radial component of the solenoid field and, thus, affects the strength of the radial confinement by weakening the hexapole field on three poles in the injection side and on the other three poles in the extraction side, the effect of the radial field on T_s was also investigated. In this sweep, carried out with 24 GHz frequency, the on-axis gradient (8.1 T/m) and B_{min} (0.60 T) as well as the injection and extraction mirror fields (3.00 T and 1.98 T) were kept constant. The result is displayed in Figure 12 showing that T_s is affected by the radial field strength.

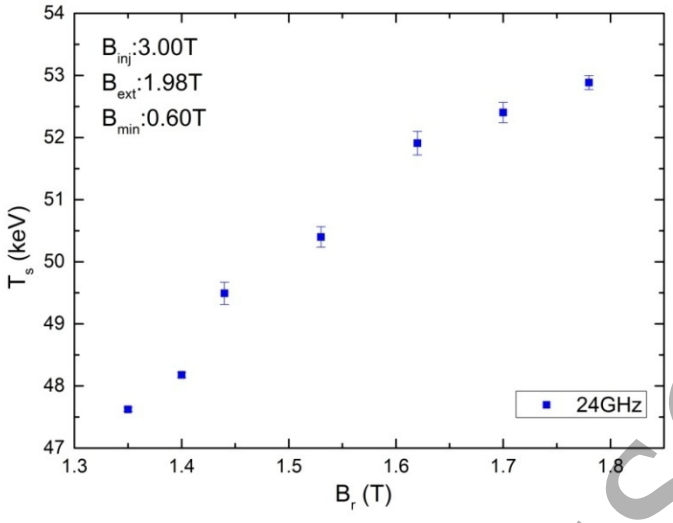

Figure 12: Spectral temperature T_s as a function of B_r. Here B_r is measured in the plane where the radial component of the solenoid field does not affect the hexapole field.

4. Discussion

The experimental results obtained in part one indicate that electron cyclotron instability appears above a threshold B_{min}, which gave us a hint to extend the B_{min} range. Figure 13 presents the summary of T_s versus extended B_{min}/B_{ecr} for two heating frequencies powered separately (18 and 24 GHz) at various magnetic field configurations. It can be seen from this figure that T_s increases approximately linearly with the increasing of B_{min}/B_{ecr} but deviates from this trend (appears to saturate) above a threshold (18 GHz: ~0.79, 24 GHz: ~0.78), i.e. in the regime where electron cyclotron instabilities are detected. This phenomenon can be explained by the fact that the spectral temperature T_s is determined by the hot electron population, and electron cyclotron instabilities would expel a significant fraction of the hot electrons into the loss cone [21]. Once the electron cyclotron instabilities are triggered, the plasma energy content (affected predominantly by the hot electrons) starts to oscillate around a certain average value [34], which is then observed as a saturation of the bremsstrahlung spectral temperature averaged over a large number of instability periods. This finding is also consistent with experimental study [33] on the energy distribution of electrons escaping minimum-B ECR plasmas, it is demonstrated that the average energy of electrons escaping axially from a minimum-B ECRIS grows with the magnetic field up to $B_{min}/B_{ecr} \sim 0.8$ and then saturates.

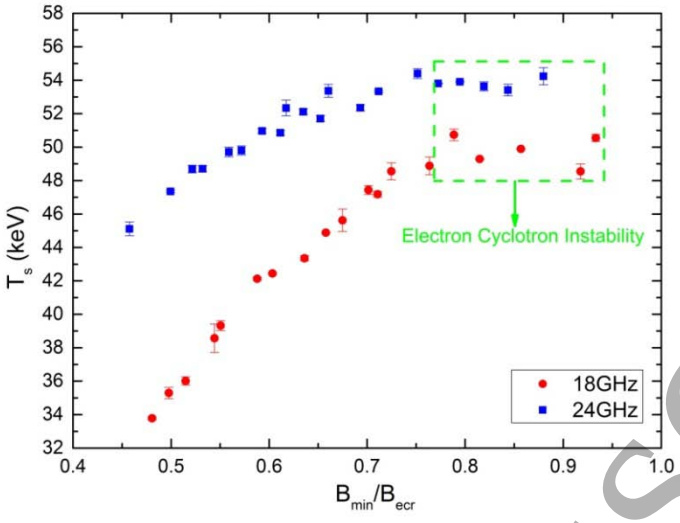

Figure 13: Spectral temperature T_s as a function of B_{min}/B_{ecr}.

Regarding part two, since B_{min} is not directly linked with the electron energy gain in single resonance crossing, conversely, the electron energy gain depends strongly on the magnetic field gradient at the resonance [41, 42]. Furthermore, the effective width of the resonance also depends on the component of the magnetic field gradient [43]. Although the spectral temperature T_s in our experiments is determined by the bremsstrahlung emitted by the electrons near the source axis and the gradient on axis is held approximately constant, one should note that the ECR heating of cold electrons takes place over the whole ECR surface for which the above parameters have been calculated. For relativistic electrons producing bremsstrahlung in the range of 80–200 keV (used for determining T_s) the situation is far more complicated as they are heated everywhere in the discharge volume where the Doppler shifted relativistic resonance condition $B_{\mathrm{ecr}} = \frac{1}{n} B_{ecr,cold}\,\gamma\left(1 \pm N_{||}k_{||}\right)$ is met. Here n is the harmonic number, γ the relativistic Lorentz gamma ($\gamma = 1 + \frac{E_k}{m_e c^2}$), $N_{||}k_{||} = \frac{v_{e,||}}{v_\varphi}$ the ratio of electron longitudinal velocity (with respect to the propagating wave) and the phase velocity of the heating microwave and the $\pm$ sign corresponds to blue- and red-shifted resonances. Hence, it should not be the on-axis gradient, which is commonly used [13, 25, 27] as a parameter to describe the magnetic field configuration of an ECRIS, but rather a global effect that determines the electron heating rate and the bremsstrahlung spectrum. In fact, there is no single parameter that could be used to describe the relativistic electron heating efficiency in Doppler-shifted resonance. In the following we will use the average gradient $< \nabla B_{ecr} > = \langle \left(\left(\vec{B} / |\vec{B}| \right) \cdot \nabla \vec{B} \right)_{ecr,cold} \rangle$ (parallel to the field lines) across the cold electron resonance surface to describe each configuration. This is preferred over the on-axis cold electron resonance gradients because the variation of $< \nabla B_{ecr} >$ is proportional to the variation of the average gradient in the whole discharge volume

where the Doppler-shifted resonance can occur.

Table 1 and figure 14 show that for 18 GHz heating of part two, the calculated [44] $<\nabla B_{ecr}>$ decreases with the increase of B_{min} and accordingly T_s decreases linearly with the increase of $<\nabla B_{ecr}>$. This consequence also applies for those cases in part one and can be used to explain the appearance of electron cyclotron instabilities: since the growth rate of electron cyclotron instabilities is proportional to the ratio of hot and cold electron densities ($\gamma \propto \frac{N_{e,hot}}{N_{e,cold}}$), when increasing B_{min} while keeping the other fields constant, decreasing average gradient over ECR surface (shown in Figure 15) will lead to an increase in the hot electron population due to the more efficient heating process. In other words, it means that the growth rate of electron cyclotron instabilities increases with the increase of B_{min}. This process will continue until the condition that the growth rate is larger than damping rate ($\gamma > \delta$) is reached, then the electron cyclotron instabilities are triggered and T_s stops increasing. It is important to note that both the instability growth and damping rates most likely depend on the magnetic field configuration through the electron energy distribution and varying plasma density and electron loss rates. However, we associate the transition between the stable and unstable regimes with the increase of the instability growth rate rather than the decrease of the damping rate as it has been shown previously that [19] the magnetic field is more influential than the neutral gas pressure (affecting the plasma density) in determining the transition. Based on the above analyses, it may be argued that separating the effect of B_{min} from the effect of $<\nabla B_{ecr}>$ is problematic while considering on the role of average gradient is more coincident with theoretical studies to explain the apparent B_{min} dependence.

Table 1: Ion source characteristics for the study of the average gradient influence on T_s.

f (GHz)	B_r (T)	B_{inj} (T)	B_{min} (T)	B_{ext} (T)	$<\nabla B_{ecr}>$ (T/m)	T_s (keV)
18	1.02	1.13	0.31	1.03	8.74	33.8
		1.21	0.33	1.09	8.38	36.1
		1.32	0.35	1.11	7.97	38.6
		1.57	0.38	1.23	7.67	42.1
		1.82	0.41	1.32	7.17	43.4
		2.12	0.43	1.43	6.79	45.6
		2.46	0.45	1.55	6.62	47.4
		2.65	0.47	1.68	6.32	48.6

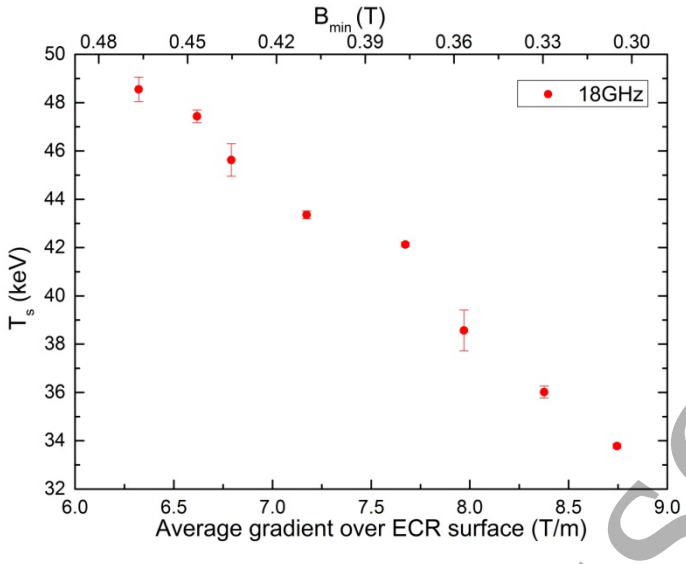

Figure 14: Spectral temperature T_s as a function of the average gradient over ECR surface.

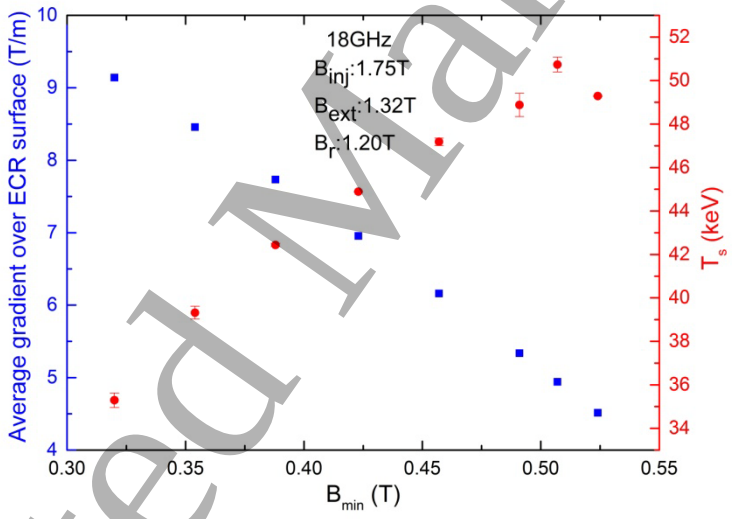

Figure 15: The average gradient over ECR surface and spectral temperature T_s as a function of B_{min}.

For the constant B_{min} cases in part three, similarly, we also take into account the influence of average gradient over ECR surface, it is found that for the 18 GHz heating, both ∇B_{ecr} on axis and $<\nabla B_{ecr}>$ increase with increasing of mirror ratio (see Table 2), hence the changing trend of T_s for these two parameters are the same (shown in Figure 16). It should be noted that in this setting of experiments, when B_{min} is kept constant, the changes of gradient (∇B_{ecr} on axis: 5.15 – 6.95 T/m; $<\nabla B_{ecr}>$: 6.92 – 7.70 T/m) and mirror ratio (B_{max}/B_{min}: 2.65 – 6.03) occur simultaneously, which means that two processes, i.e. electron heating and electron confinement are changed simultaneously.

Table 2: Ion source characteristics for the study of constant B_{min} cases of 18GHz heating.

f (GHz)	B_r (T)	B_{min} (T)	B_{inj} (T)	B_{ext} (T)	∇B_{ecr} on axis (T/m)	$<\nabla B_{ecr}>$ (T/m)
18	1.05	0.40	1.06	1.10	5.15	6.92
			1.14	1.11	5.21	6.95
			1.16	1.12	5.36	6.98
			1.26	1.13	5.60	7.05
			1.49	1.21	5.82	7.13
			1.74	1.29	6.28	7.31
			1.98	1.37	6.64	7.43
			2.23	1.45	6.82	7.57
			2.41	1.50	6.95	7.70

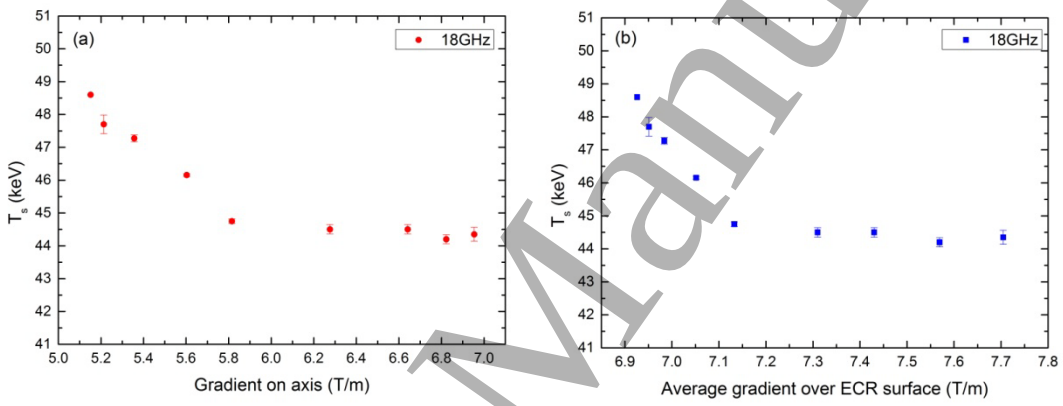

Figure 16: Spectral temperature T_s as a function of gradient on axis (a) and the average gradient over ECR surface (b).

The data in Figure 16 shows that the effect of the average gradient on T_s becomes weaker when $<\nabla B_{ecr}>$ increases, which implies that the electron heating rate alone does not define T_s. This assumption is supported by the influence of B_r on T_s: figure 12 shows that T_s increases with the increase of B_r when the axial magnetic fields are held constant. At the same time the average gradient on the ECR-surface is affected only weakly as shown in Table 3 where the magnetic field strength B_{last} defining the last closed surface takes into account the effect of the radial component of the solenoid field on the hexapole (radial field). Since B_{last} defines the overall magnetic confinement in ECR plasma [13], the result implies that T_s is affected by the electron confinement, not only by electron heating. This conclusion is corroborated by the fact that both, the bremsstrahlung count rate and maximum energy, were observed to increase with the radial field strength (last closed surface).

Table 3: Ion source characteristics for the study of the radial field.

f (GHz)	B_{inj} (T)	B_{min} (T)	B_{ext} (T)	B_r (T)	$< \nabla B_{ecr} >$ (T/m)	B_{last} (T)
24	3.00	0.60	1.98	1.35	9.09	1.05
				1.40	9.13	1.09
				1.44	9.18	1.13
				1.53	9.29	1.21
				1.62	9.39	1.29
				1.70	9.50	1.37
				1.78	9.61	1.45

5. Conclusion

The experimental results of this study show for the first time that the bremsstrahlung spectral temperature T_s increases approximately linearly with the increase of B_{min}/B_{ecr} up to ~ 0.8 and then saturates with the appearance of electron cyclotron instabilities. Based on the earlier analyses in this paper, it is suggested that once the electron cyclotron instabilities are triggered, periodic bursts of energetic electrons escaping the magnetic confinement will limit the increase of the energy content carried by the hot electron population and eventually lead to a saturation of T_s.

Previous studies have typically used either the B_{min} or the on-axis gradient as the only parameter to explain the dependence of T_s on the magnetic configuration. However, as discussed above, B_{min} is not directly linked with the electron energy gain and the on-axis gradient does not reflect the global effect of ECR heating. This study is the first attempt to demonstrate that increasing B_{min} corresponds to decreasing average (parallel) gradient over the ECR surface although the on-axis gradient remains constant, which shows the inherent link between B_{min} and average gradient over the ECR surface, and thus provides a viewpoint that is more coincident with theoretical studies to understand the apparent linear B_{min} dependence and the appearance of electron cyclotron instabilities.

In this study, it also has been shown that T_s decreases with the increasing of gradient (∇B_{ecr} on axis and $< \nabla B_{ecr} >$) at relatively low mirror ratio and is insensitive to the gradient at high mirror ratio when B_{min} is constant, which indicates that T_s depends on not only electron heating, but also depends on electron confinement. This view is supported by the dependence of T_s on the radial confinement. The conclusion is different from the one made in Ref. [25] where the radial field was kept constant and then argued that the T_s depends only on B_{min}.

Acknowledgments

The authors wish to thank J. Benitez and D. Xie of LBNL for helpful discussions. This work has been funded by Chinese Academy of Sciences President's International Fellowship Initiative (Grant No. 2016VTA009) and supported by the NSFC (contract No. 11427904), CAS (contract No. QYZDB-SSW-JSC025) and NSFC (contract No.

11705254).

References

[1] Geller R 1996 *Electron cyclotron resonance ion sources and ECR plasmas* (Bristol: Institute of Physics Publishing)
[2] Geller R 1998 *Rev. Sci. Instrum.* **69** 1302-10
[3] Liu Z W et al. 1998 *Rev. Sci. Instrum.* **69** 685-87
[4] Zhao H W, Wei B W, Liu Z W, Wang Y F and Zhao W J 2000 *Rev. Sci. Instrum.* **71** 646-50
[5] Zhao H W et al. 2002 *Rev. Sci. Instrum.* **73** 525-27
[6] Zhao H W et al. 2004 *Rev. Sci. Instrum.* **75** 1410-13
[7] Zhao H W et al. 2008 *Rev. Sci. Instrum.* **79** 02A315
[8] Lu W et al. 2016 *Rev. Sci. Instrum.* **87** 02A738
[9] Sun L et al. 2016 *Rev. Sci. Instrum.* **87** 02A707
[10] Zhao H W et al. 2018 *Rev. Sci. Instrum.* **89** 052301
[11] Zhao H Y et al. 2006 *Rev. Sci. Instrum.* **77** 03A312
[12] Zhao H Y et al. 2008 *Rev. Sci. Instrum.* **79** 02B504
[13] Zhao H Y et al. 2009 *Plasma Sources Sci. Technol.* **18** 025021
[14]Guo J W, Sun L, Niu X J, Zhang X Z, Lu W, Zhang W H, Feng Y C and Zhao H W 2016 *Rev. Sci. Instrum.* **87** 02A708
[15] Guo J W et al. 2018 *AIP Conference Proceedings* **2011** 090001
[16] Sun L et al. 2018 *AIP Conference Proceedings* **2011** 040022
[17] Lyneis C, Leitner D, Todd D, Virostek S, Loew T, Heinen A and Tarvainen O 2006 *Rev. Sci. Instrum.* **77** 03A342
[18] Thuillier T, Angot J, Benitez J Y, Hodgkinson A, Lyneis C M, Todd D S and Xie D Z 2016 *Rev. Sci. Instrum.* **87** 02A736
[19] Tarvainen O et al. 2014 *Plasma Sources Sci. Technol.* **23** 025020
[20] Tarvainen O, Laulainen J, Komppula J, Kronholm R, Kalvas T, Koivisto H, Izotov I, Mansfeld D and Skalyga V 2015 *Rev. Sci. Instrum.* **86** 023301
[21] Tarvainen O et al. 2016 *Rev. Sci. Instrum.* **87** 02A703
[22] Barue C, Briand P, Girard A, Melin G and Briffod G 1992 *Rev. Sci. Instrum.* **63** 2844-46
[23] Girard A 1992 *Rev. Sci. Instrum.* **63** 2676-82
[24] Baskaran R, Selvakurnaran T S, Rodrigues G, Kanjilal D and Roy A 2008 *Rev. Sci. Instrum.* **79** 02A324
[25] Benitez J, Lyneis C, Phair L, Todd D and Xie D 2017 *IEEE Trans. Plasma Sci.* **45** 1746-54
[26] Leitner D, Benitez J Y, Lyneis C M, Todd D S, Ropponen T, Ropponen J, Koivisto H and Gammino S 2008 *Rev. Sci. Instrum.* **79** 033302
[27] Noland J, Tarvainen O, Benitez J, Leitner D, Lyneis C and Verboncoeur J 2011 *Plasma Sources Sci. Technol.* **20** 035022
[28] Sun L et al. 2020 *Rev. Sci. Instrum.* **91** 023310
[29] http://amptek.com/products/xr-100cdte-x-ray-and-gamma-ray-detector/
[30] Bernhardi K and Wiesemann K 1982 *Plasma Phys. Controlled Fusion* **24** 867-84
[31] X-5 Monte Carlo Team 2003 *MCNP- A General Monte Carlo N-Particle Transport Code, Version 5* (NM: Los Alamos National Laboratory)
[32] Perret C, Girard A, Khodja H and Melin G 1999 *Physics of Plasmas* **6** 3408-15

[33] Izotov I, Tarvainen O, Skalyga V, Mansfeld D, Kalvas T, Koivisto H and Kronholm R 2018 *Plasma Sources Sci. Technol.* **27** 025012

[34] Shalashov A G, Gospodchikov E D, Izotov I V, Mansfeld D A, Skalyga V A and Tarvainen O 2018 *Epl* **124** 35001

[35] Ginzburg V L 1970 *The propagation of electromagnetic waves in plasmas* (Oxford: Pergamon Press)

[36] Golubev S V and Shalashov A G 2007 *Phys. Rev. Lett.* **99** 205002

[37] Golubev S V and Shalashov A G 2007 *JETP Lett.* **86** 91-97

[38] Trakhtengerts V Y and Rycroft M J 2008 *Whistler and Alfven mode cyclotron masers in space* (Cambridge: Cambridge University Press)

[39] Izotov I, Tarvainen O, Mansfeld D, Skalyga V, Koivisto H, Kalvas T, Komppula J, Kronholm R and Laulainen J 2015 *Plasma Sources Sci. Technol.* **24** 045017

[40] Naselli E et al. 2019 *Plasma Sources Sci. Technol.* **28** 085021

[41] Canobbio E 1969 *Nucl. Fusion* **9** 27-47

[42] Gammino S, Mascali D, Celona L, Maimone F and Ciavola G 2009 *Plasma Sources Sci. Technol.* **18** 045016

[43] Williamson M C, Lichtenberg A J and Lieberman M A 1992 *J. Appl. Phys.* **72** 3924-33

[44] Vaughan J R M 1972 *IEEE Trans. Electron Devices* **Ed19** 144-151

PII

INFLUENCE OF AXIAL MIRROR RATIOS ON THE KINETIC INSTABILITY THRESHOLD IN ELECTRON CYCLOTRON RESONANCE ION SOURCE PLASMA

by

Toivanen, V and Bhaskar, BS and Koivisto, H and Maunoury, L and Tarvainen, O and Thuillier, T 2022

Physics of Plasmas **29**, 1 013501

Influence of axial mirror ratios on the kinetic instability threshold in electron cyclotron resonance ion source plasma

Cite as: Phys. Plasmas **29**, 013501 (2022); https://doi.org/10.1063/5.0069638
Submitted: 01 September 2021 • Accepted: 08 December 2021 • Published Online: 03 January 2022

V. Toivanen, B. S. Bhaskar, H. Koivisto, et al.

Physics of Plasmas ARTICLE scitation.org/journal/php

Influence of axial mirror ratios on the kinetic instability threshold in electron cyclotron resonance ion source plasma

Cite as: Phys. Plasmas **29**, 013501 (2022); doi: 10.1063/5.0069638
Submitted: 1 September 2021 · Accepted: 8 December 2021 ·
Published Online: 3 January 2022

View Online Export Citation CrossMark

V. Toivanen,[1,a)] B. S. Bhaskar,[1,2] H. Koivisto,[1] L. Maunoury,[3] O. Tarvainen,[1,4] and T. Thuillier[2]

AFFILIATIONS

[1]Department of Physics, University of Jyväskylä (JYFL), 40500 Jyväskylä, Finland
[2]Univ. Grenoble Alpes, CNRS, Grenoble INP, LPSC-IN2P3, 38000 Grenoble, France
[3]Grand Accélérateur National d'Ions Lourds (GANIL), 14076 Caen Cedex 5, France
[4]STFC ISIS Pulsed Spallation Neutron and Muon Facility, Rutherford Appleton Laboratory, Harwell OX11 0QX, United Kingdom

[a)]**Author to whom correspondence should be addressed:** ville.a.toivanen@jyu.fi

ABSTRACT

Electron Cyclotron Resonance (ECR) ion source plasmas are prone to kinetic instabilities. The onset of the instabilities manifests as emission of microwaves, bursts of electrons expelled from the plasma volume, and the collapse of the extracted highly charged ion (HCI) currents. Consequently, the instabilities limit the HCI performance of ECR ion sources by limiting the parameter space available for ion source optimization. Previous studies have shown that the transition from stable to unstable plasma regime is strongly influenced by the magnetic field structure, especially the minimum field value inside the magnetic trap (B_{min}). This work focuses to study the role of the magnetic confinement on the onset of the kinetic instabilities by probing the influence of the injection and extraction mirror field variation on the instability threshold. The experiments have been performed with a room-temperature 14.5 GHz ECR ion source with an axially movable middle coil that provides flexible control over the axial field profile and especially the B_{min}, which was used to quantify the variation in the instability threshold. The experimental results show that variation of the extraction field B_{ext}, which defines the weakest magnetic mirror, correlates systematically with the variation of the instability threshold; decreasing the B_{ext} allows higher threshold B_{min}. The result demonstrates the importance of electron confinement and losses on the plasma stability. The connection between the weakest mirror field and the onset of instabilities is discussed taking into account the variation of magnetic field gradient and resonance plasma volume.

I. INTRODUCTION

Kinetic instabilities are found in various types of space and laboratory plasmas[1–11] characterized by anisotropic electron energy distribution (EED) and run-away hot electron population. It has been shown experimentally that such non-linear phenomena affect the plasma confinement in minimum-B quadrupole mirror machines[12,13] and electron cyclotron resonance ion sources (ECRIS)[14] with combined solenoid and sextupole fields. In the case of ECRIS, the appearance of the instabilities is accompanied by reduced currents of extracted high charge state ion beams,[15] which is explained by the periodic particle losses shortening the cumulative ion confinement time, thus disturbing the production of high charge state ions through stepwise ionization.

The instability is triggered by the stored electron energy accumulated[16] into the anisotropic EED with $v_{\perp} \gg v_{\parallel}$ (with respect to the confining magnetic field) and a (local) positive slope of the EED, i.e., $\frac{df(E)}{dE} > 0$. The threshold between stable and unstable plasma regimes is affected by electron heating and electron losses implying that the transition into the unstable maser regime is determined by the microwave power, neutral gas density and most importantly the magnetic field. It has been experimentally shown that in terms of the instability threshold the most influential magnetic field parameter of an ECRIS, operated with a single frequency i.e., constant B_{ECR}, is the value of the magnetic field minimum B_{min}.[17,18] When the ratio $B_{\mathrm{min}}/B_{\mathrm{ECR}}$, where B_{ECR} is the cold electron resonance field satisfying the resonance condition with the plasma heating microwave frequency $\omega_{\mathrm{RF}} = \frac{eB_{\mathrm{ECR}}}{m_e}$, exceeds a certain value, kinetic instabilities emerge. Hence, it has been argued[19] that the transition from stable to unstable plasma regime could explain the rule-of-thumb in ECRIS design, derived from the semi-empirical scaling laws[20] (see also references therein), stating that

$B_{min}/B_{ECR} \leq 0.8$. Furthermore, it has been shown that the absolute value of B_{min} correlates with the spectral temperature of plasma bremsstrahlung emission,[21] which indicates that it is the most influential parameter affecting the plasma energy content $n_e\langle E_e\rangle$.

In the pulse-periodic instability regime, the build-up and sudden release of the plasma energy content alternate in periodic cycle leading to burst of microwaves, electrons, and ions from the plasma[14] whereas it has been recently demonstrated[22] that the turbulent regime can be controlled by carefully tuning the ECRIS into a continuous plasma maser mode characterized by quasi-CW emission of microwaves and enhanced fluxes of electrons and highly charged ions. In other words, it has been demonstrated that the magnitude and repetition rate of individual instability events is affected by the particle loss rate, not only the electron heating rate. This leads to the hypothesis that the instability threshold, i.e., the transition from stable to pulse-periodic instability regime, can be controlled by adjusting the fluxes of hot electrons determined by the RF scattering rate and mirror ratios of the axial and radial loss cones as discussed by Li *et al.*[18] The magnetic field of modern ECR ion sources is designed on the basis of semi-empirical scaling laws setting desired values for the injection, radial, and extraction fields, i.e., $B_{inj} > 4B_{ECR}$, $B_{rad} > 2B_{ECR}$ and $B_{ext} \approx 0.9B_{rad}$.[20] Therefore, the scaling laws imply that the weakest magnetic mirror defining the *global loss cone* in $(v_{\parallel}, v_{\perp})$-phase space is the extraction field. It has been shown that the electron flux escaping through the extraction aperture (mirror) of an ECRIS can be increased by more than a factor of two by decreasing the extraction field B_{ext} by 15%,[23,24] which suggests that the total electron loss rate and/or the distribution of electron losses can be controlled by adjusting the weakest mirror. Based on the field topology and experimental evidence on electron losses it is argued that the extraction field could presumably affect the instability threshold, i.e., the exact B_{min}/B_{ECR}-ratio at which instabilities appear. This paper describes experiments, conducted with a room-temperature 14.5 GHz ECRIS, probing the influence of the injection and extraction fields on the B_{min} threshold of the instabilities. Following the previous arguments, it is expected that the impact of the injection field variation on the instability threshold is much weaker than the variation of the extraction field, arising from the high B_{inj}/B_{ext} ratio and how the axial losses are consequently directed mainly toward the extraction.

It is noted here that the condition that the extraction field is the weakest mirror is not necessary fulfilled for every ECR ion source, as it depends on the details of the ion source magnetic design, especially the hexapole magnet structure and the solenoid coils which provide the radial and axial confinement, respectively. In a minimum-B structure, the radial magnetic field at the chamber wall B_{rad} is not a constant set only by the hexapole; the axial coils generate a radial magnetic field component which can locally oppose the hexapole radial field along the poles of the hexapole. Depending on the ECRIS design, the local field at wall can be reduced by $10-20$ % by this effect.[25] Hence, even with the condition $B_{ext} \approx 0.9B_{rad}$ seemingly fulfilled when only the hexapole field is considered, in some cases the weakest magnetic mirror can still be at the radial wall.

The paper is organized as follows: the experimental setup and procedure are described in detail in Sec. II. The experimental results targeting to determine the relation between the axial mirror fields and the onset of plasma instabilities are presented in Sec. III, followed by a discussion in Sec. IV where we also present an outlook on how the experimental findings accompanied by earlier results could guide the ECRIS design in the future.

II. EXPERIMENTAL SETUP AND PROCEDURE

The effect of various magnetic field parameters on the maser-type instability could be best studied with superconducting ECR ion sources where the field strength and topology can be adjusted more than with room-temperature ion sources. On the other hand, the power density (microwave power/volume enclosed by the cold electron ECR zone) is typically higher in room-temperature sources and varies less with the magnetic field adjustments, which alleviates the trouble of multiple source parameters affecting the data. In both source types the instability experiments, where the magnetic mirrors are adjusted, are complicated by the fact that changing the currents of the large bore solenoid coils not only affects the mirror field, e.g., B_{ext}, but also the distribution of magnetic field gradient on the resonance surface, plasma volume enclosed by the resonance zone and distance between the resonance zone and magnetic mirror, all of them potentially acting on the EED.

The GTS (Grenoble Test Source) ECRIS[26] was chosen for the study of comparing the importance of injection and extraction fields on the B_{min}-threshold of the instability as it is one of the most flexible room-temperature ECRISs in terms of adjusting the field profile. This is largely owing to the construction of three solenoid coils with the middle coil being axially movable. In addition, the GTS Halbach-style hexapole provides a relatively high radial field of $B_{rad} = 1.2$ T at the poles on the plasma chamber wall, which helps to ensure that the weakest magnetic mirror is located at the source extraction (see the discussion at the end of this section). GTS was originally developed by CEA Grenoble and it has been operated at GANIL (Grand Accélérateur National d'Ions Lourds) since 2009. The source, currently working with 14.5 GHz plasma heating frequency, delivers multiply charged heavy ion beams for the low energy physics experiments of the ARIBE (Accélérateurs pour les Recherches Interdisciplinaires avec les Ions de Basse Energie) facility. The mechanical configuration of GTS at the time of the experiments discussed in this paper is presented in Fig. 1.

During 2016–2018 a number of refurbishments and upgrades were implemented to GTS in order to improve its performance.[27] Among these a new middle coil was installed between the main injection and extraction coils to provide more flexibility and control for adjusting the magnetic confinement of the ion source plasma. The middle coil axial location can be varied 28.5 mm from the geometric center position between the main coils toward the injection or 26.5 mm toward the extraction side of the source (see Fig. 2). The movement is limited by the mechanical construction of the middle coil support and the iron yokes of the injection and extraction coils. Three middle coil positions were used in the experiments; (1) the geometric axial center between the injection and the extraction coils (coinciding with the hexapole mid-plane, called later *center position*), (2) the coil set all the way toward the injection (*injection position*) and (3) the coil set all the way toward the extraction (*extraction position*). During this campaign, the middle coil polarity was set to be the same as the injection and extraction coils. In this configuration increase in the middle coil current increases the B_{min}. An example of the resulting axial magnetic field profiles with the three different middle coil positions is presented in Fig. 3. In all the presented cases the injection,

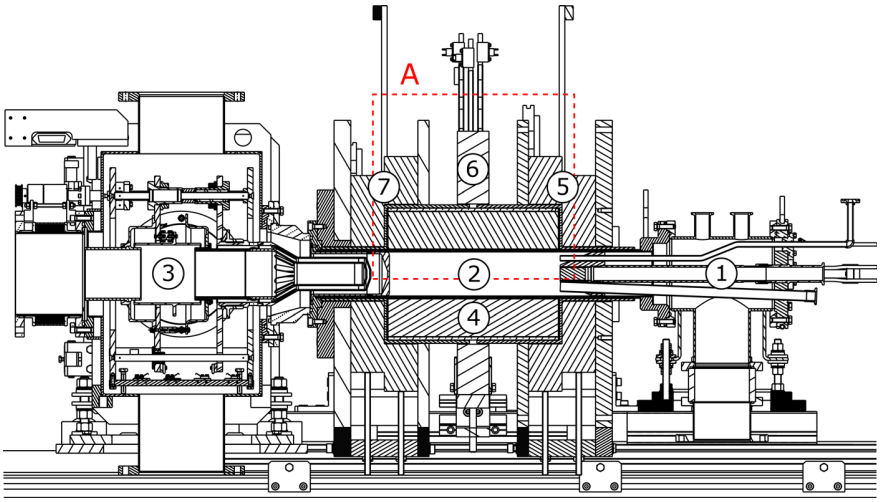

FIG. 1. A schematic of the GTS ECR ion source. The main components of the source include the injection system for microwave and gas delivery (1), the plasma chamber (2) and the beam extraction system comprising of a puller electrode and an einzel lens (3). The magnetic structure consists of a hexapole magnet (4) and the injection, the middle and the extraction coils (5, 6, and 7). The injection and extraction coils are divided into two separate pancake structures with different inner and outer radii. The section marked with (a) is shown in Fig. 2 to present the different positions of the middle coil.

middle and extraction coil currents are kept at 950, 330, and 950 A, respectively. As is seen in the figure, moving the middle coil between the two extreme positions (injection and extraction) shifts the axial location of B_{min} about 5 mm (approximately 4% of the axial length of the ECR surface for cold electrons). Varying the middle coil position has also a minor effect on the extraction and injection mirror fields; moving the coil from the center position to the extraction or the injection positions causes a variation of about $\pm 0.6\%$ to B_{ext} and about $\pm 0.3\%$ to B_{inj} with these coil currents.

The experiments were performed with neon plasma. For the base tuning in stable plasma regime GTS was operated with 400 W microwave power, −100 V bias disk voltage and 10 kV extraction voltage. In order to allow flexibility for the magnetic field variation, the ion source coils were not optimized for the production of any specific ion charge state, i.e., the device was operated in a "plasma trap" rather than ion source mode. In the initial stable plasma tuning the middle coil was set to zero and both the injection and the extraction coil currents were set to 950 A, which corresponds to $B_{inj} = 1.97$ T, $B_{ext} = 0.97$ T, and $B_{min} = 0.33$ T.

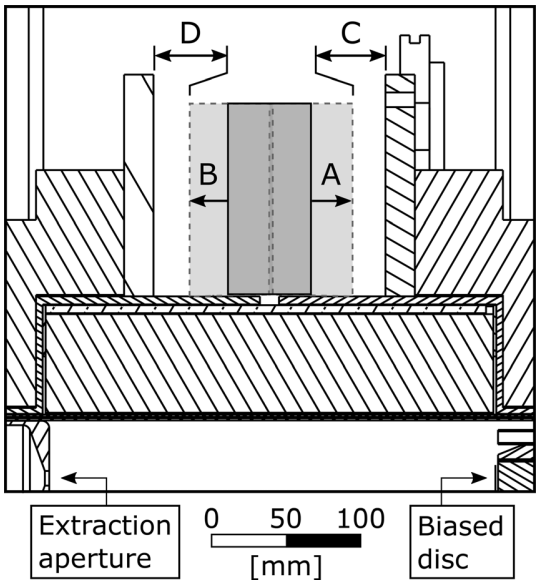

FIG. 2. The axial movement range of the GTS middle coil. The shown section is marked with (a) in Fig. 1. The coil can be moved from the geometric center position (i.e., hexapole mid-plane) 28.5 mm toward the injection (a) or 26.5 mm toward the extraction (b). In the injection position the coil is 22 mm from the iron yoke (c). In the extraction position the distance is 24 mm (d). The middle coil axial length is 57 mm. The extraction aperture and the biased disk are also indicated.

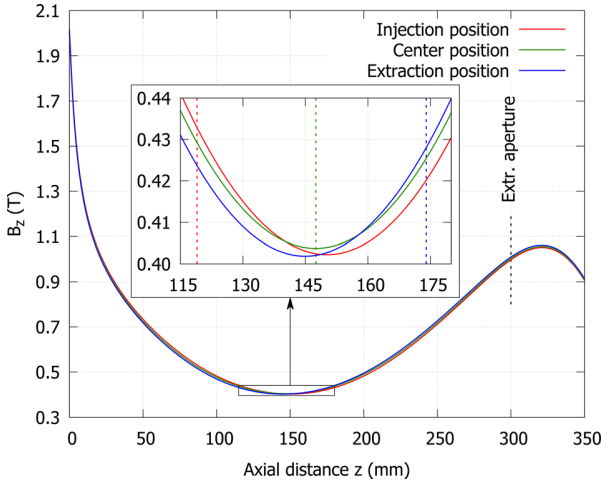

FIG. 3. Axial magnetic field profiles with the three different middle coil positions with the injection, middle and extraction coil currents set to 950, 330, and 950 A, respectively. The field profiles have been calculated with RADIA software[28,29] using a 3D magnetic model of the GTS ECRIS. The axial location $z = 0$ mm is the surface of the biased disk at the injection end of the plasma chamber. The location of the extraction aperture, which defines the B_{ext} mirror field value for plasma confinement, is also indicated. The dashed vertical lines in the subplot indicate the axial locations of the middle coil mid-plane for the different coil positions.

The axial location for the B_{inj} is defined by the surface of the biased disk at the injection end of the plasma chamber and the B_{ext} location is defined by the extraction aperture (see Fig. 2). With the baseline settings the source produced a stable 10 μA beam of $^{20}Ne^{7+}$, which, being a high charge state, suffers notably when the plasma transitions into the unstable regime.

The occurrence of plasma instabilities was monitored with two BGO (bismuth germanate) x-ray detectors placed inside the axial radiation cones on the injection and the extraction sides of the ion source. In addition, the time evolution of the extracted beam current of $^{20}Ne^{7+}$ was monitored with an oscilloscope through a Keithley picoammeter connected to a Faraday cup downstream from the q/m analyzing magnet. The onset of the plasma instabilities was determined from the appearance of periodic x-ray bursts which correlate with the time structure of the extracted beam current, as discussed in the Introduction section. Examples of instability-induced x-ray and beam current signals, similar to those used here to detect the transition into unstable regime, can be found e.g., in Ref. 14.

Three sets of measurements were performed for each of the three middle coil positions. First, the injection coil current was varied in discrete steps from 950 to 1200 A (corresponding to B_{inj} variation from 1.97 to 2.17 T) while keeping the extraction coil constant at 950 A. For each injection coil current the B_{min} was increased by adjusting the middle coil current until the instability threshold was reached. Next, the injection coil current was kept constant at 950 A and the extraction coil current was varied from 950 to 1100 A (B_{ext} from 0.97 to 1.09 T), again finding the instability threshold B_{min} by changing the middle coil current. Finally, both the injection and the extraction coil currents were varied simultaneously from 950 to 1100 A, corresponding to B_{inj} : 1.97 T → 2.11 T and B_{ext} : 0.97 T → 1.09 T, yet again finding the instability threshold B_{min} with the middle coil. In all the cases the injection and extraction coil currents were varied with fixed 25 A increments, resulting to data sets with linearly increasing B-field for the varied axial mirrors (B_{inj}, B_{ext} or both). The maximum coil currents were determined by the maximum output of the coil power supplies.

As discussed before, the radial component of the magnetic field generated by the injection, extraction and middle coils influences the total radial field on the plasma chamber walls, which causes a variation to the radial confinement when the coil currents and the middle coil position is varied. To quantify this effect, the total magnetic field on the plasma chamber wall was calculated for all the measured cases. The minimum total field on the poles of the hexapole magnet, which defines the radial mirror for the plasma confinement, was 10 − 22 % higher than B_{ext} in all the measured cases. This means that B_{ext} is always globally the weakest mirror.

III. EXPERIMENTAL RESULTS

The experimental results are presented in Figs. 4–6 for the three different middle coil positions. Each figure presents the threshold B_{min} for the plasma instability, above which the plasma is unstable, when either the injection, the extraction, or both of the coil currents are varied. The B_{inj} and B_{ext} range values presented in the figures correspond to the lowest and highest coil current values for each coil(s) sweep with the middle coil set at the B_{min} threshold value. The errors in the figures for the B_{min} threshold values are based on the size of the

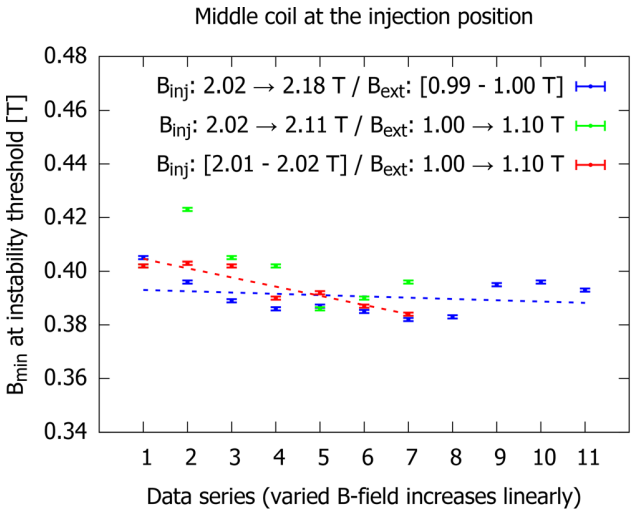

FIG. 4. B_{min} at the instability threshold with the middle coil at the injection position. Injection (blue), extraction (red) and both (green) coils were varied in steps in the different data series resulting to linear increase in the varied mirror fields over the ranges presented in the legend. The varied mirror field is indicated with an arrow in the legend between the first and the last field value of the sweep, while the range of field variation of the unaltered mirror (constant coil current) at the instability threshold B_{min} is presented in brackets. Trend lines of the instability threshold variation for the injection and the extraction coil sweeps are presented with dashed lines.

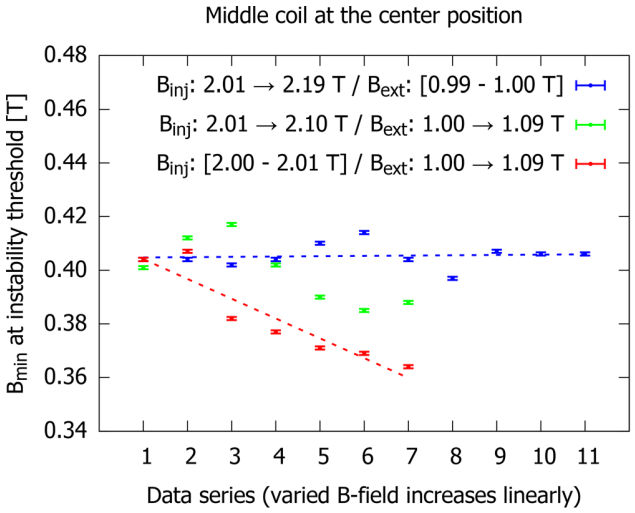

FIG. 5. B_{min} at the instability threshold with the middle coil at the center position. Injection (blue), extraction (red), and both (green) coils were varied in steps in the different data series resulting to linear increase in the varied mirror fields over the ranges presented in the legend. The varied mirror field is indicated with an arrow in the legend between the first and the last field value of the sweep, while the range of field variation of the unaltered mirror (constant coil current) at the instability threshold B_{min} is presented in brackets. Trend lines of the instability threshold variation for the injection and the extraction coil sweeps are presented with dashed lines.

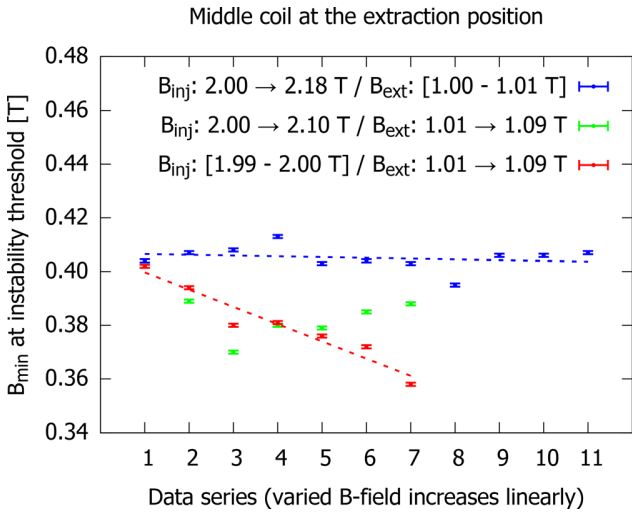

FIG. 6. B_{min} at the instability threshold with the middle coil at the extraction position. Injection (blue), extraction (red), and both (green) coils were varied in steps in the different data series resulting to linear increase in the varied mirror fields over the ranges presented in the legend. The varied mirror field is indicated with an arrow in the legend between the first and the last field value of the sweep, while the range of field variation of the unaltered mirror (constant coil current) at the instability threshold B_{min} is presented in brackets. Trend lines of the instability threshold variation for the injection and the extraction coil sweeps are presented with dashed lines.

current step in the middle coil (typically a few amperes) during which a clear transition from stable to unstable plasma regime was observed.

When the middle coil is set to injection position, see Fig. 4, varying the injection and extraction mirror fields has a relatively weak effect on the instability threshold value of B_{min}. In all cases (either sweeping the injection, extraction, or both coils) a slight decrease in the B_{min} threshold value is observed with increasing field values.

Figure 5 presents the results with the middle coil at the center location. Varying the injection field has practically no effect on the instability threshold B_{min}-value, whereas increasing the extraction field results in a clear decrease in the B_{min} threshold. A decrease in the threshold value is also observed when both the injection and the extraction fields are increased simultaneously.

Results with the middle coil at the extraction position are presented in Fig. 6. Like in the center position case, no systematic change of the B_{min} threshold for the instabilities is observed with the variation of the injection field. When the extraction field or both the injection and the extraction fields are increased, a clear decrease in the instability threshold B_{min} is found.

IV. DISCUSSION

The experimental results show that increasing the extraction mirror field strength leads to the instability threshold to occur at lower B_{min} values, whereas the variation of the injection mirror has no or only a weak effect on the threshold. The observation implies that the EED of the confined electrons is affected more by the extraction than the injection field, which could be either due to the B-field acting on the electron confinement or on the ECR heating (e.g., by affecting the field gradient at the resonance). We argue that changing electron confinement by the adjustment of the weakest magnetic mirror is the most likely explanation for the observed effect. It is emphasized that transition between stable and unstable regimes is dominated by B_{min}, which appears to be the most influential magnetic field parameter acting on the anisotropy and hot tail of the EED, thus determining the instability threshold, whereas the control of electron losses and/or heating through the adjustment of the weakest mirror is a secondary effect offering the possibility to fine-tune the transition.

Distributions of fast electrons gaining their energy through ECR heating are usually unstable with respect to excitation of electromagnetic waves in the same frequency range.[30] The amplification of the excited EM-wave (observed as a burst of microwave emission) is determined by the balance between the instability growth and damping rates, which are defined by the electron energy and velocity distributions. These are in turn affected by the plasma density, power absorption and electron confinement in an inherently complex manner. It has been shown experimentally[23,24] that adjusting B_{ext} by 10% (similar to the experiment reported here) has a significant impact on the electron flux escaping the ion source through the extraction aperture. This is arguably due to the mirror ratio $R = \frac{B_{max}}{B_{min}}$ of the magnetic configuration affecting the escape probability p of electrons as $p = a(1 - \sqrt{1 - \frac{1}{R}})$, where a is the isotropy factor of the electron velocity distribution ($a = 1$ for perfectly isotropic EVD and $a < 1$ when $v_\perp > v_\parallel$). The above proportionality implies that if B_{ext} is increased from 1.0 to 1.1 T with B_{min} of 0.4 T, the probability for electrons to escape through the extraction mirror decreases by approximately 10%, i.e., more energy is accumulated in the EED, which makes the instabilities more likely to appear. The stability can be restored by lowering B_{min}, which is the most influential magnetic field parameter affecting the appearance of the instabilities. The fact that lowering B_{ext} allows higher B_{min} at the instability threshold could make it possible to optimize the high charge state beam currents, which tend to increase with B_{min} until the transition from stable to unstable regime occurs.[19]

Thus far, we have only discussed how the extraction mirror (B_{ext}) presumably affects the instability threshold B_{min} through electron confinement. However, since the EED is affected not only by the electron confinement but also by the electron heating characteristics, both aspects discussed from experimental standpoint e.g., in Ref. 18, we need to consider how the magnetic field adjustment in our experiment is likely to affect the electron heating and plasma energy content.

The volumetric power absorption $\langle P_{abs} \rangle$ by the electrons in the absence of collisions is inversely proportional to the difference between the resonance field B_{ECR} and the local magnetic field B to the square as $\langle P_{abs} \rangle \propto 1/(B_{ECR} - B)^2$ as discussed in Ref. 31. Therefore, the electron energy gain in each resonance crossing depends strongly on the parallel magnetic field gradient at the resonance, $\frac{\vec{B}}{|B|} \cdot \nabla \vec{B}$, as discussed by many authors.[31–33] We have calculated the average parallel gradient $\langle \nabla B_{ECR} \rangle_\parallel$ on the (cold electron) ECR surface with the coil currents at the observed instability threshold. Figure 7 shows the average gradient as a function of B_{min} at the instability threshold with various mid-coil positions when the extraction coil current is swept causing the extraction field (B_{ext}) to change from 1.0 to 1.1 T with the injection field remaining constant. It is seen that the average gradient increases with increasing B_{ext} with all mid-coil positions. Thus, following the argument that the electron heating rate decreases with increasing gradient, it could be expected that increasing B_{ext} would result in higher B_{min} at

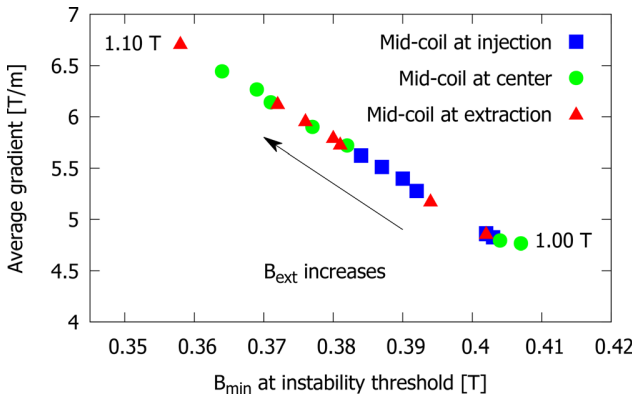

FIG. 7. The average magnetic field gradient parallel to the magnetic field on the (cold electron) resonance as a function of B_{min} at the instability threshold with different middle coil position when the extraction coil current (B_{ext}) is varied keeping the injection coil current (B_{inj}) constant.

the instability threshold. The trend in Fig. 7 is exactly the opposite suggesting that the electron confinement (defined by the strength of the weakest mirror field, B_{ext}, in this case) overpowers the effect of the gradient determining the B_{min} threshold value.

The spatial distribution of hot electrons in ECRIS plasmas has been studied both numerically and experimentally[34–36] and it has been concluded that the majority of the plasma energy content is carried by the electron population in the dense plasmoid surrounded by the ECR surface. As the instabilities are driven by the local EED, it could be argued that the volume enclosed by the resonance zone therefore affects the B_{min} at the instability threshold. Figure 8 shows the volume enclosed by the (cold electron) resonance as a function of B_{min} at the instability threshold with various mid-coil positions when the extraction coil current is swept similar to Fig. 7. The volume increases with increasing B_{ext} with all mid-coil positions. If the instability threshold was to be determined by the volumetric effect, an opposite trend, i.e., increased energy density leading to lower B_{min} threshold value, would be expected.

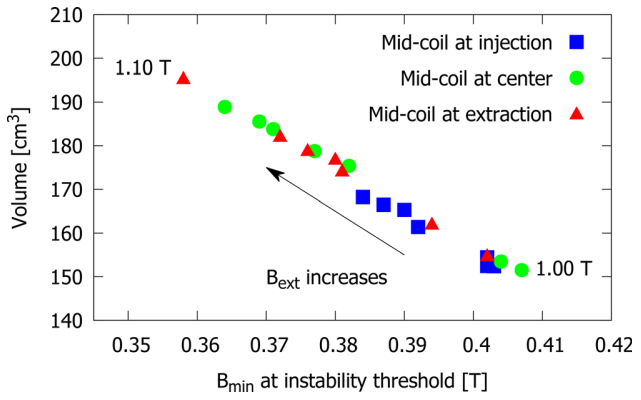

FIG. 8. The volume enclosed by the (cold electron) resonance zone as a function of B_{min} at the instability threshold with different middle coil position when the extraction coil current (B_{ext}) is varied keeping the injection coil current (B_{inj}) constant.

Considering both, the gradient and volume effects, and concluding that neither one of them matches the experimental observation strengthens the argument that the electron confinement plays an important role in determining the transition between stable and unstable discharge regimes.

Previous studies[14] have shown that the source potential (extraction voltage) also influences the instability threshold, and applying the potential shifts the threshold to lower B_{min}/B_{ECR} values. This effect is not yet completely understood, but the source potential does also influence the axial electron confinement, as it creates an electrostatic barrier at the extraction which suppresses the axial electron losses toward this direction for electron energies below the limit set by the potential. For example, in the experiments presented here the source potential was set to 10 kV, which consequently stops the axial electron losses toward the extraction for electrons with energies below 10 keV. As a result, the electron losses are drastically reduced, impacting the properties of the confined electron population. This then affects the ion population in plasma, as has been shown with optical measurements of ECR plasma.[37]

The connection between the electron confinement and the onset of the instabilities opens up the prospect of a more active control over the electron losses during ECRIS operation to suppress the plasma instabilities and optimize the source performance. In a typical ECRIS the adjustment of the magnetic system with the currents of large-bore coils impacts globally the field structure inside the plasma chamber, influencing both the plasma confinement and the plasma heating through the variation of the magnetic gradient and the plasma volume, as discussed above. However, because the instability transition can be argued to be especially sensitive to the strength of the weakest mirror, as the results presented here imply, a local modification of the B-field near this position with an additional localized magnetic system could be used to control the electron losses from the plasma without significantly disturbing the global magnetic field properties. Additionally, this would also enhance the ion flux from the plasma toward extraction and beam formation. In effect, this approach could provide an additional "tuning knob" for the instabilities without restricting the parameter space for magnetic field optimization in terms of ion production. One option to realize this local control could be to install an additional compact coil close to the extraction mirror. Studies with plasma electrode collar structures[38,39] have shown that inside an ECRIS plasma chamber there exists an amount of space around the extraction aperture which can be utilized without negatively impacting the source performance. A compact coil structure fixed in this location would be well positioned to provide a localized and adjustable modification to the extraction mirror field to control the electron losses. It is acknowledged that for practical reasons designing such a compact coil to operate continuously in vacuum with sufficiently high currents to provide significant impact on the magnetic field could be challenging. However, such a structure could provide benefits also when operated in pulsed mode, which simplifies the design. In this mode it could be used also to enhance extracted high charge state ion currents in afterglow operation. The PUMAEX (Pulsed Magnetic Extraction) experiments[40,41] have shown that a pulsed magnetic coil structure located at the extraction end of an ECRIS plasma chamber can be used to direct the plasma flux toward the beam extraction by temporarily decreasing the magnetic confinement in that region. Combining this approach with pulsed afterglow operation, the local control over the

magnetic confinement would make it possible to keep the mirror fields high during the steady state of the plasma heating cycle to accumulate a large population of highly charged ions in the plasma by mitigating the ion losses during this phase. At the cutoff of the microwaves the magnetic trap could then be emptied more efficiently by simultaneously "opening" the trap toward the extraction by a local modification of the magnetic field, providing a further enhancement of the highly charged ion currents during the afterglow burst.

Instead of a coil, the local modification of the magnetic confinement could also be realized with movable permanent magnet (or soft iron) structures to allow local adjustment of the electron losses. Although potentially simpler than the coil method, careful magnetic design would still be required to optimize the design. The main downside of these approaches is that unlike a coil, once the modifications are installed, their magnetic influence can not be easily switched off completely.

ACKNOWLEDGMENTS

This work has been supported by the Academy of Finland Project funding (No. 315855) and University of Grenoble Alpes under the EMERGENCE program.

AUTHOR DECLARATIONS

Conflict of interest

The authors have no conflicts to disclose.

DATA AVAILABILITY

The data that supports the findings of this study are available within the article.

REFERENCES

[1]R. Thorne, "Radiation belt dynamics: The importance of wave–particle interaction," Geophys. Res. Lett. **37**, L22107, https://doi.org/10.1029/2010GL044990 (2010).
[2]D. Gurnett, "The Earth as a radio source: Terrestrial kilometric radiation," J. Geophys. Res. **79**, 4227–4238, https://doi.org/10.1029/JA079i028p04227 (1974).
[3]M. Panchenko, H. Rucker, and W. Farrell, "Periodic bursts of Jovian non-Io decametric radio emission," Planet. Space Sci. **77**, 3–11 (2013).
[4]D. Melrose and G. Dulk, "Electron-cyclotron masers as the source of certain solar and stellar radio bursts," Astrophys. J. **259**, 844–858 (1982).
[5]J. Nichols, M. Burleigh, S. Casewell, S. Cowley, G. Wynn, J. Clarke, and A. West, "Origing of electron cyclotron maser induced radio emissions at ultracool dwarfs: Magnetospehere-ionosphere coupling currents," Astrophys. J. **760**, 1–9 (2012).
[6]W. Ard, R. Dandl, and R. Stetson, "Observations of instabilities in electron–cyclotron plasmas," Phys. Fluids **9**, 1498 (1966).
[7]V. Alikaev, V. Glagolev, and S. Morozov, "Anisotropic instability in a hot electron plasma, contained in an adiabatic trap," Plasma Phys. **10**, 753–774 (1968).
[8]A. Shalashov and E. Suvorov, "On cyclotron emission from toroidal plasmas near the ECR heating frequency," Plasma Phys. Controlled Fusion **45**, 1779 (2003).
[9]J. Cook, R. Dendy, and S. Chapman, "Particle-in-cell simulations of the magnetoacoustic cyclotron instability of fusion-born alpha-particles in tokamak plasmas," Plasma Phys. Controlled Fusion **55**, 065003 (2013).
[10]R. Post and W. Perkins, "Velocity-space plasma instabilities observed in a mirror machine," Phys. Rev. Lett. **6**, 85 (1961).
[11]A. Demekhov and V. Trakhtengerts, "Several questions on radiation dynamics in magnetic plasma traps," Radiophys. Quantum Electron. **29**, 848–857 (1986).
[12]R. Garner, M. Mauel, S. Hokin, R. Post, and D. Smatlak, "Warm electron-driven whistler instability in an electron-cyclotron-resonance heated, mirror-confined plasma," Phys. Rev. Lett. **59**, 1821 (1987).
[13]R. Garner, M. Mauel, S. Hokin, R. Post, and D. Smatlak, "Whistler instability in an electron-cyclotron-resonance-heated, mirror-confined plasma," Phys. Fluids B **2**, 242 (1990).
[14]O. Tarvainen, I. Izotov, D. Mansfeld, V. Skalyga, S. Golubev, T. Kalvas, H. Koivisto, J. Komppula, R. Kronholm, J. Laulainen, and V. Toivanen, "Beam current oscillations driven by cyclotron instabilities in a minimum-B electron cyclotron resonance ion source plasma," Plasma Sources Sci. Technol. **23**, 025020 (2014).
[15]O. Tarvainen, T. Kalvas, H. Koivisto, J. Komppula, R. Kronholm, J. Laulainen, I. Izotov, D. Mansfeld, V. Skalyga, V. Toivanen, and G. Machicoane, "Limitation of the ecris performance by kinetic plasma instabilities (invited)," Rev. Sci. Instrum. **87**, 02A703 (2016).
[16]A. Shalashov, S. Golubev, E. Gospodchikov, D. Mansfeld, and M. Viktorov, "Interpretation of complex patterns observed in the electron-cyclotron instability of a mirror confined plasma produced by an ECR discharge," Plasma Phys. Controlled Fusion **54**, 085023 (2012).
[17]I. Izotov, A. Shalashov, V. Skalyga, E. Gospodchikov, O. Tarvainen, V. Mironov, H. Koivisto, R. Kronholm, V. Toivanen, and B. Bhaskar, "The role of radio frequency scattering in high-energy electron losses from minimum-B ECR ion source," Plasma Phys. Controlled Fusion **63**, 045007 (2021).
[18]J. Li, L. Li, B. Bhaskar, V. Toivanen, O. Tarvainen, D. Hitz, L. Li, W. Lu, H. Koivisto, T. Thuillier, J. Guo, X. Zhang, H. Zhao, L. Sun, and H. Zhao, "Effects of magnetic configuration on hot electrons in a minimum-B ECR plasma," Plasma Phys. Controlled Fusion **62**, 095015 (2020).
[19]O. Tarvainen, J. Laulainen, J. Komppula, R. Kronholm, T. Kalvas, H. Koivisto, I. Izotov, D. Mansfeld, and V. Skalyga, "Limitations of electron cyclotron resonance ion source performances set by kinetic plasma instabilities," Rev. Sci. Instrum. **86**, 023301 (2015).
[20]D. Hitz, A. Girard, G. Melin, S. Gammino, G. Ciavola, and L. Celona, "Results and interpretation of high frequency experiments at 28 GHz in ECR ion sources, future prospects," Rev. Sci. Instrum. **73**, 509–512 (2002).
[21]J. Benitez, C. Lyneis, L. Phair, D. Todd, and D. Xie, "Dependence of the bremsstrahlung spectral temperature in minimum-B electron cyclotron resonance ion sources, future prospects," IEEE Trans. Plasma Sci. **45**, 1746–1754 (2017).
[22]V. Skalyga, I. Izotov, A. Shalashov, E. Gospodchikov, E. Kiseleva, O. Tarvainen, H. Koivisto, and V. Toivanen, "Controlled turbulence regime of electron cyclotron resonance ion source for improved multicharged ion performance," J. Phys. D: Appl. Phys. **54**, 385201 (2021).
[23]I. Izotov, O. Tarvainen, V. Skalyga, D. Mansfeld, T. Kalvas, H. Koivisto, and R. Kronholm, "Measurement of the energy distribution of electrons escaping minimum-B ECR plasmas," Plasma Sources Sci. Technol. **27**, 025012 (2018).
[24]B. S. Bhaskar, H. Koivisto, O. Tarvainen, T. Thuillier, V. Toivanen, T. Kalvas, I. Izotov, V. Skalyga, R. Kronholm, and M. Marttinen, "Correlation of bremsstrahlung and energy distribution of escaping electrons to study the dynamics of magnetically confined plasma," Plasma Phys. Controlled Fusion **63**, 095010 (2021).
[25]T. Thuillier, J. Angot, J. Y. Benitez, A. Hodgkinson, C. M. Lyneis, D. S. Todd, and D. Z. Xie, "Investigation on the electron flux to the wall in the VENUS ion source," Rev. Sci. Instrum. **87**, 02A736 (2016).
[26]D. Hitz, D. Cormier, J. Mathonnet, A. Girard, G. Melin, F. Lansaque, K. Serebrenikov, and L. Sun, "Grenoble test source GTS: A multipurpose room temperature ECRIS," *in* Proceedings of the 15th International Workshop on Electron Cyclotron Resonance Ion Sources, Jyväskylä, Finland (2002).
[27]V. Toivanen, C. Barué, C. Feierstein, P. Jardin, F. Lemagnen, L. Maunoury, F. Noury, and P. Rousseau, "Upgrade of the GTS electron cyclotron resonance ion source at GANIL," AIP Conf. Proc. **2011**, 040008 (2018).
[28]P. Elleaume, O. Chubar, and J. Chavanne, "Computing 3d magnetic fields from insertion devices," in *Proceedings of the 1997 Particle Accelerator Conference (Cat. No. 97CH36167), Vancouver, Canada* (IEEE, 1997), pp. 3509–3511.
[29]See http://www.esrf.eu/Accelerators/Groups/InsertionDevices/Software/Radia for "Radia Software Website" (last accessed October 21, 2021).
[30]A. Shalashov, E. Gospodchikov, and I. Izotov, "Electron-cyclotron heating and kinetic instabilities of a mirror-confined plasma: The quasilinear theory revised," Plasma Phys. Controlled Fusion **62**, 065005 (2020).
[31]M. Williamson, A. Lichtenberg, and M. Lieberman, "Self–consistent electron cyclotron resonance absorption in a plasma with varying parameters," J. Appl. Phys. **72**, 3924 (1992).

[32]E. Canobbio, "Gyroresonant particle acceleration in a non-uniform magnetostatic field," Nucl. Fusion **9**, 27 (1969).
[33]S. Gammino, D. Mascali, L. Celona, F. Maimone, and G. Ciavola, "Considerations on the role of the magnetic field gradient in ECR ion sources and build-up of hot electron component," Plasma Sources Sci. Technol. **18**, 045016 (2009).
[34]D. Mascali, L. Neri, L. Celona, G. Castro, G. Torrisi, S. Gammino, G. Sorbello, and G. Ciavola, "A double-layer based model of ion confinement in electron cyclotron resonance ion source," Rev. Sci. Instrum. **85**, 02A511 (2014).
[35]V. Mironov, S. Bogomolov, A. Bondarchenko, A. Efremov, V. Loginov, and D. Pugachev, "Spatial distributions of plasma potential and density in electron cyclotron resonance ion source," Plasma Sources Sci. Technol. **29**, 065010 (2020).
[36]R. Rácz, S. Biri, J. Pálinkás, D. Mascali, G. Castro, C. Caliri, L. Neri, F. Romano, and S. Gammino, "Structural information on the ECR plasma by x-ray imaging," in Proceedings of the 22nd International Workshop on Electron Cyclotron Resonance Ion Sources, Busan, Korea (2016).
[37]R. Kronholm, T. Kalvas, H. Koivisto, and O. Tarvainen, "Spectroscopic method to study low charge state ion and cold electron population in ECRIS," Rev. Sci. Instrum. **89**, 043506 (2018).
[38]V. Toivanen, O. Tarvainen, J. Komppula, and H. Koivisto, "The effect of plasma electrode collar structure on the performance of the JYFL 14 GHz electron cyclotron resonance ion source," Nucl. Instrum. Methods Phys. Res., Sect. A **726**, 41–46 (2013).
[39]V. Mironov, J. Beijers, H. Kremers, J. Mulder, S. Saminathan, and S. Brandenburg, "ECRIS development at KVI," in Proceedings of the 19th International Conference on Cyclotrons and Their Applications, Lanzhou, China (2010).
[40]L. Müller, A. Heinen, H. Ortjohann, and H. Andrä, "Magnetic pulsed extraction of highly charged ions from a plateau ECRIS," Rev. Sci. Instrum. **73**, 1140 (2002).
[41]L. Müller, B. Albers, A. Heinen, M. Kahnt, L. Nowack, H. Ortjohann, A. Täschner, C. Vitt, S. Wolosin, and H. Andrä, "The new MÜNSTER 18 GHz plateau-ECRIS," in Proceedings of the 15th International Workshop on Electron Cyclotron Resonance Ion Sources, Jyväskylä, Finland (2002).

PIII

CORRELATION OF BREMSSTRAHLUNG AND ENERGY DISTRIBUTION OF ESCAPING ELECTRONS TO STUDY THE DYNAMICS OF MAGNETICALLY CONFINED PLASMA

by

Bhaskar, BS and Koivisto, H and Tarvainen, O and Thuillier, T and Toivanen, V and Kalvas, T and Izotov, I and Skalyga, V and Kronholm, R and Marttinen, M
2021

Plasma Physics and Controlled Fusion **63**, 9 095010

Correlation of bremsstrahlung and energy distribution of escaping electrons to study the dynamics of magnetically confined plasma

B.S. Bhaskar*[1,2] , H. Koivisto[1], O. Tarvainen[3,1], T. Thuillier[2], V. Toivanen[1], T. Kalvas[1], I. Izotov[4], V. Skalyga[4], R. Kronholm[1], M. Marttinen[1]

[1] University of Jyväskylä, Department of Physics, PO Box 35 (YFL), 40500 Jyväskylä, Finland

[2]LPSC, Université Grenoble-Alpes, CNRS/IN2P3, 53 rue des Martyrs, 38026 Grenoble Cedex, France

[3]STFC ISIS Pulsed Spallation Neutron and Muon Facility, Rutherford Appleton Laboratory, Harwell, OX11 0QX, UK

[4]Institute of Applied Physics of Russian Academy of Sciences, 603950, Nizhny Novgorod, Russia.

E-mail: *bisubhas@jyu.fi

Abstract. A combination of electron and bremsstrahlung diagnostics was used to study the properties of the highly charged plasma of an Electron Cyclotron Resonance (ECR) ion source. The bremsstrahlung radiation in both axial and radial directions was correlated with the energy distribution of the electrons escaping axially from the confined plasma, i.e. the Lost Electron Energy Distribution (LEED), to achieve a more comprehensive view of the plasma. The evolution of the bremsstrahlung spectra and the LEED were determined as a function of the main operating parameters of the ion source. Also, the effects of the transition from a stable to an unstable plasma regime were determined for the bremsstrahlung and LEED. Changes in the shape of the measured LEED were found to correlate with changing bremsstrahlung spectral temperature. It was also found that the magnetic field has a strong impact on the axial and radial bremsstrahlung spectra and the LEED, affecting the bremsstrahlung intensity, spectral temperatures and the LEED high energy local maximum. A comprehensive discussion is provided to explain the observed different behaviour of axial and radial bremsstrahlung emissions with varying magnetic field based on the directionality of plasma bremsstrahlung in ECRIS specific magnetic confinement scheme. Furthermore, it was observed that the onset of kinetic plasma instabilities has a clear impact on the shape of the LEED.

1. Introduction

Electron Cyclotron Resonance Ion Sources (ECRISs) are used in production of Highly Charged Ions (HCIs) for undertaking various researches. In an ECRIS, HCIs are produced in non-equilibrium plasma confined in a magnetic structure. The magnetic confinement is realised by a superposition of solenoid and hexapole magnetic fields, thus creating a minimum-B confinement topology[1], that is, it consists of nested Iso-$|B|$ closed surfaces. The hot electron plasma is created by injecting microwave radiation interacting with the electrons crossing a $|B|$ surface where the magnetic field satisfies the relativistic resonance condition

$$B_{\mathrm{ECR}} = \frac{B_{\mathrm{ECR,cold}}}{h}\gamma(1-\delta), \tag{1}$$

where the cold electron resonance field $B_{\mathrm{ECR,cold}}$ is 0.5 T for 14 GHz microwaves, h is the harmonic number of the resonance, $\gamma = 1 + \frac{E_k}{m_e c^2}$ the relativistic Lorentz factor and $\delta = \frac{\pm v_{\|}}{v_\phi}$. Here $v_{\|}$ is the longitudinal (with respect to external magnetic field) electron velocity with the negative and positive signs corresponding to the blue and red Doppler shifts, respectively, v_ϕ is the phase velocity of the wave and E_k and $m_e c^2$ are the electron kinetic and rest mass energies. Gas or vaporised metals are introduced into the plasma chamber where they undergo step-by-step ionisation in inelastic (ionising) collisions with warm electrons. The well confined hot electron population is believed to create an electrostatic potential structure [2] in such a way that the ions are electrostatically trapped and thus reside in the discharge long enough for high charge state production [1]. This high energy electron population is also responsible for limiting the performance of ECR ion sources as it increases the heat load of the cryostat in superconducting ion sources through high energy x-ray production [3, 4] and makes the plasma kinetically unstable, which in turn affects the ion confinement and extracted beam currents of HCIs [5].

Bremsstrahlung measurements have been used previously by many authors as a basic diagnostic tool for (indirectly) studying parametric dependencies of the high energy electron population in ECRIS plasmas. These studies can be characterised based on whether or not the obtained results provide spatially and/or temporally resolved information, as well as based on the origin of the measured bremsstrahlung (plasma emission, thick target radiation induced by escaping electrons). Techniques resulting to volume integrated and time averaged results have been used most widely to probe the general plasma properties [6, 7, 8, 9, 10, 11, 12, 13, 14, 15, 16], but there has been also significant development in the use of spatially [17, 18] and temporally [19] resolved methods. However, unambiguous de-convolution of either thick-target (wall) or plasma bremsstrahlung spectra to obtain the Electron Energy Distribution (EED) of the escaping or confined electrons is seemingly impossible despite some notable efforts [13, 20, 21]. This motivates simultaneous study of the bremsstrahlung emission and the energy distribution of the electrons escaping from the confinement to further validate numerous conclusions on the electron dynamics drawn from the cited bremsstrahlung studies as reported hereafter. The main purpose of this experiment is to gain understanding of axial and radial bremsstrahlung spectra and their correlation with the electron energy distribution of electrons lost from the confinement through the extraction

mirror. The Lost Electron Energy Distribution (LEED) is different from the EED of confined electrons in plasma [22] whereas the parametric dependencies of the two can be argued to correlate with each other. The correlation between the axial bremsstrahlung spectra and LEED has been recently studied by Isherwood *et al.* [23]. The present work expands on their experiments by using calibrated transmission of electrons through the low energy beam line, thereby allowing the LEED to be corrected for transmission losses, along with a comparison of axial and radial bremsstrahlung measurements. The parametric effects on axial and radial bremsstrahlung have been studied previously by Noland *et al.* [24]. Our work corroborates those results and adds the axial LEED to comprehensively explain the observed tendencies.

The appearance of kinetic instabilities in ECRIS plasmas has been under extensive investigation recently [25, 26, 27, 28] as it has been found that such non-linear effects can be a major limitation for HCI production with ECR ion sources. Our work has also focused on the behaviour of the bremsstrahlung spectra and the LEED in different plasma stability regimes. Since the kinetic instability is driven by the anisotropy in the EEDF, we have measured how the LEED changes with the onset of the instability, first published by Izotov *et al*. [29] and most importantly whether or not one can anticipate the occurrence of instability by measuring the time-averaged bremsstrahlung emission, the latter being a widely used [30, 31, 32] non-invasive technique allowing normal operation of the ion source contrary to the LEED measurement.

2. Experimental setup

The experiments were performed with the JYFL 14 GHz ECRIS [33] in the accelerator laboratory of the Department of Physics, University of Jyväskylä (JYFL). The ion source is constructed with two solenoid coils and a Nd-Fe-B permanent magnet hexapole array to provide a minimum-B structure for electron heating and plasma confinement. The magnetic field of the ion source can be varied by adjusting the injection and the extraction coil currents, which affects the axial mirror ratios, minimum-B and the field on the plasma chamber wall (radial mirror ratio) through the radial component of the solenoid field. The nominal on-axis magnetic field maxima in the injection (B_{inj}) and extraction (B_{ext}) and the minimum field (B_{min}) are 1.93 T, 0.90 T and 0.35 T, respectively. In the experiments presented here B_{inj} was varied between 1.87 T and 2.06 T, B_{ext} between 0.86 T and 1.00 T and B_{min} between 0.32 T and 0.41 T. Additional details of the magnetic field structure are presented in the Supplementary material.

Plasma electrons are heated with 14.055 GHz microwaves. The microwave power required to sustain the discharge is provided by a klystron amplifier and is injected into the plasma chamber using a direct off-axis waveguide coupling scheme. The source can also be operated using a secondary frequency provided by a Travelling Wave Tube Amplifier (TWTA) with a bandwidth of 7.5 GHz to 18 GHz [34] through another waveguide port. The pressure inside the ion source is monitored using a Penning gauge connected to one of the radial ports of the plasma chamber. Due to its position, the gauge provides a relative measure of the chamber pressure, not the absolute value inside the chamber. The reproducibility of the

pressure setting between measurements is good, typically within 5 % in the studied pressure range. The baseline pressure was monitored between measurements to ensure that it stayed at a constant level.

The ion beam is normally extracted by connecting a high voltage power supply between the plasma chamber and the grounded beam line. The extracted beam is focused with an Einzel lens and a solenoid, and steered with an XY magnet through a 90 degree dipole magnet into a Faraday cup. A schematic layout of the setup is shown in Fig. 1.

In the experiments described here, the ion source and the beam line were modified to operate in such a way that only electrons escaping from the magnetic confinement via the extraction aperture were allowed to propagate through the dipole magnet. This was achieved by grounding the source and reversing the polarity of the dipole. It must be noted that with this approach the electrons were not actively extracted from the plasma, but rather they were allowed to leak through the extraction electrode together with ions and were subsequently transported through the beam line. Apart from the dipole, all other beam line elements were either removed or turned off and grounded to prevent accumulation of charge on floating extraction electrodes. A secondary electron amplifier was placed downstream from the dipole, which was then used as an energy dispersive separator for the extracted electrons. The LEED measurement scheme has been first introduced by Izotov *et al.* [35].

Along with the electron detection system, a setup to measure both the axial and the radial bremsstrahlung emitted by the plasma was constructed. A more detailed description of the bremsstrahlung and electron detection systems is given in the following sections.

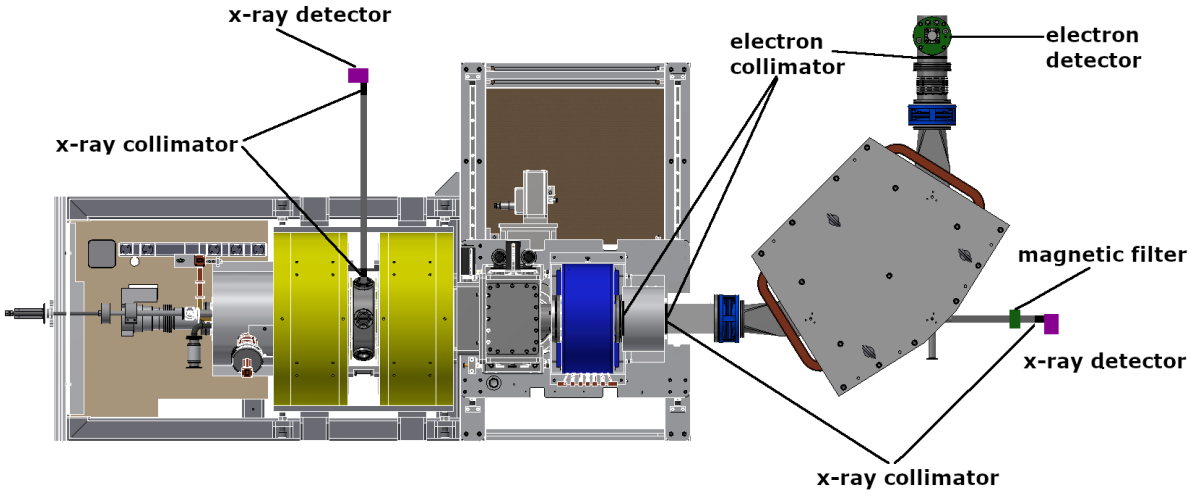

Figure 1. The JYFL 14 GHz ECR ion source and the diagnostics setup used in the measurements.

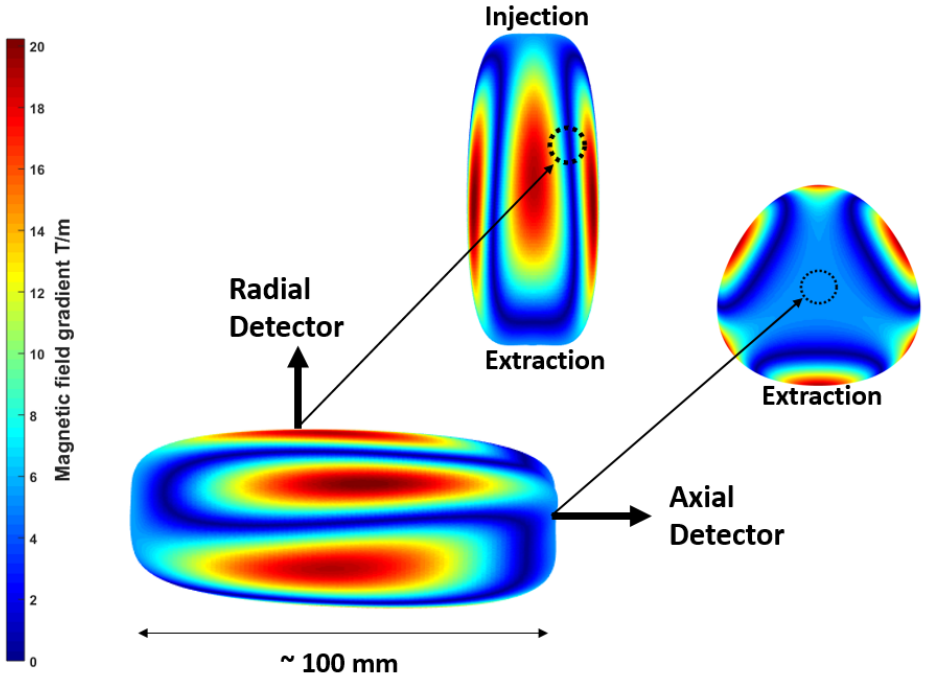

Figure 2. The field of views visible to the x-ray detectors projected to the cold electron resonance zone. The colour scale corresponds to the magnetic field gradient parallel to the field lines for B_{min}/B_{ECR} corresponding to 0.64. The location of the radial field of view with respect to the ECR surface depends on the coil currents.

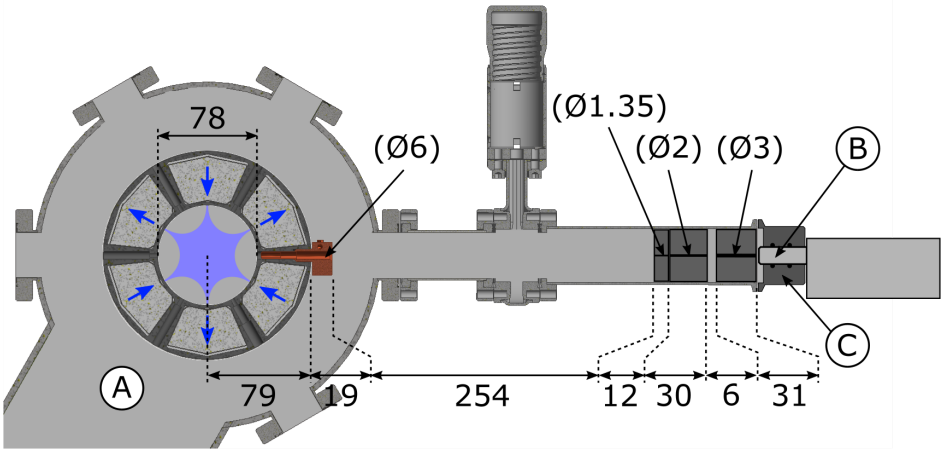

Figure 3. The collimation setup used in the radial bremsstrahlung measurements. The collimator structure is connected to one of the six radial ports of the ion source pumping chamber (A) which houses the plasma chamber and hexapole magnet structure. A copper collimator is placed on the outer edge of this structure. The head of the x-ray detector (B) is inside the ion source vacuum, placed behind three lead collimators through a vacuum feedthrough (C). All dimensions are presented in mm.

2.1. Plasma bremsstrahlung diagnostics

The bremsstrahlung emitted by the ion source plasma was measured with an Amptek XR-100CdTe detector [36]. It is a thermoelectrically cooled x-ray detector which features a Cadmium Telluride (CdTe) diode and a beryllium window, making it compatible for measurements in vacuum in the energy range from 1.5 keV to several hundreds of keV, depending on the chosen gain level. The same gain value was used for all axial measurements, with another value used for all the radial measurement due to higher count rate. Separate energy calibration was done for both gain levels. The efficiency calibration of the detector is based on the calibration data provided by Amptek and the high energy part of the calibration function was further corrected using known x-ray emitters. The characteristic peaks of americium-241 and barium-133 samples with known decay activities were used for the energy and efficiency calibrations. Further details of the calibration procedure is presented in the Supplementary material. The same detector was used to measure the plasma bremsstrahlung both in the axial and the radial directions and it was kept in the vacuum.

In the axial measurement, the detector was installed in the alignment port of the dipole magnet to provide a direct line of sight into the ion source plasma through the extraction aperture. In order to protect the detector from charged particles potentially propagating through the dipole magnet port (when the dipole is not energised), a permanent magnet filter (~ 0.11 T) was placed in front of the detector. Without any added shielding the detector would measure not only the bremsstrahlung spectrum of the photons emitted from the confined plasma but also the bremsstrahlung produced by the plasma electrons colliding with the plasma chamber walls and the bremsstrahlung produced by the extracted electrons if they collide with the dipole chamber walls. A proper collimation is therefore required to make sure that the obtained spectrum is predominantly from the confined plasma and not distorted by secondary photons generated by the interaction of the primary signal with matter located around the line of sight. The collimation setup was designed in such a way that the cross section of the detector's field of view at the extraction electrode was limited to a circle with a maximum diameter of ~ 8 mm, which matches the diameter of the extraction aperture. Figure 1 shows the location of the collimators, where the first lead collimator (5 mm aperture, 12 mm thick) was placed in between the focusing solenoid and the XY steering magnet. A second set of lead collimators (a combination of two separate pieces; first 12 mm thick with 1.35 mm aperture, second 30 mm thick with 2 mm aperture) were placed in front of the x-ray detector. The detector field of view projected onto the cold electron resonance zone calculated for typical coil currents used in the experiments is shown in Fig. 2. The colour scale in the figure represents the magnetic field gradient parallel to the field lines, i.e. $\left(\frac{\vec{B}\cdot\nabla\vec{B}}{|\vec{B}|}\right)$.

Another collimation setup, presented in detail in Fig. 3, was used for the radial bremsstrahlung measurements. The plasma chamber has six radial pumping ports, one between each of the poles of the hexapole magnet structure. These ports are located at the axial centre of the plasma chamber. One of these ports was dedicated for the radial bremsstrahlung diagnostics, to which the collimation setup was connected (see Figs. 1 and 2). The first part of the setup consisted of a 19 mm thick copper block with 6 mm diameter aperture, which was

situated at the base of the radial port, on the outer edge of the plasma chamber and hexapole structure (see Fig. 3). It blocks approximately 75 % of x-ray radiation with a maximum energy of 500 keV. In addition, similar to the axial case, the collimation scheme in front of the radial x-ray detector included a 12 mm thick lead collimator with 1.35 mm diameter aperture followed by 30 mm and 31 mm thick lead blocks with 2 mm and 3 mm diameter aperture sizes, respectively. The collimation setup provided a field of view from the detector to the entrance to the plasma chamber of $4.310^{-3} sr.$ with a half angle of 0.67 deg. This matches well with the dimensions of the radial port opening to the plasma chamber, which is a rectangular slot of 18.6 mm by 6 mm. The radial detector field of view projected onto the cold electron resonance zone calculated for typical coil currents used in the experiments is also shown in Fig. 2. It is worth noting that the detector line-of-sight is directed between the magnetic poles on the opposite side of the plasma chamber, which minimises the contribution of thick target bremsstrahlung since the electron energy does not intercept with the chamber wall at this location.

The given collimator geometries translate to $17\,\mathrm{cm}^3$ and $2.6\,\mathrm{cm}^3$ plasma chamber volumes visible to the axial and radial detectors, respectively. The plasma volumes are relevant for calculating the average volumetric emission rates of plasma bremsstrahlung as described by Sakildien et al. [37] for characteristic x-ray emission. In this paper we have not calculated the absolute value of the volumetric emission because it would be associated with a large uncertainty due to the spatial variation of plasma parameters and the contribution of wall bremsstrahlung.

As a result of a very tight collimation, the measured photon count rate was always less than 250 counts/second and the dead time of the detector during the measurement was always very low, yielding insignificant error in the measured output. The effect of pile-up events on the measured spectrum is therefore deemed negligible. The acquisition time for each spectrum was 1200 s for the axial measurement and 900 s for the radial measurement. The signal shaping time of the detector was $1\mu s$ in both cases.

2.2. Electron diagnostics

The energy distribution of the lost electrons was measured using the beam line dipole as an energy dispersive separator and detecting the electrons downstream from the dipole with a secondary electron amplifier. The amplifier functions by emitting secondary electrons from an aluminium cathode, which was biased to -3.5 kV, thus prohibiting the detection of electrons with energy less than 3.5 keV. The secondary electron signal is subsequently amplified by a chain of meshes and the final electron current is detected at the grounded anode. The electron current signal was further amplified with a transimpedance amplifier (Stanford Research Systems SR570) [38] converting the current signal to a voltage signal [35].

The polarity of the dipole was reversed compared to normal operation to grant electrons passage. The dipole current was ramped and the corresponding magnetic field was measured with a calibrated Hall probe. The dipole was ramped linearly for 45 seconds to scan a range of $0-8$ mT (i.e electron energy range of $0-1.4$ MeV). The sweep was repeated 5 times

and then averaged to achieve the final result. The magnetic field signal was recorded with a Picoscope (model 5444B)[39] in synchronisation with the electron signal to construct the electron energy distribution.

Since the transmission efficiency of the electrons through the beam line is energy dependent, a correction function is necessary for the measured electron energy distribution. This was calculated following the procedure originally presented in Ref. [35], including the corrections for the energy dependent yield of the secondary electrons and electron back scattering at the amplifier cathode. This procedure requires a specifically collimated electron beam to accurately determine the beam transport through the beam line. Three aluminium collimators (10 mm thick with 5 mm aperture) were used for this purpose. The first two were located downstream from the focusing solenoid and the XY steering magnet, respectively, and the third one was placed in front of the secondary electron amplifier (see Fig.1). The second electron collimator downstream from the ion source also doubled as an x-ray collimator (discussed in the previous section), featuring an additional 12 mm thick lead section integrated into the aluminium collimator.

2.3. Plasma instability diagnostics

During the electron and bremsstrahlung measurements, the stability of the ion source plasma was also monitored by detecting intense microwave and bremsstrahlung bursts originating from the plasma [26]. This emission of microwave bursts releasing the stored energy carried by the anisotropy in Electron Velocity Distribution (EVD) of confined electrons [40] followed by x-ray bursts is the signature of kinetic instabilities [26, 27].

The bremsstrahlung bursts induced by the electron cyclotron instability were detected using an x-ray scintillator composed of Bismuth Germanate (BGO) coupled with sodium doped caesium iodide photo multiplier tube [26] which was connected directly to an oscilloscope (Tektronix MSO 72504 DX) with 1 MΩ input impedance. The detector measures the temporal variation of the wall bremsstrahlung power flux, namely the bursts caused by instability-induced electron losses. In such configuration the scintillator can be used for distinguishing between the stable and pulse-periodic instability regimes. The signal level is affected (non-linearly) by the photomultiplier bias voltage, which was carefully adjusted together with the oscilloscope trigger level to observe the transition between the plasma regimes during the parameter sweeps, in particular the magnetic field sweep.

In order to detect the microwave emission [26], a Quarter-Wave Monopole antenna [41] was connected to a spectrum analyser (Rohde & Schwarz ZVL13) [42]. The spectrum analyser served as an instability detector and it was also used to determine the frequencies of the continuous microwave emissions which are observed in the very high B_{min}/B_{ECR} regime [41] where the instability mechanism switches into a continuous plasma maser emission as described by Shalashov *et al.* [43, 44] and discussed later in the text. Here, B_{min} is the magnetic field minimum inside the plasma chamber and B_{ECR} corresponds to the magnetic field at cold electron resonance. In the experiments described here the sweep time of the spectrum analyser was kept at 160 ms with a resolution bandwidth of 3 MHz .

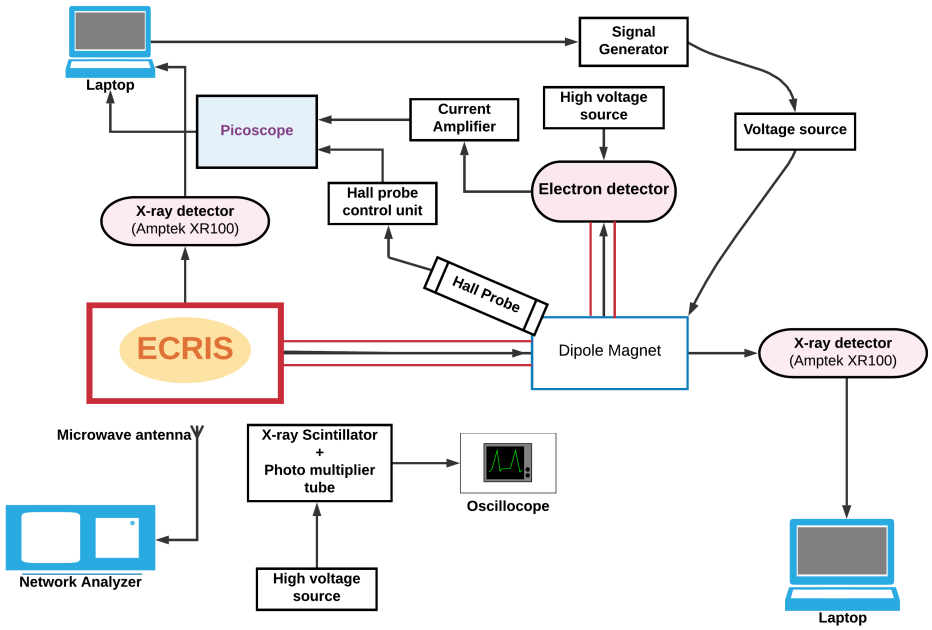

Figure 4. Schematic of the measurement setup and the flow diagram of the data acquisition system.

3. Experimental procedure and results

The bremsstrahlung spectra and the LEED were measured as a function of the microwave power, the neutral gas pressure and the magnetic field strength. The last part of the investigation was carried out in stable and unstable plasma regimes. The flow diagram of the data acquisition setup is shown in Fig. 4. All experiments described hereafter were carried out with oxygen plasma and the biased disk potential was fixed at -70 V for all the measurements. The axial bremsstrahlung spectra and the LEED were measured simultaneously, whereas the radial bremsstrahlung spectra was measured in a different instance due to limited availability of x-ray detectors. It is acknowledged that measuring the axial and radial bremsstrahlung emissions separately introduces some uncertainty because the plasma conditions are not completely reproducible. Compromising the ion source vacuum between the two campaigns can be expected to have some effect on the neutral gas pressure, which has very small effect on the bremsstrahlung and LEED characteristics even if varied across a significant range (as demonstrated later). On the other hand, the magnetic field dependence of the plasma parameters has been found very much reproducible. Thus, we estimate that the reproducibility of the plasma parameters between the axial and radial bremsstrahlung measurement campaigns introduces an uncertainty on the order of 10% as a maximum. This is smaller than the typical statistical error of the bremsstrahlung measurement at high x-ray energies (see below) and most definitely smaller than the variation of the bremsstrahlung spectral parameters between the axial and radial measurements as well as the magnetic field sweep producing the most significant result as discussed later.

The spectra were analysed to calculate the total and average photon and electron energies.

The total electron and photon energy are defined as

$$F = \int_{\varepsilon_{min}}^{\varepsilon_{max}} f(\varepsilon) \cdot d\varepsilon \tag{2}$$

and the average electron and photon energy as

$$\varepsilon_{avg} = \frac{1}{F} \int_{\varepsilon_{min}}^{\varepsilon_{max}} f(\varepsilon) \cdot \varepsilon \cdot d\varepsilon \tag{3}$$

where ε is the electron energy (in the case of LEED) or the photon energy (in the case of bremsstrahlung spectrum) and $f(\varepsilon)$ is the measured LEED or bremsstrahlung spectrum where ε_{min} and ε_{max} represents the minimum and maximum measured energies. The average and total electron/photon energy were calculated for the complete spectrum and are presented in the following section. In the case of bremsstrahlung, the calculations were performed using the measured total counts, however the measured spectra are presented in the following figures with count rates to allow clearer comparison between the axial and radial cases.

Bremsstrahlung spectra are often characterised with spectral temperature, which is an indicative measure of the electron energy distribution in the ECRIS plasma [3, 13, 23, 24]. It has been established that ECRIS plasmas are not Maxwellian but instead consist of several electron populations [35, 45, 46, 47]; hence the spectral temperature is not interpreted as a measure of the electron temperature but is used as a tool to draw conclusions from parametric sweeps and to compare the obtained results with other studies. The spectral temperature is calculated [48] for the energy range of 78 keV to 150 keV for the axial and radial bremsstrahlung spectra. This energy range is selected to avoid the characteristic x-ray emission of lead at 72 keV and to make the fit in the linear part (on logarithmic scale) of both, the axial and radial spectra, therefore allowing a comparison between the two. Further details are provided in the Supplementary material.

In order to make a better comparison of the results, all the calculated values are normalised. The normalisation is done against the measured value corresponding to the lowest value of the parameter variable, i.e. the starting point of each parameter sweep.

In the LEED measurements a distinct local maximum is observed at electron energies around 220 keV, as is demonstrated e.g. in Fig. 5. To study the variation of this ”hump”, a combination of an exponential decay function and a Gaussian function was fitted to the experimental data. A detailed presentation of this procedure is included in the Supplementary material. The total and average electron energies associated with the hump were then calculated with Eqs. 2 and 3 from the Gaussian part of the fitted function.

The origin of the hump at specific energies is not completely understood. It has been speculated, based on simulations [49, 50] that such hump could appear due to spatially varying distribution of electron density of high energy electrons projected into the axial electron losses. However, it has been recently demonstrated conclusively that the hump is caused by microwave induced pitch angle scattering [51] although the mechanism determining its exact energy range remains elusive.

3.1. Effect of microwave power

The axial and radial bremsstrahlung spectra along with the LEED were measured as a function of the 14 GHz microwave power in the stable operation regime. Figure 5 shows the spectra and the variation of the spectral characteristics with the microwave power while keeping the neutral gas pressure (plasma off) at $3.5 \cdot 10^{-7}$ mbar and $B_{min}/B_{ECR} = 0.69$. The microwave power was increased from 100 W to 700 W in steps of 100 W.

The photon count rate for the axial (Fig. 5a) and radial bremsstrahlung (Fig. 5b) as well as the electron current for the LEED (Fig. 5c) increase with the increasing microwave power. This trend is clearly seen in the linear increase of the calculated total photon and electron energies (Fig. 5e, f), where both the bremsstrahlung (axial and radial) and the LEED increase monotonically with RF power. No notable changes are observed in the shapes of the LEED spectra.

The normalised spectral temperature for radial and axial spectra is calculated and plotted in Fig. 5d. It is seen that the spectral temperature only exhibits modest changes with RF power; a maximum change of ~ 5 % in the case of the axial bremsstrahlung and ~ 10 % for the radial bremsstrahlung. One can note that the ~ 5 % relative variation for the axial spectral temperature is of the same order as the counting statistical error indicated by the errorbars.

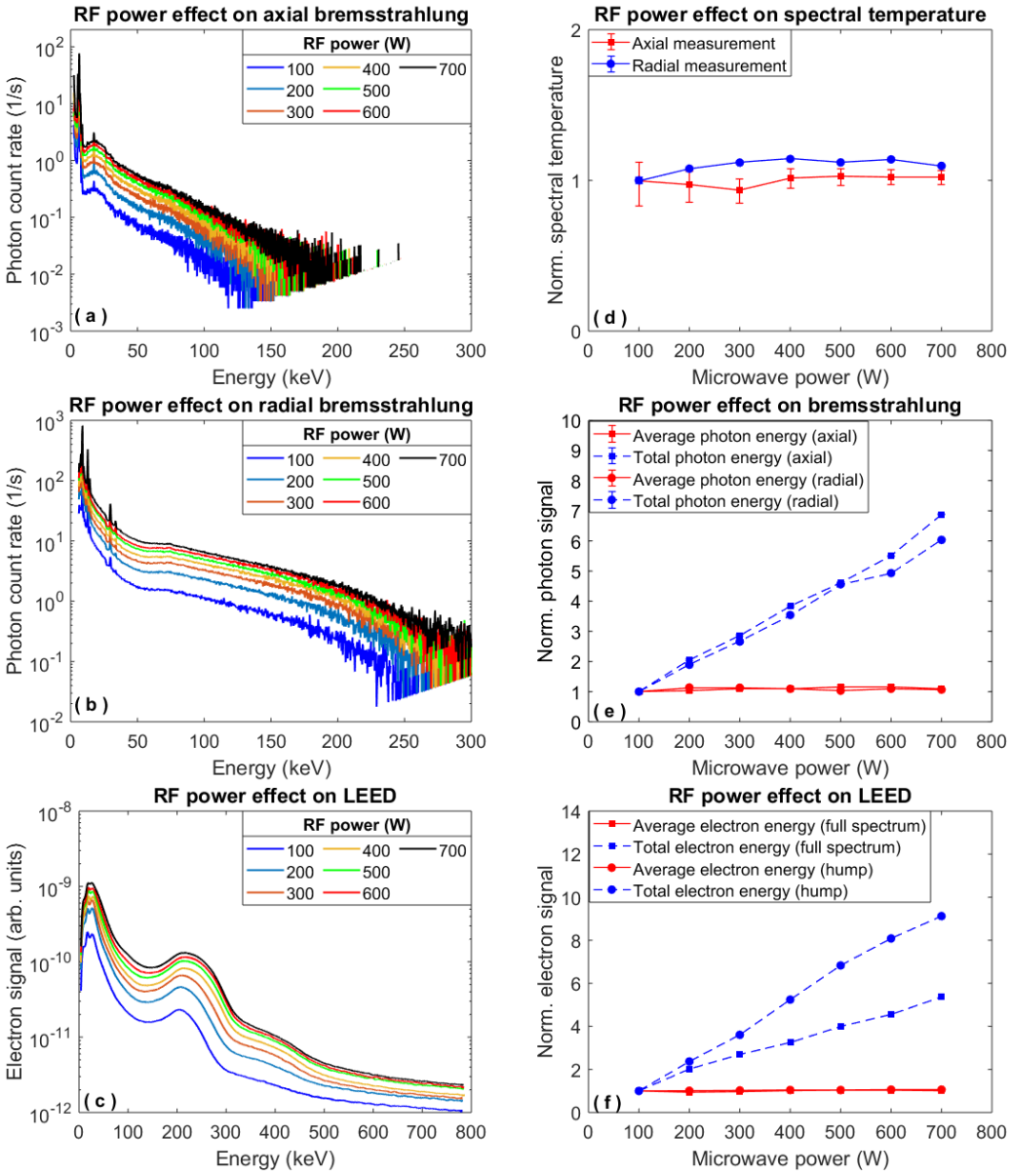

Figure 5. The effect of microwave power on axial and radial bremsstrahlung and LEED.

Figure 5e shows the effect of microwave power on the normalised total photon energy and average photon energy calculated from the radial and axial bremsstrahlung spectra. The total photon energy exhibit a notable increase across the power sweep range; about ~ 550 % in the case of axial bremsstrahlung and around ~ 500 % in the case of the radial bremsstrahlung, showing a practically linear dependence with the microwave power. The increase in the photon count rate with the increase in RF power has been observed in previous studies as well [7, 52, 53]. On the other hand, the average photon energy remains practically unchanged as a function of the microwave power for both axial and radial x-ray measurements with relative variations of the same order as the statistical measurement error, being 3-8 %.

The normalised total and average electron energy of the lost electrons escaping from the plasma is calculated and plotted in Fig. 5f. About 25 % of the total electrons lost are

found at the ∼200 keV energy hump (Fig. 5c); hence the total and average electron energies in the hump are also calculated and plotted in Fig. 5f. The total electron energy lost from the confinement through the extraction mirror increases with increasing microwave power (∼ 450 % increase) while the average electron energy remains almost constant.

One of the most prominent observations is the monotonic increase in the photon count rate (in bremsstrahlung spectra, see Fig. 5e) and similar relative increase in the electron current (in LEED) as shown in Fig. 5f. This draws a link between the parametric dependence of the bremsstrahlung and LEED. The shape of the spectra is not changing while the total signal level increases linearly with the microwave power.There are two processes that could explain the trend: (1) The plasma density increases with microwave power, which then translates to increased electron-ion (large-angle) collision frequency and escaping electron energy affecting both plasma and wall bremsstrahlung emission rates as well as the LEED signal magnitude and/or (2) the increased microwave power strengthens the EM-field amplitude in the plasma chamber, which leads to increased RF scattering rate [54], which has been shown to be the dominant loss mechanism of high energy electrons [29]. The LEED results (Fig. 5c, f) corroborate the studies made by Izotov *et al.*[35, 51]. It is worth noting that since the axial bremsstrahlung spectra do contain an unknown fraction of wall bremsstrahlung, it is expected that they and the LEED have similar dependence to a certain degree. It is also worth mentioning that once the electron density increases, we should expect the Coulomb scattering rate to increase [55]. As the Coulomb scattering is most prominent for cold electrons and the high energy electrons are mostly lost due to RF pitch angle scattering[29], the results presented here indicate that the ratio between the two loss channels is not affected by the increase of microwave power. This observation is consistent with studies probing the plasma losses through the measurement of K-alpha emission of iron vs. argon [22], where it was shown that the high energy electron losses (RF scattering) increase with microwave power. Since the shape of the LEED stays almost constant, it is concluded that also the Coulomb scattering rate increases with the power, which is interpreted as an increase of the electron density. This is commensurate with the well-known effect of the microwave power on ion beam intensities and charge state distribution.

3.2. Effect of neutral gas pressure

Figure 6 shows the axial and radial bremsstrahlung as well as the LEED spectra and their analysis with varying neutral gas pressure of oxygen. The ratio B_{min}/B_{ECR} was kept at 0.69 and the microwave power at 300 W. The neutral gas pressure (plasma off) was increased from $2 \cdot 10^{-7}$ to $10 \cdot 10^{-7}$ mbar. The lowest pressure setting corresponds to a case where practically no additional oxygen is injected into the plasma chamber. Since the pressure gauge is located outside the plasma chamber in one of the radial ports, these values do not exactly correspond to the actual pressure in the plasma chamber. Nevertheless, the sweep range covers a five-fold increase of the pressure.

Although small variations are observed, in general the bremsstrahlung spectrum and its characteristic figures are almost constant throughout the pressure range. The most prominent

effect of the neutral gas pressure is seen in Fig. 6c, where the LEED shows an increase in the electron current for electrons above 300 keV energy, which is also evident in Fig. 6f where the total electron energy is observed to increase as the neutral gas pressure increases (approximately 30 % increase). Despite the noticeable change in the LEED above 300 keV, this difference is only a few percent and does not affect the average energy of the LEED. These observations imply that the ionisation degree of the plasma is reduced with increasing neutral gas pressure. That is because the observed signals indicating the plasma energy content are approximately constant across the whole pressure range, which implies that electron density (n_e) should also stay constant because electrons carry the bulk of the plasma energy content. As the neutral gas pressure is being increased, the neutral density (n_n) increases, and the ionisation degree n_e/n_n must decrease to explain the observations, which agrees with the operational experience with the JYFL 14 GHz ECRIS, namely the shift of the charge state distribution of the extracted ion beams towards lower charge states at high neutral gas pressures. The results imply that all the injected RF power is absorbed efficiently regardless of the neutral gas pressure, which is in good agreement with the reflected power being always below 5% of the forward power. However, the origin of the observed LEED growth above 300 keV remains unclear.

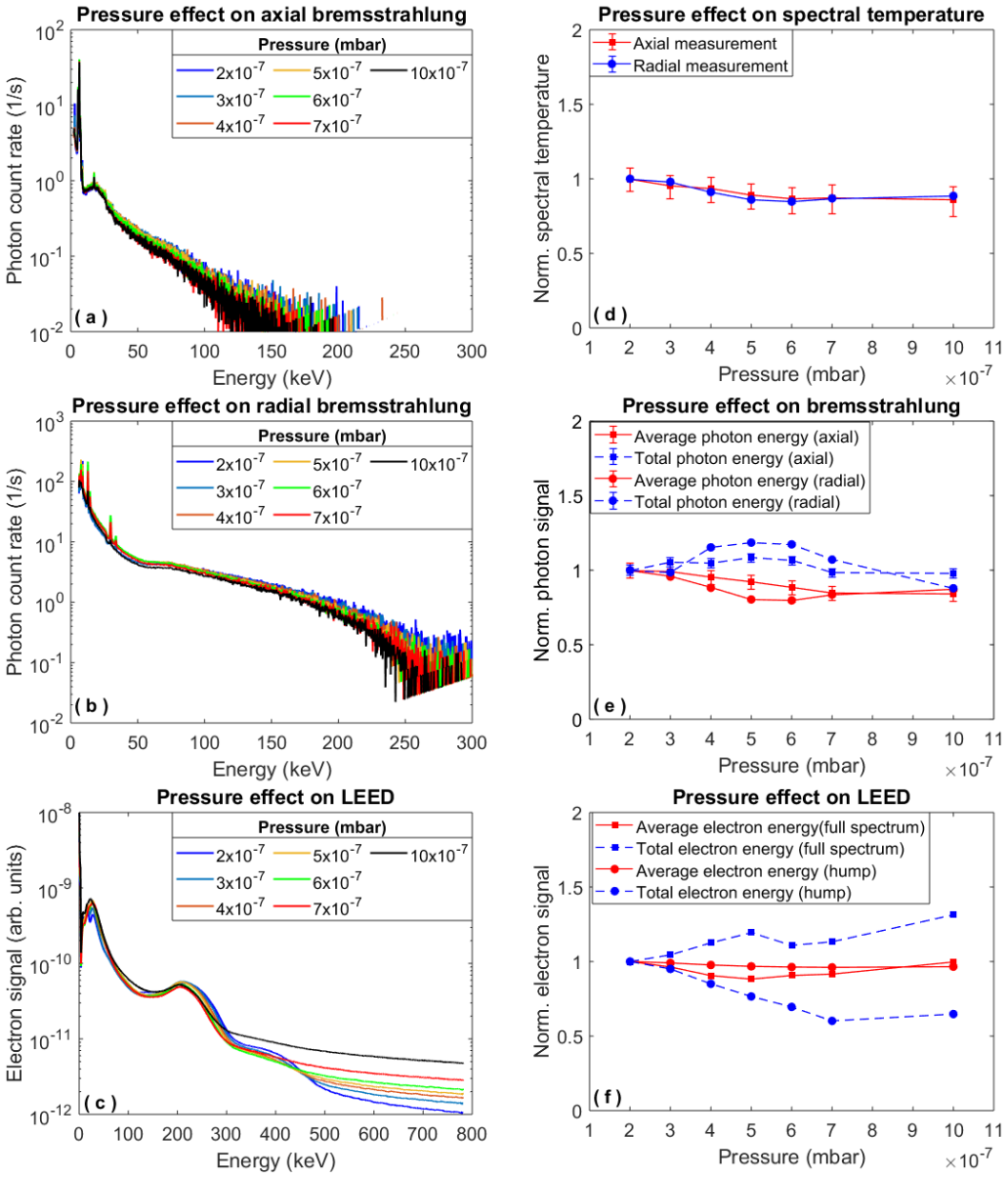

Figure 6. The effect of neutral oxygen pressure on axial and radial bremsstrahlung and LEED.

3.3. Effect of magnetic field

The axial and radial bremsstrahlung spectra along with the LEED were measured as a function of the magnetic field strength. Figure 7 shows the spectra and the analysis with varying magnetic field while keeping the neutral gas pressure (plasma off) at $3.5 \cdot 10^{-7}$ mbar and the microwave power at 300 W, with the same overall presentation as former figures (Fig. 5 and Fig. 6). The magnetic field strength was varied by ramping up both solenoid coil currents equally, thus the ratio B_{min}/B_{ECR} is varied from 0.64 to 0.82. See the Supplementary material for a complete description of the corresponding magnetic field parameters. Plasma instabilities appeared when the B_{min}/B_{ECR} value exceeded a certain threshold. It must be

noted that the axial bremsstrahlung spectra and the LEED were measured simultaneously, whereas the radial bremsstrahlung was measured later. Consequently, it was observed that at the ratio $B_{min}/B_{ECR} = 0.80$ for which instabilities were observed in the axial measurement, the plasma remained still stable in the case of the radial measurement. This implies that this point is very close to the threshold value for the instabilities, and the resulting plasma stability is sensitive to slight variations in the source conditions. The occurrence of the instability threshold around B_{min}/B_{ECR} ratio of 0.8 has been reported previously with various ion sources [25] including the JYFL 14 GHz ECRIS[27].

It is observed that the photon count rate for the axial bremsstrahlung spectra (Fig. 7a) decreases with increasing B_{min}/B_{ECR} ratio, i.e. with the increase of the axial mirror ratio, whereas the count rate for the radial bremsstrahlung (Fig. 7b) exhibits the opposite behaviour. It is also observed that the electron current of the LEED (Fig. 7c) decreases with increasing B_{min}/B_{ECR} ratio. However, unlike the bremsstrahlung spectra, the LEED shows a drastic change in the shape of the spectrum, the hump first shifting towards higher energy with the increasing field strength and then disappearing in the unstable plasma region.

Figure 7d shows the effect of magnetic field on the axial and radial spectral temperature, both of which increase with the increasing B_{min}/B_{ECR} ratio. This observation is in good agreement with previous studies conducted by Benitez *et al.* [52] and Li *et al.* [30] . The axial spectral temperature increases approximately 100 % and the radial spectral temperature approximately 250 % with the increase in the B_{min}/B_{ECR} ratio from 0.64 to 0.82. If only the stable plasma region is considered, the axial spectral temperature increases approximately 60 % and the radial one about 200 %.

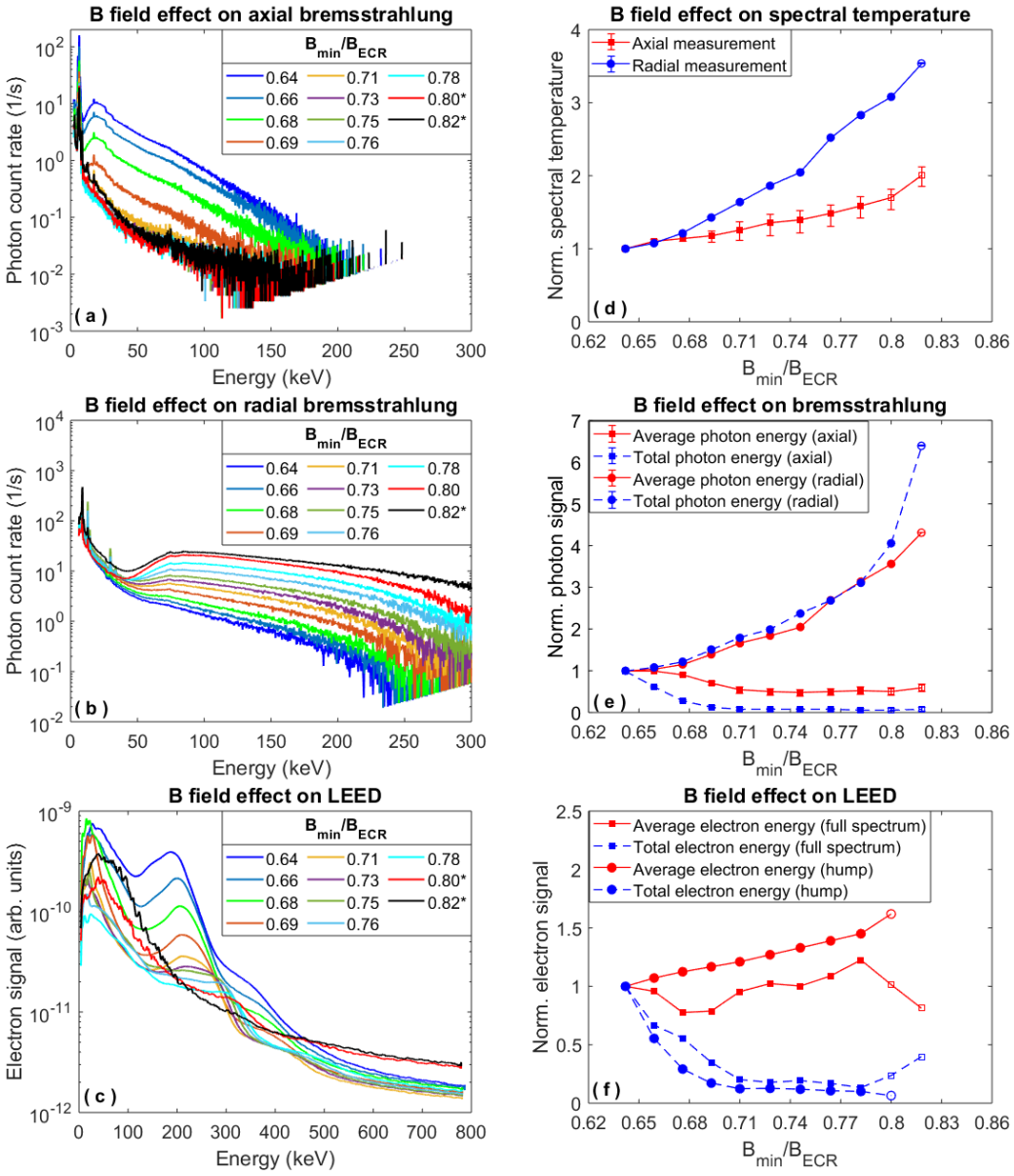

Figure 7. The effect of magnetic field strength on the axial and radial bremsstrahlung and the LEED. The unstable plasma regime is denoted with a star symbol (*) in the legend of the spectra and with open symbols (circles and squares) in the analysis results.

The effect on the total and the average photon energy of the axial and the radial bremsstrahlung is calculated and plotted in Fig. 7e. It is found that as the B_{min}/B_{ECR} ratio increases, the total as well as the average photon energy increases in the case of the radial bremsstrahlung spectra, whereas it decreases in the case of the axial bremsstrahlung spectra, reflecting the earlier observations made concerning the count rates. The total photon energy in the radial measurement increases approximately 550 % whereas the corresponding energy in the axial bremsstrahlung spectra decreases around 94 %. Similarly, the average photon energy also exhibits an increase of around 430 % in the case of the radial bremsstrahlung and a decrease of around 40 % in the axial bremsstrahlung as the magnetic field strength increases.

Further analysis yields that the total axial photon energy decreases monotonically down to ~ 6 % (94 % reduction) of the initial photon energy in the stable plasma regime. Increasing the magnetic field further crossing the threshold to unstable plasma regime then yields an increase of ~ 25 % w.r.t the total photon energy value at $B_{min}/B_{ECR} = 0.78$ (i.e. the last stable point before the instability threshold). However this average photon energy variation above the instability threshold is observed to be comparable with the calculated statistical error, which is shown by open square symbol in Fig. 7e. The increase in total and average photon energy beyond instability threshold is more prominent in the case of radial bremsstrahlung, i.e. around 60 % increase in total photon energy.

It must be noted that in the case of the calculated parameters from the time-averaged bremsstrahlung spectra, there is no clear transition observed when the plasma turns unstable, instead the spectral temperature and the calculated energies seem to continue following the same trend that was present when ramping up the magnetic field in the stable plasma regime. It is argued that this is because the instability-induced electron losses occur in rapid bursts overlooked by the temporally averaged diagnostics.

The normalised total and average electron energy of the lost electrons escaping from the plasma through the extraction mirror is calculated and plotted in Fig. 7f. The total electron energy in the LEED decreases with the increase in B_{min}/B_{ECR} ratio until the instability threshold (around $B_{min}/B_{ECR} = 0.8$) is reached and then increases. The decrease is due to the increase of the extraction mirror ratio with the increasing coil currents, which results in reduced electron energy escaping through the extraction aperture. Also, plasma instabilities are known to expel hot electrons from the plasma in periodic bursts that are temporally averaged in our measurement, which explains the observed increase in the unstable regime. It is seen that the average electron energy increases slightly (around 25 %) until the instability threshold and then starts to decrease. This is viewed as the instabilities and the associated electron bursts limiting the plasma energy content, which is predominantly carried by the hot electrons [40].

It is evident from Fig. 7c that the energy hump around 200 keV varies drastically with increasing B_{min}/B_{ECR} ratio. The total electron energy at this hump shows a monotonous decrease as the magnetic field strength increases. The LEED hump disappears in the unstable regime while the transition from the stable to unstable regime is not observable from the bremsstrahlung spectra. The average electron energy of the energy hump increases (around 60 % increase) with increasing magnetic field as reported earlier [51, 23] . The increase continues as the magnetic field crosses the instability threshold until the hump disappears at the highest B_{min}/B_{ECR} value. The physical mechanism explaining the dependence of the hump on the magnetic field strength remains elusive at this time, although a possible explanation has been provided in [51].

3.4. Effect of instability

The effect of the transition from the stable to unstable plasma regime on the bremsstrahlung spectra and the LEED was studied further with operating the ion source at different (lower)

microwave frequencies. This was done in order to establish that the observed disappearance of the LEED hump is not coincidental but indeed facilitated by the transition into unstable regime. The transition crossing was realised by varying the magnetic field strength. The experiment was conducted for three different heating frequencies (11.56 GHz, 12.00 GHz and 13.00 GHz) by using the TWTA [34] as the microwave source. The neutral gas pressure was set at $3.5 \cdot 10^{-7}$ mbar and total input power was 220 W (limited by the TWTA maximum output). As an example, Fig. 8 shows the effect of the transition from stable to unstable regime on the axial and radial bremsstrahlung spectra as well as the LEED for the 12.00 GHz case.

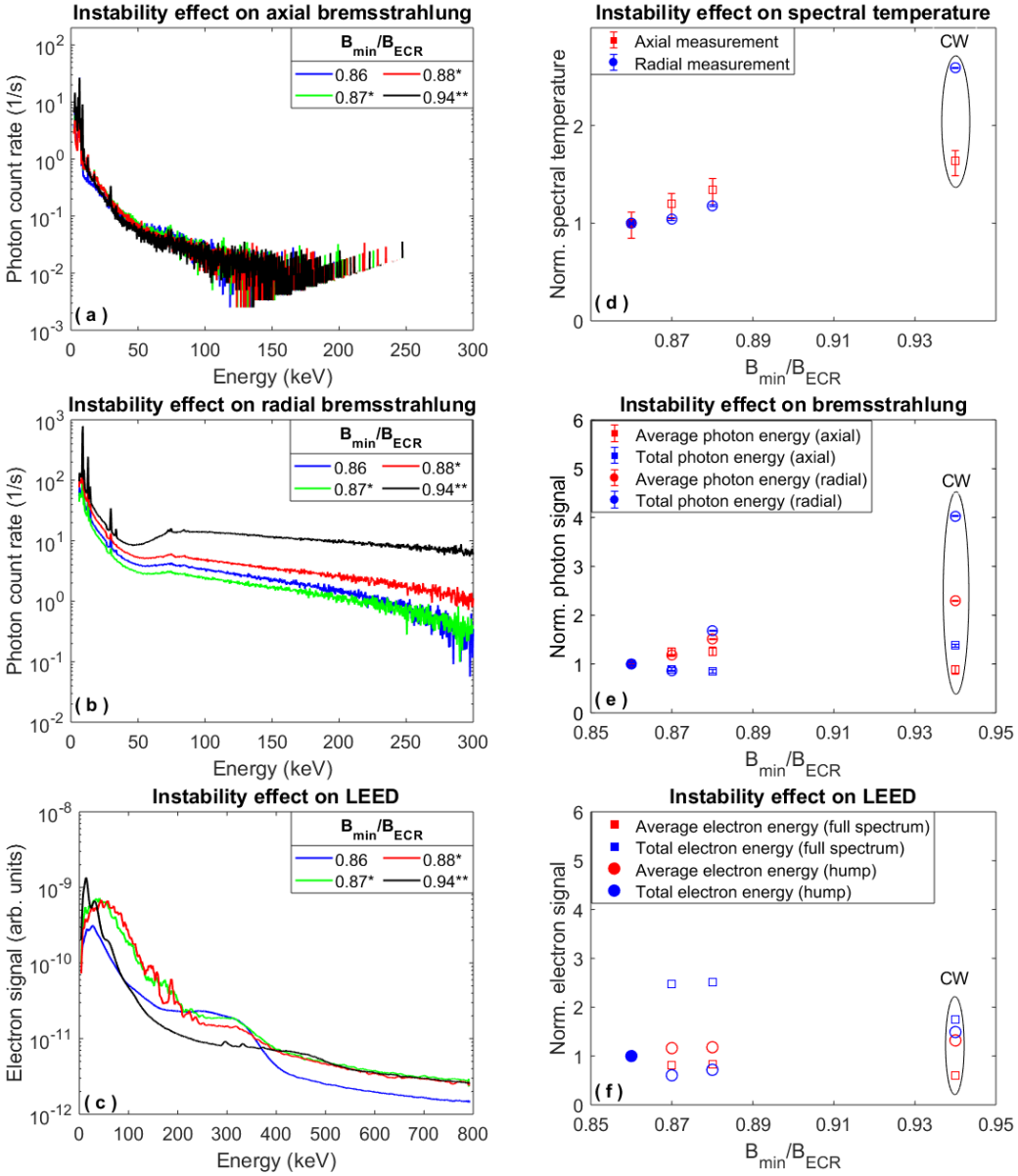

Figure 8. The effect of magnetic field strength on axial and radial bremsstrahlung and LEED at 12 GHz microwave frequency. The unstable regime is denoted with * in the spectra and with open symbols (circles and squares) in the analysis results whereas ** in the spectrum corresponds to CW microwave emission regime.

Similar to the observation made in Fig. 7, the instability threshold exhibited an increase in the total electron energy and a decrease in the average electron energy lost from the confinement for all three input heating frequencies (an example with 12 GHz is presented in Fig. 8). However, consistent differences were not observed in the bremsstrahlung spectra (both axial and radial) with the onset of instability for each plasma heating frequencies.

In all the cases, the recorded value corresponding to the highest B_{min}/B_{ECR} ratio corresponds to the so-called Continuous Wave microwave emission mode (CW mode)[41]. The CW instability mode can be observed when the pulse-periodic x-ray and microwave emission is converted to a continuous emission of a particular frequency which is measured using network analyser (employed previously by Naselli et.al [56]) in combination with the scintillator. The temporal measurement of the bremsstrahlung power is required to distinguish between pulse-periodic instabilites and the cw maser regimes, which is not possible using the network analyser alone. The frequency corresponding to the microwave emission in the CW plasma maser mode, discussed in detail in Ref. [44], is found to be 9.62 GHz, 9.71 GHz and 7.73 GHz depending on various source tuning. Despite of the change of the CW emission frequency, the conclusion remains the same: the transition to unstable regime is accompanied by the disappearance of the pronounced LEED hump which is seen in the stable regime, whereas the bremsstrahlung spectra either remain constant (axial) or continue changing monotonically (radial).

4. Discussion

The experimental results demonstrate that there is a correlation between the bremsstrahlung spectral temperature and the shift in the maximum of the LEED hump (see Fig. 7). This result confirms the measurement made by Isherwood *et al.* [23] with the added value of the LEED energy calibration.

In order to have a better understanding of the effect of wall bremsstrahlung, the normalised photon count of characteristic x-rays (K-α) of iron and molybdenum were identified from the measured spectra and compared with the total photon count of the entire spectrum as well as with the high energy section of the spectra which was used to calculate the spectral temperatures. Iron and molybdenum were chosen because they originate from the biased disk, located at the injection end of the plasma chamber, which is made of stainless steel containing these elements. It was observed that the total count of characteristic x-rays behaves similarly with the total bremsstrahlung count rate as a function of the magnetic field strength. This underlines the fact that in the case of axial bremsstrahlung measurements it is very challenging to separate the different sources of radiation. These results are presented in detail in the supplementary material. Thus, in studies that aim to focus on the x-ray emissions originating from the plasma itself, the measurements should be conducted either through the K-α emissions of the plasma particles which can be identified unambiguously, as reported by e.g. Sakildien *et al.* [37] or by using spatially resolved methods such as a pinhole and a high resolution CCD camera as suggested by Biri *et al.* [57].

It was observed that the photon count rate decreases with increase in B_{min}/B_{ECR} ratio

in the axial direction whereas it increases in the radial direction. The radial spectral temperatures were also observed to be significantly higher than the axial ones; these observations corroborate the results by Noland *et al.* [24] with a similar ion source as the one used for the current experiments. This phenomenon can be explained in two ways: (1) directionality of the volumetric plasma bremsstrahlung emission and the effect of EED anisotropy, or (2) redistribution of axial versus radial electron losses causing the possibility of wall bremsstrahlung affecting the measured spectra. We consider the first option more likely as the collimation was carefully designed to minimise the contribution of wall bremsstrahlung both in the measurements reported here and in those by Noland *et al.* [24] yielding qualitatively similar results. Consequently, the following discussion focuses on the first option. Further discussion of the second option is available in the supplementary material.

It can be argued that the anisotropy of the bremsstrahlung emission correlates with the anisotropy of the velocity distribution of the high-energy electrons confined in the dense plasma enclosed by the (relativistic and Doppler shifted) resonance zone, i.e. near the source axis [49]. That is because the bremsstrahlung emission is strongly directional with the emission angle of bremsstrahlung intensity maximum ($\theta_{\max}$) reducing rapidly with the relativistic electron velocity as [58]

$$\theta_{\max} = \cos^{-1}\left(\frac{1}{3\beta}\left(\sqrt{1+15\beta^2}-1\right)\right), \tag{4}$$

where θ is the angle between the electrons initial velocity and bremsstrahlung photon emission and $\beta = \frac{v_e}{c}$ is the electron speed in relativistic units. The electron energy dependence of the bremsstrahlung intensity maximum (angular) is shown in Fig. 9(a) where we have highlighted the range of electron energies $>$ 50 keV and $>$ 200 keV. That is because we have observed the radial bremsstrahlung spectra at photon energies above 50 keV, caused by $>$ 50 keV electrons, to depend strongly on B_{min} and, on the other hand, found the LEED hump at approximately 200 keV. In these electron energy ranges the intensity maximum of the bremsstrahlung emission is found at angles $\theta < 44°$and $\theta < 26°$, respectively. The anisotropicity of the bremsstrahlung emission was first presented by Gluckstern & Hull [59] and Koch & Motz [60]. The polar plot of bremsstrahlung directionality caused by the electron ion collision (plasma bremsstrahlung) and the dependence of photon energy on the initial electron energy is discussed in detail by Massone *et al.* [61].

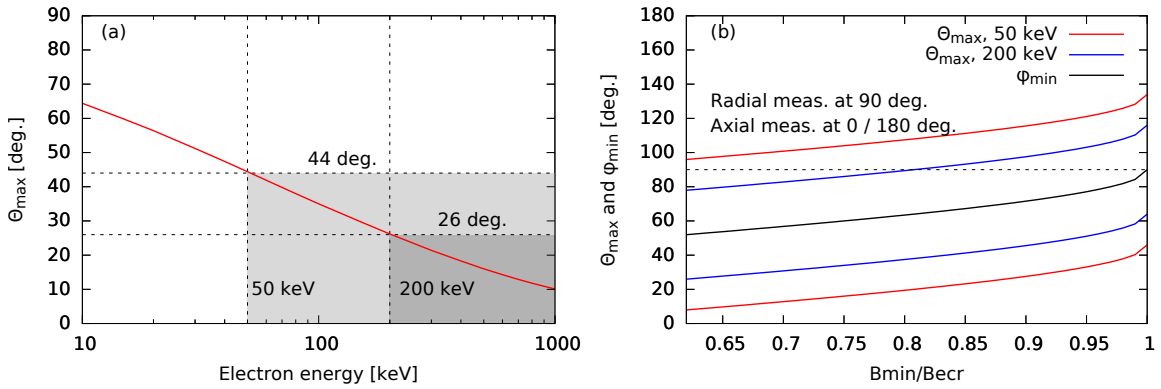

Figure 9. (a) The maximum intensity angle of bremsstrahlung emission as a function of the incident electron energy in the range relevant for the JYFL 14 GHz ECRIS. (b) The minimum pitch angle ϕ of the fast electrons and the predicted bremsstrahlung emission intensity maxima for 50 keV and 200 keV electrons as a function of B_{min}/B_{ECR}. Here 90° correspond to radial and 0°/180° axial bremsstrahlung emissions. The two curves for 50 keV and 200 keV electrons correspond to the two side lobes of the bremsstrahlung emission in polar plots.

To estimate the predominant direction of the bremsstrahlung emission in our experimental setup we consider the high-energy electrons to be confined between the on-axis resonance points of cold electrons, and ignore the relativistic effect and Doppler shift for the sake of simplicity. In this model the electrons bounce between their mirror points with their pitch angle $\phi = arcsin\left(\frac{v_\perp}{v}\right)$ varying from $\phi_{\min} = arcsin\left(\sqrt{\frac{B_{min}}{B_{ECR}}}\right)$ to 90°. In the discharge volume occupied by the hot electrons the magnetic field is almost parallel to the geometrical axis of the plasma chamber, which means that the radially detected bremsstrahlung emission corresponds to photon emission perpendicular to the magnetic field. This allows us to plot the predicted bremsstrahlung intensity maximum angle (two side lobes) in our measurement geometry for various electron energies in the range of $\frac{B_{min}}{B_{ECR}}$ used in our experiments. The result is shown in Fig. 9(b) for electron energies of 50 keV (minimum electron energy in the photon energy range of interest) and 200 keV (approximate energy of the LEED hump), corresponding to $\theta_{\max}$ of 44 and 26 degrees, respectively. Electron energies above the said thresholds result in θ_{max} in between the extremes (side lobes) shown here. In other words, as the electron energy increases, the most probable photon emission angle approaches the electron pitch angle. In Fig. 9(b) the angle of 90° corresponds to radial emission in our geometry. It can be seen that the predicted maximum (one of the side lobes) of the bremsstrahlung emission intensity of 200 keV electrons crosses 90° in the range of $\frac{B_{min}}{B_{ECR}}$ covered by our experiment, which means that the spatial distribution of the bremsstrahlung emission becomes increasingly radial in our geometry. In addition, the fact that the range of θ_{max} narrows with increasing electron energy favours emission towards the radial detector. In both cases the intensity maximum corresponding to one of the bremsstrahlung emission side lobes moves away from axial direction, which suggests that the axially emitted bremsstrahlung energy decreases with increasing magnetic field strength, which was observed experimentally. In this context we draw the reader's attention to the fact that the measurement of T_s in axial direction, being the most commonly studied observable

of ECRIS bremsstrahlung emission, is complicated by the energy-dependent redistribution of the photon emission (axial vs. radial) as a function of the magnetic field strength and electron confinement, which can easily lead to misleading conclusions.

The angular dependence of the fast electron bremsstrahlung emission (discussed above) has been thoroughly studied in the context of magnetic confinement fusion experiments, see e.g. Ref. [62] and references therein, but there are two additional ECRIS-specific peculiarities, which emphasise the redistribution of the bremsstrahlung emission (between axial and radial directions) with increasing magnetic field: (i) As the axial field strength increases, the average magnetic field gradient parallel to the field $\left(\frac{\vec{B}\cdot\nabla\vec{B}}{|\vec{B}|}\right)$ over the closed ECR surface decreases (all the magnetic field parameters corresponding to different coil current combinations are available in the Supplementary material), which implies higher electron energy gain per resonance crossing [63, 53]. Thus, the plasma energy density and the anisotropy of the EED ($v_\perp >> v_\parallel$) increase. The instability threshold being defined by the magnetic field is considered as empirical evidence for the increase of the anisotropy. The anisotropy in bremsstrahlung emission can be correlated with the increase in anisotropy of the electron energy distribution. (ii) When the magnetic field strength is increased, the volume enclosed by the closed resonance zone shrinks, which means that the plasma volume visible to the radial detector (see Fig. 2) is effectively shifted closer to the turning point of the electrons oscillating between their mirror points. This means that those electrons causing bremsstrahlung visible to the radial detector have their pitch angles close to 90 degrees which favours radial bremsstrahlung photon emission (see Fig. 9(b)). That is because the ϕ_{min} shown in the figure corresponds to the minimum pitch angle, i.e. $\phi = \phi_{min}$ when $B = B_{min}$ and elsewhere $\phi > \phi_{min}$. Hence, as the B_{min} is outside the radial detector's field-of-view, it can be expected that Fig. 9(b) underestimates the angle of maximum bremsstrahlung emission from the visible plasma volume. These considerations are in good agreement with the experimental results.

Another prominent observation is the correlation between the appearance of kinetic instabilities and the disappearance of the LEED hump (Fig. 7c). It can be concluded that the instabilities are modifying the electron energy distribution (by electron precipitation from the trap) as discussed in Ref. [29]. The measured LEED is time averaged whereas the instability induced electron losses happen in short bursts in ~ 0.5 μs [29]. Since the instabilities are expelling the hot electron fraction and it takes time to accumulate them again [64], the time-averaged LEED at high energies being a measure of the RF-scattered electrons is different (hump disappears). It can thus be deduced that the instability threshold is not only affected by electron heating but also the electron confinement; when the confinement is strong especially in axial direction, the energy accumulated in the EED of confined electrons has to be dissipated by means of instability. Increasing the axial field strength is therefore affecting the instability in two ways: (a) Since the average gradient over ECR surface decreases, the electron heating improves [30] and (b) The confinement improves which amplifies the effect (accumulation of hot electrons). Further extension of instability studies (Fig. 8) showed that the LEED exhibits a significant difference with the onset of instability which is not evident from the bremsstrahlung spectra. It is therefore concluded that the measurement

of the time averaged bremsstrahlung spectra alone is not sufficient to detect and study the electron dynamics in the presence of instabilities. The immunity to observe fast instability effects is a severe limitation of the present time averaged bremsstrahlung measurement technique, which is probably the most widely applied technique to study ECR ion sources [6, 7, 9, 8, 11, 10, 13, 23, 30], and can lead to false conclusions at high magnetic fields. The instability was observed to expel more hot electrons compared to stable mode. At the highest magnetic field we achieved a CW (maser) emission mode discussed in the literature [43, 44, 65]. The discrepancy between the radial and axial spectra in the CW emission mode implies that the anisotropy of the EED is very strong in this regime.

5. Conclusions

The main conclusions of this work can be summarised into four points. First, the experiments presented here confirmed the results presented by Isherwood *et al.* [23] concerning the correlation between the bremsstrahlung spectral temperature and the shift of the LEED hump maximum energy. The uncertainties present in the previously published work were resolved here by including the energy calibration in the electron measurements by taking into account the beamline transmission and secondary electron amplifier efficiencies.

Second, the data and discussion presented here provide a comprehensive explanation for the different axial and radial bremsstrahlung behaviour with varying axial magnetic field. As shown above, this behaviour can be linked to the anisotropy and directionality of the plasma emitted bremsstrahlung which results from the ECRIS specific magnetic confinement and heating scheme.

The third main result is the measurement of how the onset of the instabilities influence the shape of the LEED high energy hump. This correlation gives clear evidence of how the instability dissipates the excess energy in the EED and affects the electron confinement.

The final conclusion of the work presented here underlines the challenges and validity of commonly used bremsstrahlung measurement techniques in the study of ECRIS plasmas. It was clearly observed that in the case of axial measurement the plasma and the thick target bremsstrahlung can not be resolved, even with sophisticated collimation systems. Therefore other methods should be used if axially oriented measurement scheme is used to study the bremsstrahlung emitted by the plasma itself to avoid incorrect conclusions, as was discussed above. Also, the bremsstrahlung measurements conducted in stable and unstable plasma regimes revealed that time averaged bremsstrahlung measurements which are commonly used with ECR plasmas are not sufficient to detect the onset of plasma instabilities. This highlights the need of additional (time resolved) diagnostics to properly characterise the state of the plasma through the detection of emitted radiation.

Acknowledgments

We wish to acknowledge the funding from Academy of Finland under the project funding No. 315855 and University of Grenoble Alpes under the EMERGENCE program. The work

of I. Izotov and V. Skalyga was done within the state assignment of Ministry of Science and Higher Education of the Russian Federation No. 0035-2019-0002.

[1] R Geller. Electron cyclotron resonance ion sources and ECR plasmas, 1996.

[2] GD Shirkov. A classical model of ion confinement and losses in ecr ion sources. Plasma Sources Science and Technology, 2(4):250, 1993.

[3] C Lyneis, D Leitner, D Todd, S Virostek, T Loew, A Heinen, and O Tarvainen. Measurements of bremsstrahlung production and x-ray cryostat heating in venus. Review of scientific instruments, 77(3):03A342, 2006.

[4] Y Higurashi, J Ohnishi, T Nakagawa, H Haba, M Tamura, T Aihara, M. Fujimaki, M Komiyama, A Uchiyama, and O Kamigaito. Results of RIKEN superconducting electron cyclotron resonance ion source with 28 GHz. Review of Scientific Instruments, 83:02A308, 2012.

[5] O Tarvainen, T Kalvas, H Koivisto, J Komppula, R Kronholm, J Laulainen, I Izotov, D Mansfeld, and V Skalyga. Kinetic instabilities in pulsed operation mode of a 14 ghz electron cyclotron resonance ion source. Review of Scientific Instruments, 87(2):02A701, 2016.

[6] K Bernhardi and K Wiesemann. X-ray bremsstrahlung measurements on an ecr-discharge in a magnetic mirror. Plasma Physics, 24(8):867, 1982.

[7] C Barue, P Briand, A Girard, G Melin, and G Briffod. Hot electron studies in the minimafios ecr ion source. Review of scientific instruments, 63(4):2844–2846, 1992.

[8] R Friedlein, D Küchler, C Zippe, G Zschornack, and H Tyrroff. Energy dispersive x-ray spectroscopy for ecr plasma diagnostics. Hyperfine interactions, 99(1):225–234, 1996.

[9] K Wiesemann. Some plasma aspects and plasma diagnostics of ion sources. Review of Scientific Instruments, 79(2):02B506, 2008.

[10] R Baskaran, TS Selvakumaran, G Rodrigues, D Kanjilal, and A Roy. Measurements and analysis of bremsstrahlung x-ray spectrum obtained in nanogan electron cyclotron resonance ion source. Review of Scientific Instruments, 79(2):02A324, 2008.

[11] H. Y. Zhao, H. W. Zhao, L. T. Sun, H. Wang, D. Z. Xie, B. H. Ma, X. Zh Zhang, X. X. Li, X. W. Ma, Y. H. Zhu, W. Lu, and Y. Shang. Effects of magnetic configuration on hot electrons in highly charged ECR plasma. Plasma Sources Science and Technology, 18(2), 2009.

[12] A Gumberidze, M Trassinelli, N Adrouche, C I Szabo, P Indelicato, F Haranger, J-M Isac, E Lamour, E-O Le Bigot, J Mérot, C Prigent, J-P Rozet, and D Vernhet. Electronic temperatures, densities, and plasma x-ray emission of a 14.5 GHz electron-cyclotron resonance ion source. Review of Scientific Instruments, 81:033303, 2010.

[13] S Kasthurirangan, AN Agnihotri, CA Desai, and LC Tribedi. Temperature diagnostics of ecr plasma by measurement of electron bremsstrahlung. Review of Scientific Instruments, 83(7):073111, 2012.

[14] D Mascali, L Celona, F Maimone, J Maeder, G Castro, F P Romano, A Musumarra, C Altana, C Caliri, G Torrisi, L Neri, S Gammino, K Tinschert, K P Spaedtke, R Rossbach, J Lang, and G Ciavola. X-ray spectroscopy of warm and hot electron components in the CAPRICE source plasma at EIS testbench at GSI. Review of Scientific Instruments, 85:02A956, 2014.

[15] R Rácz, S Biri, Z Perduk, J Pálinkás, D Mascali, M Mazzaglia, E Naselli, G Torrisi, G Castro, L Celona, S Gammino, and A Galatà. Effect of the two-close-frequency heating to the extracted ion beam and to the X-ray flux emitted by the ECR plasma. Journal of Instrumentation, 13:C12012, 2018.

[16] G Castro, D Mascali, M Mazzaglia, S Briefi, U Fantz, and R Miracoli. Multidiagnostics investigation of the role of the magnetic field profile in a simple mirror trap. Physical Review Accelerators and Beams, 22:053404, 2019.

[17] D Mascali, G Castro, S Biri, R Rácz, J Pálinkás, C Caliri, L Celona, L Neri, F P Romano, G Torrisi, and S Gammino. Electron cyclotron resonance ion source plasma characterization by X-ray spectroscopy and X-ray imaging. Review of Scientific Instruments, 87:02A510, 2016.

[18] R Rácz, D Mascali, Sándor Biri, C Caliri, G Castro, A Galatà, S Gammino, L Neri, J Pálinkás, FP Romano, et al. Electron cyclotron resonance ion source plasma characterization by energy dispersive x-ray imaging. Plasma Sources Science and Technology, 26(7):075011, 2017.

[19] T Ropponena, O Tarvainen, P Jonesa, P Peura, T Kalvasa, P Suominen, H Koivisto, and J Ärje. The effect of magnetic field strength on the time evolution of high energy bremsstrahlung radiation created by an electron cyclotron resonance ion source. Nuclear Inst. and Methods in Physics Research, A, 600:525–533, 2009.

[20] K Bernhardi. An improved deconvolution method for bremsstrahlung spectra from hot plasmas. Computer Physics Communications, 19(1):17–21, 1980.

[21] R Friedlein and G Zschornack. Angle dispersive de-convolution of bremsstrahlung spectra from plasma. Nuclear Inst. and Methods in Physics Research, A, 349(2-3):554–557, 1994.

[22] M Sakildien, O Tarvainen, R Kronholm, I Izotov, V Skalyga, T Kalvas, P Jones, and H Koivisto. Experimental evidence on microwave induced electron losses from ecris plasma. Physics of Plasmas, 25(6):062502, 2018.

[23] B Isherwood and G Machicoane. Measurement of the energy distribution of electrons escaping confinement from an electron cyclotron resonance ion source. Review of Scientific Instruments, 91(2):025104, 2020.

[24] J Noland, JY Benitez, D Leitner, C Lyneis, and J Verboncoeur. Measurement of radial and axial high energy x-ray spectra in electron cyclotron resonance ion source plasmas. Review of Scientific Instruments, 81(2):02A308, 2010.

[25] O Tarvainen, J Angot, I Izotov, V Skalyga, H Koivisto, T Thuillier, T Kalvas, and T Lamy. Plasma instabilities of a charge breeder. AIP Conference Proceedings, 2011(1):070006, 2018.

[26] O Tarvainen, I Izotov, D A Mansfeld, V Skalyga, S Golubev, T Kalvas, H Koivisto, J Komppula, R Kronholm, J Laulainen, et al. Beam current oscillations driven by cyclotron instabilities in a minimum-b electron cyclotron resonance ion source plasma. Plasma Sources Science and Technology, 23(2):025020, 2014.

[27] O Tarvainen, J Laulainen, J Komppula, R Kronholm, T Kalvas, H Koivisto, I Izotov, D A Mansfeld, and V Skalyga. Limitations of electron cyclotron resonance ion source performances set by kinetic plasma instabilities. Review of Scientific Instruments, 86(2):023301, 2015.

[28] O Tarvainen, T Kalvas, H Koivisto, J Komppula, R Kronholm, J Laulainen, I Izotov, D A Mansfeld, V Skalyga, V Toivanen, et al. Limitation of the ecris performance by kinetic plasma instabilities. Review of Scientific Instruments, 87(2):02A703, 2016.

[29] I Izotov, O Tarvainen, V Skalyga, D A Mansfeld, H Koivisto, R Kronholm, V Toivanen, and V Mironov. Measurements of the energy distribution of electrons lost from the minimum b-field—the effect of instabilities and two-frequency heating. Review of Scientific Instruments, 91(1):013502, 2020.

[30] J.B. Li, L.X. Li, B.S. Bhaskar, V Toivanen, O Tarvainen, D Hitz, L.B. Li, W Lu, H Koivisto, T Thuillier, J.W. Guo, X.Z. Zhang, H.Y. Zhao, L.t. Sun, and H.W. Zhao. Effects of magnetic configuration on hot electrons in a minimum-b ecr plasma. Plasma Physics and Controlled Fusion, 2020.

[31] D Neben, J Fogleman, B Isherwood, D Leitner, G Machicoane, S Renteria, J Stetson, and L Tobos. X-ray investigation on the superconducting source for ions (susi). Journal of Instrumentation, 14(02):C02008, 2019.

[32] J Benitez, C Lyneis, L Phair, D Todd, and D Xie. Dependence of the bremsstrahlung spectral temperature in minimum-b electron cyclotron resonance ion sources. IEEE Transactions on Plasma Science, 45(7):1746–1754, 2017.

[33] H Koivisto, P Heikkinen, V Hänninen, A Lassila, H Leinonen, V Nieminen, J Pakarinen, K Ranttila, J Ärje, and E Liukkonen. The first results with the new jyfl 14 ghz ecr ion source. Nuclear Instruments and Methods in Physics Research Section B: Beam Interactions with Materials and Atoms, 174(3):379–384, 2001.

[34] CPI TWTA. https://www.cpii.com/docs/datasheets/18/mkt227.pdf.

[35] I Izotov, O Tarvainen, V Skalyga, D A Mansfeld, T Kalvas, H Koivisto, and R Kronholm. Measurement of the energy distribution of electrons escaping minimum-b ecr plasmas. Plasma Sources Science and Technology, 27(2):025012, 2018.

[36] Amptek CdTe detector. https://www.amptek.com/products/x-ray-detectors/cdte-x-ray-and-gamma-ray-detectors/xr-100cdte-x-ray-and-gamma-ray-detector.

[37] M Sakildien, R Kronholm, O Tarvainen, T Kalvas, P Jones, R Thomae, and H Koivisto. Inner shell ionization of argon in ecris plasma. Nuclear Instruments and Methods in Physics Research Section A: Accelerators, Spectrometers, Detectors and Associated Equipment, 900:40–52, 2018.

[38] Stanford Research Systems preamplifier. https://www.thinksrs.com/products/sr570.html.

[39] Picoscope 5000 series. https://www.picotech.com/oscilloscope/5000/flexible-resolution-oscilloscope.

[40] SV Golubev and AG Shalashov. Cyclotron-resonance maser driven by magnetic compression of rarefied plasma. Physical review letters, 99(20):205002, 2007.

[41] I Izotov, O Tarvainen, D A Mansfeld, V Skalyga, H Koivisto, T Kalvas, J Komppula, R Kronholm, and J Laulainen. Microwave emission related to cyclotron instabilities in a minimum-b electron cyclotron resonance ion source plasma. Plasma Sources Science and Technology, 24(4):045017, 2015.

[42] Rohde Schwarz spectrum analyser. https://www.rohde-schwarz.com/fi/product/zvl13-productstartpage_63493-10575.html.

[43] AG Shalashov, ED Gospodchikov, I Izotov, D A Mansfeld, V Skalyga, and O Tarvainen. Observation of poincaré-andronov-hopf bifurcation in cyclotron maser emission from a magnetic plasma trap. Physical review letters, 120(15):155001, 2018.

[44] AG Shalashov, ED Gospodchikov, IV Izotov, D A Mansfeld, VA Skalyga, and O Tarvainen. Control of electron-cyclotron instability driven by strong ecrh in open magnetic trap. EPL (Europhysics Letters), 124(3):35001, 2018.

[45] C Barué, M Lamoureux, P Briand, A Girard, and G Melin. Investigation of hot electrons in electron-cyclotron-resonance ion sources. Journal of Applied Physics, 76(5):2662–2670, 1994.

[46] Alain Girard, Christian Lécot, and Konstantin Serebrennikov. Numerical simulation of the plasma of an electron cyclotron resonance ion source. Journal of Computational Physics, 191(1):228–248, 2003.

[47] SB Singh, N Chand, and DS Patil. Langmuir probe diagnostics of microwave electron cyclotron resonance (ecr) plasma. Vacuum, 83(2):372–377, 2008.

[48] A Gumberidze, M Trassinelli, N Adrouche, CI Szabo, P Indelicato, F Haranger, J-M Isac, E Lamour, E-O Le Bigot, J Merot, et al. Electronic temperatures, densities, and plasma x-ray emission of a 14.5 ghz electron-cyclotron resonance ion source. Review of Scientific Instruments, 81(3):033303, 2010.

[49] D. Mascali, S. Gammino, L. Celona, and G. Ciavola. Towards a better comprehension of plasma formation and heating in high performances electron cyclotron resonance ion sources (invited). Review of Scientific Instruments, 83(2):02A336, 2012.

[50] Vladimir Mironov, Sergey Bogomolov, Andrej Bondarchenko, Andrej Efremov, Vladimir Loginov, and Dmitrii Pugachev. Spatial distributions of plasma potential and density in electron cyclotron resonance ion source. Plasma Sources Science and Technology, 29(6):065010, 2020.

[51] I Izotov, AG Shalashov, V Skalyga, ED Gospodchikov, O Tarvainen, V Mironov, H Koivisto, R Kronholm, V Toivanen, and BS Bhaskar. The role of rf-scattering in high-energy electron losses from minimum-b ecr ion source. Plasma Physics and Controlled Fusion, 2021.

[52] JY Benitez, JD Noland, D Leitner, C Lyneis, DS Todd, and J Verboncoeur. High energy component of x-ray spectra in ecr ion sources. LBNL, Proceedings of ECRIS08, Chicago, IL, USA, 2008.

[53] S Gammino, D Mascali, L Celona, F Maimone, and G Ciavola. Considerations on the role of the magnetic field gradient in ecr ion sources and build-up of hot electron component. Plasma Sources Science and Technology, 18(4):045016, 2009.

[54] C Perret, A Girard, H Khodja, and G Melin. Limitations to the plasma energy and density in electron cyclotron resonance ion sources. Physics of Plasmas, 6(8):3408–3415, 1999.

[55] JD Callen. Fundamentals of plasma physics (lecture notes)(madison, wi, 2003.

[56] E Naselli, D Mascali, M Mazzaglia, Sándor Biri, Richárd Péter Rácz, József Pálinkás, and Zoltán Perduk. Impact of two-close-frequency heating on ecr ion source plasma radio emission and stability. PLASMA SOURCES SCIENCE & TECHNOLOGY, 28(8), 2019.

[57] S Biri, A Valek, T Suta, E Takács, Cs Szabó, Lawrence T Hudson, B Radics, J Imrek, B Juhász, and J Pálinkás. Imaging of ecr plasmas with a pinhole x-ray camera. Review of scientific instruments, 75(5):1420–1422, 2004.

[58] J D Jackson. Classical electrodynamics. Wiley, New York, NY, 3rd ed. edition, 1999.

[59] RL Gluckstern and MH Hull Jr. Polarization dependence of the integrated bremsstrahlung cross section. Physical Review, 90(6):1030, 1953.

[60] HW Koch and JW Motz. Bremsstrahlung cross-section formulas and related data. Reviews of modern physics, 31(4):920, 1959.

[61] Anna Maria Massone, A Gordon Emslie, Eduard P Kontar, Michele Piana, Marco Prato, and John C Brown. Anisotropic bremsstrahlung emission and the form of regularized electron flux spectra in solar flares. The Astrophysical Journal, 613(2):1233, 2004.

[62] Y. Peysson and J. Decker. Fast electron bremsstrahlung in axisymmetric magnetic configuration. Physics of Plasmas, 15(9):092509, 2008.

[63] E Canobbio. Gyroresonant particle acceleration in a non-uniform magnetostatic field. Nuclear Fusion, 9(1):27, 1969.

[64] T Ropponen, O Tarvainen, I Izotov, J Noland, V Toivanen, G Machicoane, D Leitner, H Koivisto, T Kalvas, P Peura, et al. Studies of plasma breakdown and electron heating on a 14 ghz ecr ion source through measurement of plasma bremsstrahlung. Plasma Sources Science and Technology, 20(5):055007, 2011.

[65] A G Shalashov, A V Vodopyanov, S V Golubev, A G Demekhov, VG Zorin, D A Mansfeld, and SV Razin. Maser based on cyclotron resonance in a decaying plasma. JETP letters, 84(6):314–319, 2006.

Supplementary material

This document contains the supplementary material for the manuscript *"Correlation of bremsstrahlung and energy distribution of escaping electrons to study the dynamics of magnetically confined plasma"* by B.S. Bhaskar *et al.*

1. Description of the JYFL 14 GHz ECRIS magnetic field

Tables 1 and 2 list the magnetic field parameters for the solenoid field sweep at 14 GHz frequency. The parameters were calculated by obtaining axial magnetic field using finite element solver for 2D and axisymmetric magnetic field (FEMM) and then using 6th order polynomial fit and on it and obtained the analytical expression corresponding to the 2D field distribution as published by Rodney *et al.* [1] it was then superimposed with an ideal sextupole field to obtain the total magnetic field strength. Table 1 lists maximum axial magnetic field strength at injection (B_{inj} (T)), maximum axial magnetic field strength at extraction (B_{ext} (T)), ratio of minimum axial magnetic field to magnetic field corresponding to resonance (B_{min}/B_{ECR}), the magnetic field corresponding to the last closed surface obtained for 14 GHz heating frequency ($|B_{max,closed}|$ (T)) and the minimum magnetic field at the chamber walls near the poles ($|B_{min-chamberwall,poles}|$ (T)). Table 2 shows the magnetic field parameters derived from the superposition of the two field components and above-mentioned field values, i.e. average magnetic field gradient over the entire ECR surface ($< \nabla B_{ECR} >$ (T/m)), volume enclosed by the resonance zone (Volume of ECR (cc)), the radial mirror ratio calculated as the ratio of $|B_{min-chamberwall,poles}|$ to B_{ECR} (R_{radial}) and the axial mirror corresponding to the ratio of extraction magnetic field to magnetic field at resonance.

B_{inj} **(T)**	B_{ext} **(T)**	B_{min}/B_{ECR}	$\|B_{max,closed}\|$ **(T)**	$\|B_{min-chamberwall,poles}\|$ **(T)**
1.87	0.86	0.64	0.774	1.074
1.89	0.87	0.66	0.777	1.077
1.91	0.89	0.68	0.780	1.079
1.93	0.90	0.69	0.783	1.081
1.95	0.92	0.71	0.786	1.084
1.97	0.93	0.73	0.790	1.087
1.99	0.94	0.75	0.793	1.090
2.01	0.96	0.76	0.797	1.093
2.02	0.97	0.78	0.801	1.096
2.04	0.99	0.80	0.805	1.099
2.06	1.00	0.82	0.809	1.102

Table 1. Magnetic field parameters of the ECR zone corresponding to 14 GHz heating frequency.

B_{min}/B_{ECR}	$< \nabla B_{ECR} >$ (T/m)	Volume of ECR (cc)	R_{radial}	R_{axial}
0.64	7.31	199	2.134	1.710
0.66	6.99	189	2.139	1.740
0.68	6.66	179	2.144	1.769
0.69	6.33	170	2.148	1.799
0.71	6.00	160	2.154	1.828
0.73	5.67	150	2.159	1.857
0.75	5.33	141	2.165	1.886
0.76	5.00	131	2.171	1.915
0.78	4.66	121	2.177	1.944
0.80	4.33	111	2.183	1.972
0.82	4.00	102	2.190	2.001

Table 2. Table showing magnetic field parameters calculated from 3D magnetic field modelling of ECR zone.

2. Bremsstrahlung and LEED data treatment

Efficiency and energy calibration of the x-ray spectrum were done to the raw data using known characteristic peaks of americium-241 and barium-133. The calibrated efficiency curve compared with the calibration curve provided by the detector manual (Amptek CdTe) is shown in Fig. 1. Figure 2 presents an example comparison of raw and efficiency calibrated data.

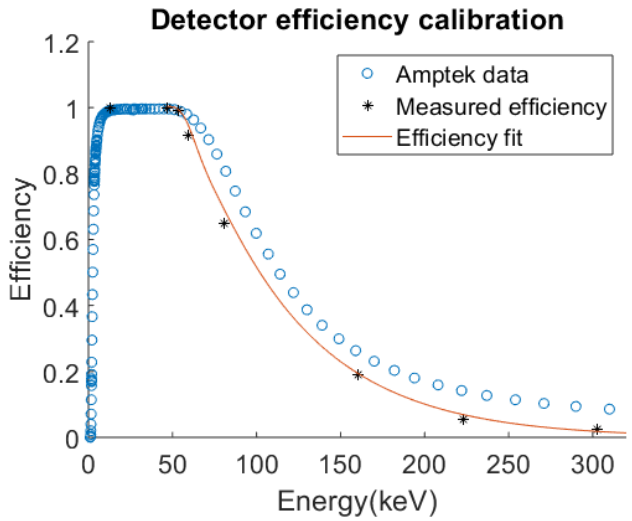

Figure 1. Plot showing calculation of detector efficiency from characteristic peaks of Am-241 and Ba-133

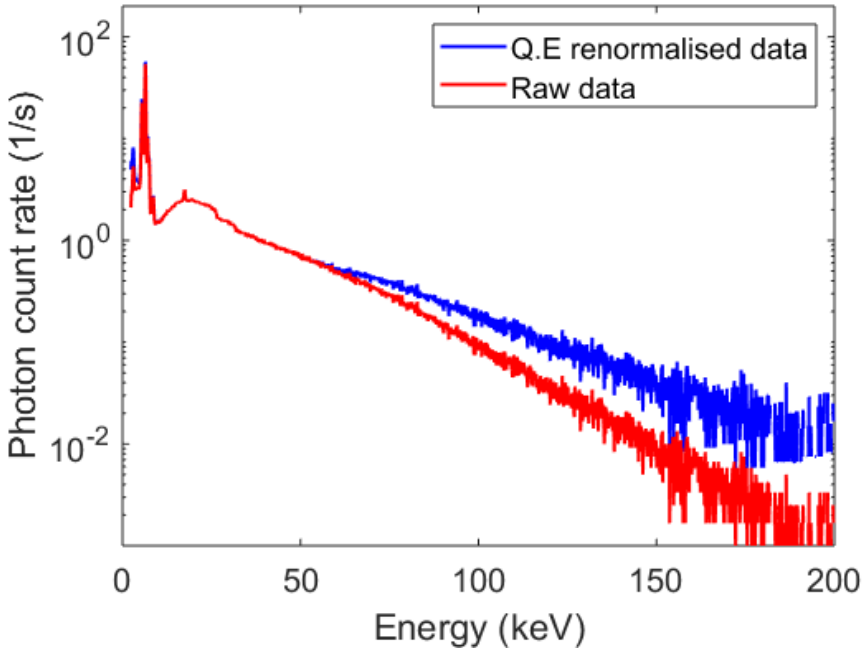

Figure 2. The axial bremsstrahlung spectra for B_{min}/B_{ECR} of 0.68 with and without efficiency calibration.

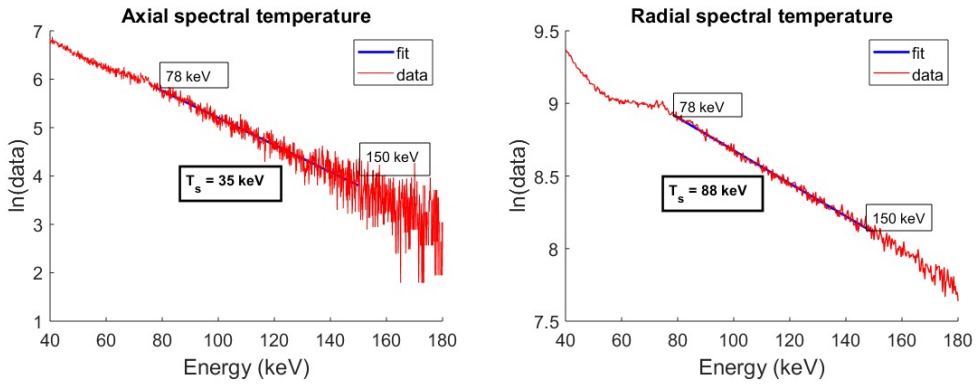

Figure 3. An example of radial and axial bremsstrahlung spectra showing the energy range for obtaining the spectral temperature.

The spectral temperature is calculated for the energy range of 78 keV to 150 keV for the axial and radial bremsstrahlung spectra. The lower limit was chosen to avoid the inclusion of a Pb characteristic peak at 72 keV. A linear function was fitted to this energy range of the measured bremsstrahlung spectra (in logarithmic scale):

$$ln(data) = mE + c \tag{1}$$

where E is the photon energy in keV and m, c are constants obtained from the fit. The spectral temperature T_s is then determined from the slope m as [2, 3]

$$T_s = -1/m \tag{2}$$

The same procedure was used in the manuscript for both the measured axial and radial spectra. An example of the fitting is shown in Fig. 3.

In the LEED measurements a distinct local maximum is observed at electron energies around 220 keV. To study the variation of this "hump", a combination of an exponential decay function (λ) and a Gaussian function (G) was fitted to the experimental data. These functions were defined as

$$\lambda(\varepsilon) = a * exp(b * \varepsilon) \tag{3}$$

and

$$G(\varepsilon) = a_1 exp(-((\varepsilon - b_1)/c_1)^2) \tag{4}$$

where a, a_1, b, b_1, c_1 are constants obtained from the fitting and ε is the electron energy in keV. An example of the fitting is presented in Fig. 4. The total and average electron energies associated with the hump were then calculated from the Gaussian part of the fitted function. The total energy was calculated with equation

$$\varepsilon_{tot} = \int_{\varepsilon_{min}}^{\varepsilon_{max}} G(\varepsilon) \cdot d\varepsilon \tag{5}$$

and the average energy with the equation

$$\varepsilon_{avg} = \frac{1}{\varepsilon_{tot}} \int_{\varepsilon_{min}}^{\varepsilon_{max}} G(\varepsilon) \cdot \varepsilon \cdot d\varepsilon \tag{6}$$

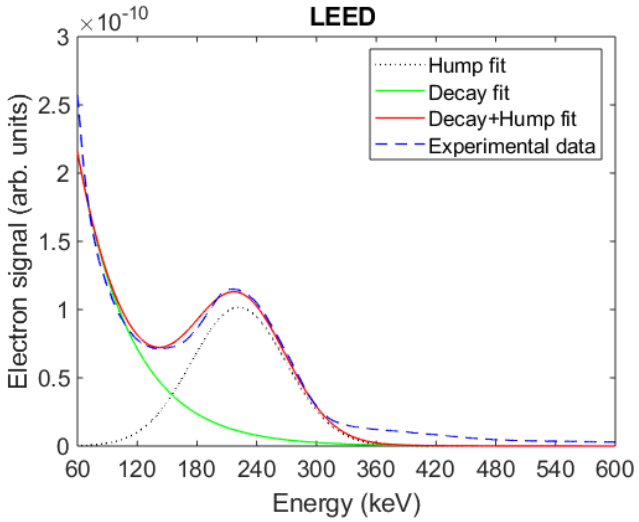

Figure 4. An example case for the method used for determining the total and average electron energy of the LEED hump by separating the high energy hump using a Gaussian fitting function. The spectrum shown here is obtained for 600 W microwave power, $B_{min}/B_{ECR} = 0.69$, -70 V bias disk and $3.5 \cdot 10^{-7}$ mbar neutral gas pressure.

3. Determination of unstable plasma regimes

Three different stability regimes were identified in the studies presented in the manuscript; stable plasma, unstable plasma with pulse-periodic instabilities and unstable plasma with

continuous maser emissions (CW mode). These regimes and the transitions from one to another can be identified using temporally resolved x-ray diagnostic (e.g. x-ray scintillator) combined with microwave spectrum diagnostic (e.g. spectrum analyser). At the onset of pulse-periodic instabilities periodic bursts of x-rays are detected with microwave emissions at different random frequencies in a broad frequency band. In the CW mode the x-ray bursts disappear and the random microwave emissions are replaced by emission at one or more fixed frequencies. An example of a typical CW emission spectrum from the experimental campaign presented in the manuscript is shown in Fig. 5.

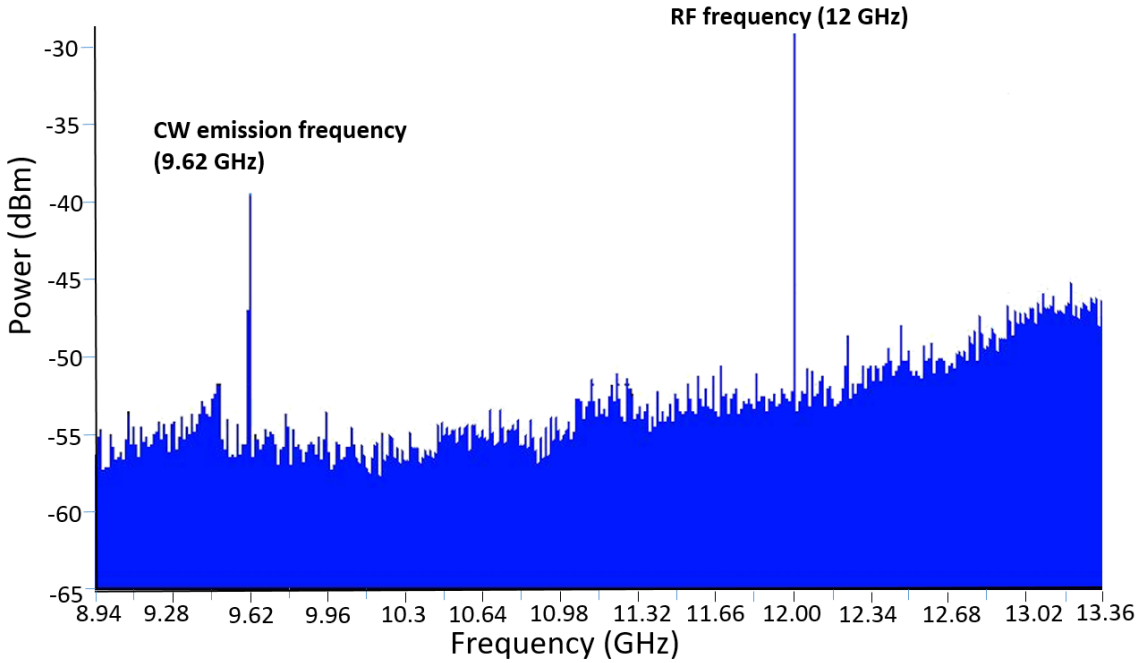

Figure 5. An example of spectrum analyser measurement of plasma emitted microwaves. The obtained spectrum shows the input heating frequency of 12 GHz and the CW microwave emission at the frequency of 9.62 GHz.

4. Contribution of thick target bremsstrahlung in axial x-ray measurements of ECRIS plasma

In the case of axial bremsstrahlung measurements of ECRIS plasmas the measured spectra can include a significant contribution of thick target radiation, even when using a sophisticated collimation scheme. Figure 6 presents the normalised photon counts of characteristic x-rays (K-α) of iron and the total counts in the measured spectra as a function of the B_{min}/B_{ECR} ratio of the JYFL 14 GHz ECRIS, measured axially through the extraction aperture. In addition to iron also molybdenum was measured, but as it exhibit identical behaviour with iron, it is not shown here. Iron and molybdenum were chosen as they are constituents of the steel bias disk which is located at the injection end of the aluminium plasma chamber of the ion source, and directly in the line of sight of the x-ray detector through the plasma volume. The fact that

these characteristic peaks are clearly present in the measured spectra makes it evident that the x-ray detector is measuring thick target bremsstrahlung from the bias disk. Furthermore, it is observed that the characteristic x-rays of iron exhibit the same trend as the total photon counts. These observations indicate that thick target bremsstrahlung contributes significantly to the measured axial signal and consequently it is not possible to separate it from the primary plasma bremsstrahlung.

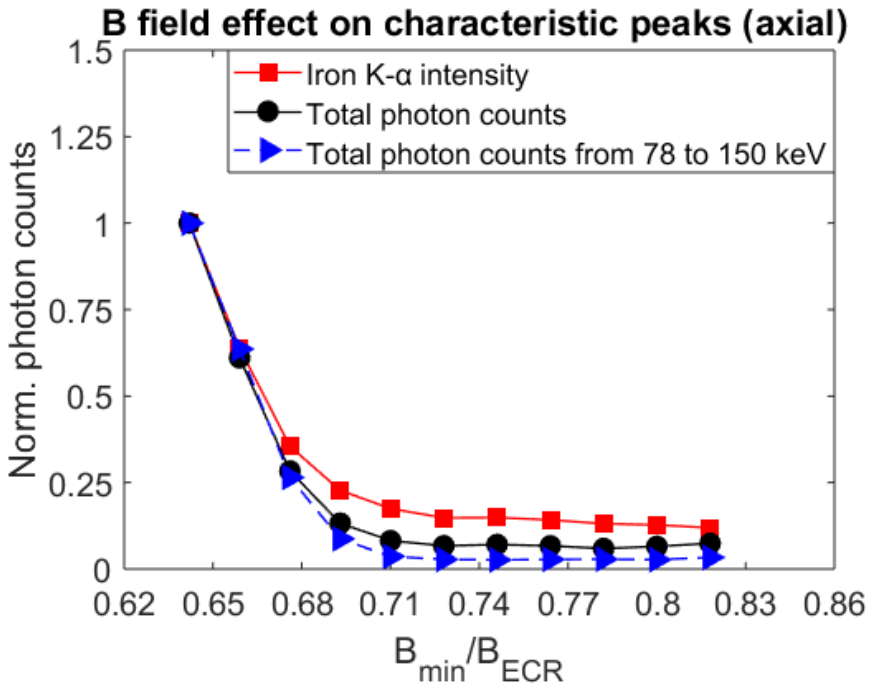

Figure 6. The effect of magnetic field on the normalised characteristic x-ray peak of iron originating from the bias disk and the total photon counts. The total photon counts have been calculated for the whole spectra and for the high energy section which is used to determine the spectral temperature.

5. Thick target bremsstrahlung from redistribution of electron losses

In the radial and axial bremsstrahlung measurements of the ECR plasma with varying axial magnetic field, there is a possibility that the redistribution of the electron losses due to shifting confinement conditions and the resulting variation in the related thick target bremsstrahlung production can contribute to the observed results. Furthermore, the decrease in electron signal strength of axially lost electrons (as observed in the LEED measurements) implies that the radial energy (electron losses) increases with the axial mirror ratio assuming that absorbed fraction of the microwave power remains constant across the magnetic field sweep. From table 1 and 2 it is evident that the solenoid magnetic field also affects the total magnetic field at the chamber wall. Both, the axial and radial mirror ratios increase as the B_{min}/B_{ECR} increases with the solenoid currents. The radial mirror ratio (calculated from the weakest total magnetic field on the magnetic pole w.r.t. B_{ECR}, see Fig. 7; where $B_{min-chamberwall,poles}$ corresponds to

weakest magnetic field at pole) increases only 3 % whereas the axial mirror ratio increases by 17 % as shown in Fig. 8. Altogether this implies that the ratio between radial and axial electron losses should increase with increasing coil current, i.e. B_{min}/B_{ECR} ratio, assuming that the distribution of electron losses via RF-scattering (which is the predominant electron loss mechanism for high energy electrons [4]) follows the mirror ratios. The redistribution of electron losses with increasing solenoid field strength is further supported by a simulation of the electron losses from the magnetic confinement of the JYFL 14 GHz ECRIS. The simulation was done by tracking single electron trajectories with random initial locations inside the ECRIS plasma chamber that satisfy the condition $B < B_{ECR}$ and by considering the effect of the magnetic field alone on the electron trajectory. A detailed explanation of the simulation technique has been published by Kalvas *et al.* [5]. Figure 9 presents the simulated fraction of radial to axial electron losses for three different electron energies; 10 keV, 100 keV and 220 keV. The simulations show that increasing the B_{min}/B_{ECR} ratio favours the radial losses of electrons, supporting the experimental bremsstrahlung and LEED observations. Thus the redistribution of the electron losses could also explain or contribute to the observed increase of the radial bremsstrahlung spectral temperature if the spectra were affected by wall bremsstrahlung. It is worth noting that the electron loss simulation suggests a factor of two increase in the ratio between radial and axial losses with the magnetic field sweep whereas the corresponding ratio in the bremsstrahlung measurement is larger. Furthermore, it must be precised that the location of radial electron impact on the plasma chamber wall is not visible from the collimated line of sight of the radial x-ray detector. Thus, the process for a hypothetical radial detection of wall generated bremsstrahlung x-ray require at least one photon scattering to change the photon direction into the solid angle of detection. However, the interpretation of this discrepancy is not unambiguous since the magnetic field affects the electron energy distribution of both, the confined and lost electrons, which in turn modifies the bremsstrahlung spectrum.

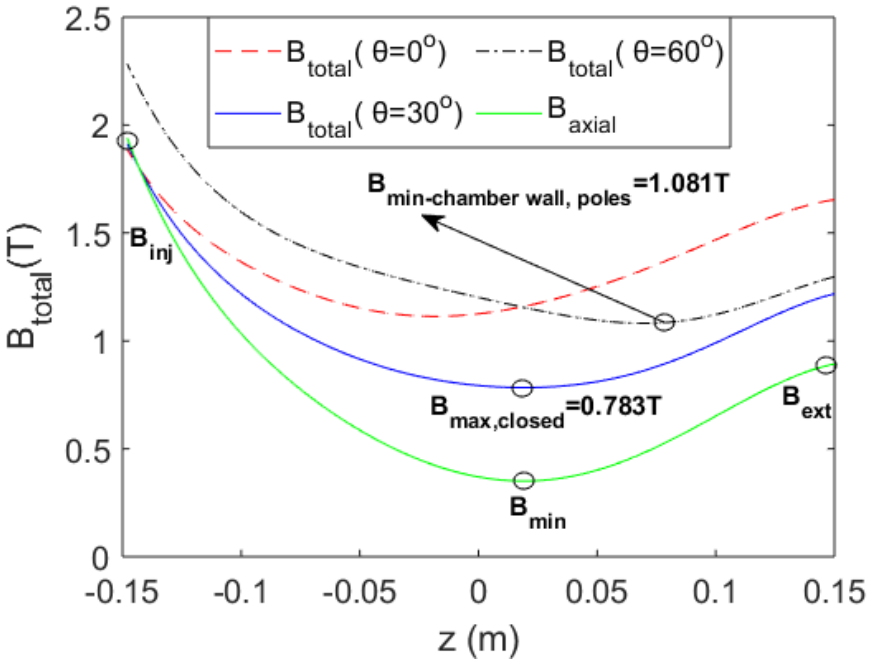

Figure 7. Figure showing variation of total magnetic field near the poles of the hexapole where $\theta = 60$ degree represents poles and the minimum magnetic field at $\theta = 30$ defines the $|B_{max,closed}|$. The plotted magnetic field corresponds to $B_{\min}/B_{\mathrm{ECR}}$ ratio = 0.69 and $|B_{min-chamberwall,poles}|$ corresponds to minimum magnetic field at the chamber walls near the poles.

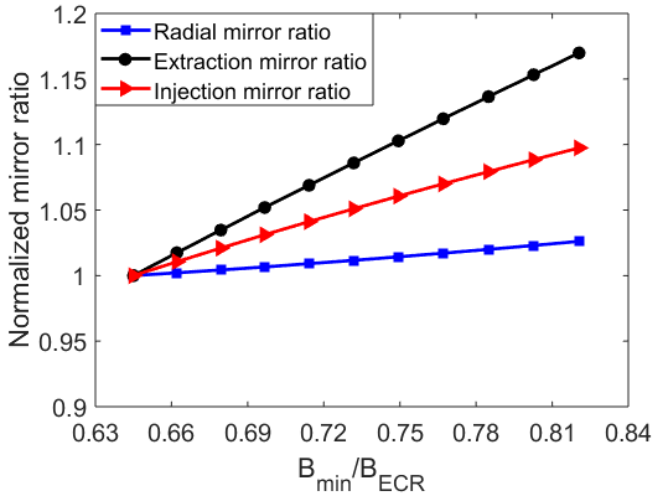

Figure 8. The change in the radial and axial mirror ratios with increasing solenoid magnetic field (characterised with the $B_{\min}/B_{\mathrm{ECR}}$ ratio).

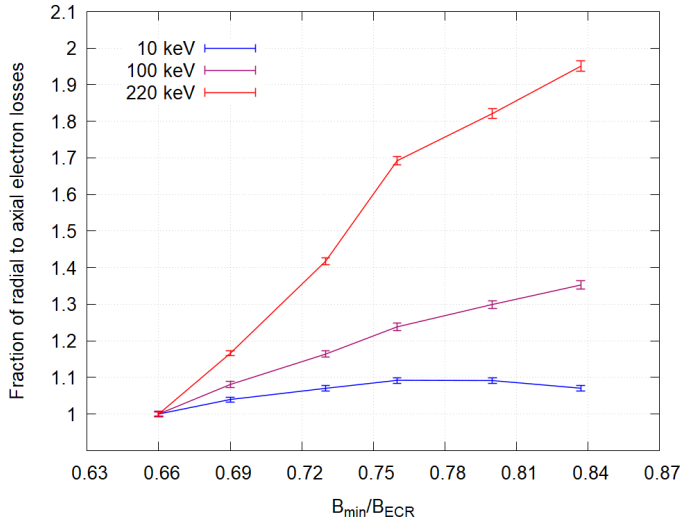

Figure 9. Simulated fraction of radial to axial electron losses from the magnetic confinement of JYFL 14 GHz ECRIS with increasing axial magnetic field. The magnetic field is characterised with the $B_{\mathrm{min}}/B_{\mathrm{ECR}}$ ratio and the results are presented for three different electron energies; 10 keV, 100 keV and 220 keV. The error estimation for the ratio of losses is calculated from the propagation of the statistical errors.

References

[1] JRM Vaughan. Representation of axisymmetric magnetic fields in computer programs. IEEE Transactions on Electron Devices, 19(2):144–151, 1972.

[2] J. Benitez, C. Lyneis, L. Phair, D. Todd, and D. Xie. Dependence of the bremsstrahlung spectral temperature in minimum-b electron cyclotron resonance ion sources. IEEE Transactions on Plasma Science, 45(7):1746–1754, 2017.

[3] A Gumberidze, M Trassinelli, N Adrouche, CI Szabo, P Indelicato, F Haranger, J-M Isac, E Lamour, E-O Le Bigot, J Merot, et al. Electronic temperatures, densities, and plasma x-ray emission of a 14.5 ghz electron-cyclotron resonance ion source. Review of Scientific Instruments, 81(3):033303, 2010.

[4] I Izotov, O Tarvainen, V Skalyga, D A Mansfeld, H Koivisto, R Kronholm, V Toivanen, and V Mironov. Measurements of the energy distribution of electrons lost from the minimum b-field—the effect of instabilities and two-frequency heating. Review of Scientific Instruments, 91(1):013502, 2020.

[5] T Kalvas, O Tarvainen, H Koivisto, and K Ranttila. Thermal design of refridgerated hexapole 18 ghz ecris hiisi. In Proceedings of ECRIS 2014: the 21st International Workshop on ECR Ion Sources, ISBN 978-3-95450-158-8. Institute of Applied Physics of the Russian Academy of Sciences, 2014.

PIV

QUASI-PERIODICAL KINETIC INSTABILITIES IN MINIMUM-B CONFINED PLASMA

by

Bhaskar, BS and Koivisto, H and Tarvainen, O and Thuillier, T and Toivanen, V
2022

AIP Advances **12**, 1 015223

Quasi-periodical kinetic instabilities in minimum-B confined plasma

Cite as: AIP Advances **12**, 015223 (2022); https://doi.org/10.1063/5.0070824
Submitted: 09 September 2021 • Accepted: 05 January 2022 • Published Online: 24 January 2022

B. S. Bhaskar, H. Koivisto, O. Tarvainen, et al.

Quasi-periodical kinetic instabilities in minimum-B confined plasma

Cite as: AIP Advances 12, 015223 (2022); doi: 10.1063/5.0070824
Submitted: 9 September 2021 • Accepted: 5 January 2022 •
Published Online: 24 January 2022

B. S. Bhaskar,[1,2,a] H. Koivisto,[1] O. Tarvainen,[1,3] T. Thuillier,[2] and V. Toivanen[1]

AFFILIATIONS

[1] Department of Physics, University of Jyväskylä, P.O. Box 35 (YFL), 40500 Jyväskylä, Finland
[2] LPSC, INP Grenoble, CNRS/IN2P3, Université Grenoble-Alpes, 53 rue des Martyrs, 38026 Grenoble Cedex, France
[3] STFC ISIS Pulsed Spallation Neutron and Muon Facility, Rutherford Appleton Laboratory, Harwell OX11 0QX, United Kingdom

[a] Author to whom correspondence should be addressed: bisubhas@jyu.fi

ABSTRACT

We present the results of an experimental investigation of quasi-periodical kinetic instabilities exhibited by magnetically confined electron cyclotron resonance heated plasmas. The instabilities were detected by measuring plasma microwave emission, electron losses, and wall bremsstrahlung. The instabilities were found to be grouped into fast sequences of periodic plasma losses, separated by ~100 μs between the bursts, followed by 1–10 ms quiescent periods before the next event. Increasing the plasma energy content by adjusting the plasma heating parameters, in particular the magnetic field strength, makes the instabilities more chaotic in the time domain. Statistical analysis reveals that the energy released in a single instability event depends on the magnetic field strength and microwave power but not on the neutral gas pressure. The effects of these ion source parameters on the instability characteristics are explained qualitatively by considering their influence on the electron energy distribution. A correlation is found between the energy dissipated in an instability event and the recovery time of the periodic bursts, i.e., a large amplitude instability leads to a long recovery time of the electron energy distribution.

I. INTRODUCTION

Cyclotron maser instabilities caused by the resonant interaction between high energy electrons and electromagnetic waves are a fundamental feature of electron cyclotron resonance (ECR)-heated open plasma traps and minimum-B configurations with strongly anisotropic electron velocity distribution.[1,2] In the past, experimental studies of such instabilities have been conducted with magnetic mirror traps intended for thermonuclear fusion experiments[3] and simple mirror plasma generators dedicated for fundamental plasma physics studies.[4] In the pulse-periodic instability regime of the minimum-B confined plasma, the plasma–electromagnetic wave interaction results in abrupt bursts of microwave emission[5,6] and electrons escaping the confinement,[7] which in turn results in strong spikes of (thick target) bremsstrahlung emission (x ray) from the plasma chamber walls.[8] The instability-induced electron losses result in fast fluctuations of the plasma potential and subsequent ion losses including the extracted ion beam current,[9] significantly decreasing the average charge state of the ions both in the plasma and in the time-averaged extracted beam.[10,11]

Systematic studies of the cyclotron maser instabilities, fundamentals of which are described in Ref. 12, in the continuous operation mode of the ECRIS have revealed several stability regimes. The transition between them can be controlled by adjusting the source parameters,[8] most notably the magnetic field strength at the minimum-B (B_{min}), which is known to influence the electron energy distribution (EED)[7,13] and the x-ray emission of minimum-B ECRISs.[14,15] These regimes can be broadly categorized as (i) stable plasma with no detectable microwave emission above the background electron cyclotron emission (ECE), (ii) pulse-periodic regime with abrupt bursts of microwave emission at specific frequencies[5,16] and electron precipitation,[7] both observed at the 0.1–1 kHz order of the magnitude repetition rate,[8,17] (iii) pulsed regime characterized by very strong instabilities (referred to as "giant pulses" by some authors[5]) occurring at irregular intervals and corresponding to a rich frequency spectrum of the microwave emission,[6] and (iv) continuous maser emission regime.[18,19]

All cyclotron maser instabilities observed in the various regimes of ECRIS plasmas are caused by the temporal modulation of the

electron distribution function due to the excitation of unstable kinetic modes.[1] This is because distributions of fast electrons formed under electron cyclotron heating are usually unstable with respect to the excitation of electromagnetic waves in the same frequency range, as described thoroughly elsewhere.[20,21] Different dynamic regimes of the cyclotron maser instability represent different sets of steady-state solutions for the electron energy distribution $\left(\frac{\partial \bar{f}}{\partial t}\right)$ and energy content $\left(\frac{\partial W}{\partial t}\right)$ balance equations. The solutions described in Ref. 20 include a continuous wave (cw) maser emission corresponding to a certain electromagnetic mode, i.e., regime (iv) mentioned above, as well as temporally modulated maser emission consisting of intense bursts of electromagnetic radiation (and subsequent electron precipitation) separated by long periods of small amplitude emission, i.e., regimes (ii) and (iii). The stable regime can be expanded notably in terms of magnetic field strength and microwave power by applying two-frequency heating.[22]

In the pulse-periodic solutions, the energy content of the EED oscillates between a minimum value following each instability burst and a maximum corresponding to the trigger level of the instability, at which the growth rate (γ) of the amplified electromagnetic (EM)-wave exceeds its damping rate (δ), i.e., $\frac{dE_\mu}{dt} \approx \langle \gamma - \delta \rangle E_\mu > 0$. The (volumetric) growth rate is proportional to the ratio of hot and cold electron densities, whereas the damping rate is determined by volumetric absorption of the wave energy by the background plasma and external (wall) losses (the reader is referred to the literature for the parametric dependencies of the growth and damping rates[23–25]). Between these extremes, the energy content of the EED builds up at a rate, which depends on the source (electron heating), $S(t)$, and loss, $L(t)$, and terms of hot electrons (rf-scattering, collisional losses, and energy damping by inelastic processes). The balance equation[20,26] for the hot electron (number) density $N_{e,hot}$ can be written as $\frac{dN_{e,hot}}{dt} \approx -\kappa N_{e,hot} E_\mu + S(t) - L(t)$, where κ is a coefficient[27] describing the amplification of the electromagnetic wave and the corresponding decrease of the hot electron number density due to direct energy loss. Thus, it can be hypothesized that the repetition rate of the instabilities is correlated with the source and loss terms during the quiescent period between instabilities, which are affected by the source parameters,[8,28] and with the energy loss associated with the instability. The latter implies that the energy accumulation time to reach the instability threshold should depend on the energy loss associated with the preceding instability event. In this scenario (a), the time between instability bursts depends on their magnitude, a large amplitude burst leading to long recovery time until the next event. Alternatively, the plasma parameters may be perturbed by the instability in such a manner that the threshold plasma energy content to trigger the instability shifts between consecutive bursts. In this scenario (b), a long accumulation time is followed by a large magnitude burst, releasing the energy stored in the hot tail of the EED.

Since both scenarios (a) and (b) are feasible and studies of magnetospheric plasmas have revealed that dynamics of the instabilities could depend on the magnitude of the energy dissipation in an instability event,[29] we have carried out an experimental campaign measuring the correlation between the instability signal amplitudes and the recovery/accumulation times (see the definitions below) in a controlled laboratory experiment with a minimum-B ECRIS. In particular, we focus on parametric dependencies of the energy dissipation by the instability and the dependence of recovery and accumulation times of the dissipated energy. This is done to demonstrate that one of the above scenarios appears to be a fundamental feature of the minimum-B trap, independent of control parameters (magnetic field strength, microwave power, and neutral gas pressure). By recovery time, we refer to the time following an instability event required to restore the unstable EED, whereas by accumulation time, we refer to the time preceding the instability event, i.e., the recovery time of instability event i is the accumulation time of event $i + 1$. One can also define the period of the instability event i as the sum of the event time i (time during which one or several bursts are observed) and the recovery time i. The main purpose of this experimental study is to support the development of the practical cyclotron maser theory[21] applicable for ECR-heated laboratory plasmas serving as a proxy for a range of naturally occurring plasmas where such phenomena can exist.[24,30–32] This is achieved by carrying out a phenomenological investigation of the instability energy dissipation and recovery/accumulation times as a function of ECRIS tuning parameters, namely, the strength of the solenoid magnetic field, microwave heating power, and neutral gas density. Based on previous studies, these parameters are believed to affect the plasma parameters as follows: the magnetic field strength affects the electron energy distribution and average energy, while the microwave power and neutral gas density affect the plasma density (for detailed discussion, see, e.g., Ref. 15 and references therein).

II. EXPERIMENTAL SETUP AND PROCEDURE

The experimental data were taken with the A-ECR type JYFL 14 GHz ECR ion source[33] at the Accelerator Laboratory of the University of Jyväskylä. The source is a room-temperature ECRIS operated at the 14.055 GHz plasma heating frequency. The minimum-B magnetic field structure for plasma confinement is produced with two solenoid coils (axial mirror fields) and a NdFeB permanent magnet hexapole (radial mirror field). The nominal on-axis magnetic field maxima are 1.93 T in the injection side of the plasma chamber (B_{inj}) and 0.90 T in the extraction side (B_{ext}). The nominal minimum field (B_{min}) inside the chamber is 0.35 T and the radial maximum at the chamber wall is B_{rad} = 1.09 T when the solenoids are not energized. The axial magnetic field can be varied by adjusting the solenoid currents, which also affects the strength of the radial field in those locations where the plasma flux meets the chamber wall.

In our experiment, the plasma density in the core plasma can be expected to range from 10^{11} to 2.5×10^{12} cm^{-3}, where the lower limit has been defined experimentally on a similar device[34] and the upper limit corresponds to the cutoff frequency of 14 GHz microwaves. The spatial variation of the plasma density can be expected to be very strong, with the core plasma surrounded by the closed ECR zone reaching the aforementioned densities,[35,36] whereas the peripheral plasma density is 1–2 orders of magnitude lower. It has been estimated that each instability onset expels ~0.1–1 μC of negative charge, with the upper limit corresponding to ~10% of the confined electron population.[9] ECRIS plasmas are strongly anisotropic and are considered to consist of cold electrons (created by ionizing electron–ion collisions and plasma–wall interaction) with an average energy $E_{\mathrm{e,cold}}$ of 10–100 eV, warm electrons responsible for the stepwise ionization with an $E_{\mathrm{e,warm}}$ of 1–10 keV, and hot electrons with an $E_{\mathrm{e,hot}}$ of 10–100 keV.[37,38] It has been shown previously[13]

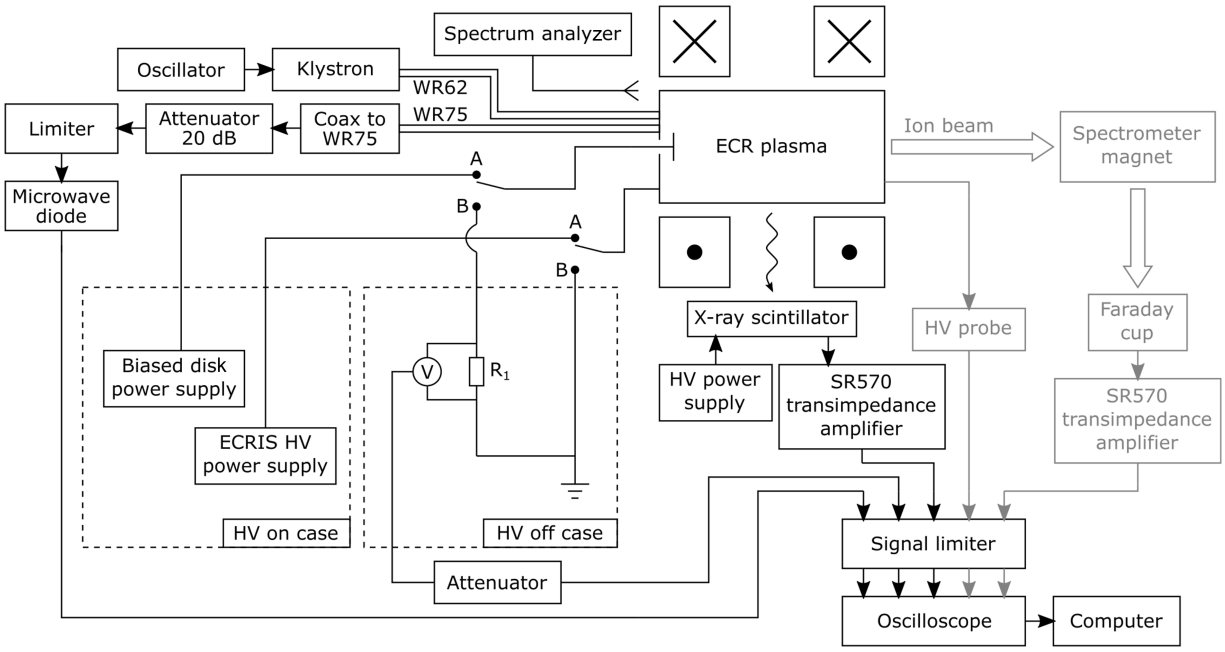

FIG. 1. A schematic presentation of the experimental setup. For simplicity, the different connections for the two measurement modes, high voltage (HV) on and HV off, have been presented with two switches, both of which are simultaneously toggled either to the *A* (HV on) or *B* (HV off) position. In order to ensure that the ion source was functioning properly during the experiments, the extracted ion beam currents and the source HV platform voltage were also monitored. These signals are not part of the reported instability analysis but are presented in the schematic (in gray) for the sake of completeness.

that in our setup, the EED (of axially escaping electrons) is strongly non-Maxwellian with a maximum electron energy of ~500 keV.

Figure 1 presents the experimental setup and the different diagnostics used in the measurements. Two waveguides can be used to transmit microwaves into the plasma chamber. The main (WR62) waveguide was used for plasma heating, connecting the plasma chamber to a klystron amplifier driven by an oscillator providing the 14.055 GHz heating frequency. The secondary (WR75) waveguide was used for microwave diagnostics. The microwave emission from the plasma was measured with a microwave-sensitive Schottky diode. A WR75-to-coax adapter was used to connect the diode to the waveguide. In addition, a 20 dB (20 W) attenuator and a microwave signal limiter were placed in the coaxial line between the ion source and the diode to protect it from the potentially very strong signals that can occur during the instability events. The microwave emission was also detected with a spectrum analyzer (Keysight FieldFox Microwave Analyzer N9918B). This was done because distributions of fast electrons formed under strong electron cyclotron heating are usually unstable with respect to excitation of electromagnetic waves in the same frequency range.[21] Thus, we use the microwave emission spectrum to confirm that the above condition for maser-type kinetic instabilities is met in our experiment. An example of the emission spectrum recorded with 7.8 s sweep time across the presented frequency range is shown in Fig. 2. It is emphasized that the spectrum analyzer cannot measure individual bursts but rather the overall emission spectrum consisting of frequencies emitted in multiple instability onsets, as thoroughly explained elsewhere.[39] The data are presented to make the point that the microwave radiation frequencies emitted by the instabilities are characteristic to our experimental setup and are predominantly lower than the plasma heating frequency (with their harmonics found above 20 GHz).[5,6]

The 21 mm diameter circular biased disk located at the injection end of the plasma chamber was used to probe the electron

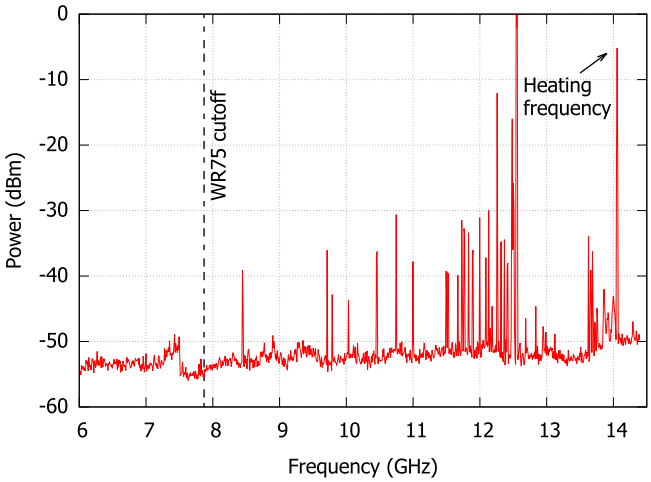

FIG. 2. Microwave emission spectrum measured with a spectrum analyzer during unstable plasma conditions. The emission frequencies are discrete. The emission peak corresponding to the plasma heating frequency (14.055 GHz) is indicated with an arrow. The WR75 waveguide cutoff frequency (7.87 GHz) is also indicated with a vertical dashed line. In the stable regime, the only detectable emission is at the heating frequency.

and ion losses during the instabilities. As demonstrated earlier,[9] the electron and ion signals recorded with the biased disk provide quantitative information on the negative and positive charge expelled from the plasma through the injection end mirror at each instability burst.

The bursts of thick target x-ray emission from the plasma chamber walls, caused by the electron losses during the instability events, were recorded with a bismuth germanate (BGO) scintillator coupled with a Na-doped CsI photocathode and a photo-multiplier tube (PMT). The detector was operating in the DC (or current) mode, allowing the detection of both the instability-induced x-ray bursts and the continuous background signal. The scintillator was placed outside the ion source plasma chamber and the hexapole. Axially the scintillator was located at the center of the plasma chamber between the iron yokes of the solenoid coils and azimuthally at one of the poles of the hexapole magnet structure. A −700 V bias was supplied to the PMT from a separate power supply. The bias voltage sets the gain and detection threshold of the PMT and, thus, the bias voltage was kept constant throughout the experimental campaign. The PMT output was amplified and converted to a voltage signal with a transimpedance amplifier (Stanford Research Systems SR570).[40] In such a configuration, the detector signal is proportional to the x-ray power flux but cannot be used for quantitative measurements of electron losses as the efficiency of the scintillator depends on the photon energy and the photon energy spectrum depends on the EED causing x-ray emission from the wall.

All the diagnostic signals were recorded with a picoscope (model 5444B).[41] The signals were routed through a diode based signal level limiter with a ±25 V limiting threshold to protect the picoscope from input signal overload, which could potentially occur in the pulsed instability regime with the strongest instability events, i.e., regime (iii) mentioned previously.

The microwave power, magnetic field, and gas feed were varied to produce a range of unstable plasma conditions within regimes (ii) and (iii). Each of these parameters was varied independently, while the others were kept constant during the parameter sweeps: The microwave power was varied between 400 and 600 W, while keeping both coil currents at 540 A ($B_{\min}/B_{\mathrm{ECR}} = 0.774$) and the plasma-off gas pressure at $3.5 \cdot 10^{-7}$ mbar, recorded with an ionization gauge connected to one of the radial ports of the plasma chamber. The coils were varied between 535 and 575 A ($B_{\min}/B_{\mathrm{ECR}}$ between 0.765 and 0.837) with 400 W microwave power and $3.5 \cdot 10^{-7}$ mbar pressure. The chamber pressure was varied between $3.0 \cdot 10^{-7}$ and $4.5 \cdot 10^{-7}$ mbar (plasma off values) with 300 W microwave power and 575 A coil currents ($B_{\min}/B_{\mathrm{ECR}} = 0.837$). In order to confirm the reproducibility of the data, the data acquisition for the magnetic field sweep was conducted twice. The reproducibility of the data is discussed and illustrated in the supplementary material (Fig. S6), showing a very good agreement between the two datasets (with a relative discrepancy ≤3.5%), which strengthens the conclusions of the study. All measurements were performed with oxygen plasmas as the majority of the published experiments (see Refs. 1, 5, 8–10, 22, and 42–49) investigating the instabilities in our setup have been conducted with oxygen. The characteristics of the instabilities are found to be similar with other gases, e.g., helium, argon, or xenon, whereas the gas affects the exact magnetic field threshold of the transition between stable and unstable regimes,[11] presumably due to different inelastic collision rates affecting the instability damping rate.

In order to allow simultaneous recording of the biased disk signal with the other diagnostics using the same measurement earthing, the experiments were performed both with and without the ion source high voltage. In the measurements with the high voltage, the source potential was set to 10 kV and the biased disk was connected to a −1 kV/10 mA power supply set to −70 V (a typical value for operation). The biased disk power supply was floating on the source potential. In this configuration, the microwave and x-ray signals were recorded concurrently. For the instability-induced biased disk electron/ion flux measurements, the plasma chamber was earthed and the disk power supply was disconnected. The current of the biased disk was monitored by measuring the voltage across a 1 kΩ series resistor, which was added between the disk and the laboratory earthing. A 12 dB attenuator was used to reduce the biased disk signal during the instabilities to a suitable level for the data acquisition. In this configuration, the microwave, biased disk, and x-ray signals were recorded simultaneously.

The operation with the high voltage on is the *modus operandi* of the ECR ion source, and it has been shown that applying the source potential affects the plasma parameters[50,51] and the instability threshold.[8] On the other hand, the x-ray signal is affected by the escaping electron energy distribution, attenuation of the photon flux in the structure of the ion source, and location of the scintillator and its efficiency, whereas the microwave emission signal strength depends on the coupling of the microwave radiation to the (diagnostics) waveguide and its attenuation in the waveguide, i.e., the amplitude of the detected signal is strongly affected by the frequency of the emitted microwaves. Hence, the instability-induced biased disk current transient (recorded with HV off) can be considered to be the most primitive diagnostics, directly measuring the

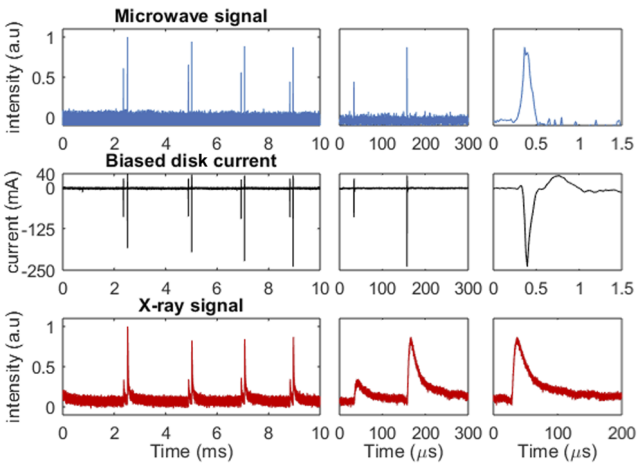

FIG. 3. An example of simultaneous detection of instability-induced signals with different diagnostic methods. Here, the instability events are separated by ∼2 ms and consist of two bursts (referred to as mode $n = 2$ later). The two stage zoom on the right illustrates the characteristic time scale between the bursts within an instability event, separated by ∼100 μs, and that of a single burst. The microwave and electron bursts of the biased disk (negative signal) last ∼0.2 μs, the latter being followed by a burst of ions (positive signal), restoring the quasi-neutrality of the plasma. The decay time of the x-ray signal is defined by the RC-constant of the transimpedance amplifier.

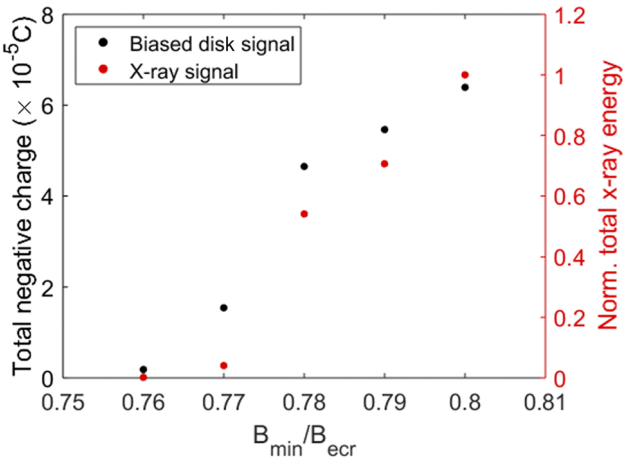

FIG. 4. The effect of the *B*-field on the total negative charge expelled by the instabilities measured from the biased disk and the measured total x-ray energy. The observables are integrated, i.e., individual burst signals are summed, over the 10 s data acquisition time at each magnetic field setting. The methodology to calculate the normalized plasma energy loss from the measured x-ray signal is described in the supplementary material. The pressure was kept constant at 3.5×10^{-7} mbar and the RF power at 600 W.

charge (negative and positive) expelled by each burst to the ion source injection end. Figure 3 shows an example of the diagnostic signals exhibiting abrupt bursts characteristic to the pulse-periodic maser instability. For each ion source setting, a total of 10 s of data were recorded to accumulate a sufficient amount of statistics. The data were recorded in 1 s segments with a temporal resolution of 16 ns used for all diagnostic signals.

In Secs. III and IV, we will use the x-ray signal for the majority of the data analysis and presentation. This is because under certain ion source parameters and instability sequences, no microwave emission bursts corresponding to instability-induced x-ray bursts were registered. Due to the physical nature of the instabilities, microwave emission can always be expected to correlate with the x-ray signal, and thus, the "missing" microwave bursts are associated with the emission at (low) frequencies[6] being suppressed or cut off by the diagnostic waveguide (an example is shown in Fig. S5 of the supplementary material). On the other hand, the energy dissipated via x-ray emission correlates well with the total electron charge Q expelled from the plasma by the instabilities and recorded from the biased disk ($Q = \int I_{BD} dt$, where I is negative), with an example from the magnetic field sweep shown in Fig. 4. This serves as a further justification to treat the x-ray signal as a more reliable diagnostic (over microwave emission) with the high voltage on.

III. DATA ANALYSIS

A. Peak detection and classification of periodic instability regimes

The data analysis was divided in two parts. Before the statistical analysis of correlation between accumulation/recovery times and instability signal amplitudes, it was necessary to classify different periodic instability regimes. In order to process the data, an inbuilt MATLAB peak detection function was used, which returns the timestamp (T) and full-width half-maximum (FWHM) corresponding to each peak of the recorded signals. For each ion source fixed set of parameters, ten measured cases of 1 s segments of data were merged together to form one 10 s dataset, after taking care of cleaning the incomplete first and last events of each 1 s data file.

The peak identification revealed the existence of several "modes" in the pulse-periodic instability regime. These are characterized by instability *events* at longer intervals, which can include a train of *bursts* at shorter time scales, i.e., a group of individual signal peaks within the event. These "modes" are defined here based on the number of individual bursts within the instability event with mode index n so that, for example, an instability event that includes three distinct separate bursts in quick succession is classified as $n = 3$. Figure 5 shows representative examples of different instability modes ($n = 1$, 2, 3, and 5) with single, double, triple and quintuple bursts in each event of instabilities. Furthermore, an index number m is defined here to indicate each separate burst within an event starting from the first one observed, so for each event of mode n, the index m runs from $m = 1, \ldots, n$. It is emphasized that these instability events, which for the given ion source settings are separated by milliseconds between them and in the order of 10–100 μs between each burst within the event, are different from the sequential instabilities occurring in μs time scale, exhibiting a falling tone of the emission microwave frequency, which have been reported in Ref. 5. The grouping of instability events to the "n-modes" discussed here resembles the patterns for a high-power gasdynamic mirror trap.[20]

The signal peak height (amplitude) of each burst was calculated from a baseline determined by the average background signal strength preceding an instability event, as illustrated in Fig. S1 of the supplementary material. It was then established with a dataset consisting of isolated ($n = 1$ mode) instability events that there is a linear correlation between the x-ray signal amplitude and area, as shown in Fig. S2 of the supplementary material. The integrated area of the x-ray peak, which is proportional to the plasma energy loss per

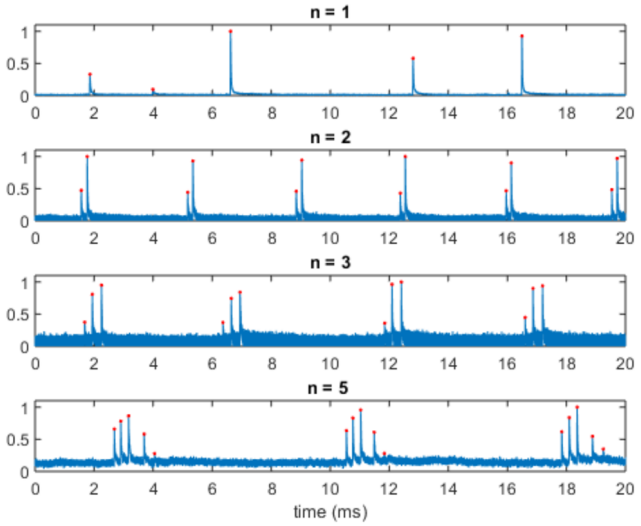

FIG. 5. An example of x-ray signals observed in different modes $n = 1$, 2, 3, and 5.

burst, was then calculated from this linear fit, allowing the code to automatically tabulate the timing, amplitude, and area of each peak.

B. Analysis of accumulation and recovery times

The occurrence of such "grouped" instabilities in event modes $n = 1, \ldots, 10$ complicates the analysis of the recovery and accumulation times as the instabilities do not appear at well-defined repetition rate but instead the time between individual instability bursts and events varies by an order of magnitude. Thus, the next step of the data analysis algorithm was set up to classify each burst (m) of each event (n). This was achieved by choosing an appropriate time threshold and comparing the time difference between a burst and its neighbors in both forward and backward directions in time, up to ten diagnostic signal peaks. The choice is based on the maximum number of bursts observed in a single grouped instability event. The time threshold was chosen by plotting the recovery time of instabilities for every burst, which typically results in two well-separated maxima of the distribution corresponding to different events n and bursts m (see Fig. S3 in the supplementary material for an example). The indexing of each peak with (n, m) allows studying the instability amplitudes and recovery/accumulation times between the events, i.e., as a function of n, as well as within each group, i.e., as a function of m. An example illustrating the n and m indexing of an event/bursts, as well as the definition of the accumulation and recovery times referring to events, is presented in Fig. 6.

IV. EXPERIMENTAL RESULTS AND DISCUSSION

A. Occurrence of instability events *n* and instability strength as a function of the ion source parameters

As a first step to interpret the data, we studied the prevalence of each instability event (n) as a function of the three main parameters of the ECRIS, i.e., magnetic field, microwave power, and neutral gas pressure. Figure 7 shows the fraction of each instability event mode n (out of all events) and the average of n for each setting. For

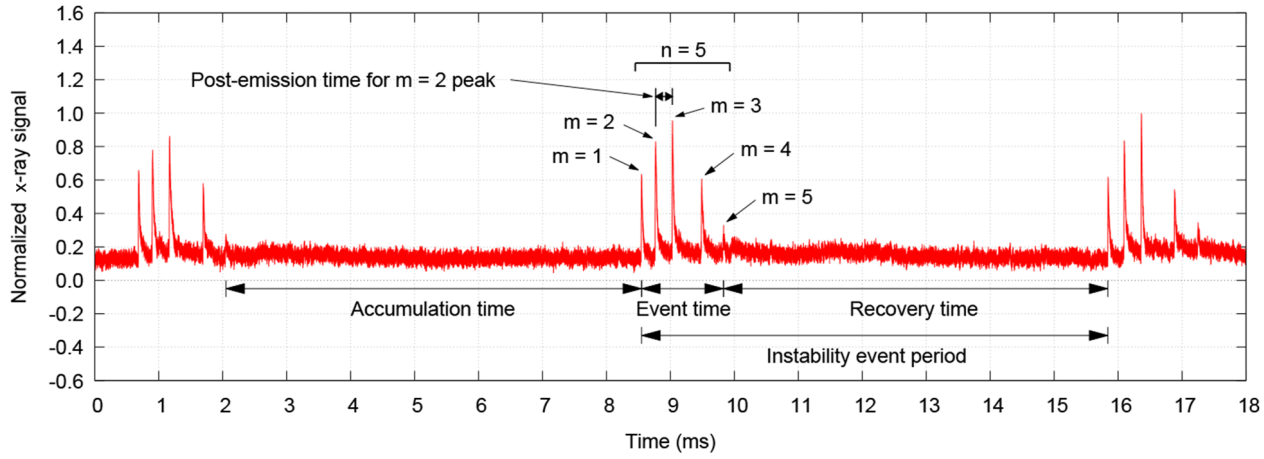

FIG. 6. An example of the determination of the burst numbers m, event (mode) number n and the accumulation time, event time, recovery time, and instability event period. The *instability event* is defined to be the group of bursts with $m = 1, \ldots, 5$, i.e., $n = 5$ in the example. The time from one burst to the next one within an event is denoted as *post-emission time*, presented here as an example for the $m = 2$ burst.

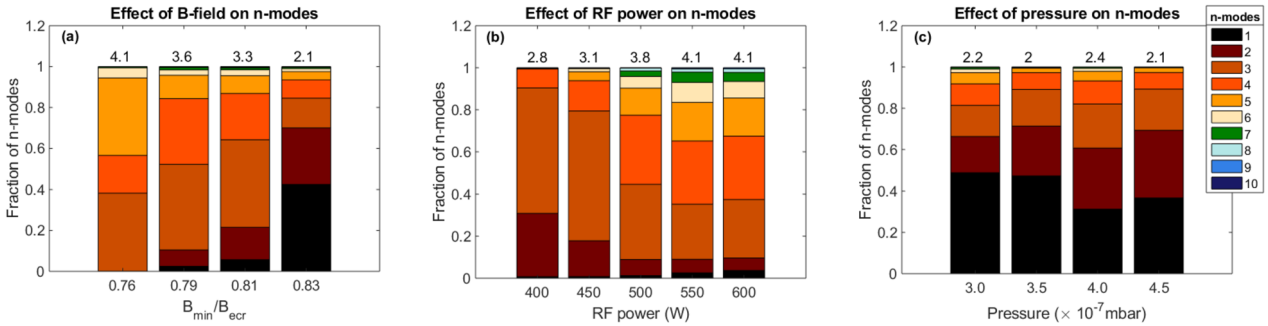

FIG. 7. The relative fraction of instability event mode n as a function of the ion source parameters. The average value of n is shown on top of each bar. In (a), B_{min}/B_{ecr} was increased keeping the neutral gas pressure and RF power constant at 3.5×10^{-7} mbar and 400 W, respectively. In (b), the RF power was increased keeping the B_{min}/B_{ecr} and neutral gas pressure constant at 0.78 and 3.5×10^{-7} mbar, respectively. In (c), the neutral gas pressure was increased keeping the B_{min}/B_{ecr} and RF power constant at 0.83 and 300 W, respectively.

the magnetic field sweep, the results are shown as a function of the B_{min}/B_{ECR} ratio, which has been found to be a good measure of the instability threshold[8] and energy content of the EED.[13]

It is seen that at low field strength, there are no isolated (n = 1) instabilities, but they become the prevalent event mode at the strongest field setting. Overall, the number of observable modes (different n) increases and the average number of bursts per instability event (average n) decreases with increasing magnetic field strength. At the same time, the total energy (power) dissipated via instabilities increases with the magnetic field strength, as seen in Fig. 8 showing the integrated area of the x-ray signals, which is proportional to total energy dissipation by the expelled electrons, as a function of the source parameters. With increasing microwave power, the number of existing modes (n) and the average number of bursts per instability event were observed to increase. At the same time, the total energy dissipated via the instabilities increases linearly with the power.

The total dissipated energy increases with the magnetic field and microwave power, as shown in Fig. 8. This can be explained with these parameters affecting the electron heating rate, i.e., the decrease of the magnetic field gradient at the resonance and the increase of the direct power input to the plasma volume. Consequently, the threshold plasma energy content to trigger the plasma instability is reached faster, which is seen as the decrease of the instability event period and thus, the total energy expelled by the instabilities in a given time increases. It is also seen in Fig. 8 that the magnetic field has a stronger impact on the total emitted energy when compared to the effect of the microwave power. This is explained by the greater influence of the magnetic field on the high energy tail of the EED compared to the effect of the microwave power observed either indirectly through bremsstrahlung spectrum[14,15] or directly through the measurement of the energy distribution of electrons escaping from the minimum-B confinement.[7,15] Furthermore, it has been shown that in the ECRIS plasmas, the magnetic field strength, especially the value at the center of the trap (B_{min}), affects the threshold between the transition from the stable to the unstable regime[8] and further into the continuous maser emission regime[18] more than the applied microwave heating power or neutral gas density. It is worth noting that the relation between the heating regime (including the magnetic field) and the related instability dynamics was first considered by Demekhov and Trakhtengerts.[52] The present data provide further input for theoretical considerations.

The neutral gas pressure has an insignificant effect on the distribution of the event modes n. In the case of the neutral gas sweep, the prevailing mode was n = 1, whereas the number of n-modes was observed to increase with decreasing neutral gas pressure with n up to nine, detected with the lowest pressure. The prevalence of n = 1 is most likely due to the magnetic field strength (B_{min}/B_{ECR} = 0.83) being more important in determining the instability dynamics than the neutral gas pressure. The total energy dissipated by the instabilities was observed to be almost constant across the range of the neutral gas pressure sweep despite the plasma density being higher for high gas pressure (indicated by the concomitant increase of the total extracted current). This implies that the strength of the instability is independent of the plasma density but rather depends on the electron heating affected by the B-field[15,53,54] and microwave power.[55]

The parametric dependencies can be explained by the effect of the magnetic field, microwave power, and neutral gas pressure on the EED. When B_{min} is increased, the hot (>100 keV part) tail of the EED is affected, which causes the instability induced bremsstrahlung power emission to increase drastically. The change in the microwave power has a weaker effect on the burst of bremsstrahlung power associated with the instabilities as it does not affect the shape of the EED but the electron density and electron flux instead. The change in the neutral gas pressure has an insignificant effect on the (hot) electron population, relevant for the instabilities, which explains the insensitivity to this parameter. All these parametric effects on the EED have been confirmed experimentally by measuring the EED of the electron flux escaping the confinement axially through the extraction aperture.[13,15] It is worth noting that the EED of the escaping electron flux could be different from the EED of the confined electrons. The effect of each parameter (B-field, microwave power, and neutral gas pressure) on the instabilities strengthens the argument that the parametric dependencies of the EED of escaping and confined electrons are similar. In summary, the parametric sweeps presented here revealed that the distribution of the instability modes n is affected most by the magnetic field strength, followed by the microwave power, and least affected by the neutral gas pressure.

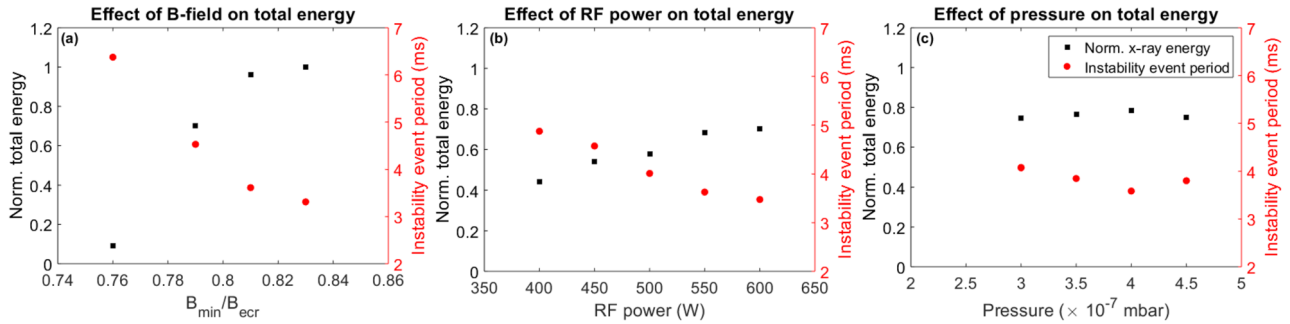

FIG. 8. The total dissipated energy (relative) as a function of the ion source parameters. In (a), B_{min}/B_{ecr} was increased keeping the neutral gas pressure and RF power constant at 3.5×10^{-7} mbar and 400 W, respectively. In (b), the RF power was increased keeping the B_{min}/B_{ecr} and neutral gas pressure constant at 0.78 and 3.5×10^{-7} mbar, respectively. In (c), the neutral gas pressure was increased keeping the B_{min}/B_{ecr} and RF power constant at 0.83 and 300 W, respectively. The normalization is performed with respect to the largest value corresponding to all three sweeps. The second y axis represents the event period (see Fig. 6 for definition).

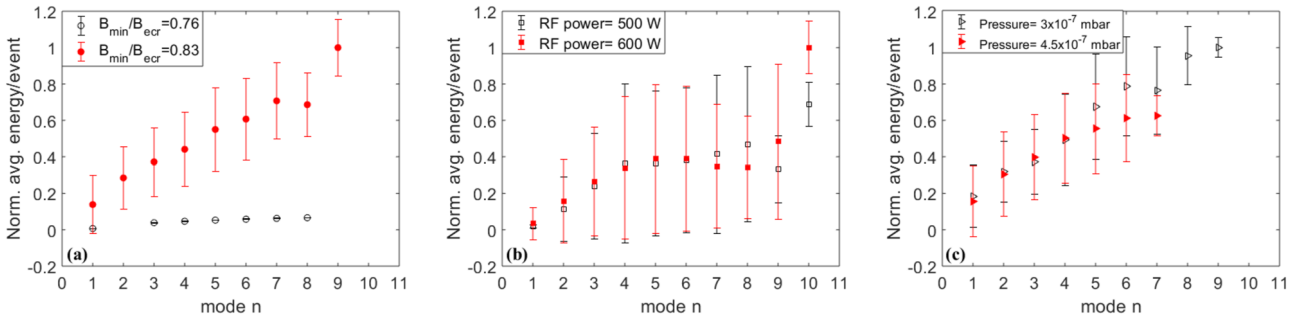

FIG. 9. The dependence of energy emitted per instability event vs n for selected examples of ion source parameters: (a) the magnetic field strength, (b) the microwave power, and (c) the neutral gas pressure. The plots are normalized to the maximum average energy/mode among all three cases.

B. Energy dissipation and characteristic times as a function of the instability event mode *n*

Next, we studied the average energy dissipated in an instability event as a function of n. It was observed that the energy tends to increase with n. This is shown in Fig. 9, displaying the average integrated area of x-ray emission peaks per event (normalized) as a function of n for two B-field, power, and pressure values, chosen as representative examples. The integration is carried out over all bursts m in each event n. The error bars correspond to the standard deviation of the total energy histograms, specifically selecting

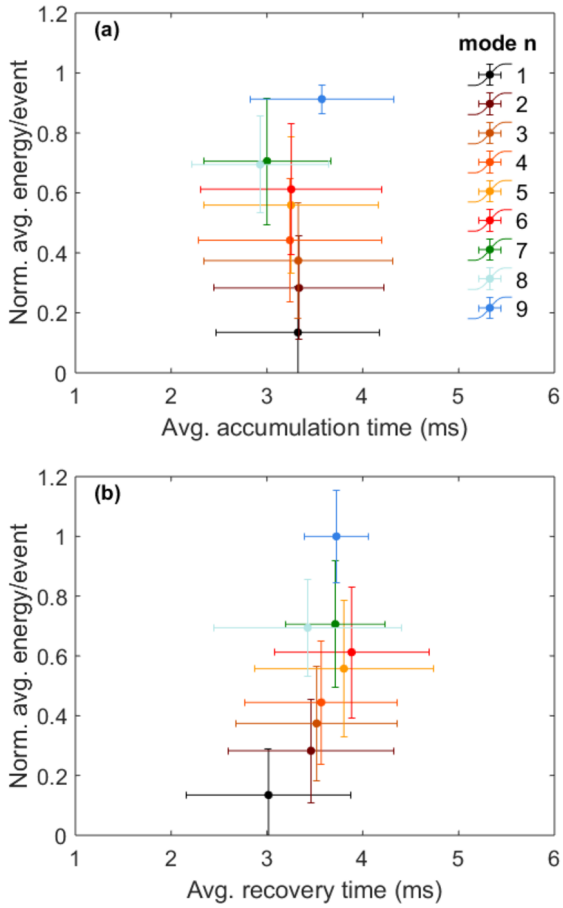

FIG. 10. The average energy emitted per event vs the accumulation (a) and recovery times (b) for a B_{min}/B_{ecr} value of 0.83, neutral gas pressure of 3.5×10^{-7} mbar, and RF power of 400 W.

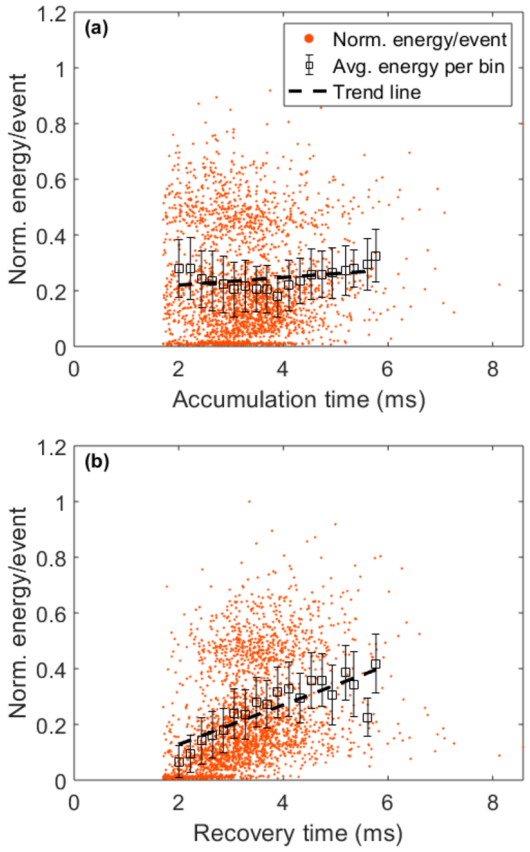

FIG. 11. The accumulation (a) and recovery times (b) as a function of the energy emitted per event. The temporal axis is divided into 20 bins, and the average energy per event and its standard deviation is calculated for each bin. The plot corresponds to a B_{min}/B_{ecr} of 0.83, 3.5×10^{-7} mbar neutral gas pressure, and 400 W RF power.

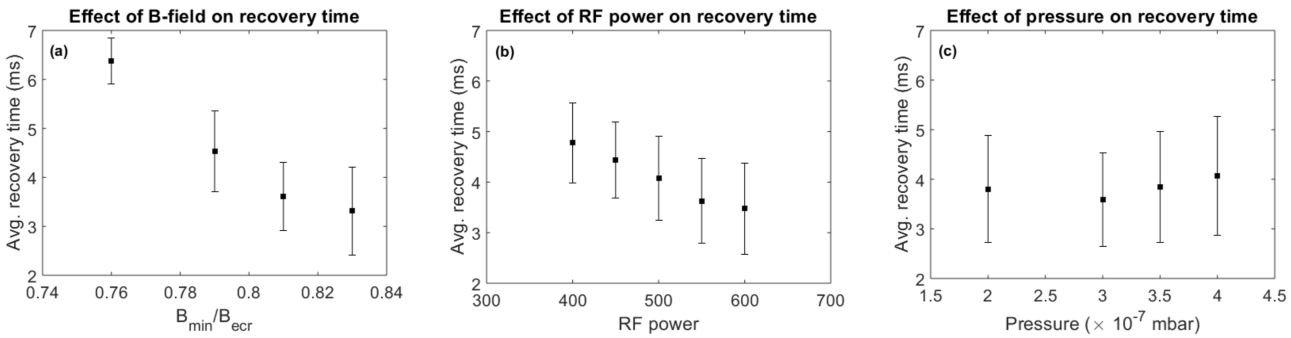

FIG. 12. The dependence of instability recovery time on (a) B_{min}/B_{ecr}, (b) RF power, and (c) neutral gas pressure.

instability events with a certain n. The energy dissipated by the instabilities increases monotonically with n at each source setting, which means that not all instability events dissipate the same energy but rather that there is a correlation between the dissipated energy and the number of bursts associated with each event. It is worth noting that the RF power or neutral gas pressure has only a small effect on the energy dissipated by the instabilities, whereas the emitted energy per instability event increases strongly with the magnetic field strength. At a B_{min}/B_{ecr} of 0.83, the $n = 1$ mode dissipates more energy than any of the higher n modes (up to $n = 8$ detected) with a B_{min}/B_{ecr} of 0.76. This observation fortifies the notion that the magnetic field strength is the most influential ECRIS parameter in terms of the instabilities.

Figure 10 shows a representative plot with the average recovery and accumulation times vs the average energy released in each instability event for different n. An example of the scatter plots from which the average energy and the average recovery and accumulation times are calculated is presented in the supplementary material (Fig. S4). Figure 10 reveals that the recovery time following each instability event increases with n, the dependence being weak though while the accumulation time is practically independent on n. The independence of the accumulation time on the released energy has

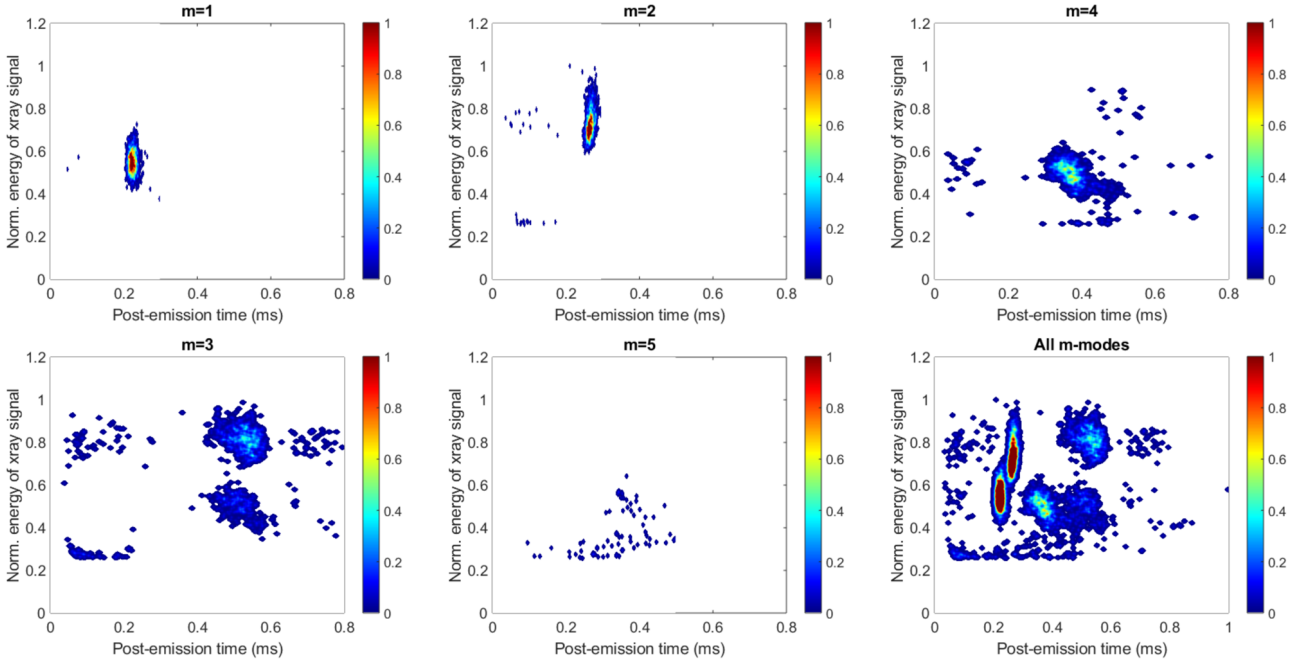

FIG. 13. The dependence of post-emission time on the energy emitted per burst mode m. The data corresponds to a B_{min}/B_{ecr} value of 0.76, neutral gas pressure of 3.5×10^{-7} mbar, and RF power of 400 W. The x-ray energy is normalized to the maximum value corresponding to all burst modes m combined. The plot shows individually each mode $m = 1, \ldots, 5$ and a combined plot of all m-modes. The false color represents the data point density, with blue representing the lowest.

been reported earlier in the context of magnetospheric plasmas, namely, the formation of pulsating auroras,[29] i.e., it seems to be a natural property of oscillatory regimes with low duty cycles, for which the energy release occurs in a much faster time scale than the accumulation of the energy.

Since the energy dissipated in each instability event increases monotonically with n, this implies that the time between instability events depends on their magnitude, a large amplitude emission leading to a longer recovery time until the next event, i.e., scenario (a) presented in the introduction is more likely than scenario (b). Our observation is similar to that made for magnetospheric plasmas where large amplitude quasi-periodic emissions lead to a long recovery time at high duty cycle regimes, i.e., when the on and off periods of the instabilities are nearly equal.[29,56] It is worth noting that at low duty cycles with randomly spaced instability bursts, the opposite, i.e., our scenario (b), was found for the magnetospheric plasma. The relevance of the recovery time over the accumulation time in our experiment is further highlighted in Fig. 11, showing an example of the (normalized) energy per event as a function of these characteristic times calculated from the scatter plots summing all event modes $n = 1, \ldots, 10$. There is a clear correlation between the released energy per event and the recovery time, whereas the accumulation time does not show much dependence on the released energy.

C. The effect of ion source parameters on the instability recovery time

After establishing that the time between instability events (recovery time) depends on the total energy of an instability event, i.e., a larger amplitude event leading to a longer recovery time until the next one, we studied the dependence of the instability recovery time on the ion source settings. The results are shown in Fig. 12. It was observed that the recovery time decreases with increasing $B_{\min}/B_{ecr}$ and microwave power, while varying the neutral gas pressure shows no prominent effect. This observation is attributed to the decrease in the instability event period (see Fig. 8), which is dominated by the recovery time. The recovery time itself is affected by the electron heating properties, namely, the magnetic field gradient and electric field strength. At the same time, the increased rate of inelastic collisions damping the cold and warm electron energy (<10 keV order of magnitude) at higher gas density has an insignificant effect on the development of the EED toward the instability threshold. This is attributed to the fact that the instabilities are driven by the high energy electrons for which the inelastic collision cross section is small.

D. Preliminary burst mode *m* analysis

In order to illustrate the temporal distribution of the m-mode bursts at a sub-millisecond time scale (within each n-mode event), a new parameter, *post-emission time,* is defined as shown in Fig. 6. It is defined as the time between two emission bursts (m) within an event (n) i.e., the post-emission time corresponding to burst $m = i$ is the time difference between bursts $m = i$ and $m = i + 1$. Figure 13 shows an example of the m-mode analysis, where the dependence of the post-emission time on the energy emitted per burst is presented as heat maps for $m = 1, \ldots, 5$. It is seen that the burst m emissions populate discrete regions when the (normalized) energy of the x-ray signal is plotted as a function of the post-emission time. This suggests that close to the instability threshold, the plasma self-organizes to release the excess energy, restoring stable conditions in a deterministic way, with quasi-periodic microwave and particle bursts.

When the rate of change of the plasma energy content and anisotropy (electron heating) is increased by making the $B_{\min}/B_{ecr}$ ratio higher and the average field gradient on the resonance surface lower, the quantized behavior becomes less evident. This is demonstrated in Fig. 14, showing the heat map distribution of bursts m in x-ray energy vs post-emission time phase space for two $B_{\min}/B_{ecr}$ values. In the case of higher $B_{\min}$, the x-ray emissions occupy a wider range of energies, yet most of them are found at the same level as with the lower $B_{\min}$. At the same time, the distribution of post-emission times approaches a continuum. On the other hand, as shown in Fig. 15, the average event time increases almost linearly

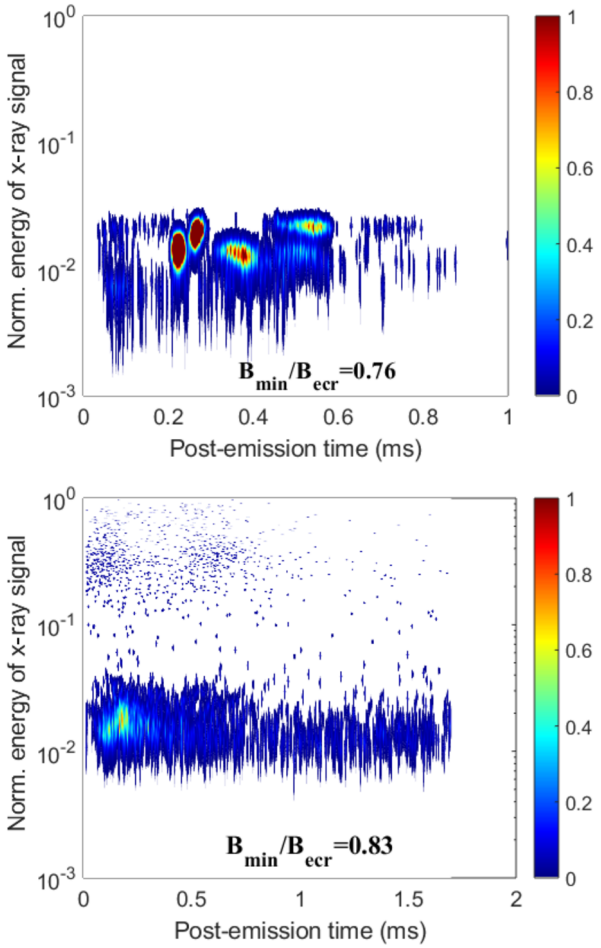

FIG. 14. The dependence of the post-emission time on the energy emitted per burst m. The data corresponds to a $B_{\min}/B_{ecr}$ value 0.76 and 0.83, neutral gas pressure of 3.5×10^{-7} mbar, and RF power of 400 W. The x-ray energy range on the vertical axes is normalized to the maximum value corresponding to the higher $B_{\min}/B_{ecr}$ value.

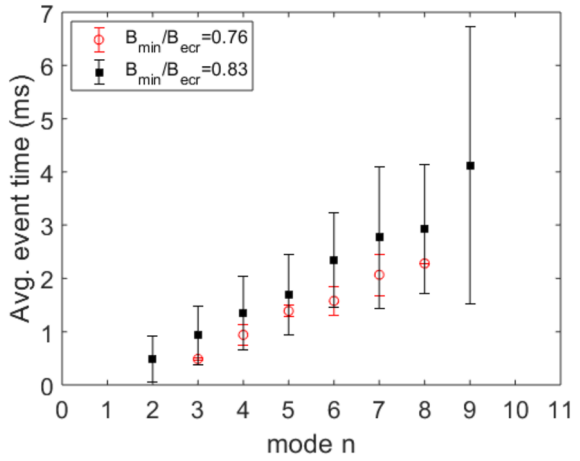

FIG. 15. The event time as a function of n for two different B_{min}/B_{ecr} values with 400 W RF power and 3.5×10^{-7} mbar neutral gas pressure.

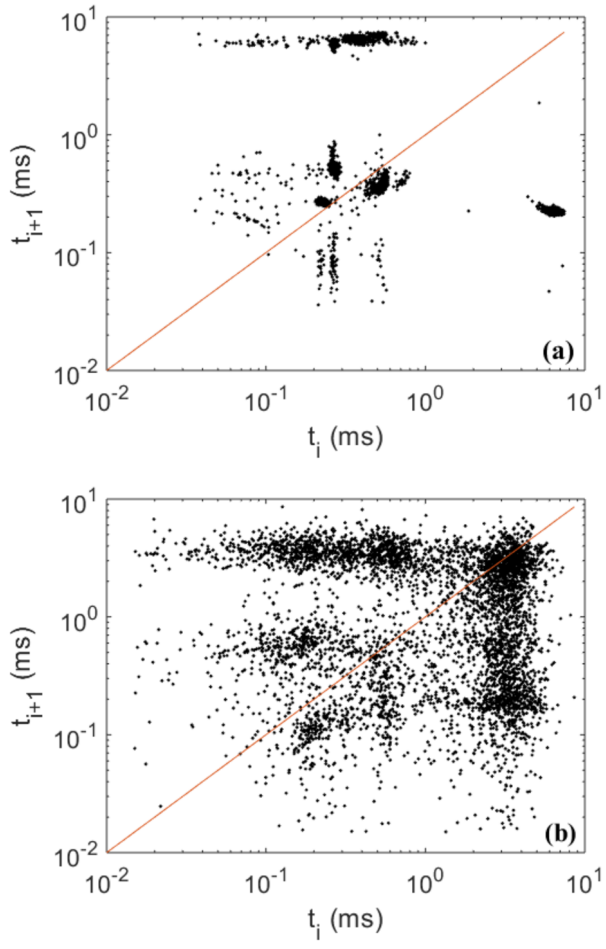

FIG. 16. Poincaré maps showing the time difference between a particular emission burst i and the following burst $i + 1$. (a) B_{min}/B_{ecr} of 0.76 and (b) B_{min}/B_{ecr} of 0.83. The neutral gas pressure is 3.5×10^{-7} mbar and the RF power is 400 W in both cases.

with n but is not strongly affected by the field strength, whereas its standard deviation becomes larger at high B_{min}. This follows from the fact that the instability bursts within each event become more sporadic as the plasma energy content and anisotropy of the EED increase.

In qualitative terms, the data in Fig. 14 can be interpreted as a transition of the non-linear system (quasi-periodic maser-type cyclotron instability) from an organized chaotic system to an unorganized one with the increase of the energy content and anisotropy of the EED. This behavior is analogous to the famous dripping faucet experiment;[57,58] the expulsion of energy from the plasma can be compared to the behavior of the droplet formation interval. The development of chaos is well described by a Poincaré map, which consists of plotting the time lapse before vs after the occurrence of several consecutive instability events.

The Poincaré maps shown in Fig. 16 represent the data collected at B_{min}/B_{ecr} values of 0.76 and 0.83. The plots compile all successive instability bursts measured during the 10 s data acquisition, i.e., neither n or m mode dichotomy is considered. At a B_{min}/B_{ecr} of 0.76 the Poincaré map consists of separate regions populated by data points. Increasing the B_{min} results in a (semi-)continuous distribution of instability bursts in the time domain, which, following the literature,[57,58] is interpreted as a transition toward a more chaotic instability regime, where the energy release and its periodicity become erratic.

V. CONCLUSION

In this paper, we have presented the main findings of a phenomenological investigation of the occurrence of cyclotron maser instabilities in a minimum-B magnetic device (ECR ion source). These can be summarized as follows:

- The quasi-periodic plasma instabilities are often grouped into bursts of microwaves and electrons from the magnetic confinement. Such grouping has been observed previously in a minimum-B ECRIS as a by-product of experiments focusing on the suppression of the instabilities,[22] but it has not been discussed at all in the literature. The occurrence of grouped instability bursts implies that there is a fundamental limit of the energy dissipated by a single burst, i.e., the release of the stored energy carried by the hot tail of the EED requires several instability onsets within an event. The physical reason for the grouping in the minimum-B trap is not currently understood. It is worth noting that the oscillatory behavior of the cyclotron instability with clearly distinguishable on and off phases is a key mechanism applied for explaining quasi-periodic low frequency emissions and related auroral pulsations in magnetospheric plasmas.[59,60] The relation between the characteristic times of the oscillating instability regimes has been considered for these natural phenomena both theoretically and experimentally.[29,56] Our work demonstrates that controllable minimum-B laboratory plasmas could be used as a proxy for naturally occurring large-scale plasmas and invites further theoretical studies to explain the observations.
- The instability event period and recovery time decrease with an increase in B_{min}/B_{ecr} ratio and RF power and not with

pressure, which can be attributed to the increase in plasma energy density.[61]

- The quiescent time between instability events depends on the energy dissipated by the instabilities, i.e., a sequence of bursts dissipating a larger amount of energy leads to a longer recovery time until the next event than the bursts dissipating less energy. In other words, there is a correlation between the instability recovery time and the dissipated energy, whereas there is no correlation between the instability accumulation time and the dissipated energy. We explain this (qualitatively) as follows: Instabilities dissipating a large amount of energy restore a stable EED with a lower energy content than small amplitude instabilities. The energy content of the EED is then accumulating at the rate defined by the electron heating affected by magnetic field and microwave power (indicated by the decreasing instability event period/increasing repetition rate with these parameters shown in Fig. 8) until the instability threshold level of EED anisotropy is reached again.
- Plasma energy losses associated with each instability burst appear to be self-organized near the instability threshold (at low $B_{\min}/B_{ecr}$ and RF power), i.e., the bursts are periodic and are associated with quantized energy (particle) losses. However, as the energy content of the plasma increases with the magnetic field strength, the energy release associated with the instability shifts from deterministic to chaotic with trains of randomly spaced (in time) energy and particle bursts of varying amplitude.

We invite the plasma theory community to explain our experimental findings, especially the grouping of events and discrete timing of the instability bursts within the events.

SUPPLEMENTARY MATERIAL

See the supplementary material for additional details of the instability signal treatment, data analysis, selection of diagnostic signals for analysis, and reproducibility of the results.

ACKNOWLEDGMENTS

We would like to thank Ivan Izotov and Vadim Skalyga of the IAP-RAS for fruitful discussions regarding the experiment. We would also like to thank Risto Kronholm of JYFL for providing the necessary technical assistance. This work was supported by the Academy of Finland Project funding (Grant No. 315855) and the University of Grenoble Alpes under the EMERGENCE program.

AUTHOR DECLARATIONS

Conflict of Interest

The authors have no conflicts to disclose.

DATA AVAILABILITY

The data that support the findings of this study are available from the corresponding author upon reasonable request.

REFERENCES

[1] A. G. Shalashov, E. D. Gospodchikov, I. V. Izotov, D. A. Mansfeld, V. A. Skalyga, and O. Tarvainen, "Control of electron-cyclotron instability driven driven by strong ECRH in open magnetic trap," Europhys. Lett. **124**(3), 35001 (2018).
[2] B. Eliasson, M. Viktorov, D. C. Speirs, K. Ronald, D. Mansfeld, and A. D. R. Phelps, "Observation of electron cyclotron harmonic emissions due to electrostatic instabilities in mirror-confined plasma," Phys. Rev. Res. **2**, 043272 (2020).
[3] R. C. Garner, M. E. Mauel, S. A. Hokin, R. S. Post, and D. L. Smatlak, "Warm electron driven whistler instability in an electron-cyclotron-resonance heated, mirror-confined plasma," Phys. Rev. Lett. **59**(16), 1821–1824 (1987).
[4] A. Vodopyanov, S. Golubev, A. Demekhov, V. Zorin, D. Mansfeld, S. Razin, and V. Trakhtengerts, "Laboratory modeling of nonstationary processes in space cyclotron masers: First results and prospects," Plasma Phys. Rep. **31**(11), 927–937 (2005).
[5] I. Izotov, O. Tarvainen, D. Mansfeld, V. Skalyga, H. Koivisto, T. Kalvas, J. Komppula, R. Kronholm, and J. Laulainen, "Microwave emission related to cyclotron instabilities in a minimum-B electron cyclotron resonance ion source plasma," Plasma Sources Sci. Technol. **24**(4), 045017 (2015).
[6] I. Izotov, T. Kalvas, H. Koivisto, R. Kronholm, D. Mansfeld, V. Skalyga, and O. Tarvainen, "Broadband microwave emission spectrum associated with kinetic instabilities in minimum-B ECR plasmas," Phys. Plasmas **24**(4), 043515 (2017).
[7] I. Izotov, O. Tarvainen, V. Skalyga, D. Mansfeld, H. Koivisto, R. Kronholm, V. Toivanen, and V. Mironov, "Measurements of the energy distribution of electrons lost from the minimum B-field-the effect of instabilities and two-frequency heating," Rev. Sci. Instrum. **91**(1), 013502 (2020).
[8] O. Tarvainen, I. Izotov, D. Mansfeld, V. Skalyga, S. Golubev, T. Kalvas, H. Koivisto, J. Komppula, R. Kronholm, J. Laulainen, and V. Toivanen, "Beam current oscillations driven by cyclotron instabilities in a minimum-B electron cyclotron resonance ion source plasma," Plasma Sources Sci. Technol. **23**(2), 025020 (2014).
[9] O. Tarvainen, R. Kronholm, T. Kalvas, H. Koivisto, I. Izotov, V. Skalyga, V. Toivanen, and L. Maunoury, "The biased disc of an electron cyclotron resonance ion source as a probe of instability-induced electron and ion losses," Rev. Sci. Instrum. **90**(12), 123303 (2019).
[10] O. Tarvainen, J. Laulainen, J. Komppula, R. Kronholm, T. Kalvas, H. Koivisto, I. Izotov, D. Mansfeld, and V. Skalyga, "Limitations of electron cyclotron resonance ion source performances set by kinetic plasma instabilities," Rev. Sci. Instrum. **86**(2), 023301 (2015).
[11] O. Tarvainen, T. Kalvas, H. Koivisto, J. Komppula, R. Kronholm, J. Laulainen, I. Izotov, D. Mansfeld, V. Skalyga, V. Toivanen, and G. Machicoane, "Limitation of the ECRIS performance by kinetic plasma instabilities," Rev. Sci. Instrum. **87**(2), 02A703 (2016).
[12] S. V. Golubev and A. G. Shalashov, "Cyclotron-resonance maser driven by magnetic compression of rarefied plasma," Phys. Rev. Lett. **99**(20), 205002 (2007).
[13] I. V. Izotov, A. G. Shalashov, V. A. Skalyga, E. D. Gospodchikov, O. Tarvainen, V. E. Mironov, H. Koivisto, R. Kronholm, V. Toivanen, and B. Bhaskar, "The role of radio frequency scattering in high-energy electron losses from minimum-B ECR ion source," Plasma Phys. Controlled Fusion **63**(4), 045007 (2021).
[14] J. Benitez, C. Lyneis, L. Phair, D. Todd, and D. Xie, "Dependence of the bremsstrahlung spectral temperature in minimum-B electron cyclotron resonance ion sources," IEEE Trans. Plasma Sci. **45**(7), 1746–1754 (2017).
[15] B. S. Bhaskar, H. Koivisto, O. Tarvainen, T. Thuillier, V. Toivanen, T. Kalvas, I. Izotov, V. Skalyga, R. Kronholm, and M. Marttinen, "Correlation of bremsstrahlung and energy distribution of escaping electrons to study the dynamics of magnetically confined plasma," Plasma Phys. Controlled Fusion **63**(9), 095010 (2021).
[16] E. Naselli, D. Mascali, M. Mazzaglia, S. Biri, R. Rácz, J. Pálinkás, Z. Perduk, A. Galatá, G. Castro, L. Celona, S. Gammino, and G. Torrisi, "Impact of two-close-frequency heating on ECR ion source plasma radio emission and stability," Plasma Sources Sci. Technol. **28**(8), 085021 (2019).
[17] B. Isherwood, "Characterization of electron cyclotron resonance ion source instabilities by charged particle diagnostics," Ph.D. thesis, Michigan State University, 2020, https://pa.msu.edu/sites/_pa/assets/File/Isherwood_Thesis.pdf.

[18]V. A. Skalyga, I. V. Izotov, A. G. Shalashov, E. D. Gospodchikov, E. M. Kiseleva, O. Tarvainen *et al.*, "Controlled turbulence regime of electron cyclotron resonance ion source for improved multicharged ion performance," J. Phys. D: Appl. Phys. **54**(38), 385201 (2021).
[19]A. G. Shalashov, E. D. Gospodchikov, I. V. Izotov, D. A. Mansfeld, V. A. Skalyga, and O. Tarvainen, "Observation of Poincaré-Andronov-Hopf bifurcation in cyclotron maser emission from a magnetic plasma trap," Phys. Rev. Lett. **120**, 1555001 (2018).
[20]A. G. Shalashov, S. V. Golubev, E. D. Gospodchikov, D. A. Mansfeld, and M. E. Viktorov, "Interpretation of complex patterns observed in the electron-cyclotron instability of a mirror confined plasma produced by an ECR discharge," Plasma Phys. Controlled Fusion **54**(8), 085023 (2012).
[21] A. G. Shalashov, E. D. Gospodchikov, and I. V. Izotov, "Electron-cyclotron heating and kinetic instabilities of a mirror-confined plasma: The quasilinear theory revised," Plasma Phys. Controlled Fusion **62**(6), 065005 (2020).
[22]V. Skalyga, I. Izotov, T. Kalvas, H. Koivisto, J. Komppula, R. Kronholm, J. Laulainen, D. Mansfeld, and O. Tarvainen, "Suppression of cyclotron instability in electron cyclotron resonance ion sources by two-frequency heating," Phys. Plasmas **22**, 083509 (2015).
[23]S. V. Golubev and A. G. Shalashov, "Cyclotron-resonance maser with adiabatic magnetic pumping in a low-density plasma," JETP Lett. **86**(2), 91–97 (2007).
[24]V. Trakhtengerts and M. Rycroft, *Whistler and Alfven Mode Cyclotron Masers in Space* (Cambridge University Press, 2008).
[25]V. Ginzburg, *The Propagation of Electromagnetic Waves in Plasmas* (Pergamon, Oxford, 1970).
[26]A. G. Demekhov, "Cyclotron instability of the slow extraordinary wave in a magnetoactive plasma," Radiophys. Quantum Electron. **30**, 547–557 (1987).
[27]A. V. Vodopyanov, S. V. Golubev, A. G. Demekhov, V. G. Zorin, D. A. Mansfeld, S. V. Razin, and A. G. Shalashov, "Observation of pulsed fast electron precipitations and the cyclotron generation mechanism of burst activity in a decaying ECR discharge plasma," J. Exp. Theor. Phys. **104**, 296–306 (2007).
[28]B. Isherwood, G. Machicoane, D. Neben, G. Pozdeyev, and J. Stetson, "Plasma instability studies of the SuSI 18 GHz source," in *Proceedings of the 23rd International Workshop on ECR Ion Sources (ECRIS'18), International Workshop on ECR Ion Sources*, Catania, Italy, 10–14 September 2018, http://www.jacow.org, pp. 157–161.
[29]A. G. Demekhov and V. Y. Trakhtengerts, "A mechanism of formation of pulsating aurorae," J. Geophys. Res. **99**(4), 5831–5841, https://doi.org/10.1029/93ja01804 (1994).
[30]E. A. Benediktov, G. G. Getmantsev, N. A. Mityakov, V. O. Rapoport, and A. F. Tarasov, "On relationship of sporadic radio emission registered on satellites of the 'Elektron' series with the geomagnetic activity," Cosmic Res. **6**, 791 (1968), https://ntrs.nasa.gov/citations/19690006158.
[31] D. Grunett, "Electromagnetic plasma wave emissions from the auroral field lines," J. Geomagn. Geoelectr. **30**(3), 257–272 (1978).
[32]C. Trigilio, P. Leto, G. Umana, C. S. Buemi, and F. Leone, "Auroral radio emission from stars: The case of CU virginis," Astrophys. J., Lett. **739**(1), L10 (2011).
[33]H. Koivisto, P. Heikkinen, V. Hänninen, A. Lassila, H. Leinonen, V. Nieminen, J. Pakarinen, K. Ranttila, J. Ärje, and E. Liukkonen, "The first results with the new JYFL 14 GHz ECR ion source," Nucl. Instrum. Methods Phys. Res., Sect. B **174**(3), 379–384 (2001).
[34]O. Tarvainen, T. Lamy, J. Angot, T. Thuillier, P. Delahaye, L. Maunoury, J. Choinski, L. Standylo, A. Galatà, G. Patti, and H. Koivisto, "Injected 1+ ion beam as a diagnostics tool of charge breeder ECR ion source plasmas," Plasma Sources Sci. Technol. **24**, 035014 (2015).
[35]V. Mironov, S. Bogomolov, A. Bondarchenko, A. Efremov, V. Loginov, and D. Pugachev, "Spatial distributions of plasma potential and density in electron cyclotron resonance ion source," Plasma Sources Sci. Technol. **29**, 065010 (2020).
[36]D. Mascali, L. Neri, L. Celona, G. Castro, G. Torrisi, S. Gammino, G. Sorbello, and G. Ciavola, "A double-layer based model of ion confinement in electron cyclotron resonance ion source," Rev. Sci. Instrum. **85**, 02A511 (2014).
[37]C. Barué, M. Lamoureux, P. Briand, A. Girard, and G. Melin, "Investigation of hot electrons in electron-cyclotron-resonance ion sources," J. Appl. Phys. **76**, 2662 (1994).
[38]G. Douysset, H. Khodja, A. Girard, and J. P. Briand, "Highly charged ion densities and ion confinement properties in an electron-cyclotron-resonance ion source," Phys. Rev. E **61**(3), 3015–2022 (2000).
[39]V. Toivanen, B. S. Bhaskar, I. V. Izotov, H. Koivisto, and O. Tarvainen, "Diagnostic techniques of minimum-B ECR ion source plasma instabilities," Rev. Sci. Instrum. **93**(1), 013302 (2022).
[40]See https://www.thinksrs.com/products/sr570.html for Stanford Research Systems preamplifier.
[41] See https://www.picotech.com/oscilloscope/5000/flexible-resolution-oscilloscope for Picoscope 5000 series.
[42]O. Tarvainen, T. Kalvas, H. Koivisto, J. Komppula, R. Kronholm, J. Laulainen, I. Izotov, D. Mansfeld, and V. Skalyga, "Kinetic instabilities in pulsed operation mode of a 14 GHz electron cyclotron resonance ion source," Rev. Sci. Instrum. **87**, 02A701 (2016).
[43]I. Izotov, D. Mansfeld, V. Skalyga, V. Zorin, T. Grahn, T. Kalvas, H. Koivisto, J. Komppula, P. Peura, O. Tarvainen, and V.Toivanen, "Plasma instability in the afterglow of electron cyclotron resonance discharge sustained in a mirror trap," Phys. Plasmas **19**, 122501 (2012).
[44]I. Izotov, T. Kalvas, H. Koivisto, J. Komppula, R. Kronholm, J. Laulainen, D. Mansfeld, V. Skalyga, and O. Tarvainen, "Cyclotron instability in the afterglow mode of minimum-B ECRIS," Rev. Sci. Instrum. **87**, 02A729 (2016).
[45]J. Orpana, O. Tarvainen, T. Kalvas, H. Koivisto, R. Kronholm, J. Laulainen, I. Izotov, D. Mansfeld, and V. Skalyga, "Measurement of microwave frequencies emitted by instabilities of ECRIS plasma with waveguide filters and microwave sensitive diodes," in *Proceedings of the 22nd International Workshop on ECR Ion Sources (ECRIS2016), International Workshop on ECR Ion Sources*, Busan, Korea, 28 August–1 September 2016, http://www.jacow.org, pp. 133–136.
[46]O. Tarvainen, J. Angot, I. Izotov, V. Skalyga, H. Koivisto, T. Thuillier, T. Kalvas, and T. Lamy, "Plasma instabilities of a charge breeder ECRIS," Plasma Sources Sci. Technol. **26**, 105002 (2017).
[47]O. Tarvainen, V. Toivanen, J. Komppula, T. Kalvas, and H. Koivisto, "Transverse distribution of beam current oscillations of a 14 GHz electron cyclotron resonance ion source," Rev. Sci. Instrum. **85**, 02A909 (2014).
[48]O. Tarvainen, J. Angot, I. Izotov, V. Skalyga, H. Koivisto, T. Thuillier, T. Kalvas, V. Toivanen, R. Kronholm, and L. Lamy, "The effect of plasma instabilities on the background impurities in charge breeder ECRIS," AIP Conf. Proc. **2011**, 070006 (2018).
[49]V. Toivanen, O. Tarvainen, J. Komppula, and H. Koivisto, "Oscillations of ECR ion source beam current along the beam transport of the JYFL K-130 cyclotron," J. Instrum. **8**(2), T02005 (2013).
[50]R. Kronholm, T. Kalvas, H. Koivisto, and O. Tarvainen, "Spectroscopic method to study low charge state ion and cold electron population in ECRIS plasma," Rev. Sci. Instrum. **89**(4), 043506 (2018).
[51] R. Kronholm, T. Kalvas, H. Koivisto, S. Kosonen, M. Marttinen, D. Neben, M. Sakildien, O. Tarvainen, and V. Toivanen, "ECRIS plasma spectroscopy with a high resolution spectrometer," Rev. Sci. Instrum. **91**(1), 013318 (2020).
[52]A. G. Demekhov and V. Y. Trakhtengerts, "Several questions on radiation dynamics in magnetic plasma traps," Radiophys. Quantum Electron. **29**, 848–857 (1986).
[53]S. Gammino, D. Mascali, L. Celona, F. Maimone, and G. Ciavola, "Considerations on the role of the magnetic field gradient in ECR ion sources and build-up of hot electron component," Plasma Sources Sci. Technol. **18**(4), 045016 (2009).
[54]J. B. Li, L. X. Li, B. S. Bhaskar, V. Toivanen, O. Tarvainen, D. Hitz, L. B. Li, W. Lu, H. Koivisto, T. Thuillier, J. W. Guo, X. Z. Zhang, H. Y. Zhao, L. T. Sun, and H. W. Zhao, "Effects of magnetic configuration on hot electrons in a minimum-B ECR plasma," Plasma Phys. Controlled Fusion **62**(9), 095015 (2020).
[55]M. C. Williamson, A. J. Lichtenberg, and M. A. Lieberman, "Self-consistent electron cyclotron resonance absorption in a plasma with varying parameters," J. Appl. Phys. **72**(9), 3924–3933 (1992).

[56]D. L. Pasmanik, A. G. Demekhov, M. Hayoš, F. NĚmec, O. Santolík, and M. Parrot, "Quasiperiodic ELF/VLF emissions detected onboard the DEMETER spacecraft: Theoretical analysis and comparison with observations," J. Geophys. Res.: Space Phys. **124**(7), 5278–5288, https://doi.org/10.1029/2018ja026444 (2019).
[57]P. Martien, S. C. Pope, P. L. Scott, and R. S. Shaw, "The chaotic behavior of the leaky faucet," Phys. Lett. A **110**(7–8), 399–404 (1985).
[58]R. F. Cahalan, H. Leidecker, and G. D. Cahalan, "Chaotic rhythms of a dripping faucet: A simple drop detector transforms the computer into a temporal microscope, revealing a variety of rhythms in the common leaky tap," Comput. Phys. **4**(4), 368–382 (1990).
[59]G. T. Davidson and Y. T. Chiu, "A closed nonlinear model of wave-particle interactions in the outer trapping and morningside auroral regions," J. Geophys. Res.: Space Phys. **91**(A12), 13705–13710, https://doi.org/10.1029/ja091ia12p13705 (1986).
[60]V. Yu. Trakhtengerts, V. R. Tagirov, and S. A. Chernouss, "A circulating cyclotron maser and pulsed VLF emissions," Geomagn. Aeron. **26**(1), 77–82 (1986).
[61]J. Noland, "Measurements of plasma bremsstrahlung and plasma energy density produced by electron cyclotron resonance ion source plasmas," Ph.D. thesis, University of California, Berkeley, 2011, https://digitalassets.lib.berkeley.edu/etd/ucb/text/Noland_berkeley_0028E_11247.pdf.

Supplementary material for manuscript "Quasi-periodical kinetic instabilities in minimum-B confined plasma"

I. DATA ANALYSIS

Figure 1 shows an example of typical signal, i.e. single instability burst (red curve superimposed on the blue background) measured using the scintillator x-ray diagnostics. The peak amplitude is calculated from the average background signal preceding the instability burst and the peak area is integrated starting from the point where the leading edge of the instability signal is 5 % above the baseline until the point when the signal at the trailing edge of the instability has reached the baseline value.

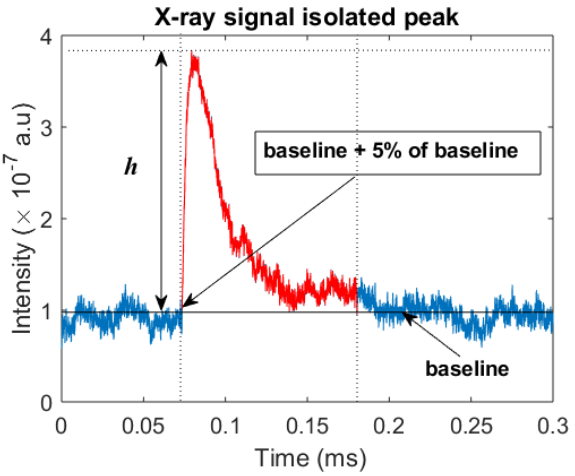

FIG. 1. An example of the x-ray burst associated to the instability. The determination of the baseline signal and boundaries of the peak area integration are highlighted.

The area of the peak is proportional to the plasma energy loss caused by the instability. In order to find a relation connecting the peak amplitude h and peak area, a suitable data set of single burst cases (mode $n=1$ in the main article) was selected for detailed analysis. Figure 2 shows that the x-ray peak area depends linearly on the peak amplitude. The linear fit shown here is used for calculating the corresponding area (relative plasma energy loss) from the amplitude of the x-ray signal in the main article. The linear dependence follows from the operating principle of the scintillator-PMT detector where the incident power flux is converted to electric charge.

The method for determining the time threshold to classify each burst (m) and event (n) is illustrated in Fig. 3. The figure shows the time difference (Δt) distribution between consecutive x-ray peaks from several 10 s data sets acquired with different ion source parameters. The resulting distribution has two well-separated peaks.

The first distribution corresponds to the time difference of bursts within the instability event, i.e. m-modes and the second one to the time difference between the instability events,

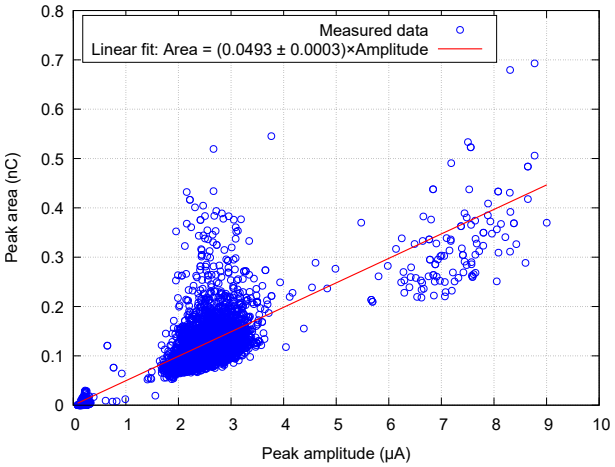

FIG. 2. The linear fit to determine the correlation between the peak area and the measured peak amplitude for the x-ray data. The experimental data corresponds to about 8630 instances of $n=1$ (single burst) x-ray events measured with the X-ray scintillator with varying plasma parameters.

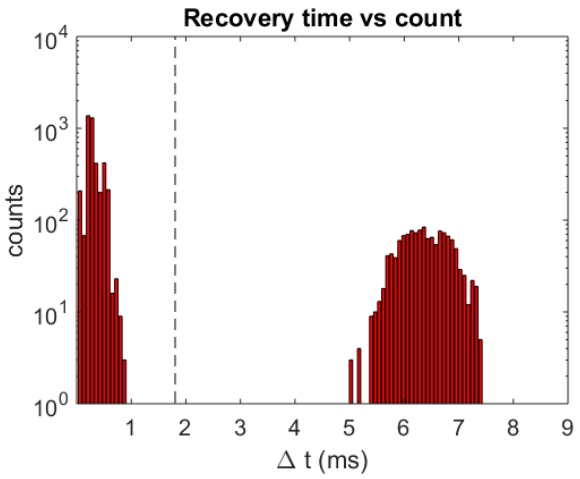

FIG. 3. Illustration of the time threshold determination for classifying instability emission bursts and events into various m and n modes with the distribution on the left side represents the m modes and the one on the right side the n modes.

i.e. n-modes (see also Fig. 4 in the main article for the clarification). The time threshold of 1.7 ms for the classification of different modes was obtained by finding the minimum between the two maxima of the temporal distribution.

Figure 4 shows an example of the energy flux of an event as a function of the recovery/accumulation time. The average values and their standard deviation (e.g. Fig. 9 of the main article) are calculated from the scatter plots.

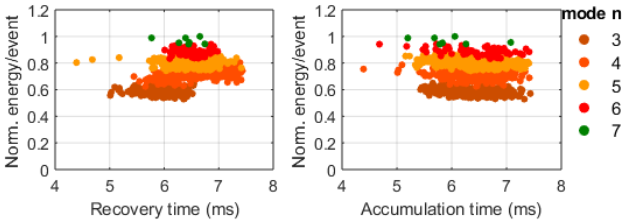

FIG. 4. An example of the normalized energy of an event as a function of the recovery/accumulation time. The plot corresponds to B_{min}/B_{ecr}-value of 0.76, 3.5×10^{-7} mbar oxygen pressure and 400 W RF power.

II. SELECTION OF X-RAY SIGNAL OVER MICROWAVE SIGNAL

The experiments described in the manuscript were conducted with several complimentary diagnostics. Although the microwave emission is the primary signal revealing the existence of maser-type instability, the x-ray signal induced by losses of electrons to the plasma chamber walls proved to be more reliable for statistical analysis. That is because, the Schottky diode employed for microwave detection, sometimes failed to register emission signals, typically the last (weakest) ones of a multi-peak event as demonstrated in an example shown in Fig. 5. We attribute the effect to the frequency-dependent coupling of the emission signal into the diagnostics waveguide and its cut-off frequency. Hence, the data analysis was performed for the x-ray signal alone.

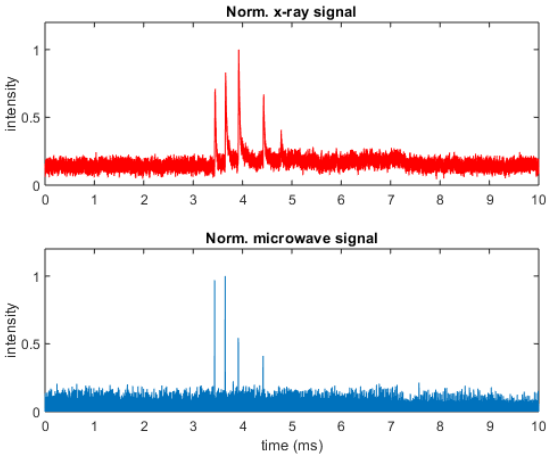

FIG. 5. An illustration of why the bremsstrahlung (x-ray) signal was preferred over the microwave diode detector. The data corresponds to B_{min}/B_{ecr} value of 0.76, pressure of 3.5×10^{-7} mbar and RF power of 400 W. Four microwave and x-ray emission peaks are observed in co-incidence. However, the fifth x-ray emission, which is the weakest of the bursts, is not associated with *detected* microwave emission, i.e. using the microwave signal would lead to false classification of the $n = 5$ event to $n = 4$ event.

III. DATA REPRODUCIBILITY

The reproducibility of the data was confirmed by acquiring the magnetic field sweep data twice. In each case the analysed data consists of 10 s of recorded data at each coil setting. It was found that the total number of instability bursts and the total emitted energy varied not more than 3.5 % at each point of the sweep between the two data sets. Figure S6 shows the relative fraction of instability event mode n (a), the average energy emitted per event versus the accumulation time (b), the average energy emitted per event versus the recovery time (c), and the dependence of the post-emission time on the energy emitted per burst m (d) for the two magnetic field sweeps. The figure illustrates that the main results of the study are reproduced very well for both, n and m

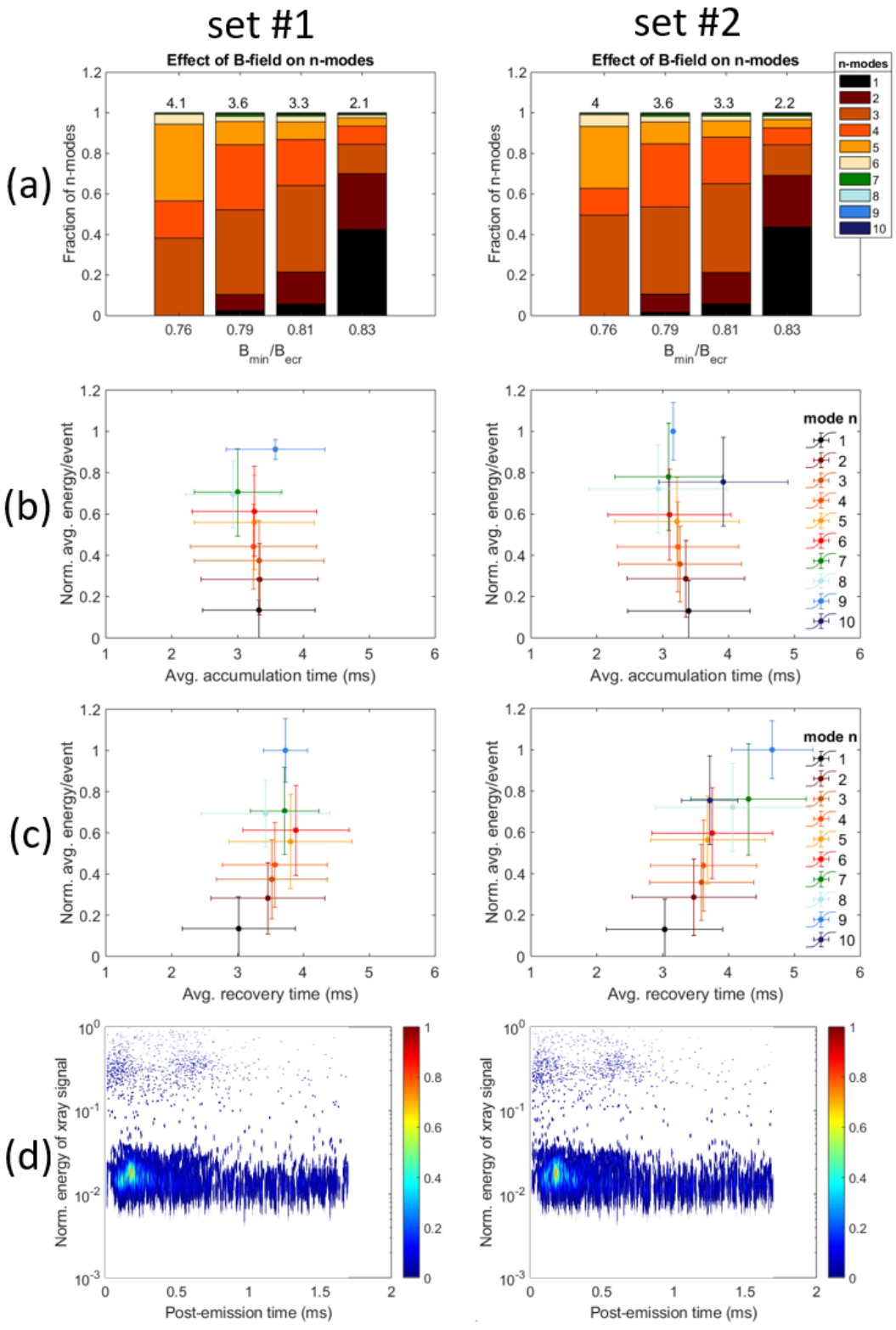

FIG. 6. Comparison of results from two identical magnetic field sweeps demonstrating the reproducibility of the acquired data; the relative fraction of instability event mode n (a), the average energy emitted per event versus the accumulation time (b), the average energy emitted per event versus the recovery time (c), and the dependence of the post-emission time on the energy emitted per burst m (d) for the two magnetic field sweeps. The plots labeled as *'Set #1'* (left column) show the data presented in the main manuscript and *'Set #2'* (right column) the data for the repeated measurement.

Résumé de la thèse en Français (Dissertation summary in French)

Introduction

Les applications des sources d'ions à la résonance cyclotronique électronique (ECRIS) ont considérablement augmenté au cours des dernières décennies. Les sources d'ions ECR sont utilisées pour produire des ions hautement chargés (HCI) à des fins diverses, notamment des expériences de physique atomique et nucléaire, des tests de dureté aux rayonnements de l'électronique spatiale, la radiothérapie pour le traitement du cancer, des expériences de physique des particules, etc. Dans la recherche en physique nucléaire et en physique des particules, les sources d'ions ECR sont utilisées comme injecteurs pour les accélérateurs linéaires, les générateurs Van-de-Graff, les synchrotrons et les cyclotrons. En physique atomique et des surfaces, les sources d'ions ECR fournissent des faisceaux intensifs d'ions hautement chargés pour des expériences de collision ou des examens de surface. Un avantage significatif de ce type de générateur d'ions est que des ions de tous les éléments peuvent être créés. En outre, la source d'ions ne comporte pratiquement aucune pièce d'usure, comme les filaments. Par conséquent, il est possible de réaliser des faisceaux d'ions stables pendant de longues périodes (de quelques jours à quelques mois), la seule limite étant la consommation de matériau de l'élément utilisé. Les métaux qui sont injectés dans la source sous forme d'atomes qui sont pulvérisés dans le plasma, ou qui sont évaporés d'un four, doivent être remplacés après un temps déterminé. Les sources d'ions ECR fonctionnent à une faible pression de gaz et ont un rendement élevé d'ionisation du plasma. De ce fait, elles sont particulièrement adaptées à la production de faisceaux d'ions d'éléments radioactifs, rares ou extrêmement coûteux. Depuis la première mise en service d'une source d'ions ECR en 1975, les performances en termes d'états de charge possibles et de leur intensité se sont rapidement améliorées. Dans une ECRIS, les ions hautement chargés sont produits dans un plasma hors équilibre confiné dans une structure magnétique. Le confinement magnétique est réalisé par une superposition de champs magnétiques solénoïdal et hexapolaire, créant ainsi une topologie de confinement à minimum-B. Il a été démontré que les plasmas ECRIS présentent des instabilités cinétiques, ce qui limite fortement l'intensité des faisceaux d'ions hautement chargés. Ces instabilités cinétiques sont dues à l'anisotropie en vitesse et à la non-monotonie de la queue haute énergie de distribution en énergie des électrons (EED) du plasma de source ECR. L'EED est affectée par le champ magnétique de l'ECRIS. L'objectif de ce travail est d'affiner la compréhension des mécanismes physiques qui déterminent la relation complexe entre les paramètres du champ magnétique de l'ECRIS et la transition d'un régime de fonctionnement stable à un régime instable.

Il est reconnu depuis longtemps que le contrôle des instabilités cinétiques est l'une des questions les plus difficiles dans le développement des plasmas de fusion à haute température et des accélérateurs médicaux. De plus, de telles

instabilités ont également été observées dans des plasmas spatiaux provoquant des émissions radio cohérentes de la couronne solaire et de la magnétosphère terrestre. Cette thèse se concentre également sur le regroupement temporel des émissions cyclotroniques dues aux instabilités qui ont été largement observées sur les plasmas spatiaux mais qui sont rapportées pour la première fois ici avec des études systématiques utilisant des plasmas de laboratoire chauffés par le mécanisme ECR. En conséquence, les études d'instabilité cinétique réalisées avec les ECRIS contribuent à une meilleure compréhension des instabilités qui se produisent dans divers plasmas de laboratoire et dans les plasmas spatiaux, ce qui est le sujet principal de cette thèse.

Cette thèse est organisée comme suit : Le deuxième chapitre traite des fondements théoriques nécessaires à la compréhension du fonctionnement des plasmas ECR et fournit une brève discussion du contexte théorique des instabilités cinétiques qui y sont observées. Le troisième chapitre décrit les sources d'ions, les montages expérimentaux et les méthodes de diagnostic qui ont été utilisés dans la partie expérimentale de ce travail. Une attention particulière a été accordée à la source d'ions ECR JYFL 14 GHz, qui est exploitée au laboratoire d'accélération du département de physique de l'université de Jyväskylä, puisque la plupart des expériences ont été menées avec cette source d'ions. Le chapitre 4 décrit le développement d'un outil de calcul robuste pour obtenir la distribution du champ magnétique dans une ECRIS, ainsi que le développement d'un outil de traitement du signal et d'analyse des données pour étudier l'évolution temporelle des signaux induits par l'instabilité. Le chapitre 5 résume les principaux résultats du travail expérimental. Le chapitre est organisé en quatre sections : la première section contient les résultats démontrant comment les facteurs du champ magnétique affectent l'instabilité de diverses sources d'ions, ainsi qu'une comparaison de cinq sources d'ions distinctes employées dans ce travail de thèse. La deuxième section se concentre sur le rôle joué par les rapports de miroir axial dans l'atténuation des électrons chauds et leur influence sur les instabilités cinétiques. La troisième section du chapitre 5 se concentre sur le bremsstrahlung du plasma et la distribution d'énergie des électrons perdus, en mettant l'accent sur l'instabilité cinétique. La quatrième section présente la première étude systématique de la structure temporelle et de l'intensité des instabilités cinétiques dans le plasma ECR. Le chapitre 6 contient une discussion approfondie ainsi que les implications qui peuvent en être tirées.

Synthèse

Le deuxième chapitre de la thèse est intitulé "Theoretical aspects of ECR plasma", et donne le contexte théorique nécessaire à la compréhension du fonctionnement des sources d'ions ECR, ainsi qu'un bref aperçu théorique des instabilités cinétiques trouvées dans les sources d'ions ECR. Ce chapitre est divisé en trois sections. La première, intitulée "Introduction à la physique des plasmas", traite des caractéristiques fondamentales des plasmas et des critères permettant de classer un système comme un plasma. Parmi ceux-ci figurent les définitions de la quasi-neutralité, de la fréquence plasma, de la gaine plasma et du potentiel plasma. La deuxième section, intitulée "Principes de fonctionnement du plasma ECR", traite de la physique qui sous-tend le fonctionnement des sources d'ions ECR. Cette section détaille la technique de confinement du plasma par un champ magnétique externe employée dans l'ECRIS, ainsi que le rôle du champ magnétique dans le processus de chauffage des électrons. En outre, cette section décrit le mécanisme de chauffage des électrons par l'apport d'une onde électromagnétique radiofréquence externe. Le processus d'ionisation étape par étape des particules fournies par l'extérieur et la production ultérieure d'ions hautement chargés sont également détaillés dans cette section. Vers la fin de cette section, l'ensemble du processus de production d'ions hautement chargés est résumé dans le contexte des sources d'ions ECR. La dernière section, intitulée "Instabilités cinétiques dans le plasma ECR", traite des instabilités cinétiques observées dans les sources d'ions ECR et donne un bref aperçu des études antérieures sur les instabilités cinétiques. Cette section comprend également une brève explication théorique sur le développement des instabilités cinétiques basée sur les études récentes.

Le troisième chapitre est intitulé "Experimental setup and methods" et est divisé en deux sections. La première section est divisée en deux sous-sections dont la première détaille les informations techniques d'une source d'ions ECR. La plupart des expériences réalisées dans le cadre de cette thèse l'ont été dans l'ECRIS 14 GHz de JYFL, une source d'ions ECR de deuxième génération située à Jyväskylä, en Finlande ; par conséquent, les détails techniques de cette source d'ions ont été détaillés dans cette section. En fonction de l'objectif de chaque partie de la source d'ions, l'ECRIS 14 GHz de JYFL a été divisée en trois parties. Il s'agit de (a) la section de production d'ions, (b) la section de formation du faisceau d'ions et (c) la section de séparation charge-masse et de mesure du courant ionique. La sous-section (a) explique en profondeur les conditions de vide requises pour la source d'ions, la méthode de chauffage du plasma et les méthodes d'injection des particules. Le système d'extraction des faisceaux d'ions et la formation des faisceaux sont expliqués dans la sous-section (b), et la séparation des faisceaux extraits en fonction de leur rapport charge/masse correspondant à l'aide d'un aimant dipôle, ainsi que la détection du courant ionique à l'aide d'une coupe de Faraday, sont expliquées dans la sous-section (c). Les études d'instabilité ont égale-

ment été menées dans quatre autres sources d'ions ECR, notamment PHOENIX Booster et PHOENIX V3 au LPSC en France, la source d'ions GTS au GANIL en France, et la source d'ions ECR supraconductrice de troisième génération SECRAL-II à l'IMP-CAS en Chine. Par conséquent, la deuxième sous-section est incluse pour fournir un bref synopsis de toutes ces sources d'ions. Les différences de structures géométriques entre ces sources d'ions sont également présentées dans cette sous-section. La deuxième section du troisième chapitre est consacrée aux différents diagnostics utilisés pour détecter le début de l'instabilité. Cette section a été divisée en quatre sous-sections en fonction de chaque signal de diagnostic détecté. Tout d'abord, les méthodes de détection utilisées pour les micro-ondes émises par le plasma sont expliquées. L'émission de micro-ondes pendant le seuil d'instabilité est détectée à l'aide de deux méthodes différentes : (a) en utilisant une diode Schottky à faible tension de seuil et (b) en utilisant un analyseur de spectre micro-ondes. Les deux méthodes de détection sont décrites et un échantillon des signaux obtenus à l'aide de ces diagnostics est présenté dans cette section. Ensuite, la détection des électrons chauds émis lors du début de l'instabilité est présentée à l'aide de deux diagnostics différents. A savoir, 1) en mesurant la distribution en énergie des électrons s'échappant du confinement de la source à l'aide d'un aimant dipolaire agissant comme un séparateur dispersif d'énergie et 2) en mesurant les émissions de particules associées à chaque rafale d'instabilité à l'aide d'un disque polarisé fixé à l'extrémité de l'injection de la source d'ions. Le dispositif expérimental et l'échantillon des signaux obtenus ainsi que la technique d'extraction des données à partir de la distribution d'énergie des électrons perdus en utilisant ce dispositif ont également été fournis dans cette section. Troisièmement, la mesure des signaux bremsstrahlung pendant les salves d'instabilité ainsi que la mesure directe des émissions bremsstrahlung du plasma confiné sont réalisées à l'aide de deux méthodes de diagnostic. La première méthode utilise un scintillateur plastique couplé à un photomultiplicateur, placé à l'extérieur de la source d'ions. La deuxième méthode utilise un détecteur à semi-conducteurs placé sur l'axe de la source d'ions (ou éventuellement radialement) avec une ligne de visée directe vers le plasma. Le signal obtenu à l'aide de cette configuration et l'analyse du signal sont également présentés dans cette section. Enfin, le montage de diagnostic pour détecter la variation du courant du faisceau d'ions due au début de l'instabilité est décrit. Ce signal est mesuré à l'aide d'une coupe de Faraday placée en aval du dipole. Un exemple du signal détecté montrant le début de l'instabilité est également fourni dans cette section.

Le quatrième chapitre de la thèse est intitulé "Development of computational tools" et est divisé en deux sections. La première section explique la procédure de développement de l'outil de calcul pour modéliser la distribution tridimensionnelle du champ magnétique. Cette section décrit comment déterminer analytiquement la distribution du champ magnétique d'une ECRIS et comment

extraire la surface résonante à l'aide d'un outil de calcul. Le champ magnétique dans une ECRIS est calculé analytiquement par la superposition des champs magnétiques solénoïdal et hexapolaire. La modélisation du champ magnétique décrite dans cette partie est réalisée en obtenant le champ magnétique le long de l'axe de la chambre et les champs magnétiques radial et azimutal le long des parois de la chambre à plasma cylindrique à l'aide de solveurs d'éléments finis bidimensionnels tels que FEMM. Cette section détaille la procédure de dérivation d'un champ magnétique tridimensionnel à partir d'un champ magnétique bidimensionnel. En outre, l'outil de calcul créé est capable d'extraire la surface résonante tridimensionnelle de l'ECR et de calculer la distribution du gradient de champ magnétique sur la surface de résonance ECR. Le développement étape par étape de ces méthodes est expliqué dans cette section. Ainsi, cet outil de calcul développé peut être utilisé pour toutes les sources d'ions ECR, à condition que la distribution du champ magnétique le long de l'axe et la distribution radiale et azimutale du champ magnétique le long de la paroi de la chambre à plasma soient connues. La deuxième section de ce chapitre fournit les détails d'un outil d'analyse de données temporelles dédié, développé dans le cadre de l'une des campagnes expérimentales. La campagne expérimentale a été conçue pour étudier l'émission quasi-périodique des sursauts d'instabilité en analysant de multiples signaux de diagnostic. L'outil d'analyse permet d'effectuer une analyse statistique sur une grande quantité de données collectées avec des signaux haute résolution (de l'ordre de 16 ns) enregistrés pendant dix secondes chacun. L'outil d'analyse est utilisé pour obtenir l'amplitude des salves d'instabilité ainsi que sa structure temporelle. Cette campagne a également permis de mettre en évidence des regroupements de salves d'instabilité de l'ordre de centaines de microsecondes suivis de longues périodes de repos de 1 à 10 millisecondes. Le code d'analyse est également capable de classer ces salves d'instabilité "groupées" en modes. La méthode d'analyse détaillée pour extraire ces données ainsi que l'algorithme de classification des modes observés sont expliqués dans cette section.

Le quatrième chapitre de cette thèse est intitulé "Development of computational tools" et est divisé en deux sections. La première section explique la procédure de développement de l'outil de calcul pour modéliser la distribution tridimensionnelle du champ magnétique. Cette section décrit comment déterminer analytiquement la distribution du champ magnétique d'un ECRIS et comment extraire la surface résonante à l'aide d'un outil de calcul. Le champ magnétique dans un ECRIS est calculé analytiquement par superposition des champs magnétiques solénoïdal et hexapolaire. La modélisation du champ magnétique décrite dans cette partie est réalisée en obtenant le champ magnétique le long de l'axe de la chambre et les champs magnétiques radial et azimutal le long des parois de la chambre à l'aide de solveurs d'éléments finis bidimensionnels tels que FEMM. Par conséquent, cette section détaille la procédure de dérivation d'un champ magné-

tique tridimensionnel à partir d'un champ magnétique bidimensionnel. En outre, l'outil de calcul créé était capable d'extraire la surface résonante tridimensionnelle de l'ECR et de calculer la distribution du gradient de champ magnétique sur la surface de l'ECR. Le développement étape par étape de ces méthodes a été expliqué dans cette section. Ainsi, cet outil de calcul développé peut être utilisé pour toutes les sources d'ions ECR, à condition que la distribution du champ magnétique le long de l'axe et la distribution radiale et azimutale du champ magnétique le long de la paroi de la chambre à plasma soient connues. La deuxième section de ce chapitre fournit les détails d'un outil d'analyse de données dédié développé dans le cadre de l'une des campagnes expérimentales. La campagne expérimentale a été conçue pour étudier l'émission quasi-périodique des sursauts d'instabilité en analysant de multiples signaux de diagnostic. Un outil d'analyse dédié a dû être développé afin d'effectuer une analyse statistique sur une énorme quantité de données collectées avec des signaux haute résolution (de l'ordre de 16 ns) enregistrés pendant dix secondes chacun. L'outil d'analyse développé est utilisé pour obtenir l'amplitude des salves d'instabilité ainsi que sa structure temporelle. Cette campagne a également permis de mettre en évidence des regroupements de salves d'instabilité de l'ordre de centaines de microsecondes suivis de longues périodes de repos de 1 à 10 millisecondes. Le code d'analyse développé est également capable de classer ces salves d'instabilité "groupées" en modes. La méthode d'analyse détaillée pour extraire ces données ainsi que l'algorithme de classification des modes observés sont expliqués dans cette section.

Le cinquième chapitre est intitulé "Experimental works and main results" et est divisé en quatre sections. Chaque section de ce chapitre se concentre sur les différentes campagnes expérimentales réalisées dans le cadre de cette thèse. Chaque section résume la motivation principale de chacune des campagnes expérimentales, sa méthodologie et les résultats les plus significatifs obtenus lors de chaque campagne. La première section de ce chapitre est intitulée "Implémentation du code de modélisation du champ magnétique" et illustre la pertinence de l'outil de modélisation du champ magnétique développé dans le cadre de cette thèse. Cette section est divisée en trois sous-sections. La première sous-section traite des caractéristiques globales du champ magnétique partagées par toutes les sources d'ions modélisées. Cette étude a révélé une relation cruciale entre le gradient moyen du champ magnétique (dans la surface de l'ECR) calculé à l'aide de l'outil de calcul développé et le rapport entre l'intensité minimale du champ magnétique et l'intensité du champ magnétique dans la zone de résonance. La deuxième sous-section décrit l'application de l'outil de modélisation du champ magnétique à l'étude des valeurs de seuil d'instabilité déterminées expérimentalement pour diverses sources d'ions ECR. Cette étude a révélé que le seuil d'instabilité ne peut être défini sur la base d'un seul paramètre de champ magnétique ; il est plutôt influencé par une combinaison de paramètres. La dernière sous-section

illustre la manière dont l'outil de modélisation a été utilisé pour expliquer les résultats d'une expérience menée avec la source d'ions SECRAL-II (à l'IMP-CAS, en Chine), qui visait à étudier le rôle de la configuration du champ magnétique dans la population d'électrons chauds. Cette étude a révélé que la diminution du gradient de champ magnétique moyen entraîne une augmentation de la température spectrale, laquelle reflète l'augmentation de la population d'électrons chauds. La deuxième section du cinquième chapitre résume l'expérience réalisée dans la source d'ions GTS afin d'identifier l'effet des rapports de miroir axiaux de la source d'ions GTS (au GANIL, France) sur le seuil d'apparition de l'instabilité. Cette expérience a révélé qu'en faisant varier le rapport global des miroirs, on pouvait affecter la population d'électrons chauds et donc modifier le seuil de déclenchement de l'instabilité. La troisième section de ce chapitre présente la campagne expérimentale menée sur la source ECRIS JYFL 14 GHz (JYU, Finlande) afin d'identifier la corrélation entre l'émission de bremsstrahlung du plasma confiné et la distribution en énergie des électrons perdus par le confinement, ainsi que son comportement pendant le début de l'instabilité. Il a été observé que la température spectrale obtenue à partir des mesures de bremsstrahlung est en corrélation avec l'énergie moyenne de la bosse de haute énergie observée dans la distribution en énergie des électrons perdus par le plasma. Cette expérience a également révélé que la bosse de haute énergie disparaît avec le début de l'instabilité. La dernière section de ce chapitre traite de la campagne expérimentale qui a été menée pour mieux comprendre la nature temporelle des salves d'instabilité et leur relation avec l'ampleur de l'émission d'instabilité. Cette campagne expérimentale a révélé que plus l'amplitude de l'instabilité est élevée, plus le temps de repos après les salves d'instabilité est important. Elle a également révélé un regroupement des rafales d'instabilité qui avait été observé précédemment dans les plasmas magnétosphériques.

Le dernier chapitre est intitulé "Discussions and conclusions". Ce chapitre résume l'ensemble des recherches entreprises pour cette thèse. Le chapitre discute des principaux résultats des diverses modélisations expérimentales et informatiques en termes de cadre théorique établi. De plus, ce chapitre discute des futurs travaux expérimentaux et théoriques qui pourraient être menés pour approfondir notre compréhension des instabilités cinétiques présentées par les sources d'ions ECR.